

**A STUDY OF MOLYBDENUM CARBIDE CATALYSTS SUPPORTED ON CARBON
DERIVED FROM PETROLEUM COKE FOR HYDROTREATING**

by

Haiyan Wang

M.Sc., China University of Petroleum (Beijing), 2013

B.Sc., China University of Mining and Technology, 2010

A THESIS SUBMITTED IN PARTIAL FULFILLMENT OF

THE REQUIREMENTS FOR THE DEGREE OF

DOCTOR OF PHILOSOPHY

in

THE FACULTY OF GRADUATE AND POSTDOCTORAL STUDIES

(Chemical and Biological Engineering)

THE UNIVERSITY OF BRITISH COLUMBIA

(Vancouver)

November 2018

© Haiyan Wang, 2018

The following individuals certify that they have read, and recommend to the Faculty of Graduate and Postdoctoral Studies for acceptance, the dissertation entitled:

A Study of Molybdenum Carbide Catalysts Supported on Carbon Derived from Petroleum Coke for Hydrotreating

submitted by Haiyan Wang in partial fulfillment of the requirements for

the degree of Doctor of Philosophy

in Chemical and Biochemical Engineering

Examining Committee:

Kevin J. Smith, Chemical and Biological Engineering
Supervisor

Naoko Ellis, Chemical and Biological Engineering
Supervisory Committee Member

Keng C Chou, Department of Chemistry
Supervisory Committee Member

Elod Gyenge, Department of Chemical Engineering
University Examiner

Jennifer Love, Department of Chemistry
University Examiner

Additional Supervisory Committee Members:

Supervisory Committee Member

Supervisory Committee Member

Abstract

Mo₂C catalysts supported on carbon have been investigated for use in hydrotreating reactions that remove S, N and O from oil fractions. The thesis reports on the stability of the catalysts in the presence of different model reactants. The synthesis of mesoporous carbons derived from petroleum coke (petcoke), a by-product of Canadian oilsand upgrading, is described. The impact of the mesoporous carbon as a support of the Mo₂C catalysts is also examined.

An activated charcoal (AC) was initially used as the carbon source to prepare Mo₂C/AC and Ni-Mo₂C/AC catalysts by carbothermal hydrogen reduction (CHR). The most active catalyst for 4-methylphenol (4-MP) hydrodeoxygenation (HDO) was obtained at a CHR temperature of 650 °C. The direct deoxygenation selectivity of this catalyst was > 78%, indicative of high O removal with low H₂ consumption. The effect of a Ni promoter on the synthesis and activity of Ni-Mo₂C/AC catalysts was also assessed. The presence of Ni significantly reduced the CHR temperature required for Mo₂C formation by 100 °C. However, the Ni accelerated catalyst sulfidation during hydrodesulphurization (HDS) and formed a unique core-shell Mo₂C-MoS₂ structure. Additionally, there was an improved activity in HDS of dibenzothiophene (DBT) in the presence of Ni, provided the Ni:Mo < 0.44.

Extending these results to petcoke, the transition of Mo species and the corresponding changes to the activated petroleum coke (APC) morphology that occur during CHR were determined. A maximum mesoporosity of 37% was achieved for a sample reduced to 750 °C. The activity of the Mo₂C/APC catalysts for the HDO of 4-MP was > 3x's higher than that of Mo₂C/AC because of

the high surface area ($\sim 2000 \text{ m}^2/\text{g}$) of the $\text{Mo}_2\text{C}/\text{APC}$ catalyst, and the high dispersion of the Mo_2C nanoparticles.

Finally, the stability of the $\text{Mo}_2\text{C}/\text{APC}$ catalysts during the HDS, hydrodenitrogenation and HDO of DBT, carbazole and dibenzofuran, respectively, was determined as a function of the Mo_2C average particle size. DFT calculations were combined with experimental data to explain the selectivity change from hydrogenation to DDS observed during the HDS of DBT. Both S and N irreversibly deactivated the catalysts; whereas, the effect of O was reversible.

Lay Summary

The goal of this study was to prepare new catalysts from Canadian oilsands petroleum coke, a by-product of the oilsands upgrading operations. The catalysts were used to remove contaminants (S, N and O) from oil fractions. Initial work showed that the new catalyst, based on the formation of molybdenum carbide (Mo_2C), had good performance in removing O from a model reactant. Nickel added to the catalyst reduced the temperature required for the catalyst synthesis. The mechanism of formation of the Mo_2C supported on the activated petroleum coke was also studied, together with the development of porosity within the coke. Finally, the impact of the different heteroatoms (S, N and O) present in the oil on the stability of the catalyst was studied to assess the possibility of using these new catalysts in oil-refining processes.

Preface

This Ph.D. dissertation consists of seven chapters. Chapter 2, 3, and 4 have been published previously in peer-reviewed journals. A version of Chapter 5 is in preparation to be submitted for publication. The Ph.D. study was conducted by Haiyan Wang under the direct supervision of Professor Kevin J. Smith in the Department of Chemical and Biological Engineering at UBC. The literature review, catalyst synthesis and characterization, reactor set-up, catalyst testing, data collection and interpretation, kinetic modeling, and preparation of the dissertation were done by Haiyan Wang under the direct supervision of Professor Kevin Smith.

The list of the publications included in this thesis is given below:

1. H. Wang, S. Liu, and K. J. Smith, "Synthesis and hydrodeoxygenation activity of carbon supported molybdenum carbide and oxycarbide catalysts", *Energy and Fuels* (2016) 30 (7): 6039-6049. A version of this manuscript is included in Chapter 2.

The carbon supported Mo_2C preparation, characterizations, hydrodeoxygenation reactions, kinetic modeling, as well as data analysis and interpretation were done by Haiyan Wang under the direct supervision of Professor Kevin. J. Smith. In addition, the preparation and writing of the manuscript were done by Haiyan Wang with final approval of Professor Kevin J. Smith. The XPS measurements were performed by Dr. Ken Wong from the Interfacial Analysis and Reactivity Laboratory at UBC. The TEM images were done by Shida Liu in FRIPP, China.

2. H. Wang, S. Liu, R. Govindarajan, and K. J. Smith, "Preparation of Ni-Mo₂C/carbon catalysts and their stability in the HDS of dibenzothiophene," *Applied Catalysis A: General* (2017) 539 (5): 114-127. A version of this manuscript is included in Chapter 3.

The catalysts preparation and characterization, experimental design and set-up, HDS reaction of DBT, sample testing and analysis, and kinetic modeling were performed by Haiyan Wang under the direct supervision of Professor Kevin J. Smith. Shida Liu contributed to the discussion of the results of this work. Some of the catalyst precursors were prepared by Ruben Govindarajan. The XPS and TOF-SIMS measurements were performed by Dr. Ken Wong and Dr. John Kim, respectively from the Interfacial Analysis and Reactivity Laboratory at UBC. STEM measurements were conducted by Dr. Xin Zhang from 4D labs at SFU. Finally, the writing of this manuscript was done by Haiyan Wang with the final approval of Professor Kevin J. Smith.

3. H. Wang, S. Liu., B. Liu, V. Montes, J. M. Hill, and K. J. Smith, "Carbon and Mo transformation during the synthesis of mesoporous Mo₂C/carbon catalysts by carbothermal hydrogen reduction," *Journal of Solid State Chemistry* (2018) 258: 818-824. A version of this manuscript is included in Chapter 4.

All the catalyst synthesis and characterization, HDO reactions, data collection and interpretation were done by Haiyan Wang under the direct supervision of Professor Kevin J. Smith. The manuscript preparation and writing were done by Haiyan Wang with the final approval of Professor Kevin J. Smith. Shida Liu contributed to the experimental

design and data interpretation. Dr. Bing Liu performed the DFT calculations using VASP. Dr. Vicente Montes and Professor Josephine M. Hill contributed to the data interpretation of carbon based materials and manuscript revision. The XPS measurement was performed by Dr. Ken Wong from the Interfacial Analysis and Reactivity Laboratory at UBC.

4. H. Wang, S. Liu, and K. J. Smith, “Understanding selectivity changes during hydrodesulfurization of dibenzothiophene on Mo₂C/carbon catalysts”, *Journal of Catalysis* (2018), in preparation. A version of this manuscript is included in Chapter 5.

The catalyst preparation, characterization, reactor modification, experimental design, sample collection and data analysis were done by Haiyan Wang under the direct supervision of Professor Kevin J. Smith. The effect of S on different particle size Mo₂C catalysts were studied in a fixed bed reactor. All the DFT calculations were conducted by Shida Liu using VASP software. The manuscript was prepared and written by Haiyan Wang with final approval of Professor Kevin J. Smith. The XPS measurement was performed by Dr. Ken Wong from the Interfacial Analysis and Reactivity Laboratory at UBC.

Additionally, the following list summarizes the conference papers in proceedings of various international conferences:

- H. Wang, K. J. Smith, (2015) “*Synthesis and hydrodeoxygenation activity of carbon supported molybdenum carbide and oxycarbide catalysts*”. 65th Canadian Chemical Engineering (CSCChE) Conference, Calgary, Canada.
- H. Wang, S. Liu and K. J. Smith, (2016) “*Carbon supported Ni-Mo₂C for hydrodesulfurization*”. 16th International Congress on Catalysis (ICC), Beijing, China.
- H. Wang, S. Liu and K. J. Smith, (2017) “*The activity and stability of Mo₂C supported on activated petroleum coke in hydrotreating reactions*”. 2017 American Institute of Chemical Engineers (AIChE) Annual Meeting, Minnesota, USA.
- H. Wang, S. Liu and K. J. Smith, (2018) “*Transition of Mo₂C/carbon catalyst in HDS of dibenzothiophene: the effect of different particle sizes, CHR temperatures and promoters*”. 25th Canadian Symposium on Catalysis (CSC), Saskatoon, Canada.

Table of Contents

Abstract.....	iii
Lay Summary	v
Preface.....	vi
Table of Contents	x
List of Tables	xviii
List of Figures.....	xxv
List of Nomenclature	xxxiv
List of Abbreviations	iv
Acknowledgements	viii
Chapter 1: Introduction	1
1.1 Background	1
1.1.1 Synthesis Methods of Molybdenum Carbide (Mo ₂ C) Catalysts.....	1
1.1.2 Carbon Supported Catalysts and their Application in Hydrotreating Reaction	3
1.1.2.1 Hydrotreating Technology	3
1.1.2.2 Carbon Supported Catalysts in Hydrodesulphurization (HDS) and Hydrodenitrogenation (HDN).....	4
1.1.2.3 Carbon Supported Catalysts in Hydrodeoxygenation (HDO)	4
1.1.3 Activation Methods of Carbonaceous Materials.....	6
1.1.3.1 Physical Activation	6
1.1.3.2 Chemical Activation	8
1.1.3.3 Catalytic Activation by Metals	11
1.1.3.4 Petroleum Coke.....	13

1.1.4	Summary	15
1.2	Objectives of the Thesis	16
1.3	Approach.....	17
1.4	Outline of the Dissertation	18
Chapter 2: Synthesis of Mo₂C/AC Catalysts and the Application in HDO of 4-methylphenol		
.....		21
2.1	Introduction.....	21
2.2	Experimental	22
2.2.1	Materials	22
2.2.2	Catalyst Preparation	23
2.2.3	Catalyst Characterization	24
2.2.3.1	N ₂ Adsorption and Desorption.....	24
2.2.3.2	X-ray Diffraction (XRD)	24
2.2.3.3	X-ray Photoelectron Spectroscopy (XPS)	25
2.2.3.4	CO Chemisorption	25
2.2.3.5	O Content Anlysis.....	26
2.2.3.6	Transmission Electron Microscopy (TEM)	26
2.2.4	Hydrodeoxygenation of 4-methylphenol	26
2.3	Results.....	28
2.3.1	Catalyst Characterization	28
2.3.1.1	Textural Properties by BET Analysis and Carbon Loss during CHR	28
2.3.1.2	XRD Analysis	30
2.3.1.3	XPS, O Analysis and CO Uptake	32

2.3.1.4	TEM Analysis	36
2.3.2	Catalytic Performance in HDO of 4-MP	39
2.4	Discussion	45
2.5	Conclusions	51
Chapter 3: Preparation of Mo₂C/AC and Ni-Mo₂C/AC Catalysts and their Stability in HDS		
of Dibenzothiophene		53
3.1	Introduction	53
3.2	Experimental	55
3.2.1	Catalyst Preparation	55
3.2.2	Catalyst Characterization	56
3.2.2.1	Elemental Analysis	56
3.2.2.2	N ₂ Adsorption and Desorption	57
3.2.2.3	X-ray Diffraction (XRD)	57
3.2.2.4	X-ray Photoelectron Spectroscopy (XPS)	57
3.2.2.5	Transmission Electron Microscopy (TEM)	57
3.2.2.6	Time of Flight Secondary Ion Mass Spectroscopy (TOF-SIMS)	58
3.2.3	Catalyst Activity Tests	59
3.3	Results	62
3.3.1	Fresh Catalysts Characterization	62
3.3.2	Catalysts Characterization after HDS Reaction	70
3.3.2.1	XRD and BET Analysis	71
3.3.2.2	XPS and CHNS Analysis	72
3.3.2.3	TOF-SIMS Analysis	77

3.3.2.4	TEM Analysis	78
3.3.3	Catalyst Performance in HDS of DBT	82
3.4	Discussion	93
3.5	Conclusions	100
Chapter 4: Synthesis of Mesoporous Mo₂C/Carbon Catalysts by Carbothermal Hydrogen		
Reduction using Petroleum Coke		101
4.1	Introduction	101
4.2	Experimental and Computational Methods	102
4.2.1	Catalyst Preparation	102
4.2.2	Catalyst Characterization	103
4.2.3	Catalyst Activity Tests	104
4.2.4	Computational Method	104
4.3	Results and Discussion	105
4.3.1	Characterization Results	105
4.3.2	Mo Species Transformation	113
4.3.3	Pore Development during Carbothermal Hydrogen Reduction (CHR)	119
4.3.4	Activity Test in HDO of 4-methylphenol	121
4.4	Conclusion	122
Chapter 5: The Effect of S on Mo₂C/APC Catalysts with Various Particle Sizes		123
5.1	Introduction	123
5.2	Experimental	124
5.2.1	Preparation of Catalysts	124
5.2.2	Catalyst Characterization	125

5.2.3	Catalytic Performance Measurement in HDS.....	126
5.2.4	Computational Model and Methods.....	127
5.3	Results.....	130
5.3.1	Fresh Catalyst Characterization	130
5.3.1.1	XRD and Physical Properties Analysis.....	130
5.3.1.2	XPS Analysis	132
5.3.1.3	TEM/STEM-EDX Analysis and CO Uptake.....	135
5.3.2	Catalyst Activity and Stability	138
5.3.3	Used Catalyst Characterization.....	142
5.3.3.1	XRD and Physical Properties Analysis.....	142
5.3.3.2	XPS Analysis	142
5.3.3.3	TEM/STEM-EDX Analysis.....	145
5.4	Discussion and DFT Analysis.....	148
5.5	Conclusions.....	154
Chapter 6: The Effect of Other Heteroatoms (N and O) on Mo₂C/APC Catalysts		156
6.1	Introduction.....	156
6.2	Experimental	156
6.3	Results and Discussion	157
6.3.1	Catalyst Activities in HDN of Carbazole.....	157
6.3.2	Catalyst Activities in HDO of Dibenzofuran.....	166
6.4	Conclusion	168
Chapter 7: Conclusions and Recommendations		169
7.1	Conclusions.....	169

7.2	Recommendations.....	171
7.2.1	Mo ₂ C Catalyst Properties.....	171
7.2.2	Promoter Effect in HDS Reaction.....	172
7.2.3	Deactivation of Mo ₂ C and Ni-Mo ₂ C in HDS	173
7.2.4	Effect of N and O on Mo ₂ C Catalysts.....	173
7.2.5	Mesoporous Carbon Applications.....	174
	Bibliography	176
	Appendices.....	201
	Appendix A Catalyst Preparation	202
A.1	Raw Petroleum Coke (PC) and Activated Petcoke (APC)	202
A.2	Mo ₂ C/C based Catalyst Precursors and Catalysts Preparation	204
A.3	Methodology of Petroleum Coke Activation	207
	Appendix B Catalyst Characterization.....	210
B.1	Physical Properties Test.....	210
B.2	XRD	214
B.3	XPS	217
B.4	CO Chemisorption	219
B.5	GC-FID/TCD	223
	Appendix C Sample Calculation.....	227
C.1	Feed and Products Calculation.....	227
C.2	Calculation Procedure of MoO _x C _y Formula	231
C.3	Calculation of Presulfiding Parameters for MoS ₂ /AC Catalyst Preparation	233
C.4	Stacking Degree (N) Calculation for MoS ₂ from TEM Images	235

C.5	Experimental Details for Chapter 4	236
C.6	Rate Constants Calculation Reported in Chapter 4.....	237
C.7	Calculation of Activation Energy of Carbon Hydrogenation in Chapter 4	238
C.8	Reaction Phase Determination from ASPEN Plus Calculation	240
C.9	System Dynamic Response in Fixed-bed Reactor	243
Appendix D Kinetic Model Code		245
D.1	Matlab Code for HDO of 4-methylphenol in Batch Reactor	245
D.2	Matlab Code for HDS of Dibenzothiophene in Batch Reactor.....	252
D.3	Matlab Code for Deactivation Constant Calculation	266
Appendix E Supplementary Figures and Tables.....		272
E.1	Supplementary Information for Chapter 2	272
E.2	Supplementary Information for Chapter 3	276
E.3	Supplementary Information for Chapter 4.....	282
E.4	Supplementary Information for Chapter 5	289
E.5	Supplementary Information for Chapter 6.....	298
Appendix F Error Analysis and Repeatability		300
F.1	Carbon Balance.....	300
F.2	Petcoke Activation Repeatability.....	301
F.3	Reaction Repeatability	301
F.4	Statistical Analysis of Kinetic Model	306
F.5	Characterization Repeatability	309
Appendix G Mass Transfers and Heat Transfer Effects		314
G.1	External Mass Transfer Effect	316

G.2	Internal Mass Transfer Effect	319
G.3	Heat Transfer Effect.....	320
G.4	Precheck of Fixed-bed Reactor Operating Condition.....	321
G.5	External and Internal Mass Transfers in Batch Reactor	322
Appendix H Additional Calculation and Experimental Data		323
H.1	Carbon Efficiency Calculation for Mo ₂ C Formation.....	323
H.2	Comparison between 10% MoS ₂ /Al ₂ O ₃ , 10% MoS ₂ /AC, and 10% Mo ₂ C/AC Catalysts	323
H.3	Mesoporous Carbon Development by Ni-Mo ₂ C on APC.....	325

List of Tables

Table 1.1 Comparison between bio-oil and crude oil [55].	4
Table 1.2: Different thermal activation methods for the development of carbon material derived from petroleum coke.	10
Table 1.3: Proximate, ultimate analysis and N ₂ specific surface area of delayed petroleum coke [99].	14
Table 2.1: Textural properties of Mo-based catalysts prepared by CHR method at different temperatures.	28
Table 2.2: The crystallite and particle size of Mo/AC prepared at different temperatures.	30
Table 2.3: XPS analysis of Mo (3d) of 10% Mo/AC catalysts prepared at different CHR temperatures.	34
Table 2.4: The calculated formulas of Mo oxycarbide with different CHR temperatures and the CO uptake measurements	36
Table 2.5: Kinetic rate constants of catalysts prepared at different CHR temperatures at different reaction temperatures.	43
Table 2.6: 4-MP HDO conversion and product selectivity at different reaction temperatures for Mo ₂ C catalysts prepared at different CHR temperatures.	43
Table 2.7: Pre-exponential factors and apparent activation energies extracted from 1 st -order rate constants for the DDO and HYD of 4-MP over Mo ₂ C catalysts prepared at different CHR temperatures.	44
Table 2.8: Kinetic rate constants for the conversion of 4-MP over different Mo-based catalysts at 350 °C.	45
Table 2.9: XPS Analysis of Mo 3d for 10% Mo/AC-650 catalyst after reaction.	48

Table 3.1: XRD analysis of Ni _x Mo ₂ C/AC-600 catalysts and Mo ₂ C/AC-750 catalyst.	65
Table 3.2: Catalyst composition of fresh Mo ₂ C/AC-650 and Ni-Mo ₂ C/AC catalysts.	66
Table 3.3: Physical properties of fresh and used Ni-Mo ₂ C/AC catalysts prepared at reduction temperatures of 550 °C and 600 °C.....	70
Table 3.4: XPS and CHNS analysis of used (Ni)-Mo ₂ C/AC catalysts with different Ni:Mo ratios and different reduction temperatures.	72
Table 3.5: XPS and CHNS analysis of used catalysts (Mo ₂ C/AC-650 and Ni _{0.19} Mo ₂ C/AC-600) after HDS reaction in the batch reactor for different reaction periods.	76
Table 3.6: Normalized intensity of selected ions (containing the most abundant isotope ³² S) calculated based on TOF-SIMS spectra of used catalysts of 10%Mo ₂ C/AC-650 and Ni _{0.19} Mo ₂ C/AC-600.	78
Table 3.7: DBT conversion for (Ni)-Mo ₂ C/AC catalysts at 350 °C and an initial pressure of 2.1 MPa.	83
Table 3.8: Kinetic model parameters estimated for the HDS of DBT after the 1 st hour of the reaction in the batch reactor over Ni-Mo ₂ C/AC catalysts at 350 °C and initial P _{H2} =2.1 MPa.	89
Table 4.1: XPS analysis of Mo (3d) for Mo/APC samples prepared at different CHR temperatures.	108
Table 4.2: Physical properties of Mo ₂ C/APC catalysts produced at different CHR temperatures.	111
Table 4.3: Bulk kinetic rate constants for the conversion of 4-MP over different Mo-based catalysts at 350 °C.....	122
Table 5.1: Physical properties of catalyst precursors, fresh, and used Mo ₂ C/APC catalysts with different Mo loadings.....	131

Table 5.2: XPS analysis of fresh Mo ₂ C/APC catalysts with different Mo loadings.....	134
Table 5.3: The particle size and CO uptake of fresh and used Mo ₂ C/APC catalysts.	138
Table 5.4: Conversion and product selectivity for the hydrodesuphfurization of dibenzothiophene over Mo ₂ C/APC and MoS ₂ /APC catalysts at 350 °C and 4.1 MPa after stabilization and TOS > 150 mins.....	141
Table 5.5: XPS analysis of used Mo ₂ C/APC catalysts with different Mo loadings.	144
Table 5.6: The calculated Gibbs free adsorption energy of DBT on S replaced Mo ₂ C (101) surface with different adsorption angles.	153
Table 6.1: Identified products from HDN of carbazole with Mo ₂ C/APC catalysts at 350 °C and 4.1 MPa.	158
Table 6.2: Conversion and product selectivity for HDN of CBZ over Mo ₂ C/APC catalysts at 350 °C and 4.1 MPa.	162
Table 6.3: The calculated decay constants (k _d) of Mo ₂ C/APC catalysts with various metal loadings in HDN of carbazole at 350 °C and 4.1 MPa.	163
Table 6.4: Identified products from HDO of dibenzofuran with Mo ₂ C/APC catalysts at 350 °C and 4.1 MPa.	166
Table A.1: CHNS/O wt% analysis of raw petroleum coke and activated petroleum coke.	202
Table A.2: EDX analysis of raw petroleum coke (PC) and activated petroleum coke (APC). ..	203
Table B.1: Isotherm data both from experimentally measured and 2D-NLDFT-HS model fitted.	212
Table B.2: Peak table of adsorbed CO on in-situ synthesized 10% Mo ₂ C/AC-600 catalyst.....	220
Table B.3: Peak table of adsorbed CO on reduced passivated 10% Mo ₂ C/AC-600 catalyst.	222
Table B.4: Temperature program used for GC-FID/TCD analysis.	223

Table B.5: The mole composition of the mixture gas.....	224
Table B.6: Gas calibration result for carrier gas H ₂	224
Table B.7: Calculation of mol. concentration of each gas in gas mixture.	225
Table B.8: Linear correlation between CH ₄ mole concentration and measured peak area of CH ₄	226
Table C.1: Feed compositions for HDO of 4-methylphenol.....	227
Table C.2: Feed compositions for HDS of dibenzothiophene.	228
Table C.3: GC-MS calibration table for DBT concentration with the addition of DPE as internal standard (IS).....	229
Table C.4: The calculation procedure for Mo ₂ C and MoO _x C _y contents in 10%Mo/AC catalysts.	231
Table C.5: MoS ₂ stacking degree (<i>N</i>) of different used Ni-Mo ₂ C/AC catalysts as reported in Chapter 3.	235
Table C.6: Experimental lists of HDO of 4-MP in Chapter 2.	236
Table C.7: Activity, selectivity, and kinetic rate constants for HDO of 4-methylphenol reported in Chapter 2.....	237
Table C.8: Experimental data of in-situ exit gas analysis of Mo800_APC catalyst by carbothermal hydrogenation reduction.	238
Table C.9: Mole flow rates of different components in HDS of dibenzothiophene in fixed bed reactor.	240
Table C.10: Calculated heat and material balance table.	241
Table D.1: Products distribution of HDO of 4-methylphenol at 350 °C with 10%Mo/AC-650 catalyst.	245

Table D.2: Calculated rated constants of APC supported Mo ₂ C catalysts prepared at 600 and 650 °C.....	251
Table D.3: DBT conversion and initial rate of reaction in HDS of DBT for 10% Mo ₂ C/APC catalyst as a function of time on stream.....	266
Table D.4: Calculated decay constant (k_d) from exponential decay rate law for 10Mo ₂ C/APC in HDS of DBT at 350 °C and 4.1 MPa.....	271
Table E.1: Kinetic parameters measured for thermal reaction of 4-methylphenol.....	275
Table E.2: Elemental compositions of fresh and used Mo/APC (after HDO of 4-MP) samples with different CHR temperatures holding for 90 min.....	284
Table E.3: H adsorption energy on MoO ₃ (010), MoO ₃ (010) with one oxygen vacancy and MoO ₃ C (010).	288
Table E.4: Gibbs free adsorption energy of DBT on Mo-t1 site of Mo ₂ C (101) clean surface with different orientations.	296
Table E.5: Gibbs free adsorption energy of DBT on Mo-t1 site of S adsorbed Mo ₂ C (101) surface with different orientations.	297
Table F.1: Reactant (DBT) and products concentration for HDS of dibenzothiophene over Ni _{0.19} Mo ₂ C/AC-550 and Ni _{0.38} Mo ₂ C/AC-550 catalysts.....	300
Table F.2: Petroleum coke activation results from different batches.	301
Table F.3: Kinetic parameters for HDS of dibenzothiophene in batch reactor.	302
Table F.4: Catalyst properties of 2% Mo ₂ C/APC catalyst.....	302
Table F.5: Experimental data of 2% Mo ₂ C/APC in HDS of DBT at 350 °C and 4.1 MPa from experiment T8.	303

Table F.6: Experimental data of 2%Mo ₂ C/APC in HDS of DBT at 350 °C and 4.1 MPa from experiment T13.	304
Table F.7: Comparison between experimental and kinetic model fitted data of different products and reactant in HDS of DBT by Ni _{0.19} Mo ₂ C/AC-550 catalyst.	306
Table F.8: Summary of ANOVA used calculation formula.	306
Table F.9: ANOVA analysis of DBT concentration data in HDS of DBT by Ni _{0.19} Mo ₂ C/AC-550 catalyst.	307
Table F.10: ANOVA analysis of CHB concentration data in HDS of DBT by Ni _{0.19} Mo ₂ C/AC-550 catalyst.	307
Table F.11: ANOVA analysis of BPh concentration data in HDS of DBT by Ni _{0.19} Mo ₂ C/AC-550 catalyst.	307
Table F.12: ANOVA analysis of THDBT concentration data in HDS of DBT by Ni _{0.19} Mo ₂ C/AC-550 catalyst.	308
Table F.13: Calculated error associated with the physical properties test of activated petroleum coke (APC).....	309
Table F.14: Calculated error associated with the CO uptake.....	310
Table F.15: Calculated error associated with CHNS analysis for raw petroleum coke.....	310
Table F.16: Calculated error associated with EDX-mappings for raw petroleum coke and APC_800.....	311
Table F.17: Calculated error associated with TOF-SIMS analysis for used 10%Mo ₂ C/AC-650 and Ni _{0.19} Mo ₂ C/AC-600 catalysts after HDS of DBT in batch reactor (Chapter 3).	312
Table F.18: Calculated error associated with in-situ exit gas analysis of 2%Mo ₂ C/APC-700 by carbothermal hydrogen reduction.	313

Table G.1: The details of catalyst bed, catalyst physical properties and related kinetic parameters.	315
Table G.2: The details of reaction conditions and feed properties as calculated from Aspen Plus.	316
Table G.3: The details of external mass transfer calculation by Mears criterion.	317
Table G.4: The details of internal mass transfer by Weisz-Prater criterion.....	319
Table G.5: The details of heat transfer calculation by Mears Criterion.....	320
Table G.6: The geometry parameters for prechecking of fixed-bed reactor operating condition.	321
Table G.7: A detailed list of external and internal mass transfer coefficient calculation for Ni _{0.09} Mo ₂ C/AC-550 in HDS of DBT in batch reactor.	322
Table H.1: DBT conversion and products selectivity of 10%MoS ₂ /Al ₂ O ₃ , 10%MoS ₂ /AC, and 10%Mo ₂ C/AC catalysts in HDS of DBT at 350 °C and initial pressure of 2.1 MPa.....	324
Table H.2: Physical properties of APC supported Ni-Mo ₂ C catalysts.	325

List of Figures

Figure 1.1 Reaction network of hydrodesulphurization (HDS) of dimethyldibenzothiophene (DMDBT) [33]. (Copyright © 2007, Elsevier Inc., reproduced with permission)	1
Figure 1.2: (a) Petroleum coke generation process; (b) physical appearance of raw petcoke.....	14
Figure 1.3: Schematic illustration of carbon supported Mo ₂ C catalysts in the application of hydrotreating reactions.....	20
Figure 2.1: XRD patterns of 10% Mo/AC catalysts prepared at different CHR temperatures under H ₂ ((◇) SiO ₂ ; (*) β-Mo ₂ C).....	31
Figure 2.2: XPS narrow scan spectra deconvolution of Mo 3d and O1s for fresh 10% Mo/AC catalysts prepared at different temperatures: (a)10%Mo/AC-600; (b)10%Mo/AC-650; and (c)10%Mo/AC-700.	33
Figure 2.3: TEM images of 10%Mo/AC prepared at different reduction temperatures: (a, b) 10%Mo/AC-650 with insert of lattice fringe d-spacing estimated at 2.28 Å for the (101) plane; (c) 10% Mo/AC-675; (d) 10% Mo/AC-700; (e) 10% Mo/AC-750; and (f) 10% Mo/AC-800. ...	38
Figure 2.4: Experimental and model concentration data versus reaction time of different catalysts at different reaction temperatures: 4-methylphenol (■), DDO product (▲), HYD product (●), kinetic model fit (--).	40
Figure 2.5: Simplified kinetic steps of 4-methylphenol HDO showing 1 st -order reaction paths for DDO and HYD over all Mo ₂ C catalysts prepared at various CHR temperatures. (The product presented in the dashed box is an intermediate-product).....	41
Figure 2.6: 1 st -order pre-exponential constant for DDO and HYD over all Mo ₂ C catalysts prepared at various CHR temperatures. (The error bar reflects the calculated 95% CI)	49

Figure 3.1: Schematic diagram of high pressure fixed-bed reactor for HDS of DBT.	61
Figure 3.2: XRD patterns of Ni-Mo ₂ C/AC catalysts with different ratios of Ni:Mo (0 ~ 0.76) prepared at different reduction temperatures: (a) Reduced at 550 °C; (b) Reduced at 600 °C. (◆) Mo ₂ C; (o) Ni; (*) Ni ₆ Mo ₆ C ₂	64
Figure 3.3: Profile of detected CH ₄ (mol%) during carbothermal hydrogen reduction of the catalyst generation: (a) Mo ₂ C/AC-650 (■); (b) Ni-Mo ₂ C/AC with different ratios of Ni:Mo ((●) Ni _{0.09} Mo ₂ C/AC-600; (▲) Ni _{0.19} Mo ₂ C/AC-600; (▼) Ni _{0.76} Mo ₂ C/AC-600).	68
Figure 3.4: A correlation between mass burn-off (wt%) and formed CH ₄ (mol%) during CHR process. The solid line represents the correlation equation: Mass burn-off (wt%) = 7.5847 × CH ₄ (mol%), Std.Dev.= 0.4055. (R ² =0.9918)	69
Figure 3.5: X-ray diffraction patterns for fresh and used Ni-Mo ₂ C/AC catalysts.	71
Figure 3.6: XPS narrow scan spectra of used MoS ₂ /AC, Mo ₂ C/AC and Ni _x Mo ₂ C/AC-y catalysts: (a, c) Mo 3d; (b, d) S 2p. (The dashed lines in (a, c) indicate the position of Mo ²⁺ species from Mo ₂ C; the dashed lines in (b, d) indicate the position of S ²⁻ species from MoS ₂ .)	73
Figure 3.7: XPS narrow scan spectra of used Ni _{0.19} Mo ₂ C/AC-550 catalyst after HDS reaction for different reaction periods. (a) Mo 3d; (b) S 2p.	74
Figure 3.8: TEM images and cluster size distribution of used Ni-Mo ₂ C/AC catalysts with different Ni contents. (a) Ni _{0.02} Mo ₂ C/AC-600; (b) Ni _{0.09} Mo ₂ C/AC-600; (c) Ni _{0.19} Mo ₂ C/AC-600; (d) Ni _{0.38} Mo ₂ C/AC-600; (e) Ni _{0.44} Mo ₂ C/AC-600; and (f) Ni _{0.76} Mo ₂ C/AC-600.	80
Figure 3.9: Distribution of MoS ₂ layer numbers for used catalysts. (a) Ni _{0.09} Mo ₂ C/AC-600; (b) Ni _{0.19} Mo ₂ C/AC-600; (c) Ni _{0.38} Mo ₂ C/AC-600; (d) Ni _{0.44} Mo ₂ C/AC-600; (e) Ni _{0.76} Mo ₂ C/AC-600; (f) Enlarged Ni _{0.19} Mo ₂ C/AC-600; and (g) Enlarged Ni _{0.44} Mo ₂ C/AC-600.	82

Figure 3.10: DBT conversion and product selectivity versus time on stream for Ni_{0.19}Mo₂C/AC-600 and Mo₂C/AC-650 catalyst, measured in the down flow fixed-bed reactor is at 310 °C, 4.1 MPa, H₂/feed volumetric ratio = 600 and LHSV = 8 h⁻¹. 86

Figure 3.11: Simplified kinetic steps HDS of DBT showing 1st order reaction paths over all Ni-Mo₂C/AC catalysts with different ratios of Ni:Mo and different reduction temperatures. 87

Figure 3.12: Kinetic parameters k_1 , k_2 vs. Ni:Mo ratio of Ni-Mo₂C/AC catalysts: (a) reduced at 550 °C; (b) reduced at 600 °C. (... Trend line) 90

Figure 3.13: The selectivity to biphenyl (BPh), tetrahydro-dibenzothiophene (THDBT) and cyclohydrobenzene (CHB) vs. DBT conversion: (a-c) reduced at 550 °C; (d-e) reduced at 600 °C. 92

Figure 3.14: The correlation of Ni:Mo ratio to MoS₂ stacking degree (N) (a) and the average particle size (b). —is the fitted line 96

Figure 3.15: High angle annular dark field scanning (HAADF-STEM) image and energy-dispersive X-ray (EDX) elemental mapping of used Ni_{0.19}Mo₂C/AC-600 catalyst for elements Mo, Ni, S, O, C, and Si. 98

Figure 4.1: The CH₄ concentration (mol%) in the U-tube reactor exit gas measured during CHR of Mo800_APC (□) and APC support (Δ). Inset: Particle size of generated Mo₂C at different CHR temperatures (◆). 106

Figure 4.2: TEM graphs of different samples: (a) Mo600_APC; (b) Mo700_APC; and (c) Mo800_APC. 109

Figure 4.3: Particle size distribution from TEM micrographs and fitted lognormal distribution: (a) Mo600_APC; (b) Mo650_APC; (c) Mo700_APC; (d) Mo750_APC; and (e) Mo800_APC. 110

Figure 4.4: Arrhenius plot of temperature dependence in the range of 550~700 °C.	117
Figure 4.5: Schematic representation of Mo species transformation during CHR process. (Sizes of Mo species particles are not drawn to scale.)	119
Figure 4.6: Pore size distribution of Mo ₂ C/APC catalysts prepared at different CHR temperatures calculated from NLDFT model.....	120
Figure 5.1: XRD diffraction patterns of fresh and used Mo ₂ C/APC catalysts: (◆) carbon support; (*) Mo ₂ C.	130
Figure 5.2: The deconvolution of Mo 3d of fresh Mo ₂ C/APC catalysts: (a) 2Mo ₂ C/APC; (b) 5Mo ₂ C/APC; and (c) 10Mo ₂ C/APC.	134
Figure 5.3: TEM images and cluster size distribution of Mo ₂ C/APC with different metal Mo loadings. (a) 2Mo ₂ C/APC fresh; (b) 2Mo ₂ C/APC used; (c) 5Mo ₂ C/APC fresh; (d) 5Mo ₂ C/APC used; (e) 10Mo ₂ C/APC fresh; and (f) 10Mo ₂ C/APC used.....	137
Figure 5.4: DBT conversion and selectivity of Mo ₂ C/APC catalysts with different Mo loadings with TOS. (All the experiments were done with the same amount of Mo loading in the reactor): (a) 2Mo ₂ C/APC; (b) 5Mo ₂ C/APC; (c) 10Mo ₂ C/APC; and (d) DBT conversion and HDS conversion for Mo ₂ C/APC catalysts with different Mo loadings as a function of TOS.....	139
Figure 5.5: XPS spectra of Mo ₂ C catalysts: (a) Survey scan of fresh and used 10Mo ₂ C/APC catalyst; (b) Narrow scan of Mo 3d spectra for used Mo ₂ C catalysts with different metal loadings and used 5MoS ₂ /APC.	143
Figure 5.6: High angle annular dark field TEM scanning image (HAADF-STEM) of used 2Mo ₂ C/APC catalyst (a); (b-e) Energy dispersive X-ray (EDX) elemental mappings of Mo, S, O and C; and (f) Overlay of C, Mo, and S distributions.....	146

Figure 5.7: (a) TEM image of used 10Mo ₂ C/APC catalyst; (b) High angle annular dark field TEM scanning image (HAADF-STEM); and (c) Line scanning on selected particle.....	147
Figure 5.8: Simplified reaction pathway of dibenzothiophene HDS via HYD and DDS routes over all Mo ₂ C/APC catalysts with different Mo loadings.	151
Figure 6.1: Reaction network of hydrodenitrogenation of carbazole over Mo ₂ C/APC catalyst.	158
Figure 6.2: CBZ conversion and selectivity of Mo ₂ C/APC catalysts with different Mo loadings with time on stream. (Mo loading held constant at 0.019 g in the reactor): (a) 2Mo ₂ C/APC; (b) 5Mo ₂ C/APC; (c) 10Mo ₂ C/APC; and (d) CBZ conversion and HDN conversion for Mo ₂ C/APC catalysts with different Mo loadings as a function of TOS.	160
Figure 6.3: Catalyst regeneration (Phase I and II) of 10%Mo ₂ C/APC after HDN reaction of carbazole: (a) Conversion of CBZ; and (b) Selectivity of the products.	165
Figure 6.4: Reaction network of hydrodeoxygenation of dibenzofuran over Mo ₂ C/APC catalyst.	166
Figure 6.5: DBF conversion and selectivity of Mo ₂ C/APC catalysts with different Mo loadings with time on stream. (Mo loading held constant at 0.019 g in the reactor): (a) 2Mo ₂ C/APC; (b) 5Mo ₂ C/APC; and (c) 10Mo ₂ C/APC.	167
Figure A.1: XRD scan of raw petroleum coke and activated petroleum coke.	202
Figure A.2: SEM graphs of raw petroleum coke (Left) and activated petroleum coke (Right).	203
Figure A.3: Raman spectroscopy of raw petroleum coke (PC) and activated petroleum coke (APC_800).	204
Figure A.4: Schematic illustration of the preparation of Mo ₂ C/C catalysts in quartz U-tube.	207
Figure A.5: Schematic illustration of the tubular furnace for petroleum coke activation.	209
Figure B.1: Gas physisorption isotherms. (Reprinted with permission from [186])	211

Figure B.2: Fitted isotherm by 2D-NLDFT-HS model. (“o” represents measured experimental data).....	213
Figure B.3: Cumulative surface area by 2D-NLDFT-HS model.....	213
Figure B.4: XRD profile of 10Mo ₂ C/APC_750 catalyst and Gaussian curve fitting for (002) (Left peak) and (101) (Right peak) planes.	215
Figure B.5: XPS survey scan of used 1%Ni-10%Mo ₂ C/APC catalyst.....	218
Figure B.6: Quantification results of used 1%Ni-10%Mo ₂ C/APC catalyst. (Note: the integration of each element was based on Figure B.2)	218
Figure B.7: TCD signal vs. time for in-situ synthesized 10% Mo ₂ C/AC-600 catalyst at 32 °C.	220
Figure B.8: TCD signal vs. time for reduced passivated 10% Mo ₂ C/AC-600 catalyst at 33 °C.	222
Figure B.9: Linear correlation of set point vs. H ₂ flow rate.	225
Figure B.10: Linear correlation of measured peak area of CH ₄ from GC-FID vs. CH ₄ mole concentration.....	226
Figure C.1: A linear correlation between area ratio of DBT to DPE and wt% of DBT to DPE in high concentration range.....	230
Figure C.2: A linear correlation between area ratio of DBT to DPE and wt% of DBT to DPE in low concentration range.....	230
Figure C.3: Arrhenius plot of temperature dependence in the range of 550~700 °C for CH ₄ formation.....	239
Figure C.4: Calculated activation energy (E _a) for carbon hydrogenation.....	239
Figure C.5: Aspen flowsheet for H ₂ and feedmix in a flash reactor.	241
Figure C.6: Total C mol.% in fixed-bed system at 350 °C and LHSV=4 h ⁻¹	243

Figure E.1: XRD pattern of 10% Mo/AC-650 prepared in Ar atmosphere. (\diamond) - SiO ₂ ; (*) - MoO ₂	272
Figure E.2: Product concentrations as a function of reaction time during 4-methylphenol hydrodeoxygenation at 350°C and 4.3 MPa H ₂ . (\square) 10%Mo-AC600, (o) 10%Mo-AC-650 and (Δ) 10%Mo-AC-700.	273
Figure E.3: Arrhenius plots for 1 st -order rate constants of (a) DDO and (b) HYD reactions. Data centered at T ₀ = 350°C.....	274
Figure E.4: XRD patterns of calcined Ni-Mo ₂ C/AC catalyst precursors.	276
Figure E.5: N ₂ adsorption-desorption isotherms of nitrogen at -193 °C for the AC support and Ni-Mo ₂ C/AC catalysts.....	277
Figure E.6: The effect of Ni:Mo on (a) surface area, (b) pore size, (c) V _{meso} /V _{total} , for fresh and used Ni-Mo ₂ C/AC catalysts at reduction temperatures of 550 °C and 600 °C. — Trend line....	277
Figure E.7: Experimental and model concentration data versus reaction time of different Ni-Mo ₂ C catalysts prepared at 550 °C: Dibenzothiophene (DBT, \blacktriangledown); Biphenyl (BPh, \bullet); tetrahydro-dibenzothiophene (THDBT, \blacktriangle); cyclohexylbenzene (CHB, \blacksquare). (a) Ni _{0.02} Mo ₂ C/AC-550; (b) Ni _{0.09} Mo ₂ C/AC-550; (c) Ni _{0.19} Mo ₂ C/AC-550; (d) Ni _{0.38} Mo ₂ C/AC-550; (e) Ni _{0.44} Mo ₂ C/AC-550; (f) Ni _{0.76} Mo ₂ C/AC-550.....	278
Figure E.8: Experimental and model concentration data versus reaction time of different Ni-Mo ₂ C catalysts prepared at 600 °C: Dibenzothiophene (DBT, \blacktriangledown); Biphenyl (BPh, \bullet); tetrahydro-dibenzothiophene (THDBT, \blacktriangle); cyclohexylbenzene (CHB, \blacksquare). (a) Ni _{0.02} Mo ₂ C/AC-600; (b) Ni _{0.09} Mo ₂ C/AC-600; (c) Ni _{0.19} Mo ₂ C/AC-600; (d) Ni _{0.38} Mo ₂ C/AC-600; (e) Ni _{0.44} Mo ₂ C/AC-600; (f) Ni _{0.76} Mo ₂ C/AC-600.....	279

Figure E.9: Correlation of Ni/Mo ratio determined by ICP and adsorbed S wt% determined by CHNS analyzer for Ni-Mo ₂ C/AC reduced at different temperatures (□: reduced at 550 °C; ○: reduced at 600 °C).....	280
Figure E.10: TOF-SIMS spectrum of used Ni _{0.19} Mo ₂ C/AC-550 catalyst based on spot of scan area.....	281
Figure E.11: Mo (3d) XPS narrow scan spectra deconvolution of APC supported Mo ₂ C catalysts at different CHR temperatures: (a) Mo400_APC; (b) Mo500_APC; (c) Mo550_APC; (d) Mo600_APC; (e) Mo650_APC; (f) Mo700_APC; (g) Mo750_APC; (h) Mo800_APC.....	282
Figure E.12: The deconvolution of Mo 3d narrow scan spectra of fresh Mo/APC samples with different CHR temperatures holding for 90 min: (a) survey scan of Mo600_APC; (b) Mo600_APC; (c) Mo650_APC; (d) Mo700_APC. (“—” Mo ²⁺ ; “—” Mo ³⁺ ; “—” Mo ⁴⁺ ; “—” Mo ⁵⁺ ; “—” Mo ⁶⁺).....	283
Figure E.13: Isotherms of APC supported Mo ₂ C catalysts with different CHR temperatures...	285
Figure E.14: Isotherms of APC supported Mo ₂ C catalysts with different CHR temperatures holding for 90 min: (a) Mo600_APC-90; (B) Mo650_APC-90; (c) Mo700_APC-90.....	286
Figure E.15: H adsorption energy on MoO ₃ (010), MoO ₃ (010) with one oxygen vacancy and MoO ₃ C(010).	287
Figure E.16: Experimental and model concentration data versus reaction time of different catalysts with different CHR temperatures. (a) Mo600_APC-90; (b) Mo650_APC-90; (c) Mo700_APC-90. (■) Reactant: 4-MP; (●) HYD products; (▲) DDO products.....	288
Figure E.17: A correlation of Mo loadings for the fresh Mo ₂ C/APC catalysts with various Mo loadings and I _{Mo} /I _C	289

Figure E.18: The deconvolution of S 2p of used Mo ₂ C/APC catalysts: (a) 2Mo ₂ C/APC; (b) 5Mo ₂ C/APC; (c) 10Mo ₂ C/APC; (d) 5MoS ₂ /APC.	290
Figure E.19: A correlation of Mo, C, and S from HADDF-STEM-EDX mapping with two selected areas.	291
Figure E.20: EDX mapping for two selected areas of used 2Mo ₂ C/APC catalyst.	292
Figure E.21: Terminal positions of Mo ₂ C (101) surface used in DFT calculation. (Terminal Mo site: Mo-t1; terminal C sites: C-t1 and C-t2, respectively).....	293
Figure E.22: Diagram of different S atoms replaced Mo ₂ C (101) surface for DBT adsorption energy calculation (Top and side views).	294
Figure E.23: Potential energy during dissociative adsorption of H ₂ on three surfaces: (a) clean Mo ₂ C (101) surface; (b) S adsorbed Mo ₂ C (101) surface; (c) S replaced Mo ₂ C (101) surface.	295
Figure E.24: Designed experiments for N effect study of 10Mo ₂ C/APC catalyst at 350 °C and 4.1 MPa: (a) naphthalene hydrogenation reaction at 250 °C and LHSV = 4 h ⁻¹ ; (b) Part I-naphthalene hydrogenation, Part II-HDN of carbazole at 350 °C and 4.1 MPa, Part III-naphthalene hydrogenation; (c) Part I-naphthalene hydrogenation; Part II-NH ₃ /H ₂ treatment at 350 °C and 4.1 MPa; Part III-Naphthalene hydrogenation.	298
Figure F.1: DBT conversion and products selectivity for 2%Mo ₂ C/APC catalyst as a function of time on stream in two trails (T8 and T13).	305

List of Nomenclature

(h, k, l)	Miller index
A	Cross section area of the reactor, m^2
B	Line broadening at half the maximum intensity, radians
C_{DBT}	Bulk gas concentration of DBT at 350 °C and 4.1 MPa, $kmol/m^3$
C_{H_2}	Bulk gas concentration of H_2 at 350 °C and 4.1 MPa, $kmol/m^3$
C_i	Atomic concentration of an element, %
$\hat{C}_{p(H_2)}$	Heat capacity of H_2 at reaction temperature, $J/Kg.K$
C_{wp}	Weisz-Prater criterion
d	Distance between atomic layers, Å
D	Mean crystallize size, nm
D_{bed}	Fixed-bed tube diameter, m
D_{DBT-H_2}	Binary bulk phase diffusivity, m^2/s
D_{DBT-H_2}	Binary bulk phase diffusivity, m^2/s
$D_{eff, DBT-H_2}$	Effective diffusivity, m^2/s
$D_{eff, rxn}$	Effective diffusivity in this reaction, m^2/s
$D_{eff, knudsen}$	Effective Knudsen diffusivity, m^2/s
$D_{knudsen}$	Knudsen diffusivity, m^2/s
d_p	Catalyst particle diameter, m
d_{pore}	Pore diameter, Å
E_a	Activation energy, kJ/mol
E_b	Binding energy, eV

E_k	Kinetic energy of the photoelectron, eV
h	Heat transfer coefficient, W/(m ² .K)
I_D/I_G	The ratio of the relative intensity of D band to G band
I_i	Peak intensity of element i
K	Dimensionless shape factor
k_1	Stabilized kinetic parameter, s ⁻¹
k_c	Mass transfer coefficient, m/s
k_d	Decay constant, h ⁻¹
k_{DDO}	Kinetic rate constant for DDO route, mL/(g _{M0} .min)
k_{HYD}	Kinetic rate constant for HYD route, mL/(g _{M0} .min)
k_{DDO}^T	Kinetic rate constant for DDO route from thermal reaction, mL/(g _{M0} .min)
k_{HYD}^T	Kinetic rate constant for HYD route from thermal reaction, mL/(g _{M0} .min)
k_{HYD}^o	Pre-exponential factor for HYD route, mL/(g _{M0} .min)
k_{DDO}^o	Pre-exponential factor for DDO route, mL/(g _{M0} .min)
kt	Thermal conductivity calculated by semi-empirical method for polyatomic gases, W/(m.K)
L_{bed}	Length of the catalyst bed, cm
k_{La}	Liquid side mass transfer coefficient, s ⁻¹
MC	Mears' criterion for external diffusion
MC'	Mears' criterion for isothermal operation
m_{cat}	Mass of loaded catalyst, g
M_{DBT}	Mole weight of DBT, g/mol

M_{Decalin}	Mole weight of Decalin, g/mol
M_{H_2}	Mole weight of H_2 , g/mol
M_{mix}	Feed molecular weight, g/mol
m_{SiC}	Mass of SiC, g
m_{total}	Mass of loaded catalyst bed, g
n	Reaction order
Nu	Nusselt number
\emptyset	Work function from the XPS instrument
ϕ	Porosity or void fraction of packed bed
ϕ_1	Thiele modulus for 1 st order reaction
ϕ_p	Catalyst particle porosity
P_{DBT}	Partial pressure of DBT, atm
P_{Decalin}	Partial pressure of decalin, atm
P_{H_2}	Partial pressure of H_2 , atm
P_{rxn}	Reaction pressure, atm
Pr	Prandtl number
P_{total}	Total pressure in the system, atm
PV	Pore volume, cm^3/g
R	Catalyst particle radius, m
$-r_{\text{DBT(obs)}}$	Observed reaction rate, $\text{kmol}/\text{g}_{\text{cat}}\cdot\text{s}$
Re	Reynolds number
Re'	Reynolds number considering void fraction

R_g	Gas constant, J/(mol.K)
r_{HYD}	Rate of reaction for HYD route, min^{-1}
r_{pore}	Pore radii of the catalyst, cm
SA	Surface area, m^2/g
Sc	Schmidt number
$S_{\text{cat.}}$	Surface area of the catalyst by NLDFT model, m^2/g
$S_{\text{DDS/HYD}}$	Selectivity between DDS to HYD route
Sh	Sherwood number
Si	Sensitivity factor for peak i
T^*	Dimensionless temperature
$T_{\text{DBT,c}}$	Critical point temperature of DBT, K
T_o	Center temperature of 350 °C
T_{rxn}	Reaction temperature, K
U	Superficial gas velocity, m/s
V_{bed}	Total volume of catalyst bed, mL
V_c	Loaded catalyst volume, mL
$\tilde{V}_{\text{DBT,c}}$	Critical volume of DBT, mL/g-mol
V_{meso}	Mesopore volume, cm^3/g
V_{micro}	Micropore volume, cm^3/g
V_o	Total pore volume of the catalyst, cm^3/g
V_{sic}	Loaded inert volume, mL
V_{total}	Total pore volume, cm^3/g

X_{4-MP}

4-methylphenol conversion, %

Greek letters

γ	Shape factor
ΔH_{rxn}	Heat of reaction, kJ/mol
$\epsilon_{\text{DBT/K}}$	Lennard-Jones parameters for DBT/Boltzmann's constant, K
$\epsilon_{\text{DBT-H}_2/\text{K}}$	Lennard-Jones parameters for DBT-H ₂ /Boltzmann's constant, K
$\epsilon_{\text{H}_2/\text{K}}$	Lennard-Jones parameters for H ₂ /Boltzmann's constant, K
η	Internal effectiveness factor
θ	Angles of incidence
λ	Wavelength of the incident X-ray beam, cm ⁻¹
ν_{mix}	Kinetic viscosity of mixture, m ² /s
ρ_{b}	Bulk density of catalyst bed, g/cm ³
ρ_{bsic}	Catalyst bed density with SiC and catalyst, g/cm ³
ρ_{c}	Catalyst density, g/cm ³
ρ_{mix}	Density of feed mixture density at 350 °C and 4.1 MPa, kg/m ³
ρ_{sic}	SiC density, g/cm ³
ρ_{solid}	Solid catalyst density, g/cm ³
σ_{DBT}	Lennard-Jones parameters for DBT/characteristic length, Å
$\sigma_{\text{DBT-H}_2}$	Lennard-Jones parameters for DBT-H ₂ /characteristic length, Å
σ_{H_2}	Lennard-Jones parameters for H ₂ /characteristic length, Å
σ_{c}	Constriction factor
τ	Tortuosity factor
$\Omega_{\text{D, DBT-H}_2}$	Collision integral, calculated by ignore the last two terms

Ω	Overall effectiveness factor
γ_{mix}	Volumatic flow rate, cm^3/s
μ_{mix}	Dynamic viscosity of the mixture, $\text{kg}/\text{m}\cdot\text{s}$

List of Abbreviations

10%Mo ₂ C/AC-650	Activated charcoal supported Mo ₂ C with 10 wt% of Mo loadings
2-CHP	Phenol, 2-cyclohexyl-
2D-NLDFT	2-D Non-local density functional theory
2D-NLDFT-HS	2-D Non-local density functional theory with heterogeneous surface
4,6-DMDBT	4,6-dimethyldibenzothiophene
4-MP	4-methylphenol
AC	Activated charcoal
AHM	Ammonium heptamolybdate tetrahydrate
APC	Activated petroleum coke
APC_800	Activated petroleum coke at 800 °C
Ar-OCH ₃	Methoxy group
Ar-OH	Phenolic group
Ave. (μ)	Average value
B.E.	Binding energy, eV
BCH	Bicyclohexyl
BET	Brunauer-Emmett-Teller
BPh	Biphenyl
CBZ	Carbazole
CH	Cyclohexane
CHB	Cyclohexylbenzene
CHBA	2-Cyclohexyl-benzenamine

CHCHE	Cyclohexyl-cyclohexene
CHR	Carbothermal hydrogen reduction
CH _x	Hydrocarbons
CNF	Carbon nanofiber
CNT	Carbon nanotubes
CPCHX	Cyclopentylmethyl-cyclohexane
CUS	Coordinatively unsaturated sites
DBF	Dibenzofuran
DBT	Dibenzothiophene
DDS	Direct desulfurization
df _{BG}	Degrees of freedom between groups
DFT	Density Functional Theory
df _{WG}	Degrees of freedom within groups
DHCBZ	Dodecahydro-1H-carbazole
DI water	Deionized water
DMBP	Dimethylbiphenyl
DPM	Diphenylmethane
EDX	Energy dispersive X-ray
F _{ANOVA}	F value by ANOVA
GC/FID	Gas chromatography-flame ionization detector
GC/MS	Gas chromatography-mass spectrometry
GC/TCD	Gas chromatography-thermal conductivity detector

GHG	Greenhouse gas
HAADF-STEM	High angle annular dark field-scanning electron microscopy
HCH	Hexylcyclohexane, C ₁₂ H ₂₄
HDN	Hydrodenitrogenation
HDO	Hydrodeoxygenation
HDS	Hydrodesulphurization
HYD	Hydrogenation
ICP-OES	Inductively coupled plasma-optical emission spectroscopy
LHSV	Liquid-hourly space velocity
L-M model	Levenberg-Marquardt nonlinear regression methodology
Mo ₂ C	Molybdenum carbide
MoO _x C _y	Mo oxycarbide
MoO _x S _y	Mo oxysulfide
MoS ₂ /AC	Activated charcoal supported MoS ₂
MS _{BG}	Mean square between groups
MS _{WG}	Mean square within groups
MWNT	Multiwalled carbon nanotubes
<i>N</i>	Stacking degree of MoS ₂
Ni-Mo ₂ C	Ni promoted Mo ₂ C catalyst
NLDFT	Non-local density functional theory
ODEs	Ordinary differential equations
P/P ₀	Relative pressure

PC	Raw petroleum coke (petcoke)
RI	The normalized ion intensity yield
RI'	The distribution of identified Mo oxysulfide species
SEM	Scanning electron microscope
SEM-EDX	Scanning electron microscopy-energy dispersive X-ray spectroscopy
SS _{BG}	Sum of squares between groups
SS _T	Total sum of squares
SS _{WG}	Sum of squares within groups
Std. Dev. (SD)	Standard deviation
TEM	Transmission electron microscopy
THCZ	Tetrahydrocarbazole
THDBF	Tetrahydrodibenzofuran
THDBT	1,2,3,4-tetrahydrodibenzothiophene
TOF-SIMS	Time of flight secondary ion mass spectrometer
TPD	Temperature programmed desorption
TPR	Temperature programmed reduction
TPR	Temperature programmed reduction
VASP	Vienna ab initio simulation package
XPS	X-ray photoelectron spectroscopy
XRD	X-ray diffraction

Acknowledgements

First and foremost, I would like to express my deepest and sincerest gratitude to my supervisor, Professor Kevin J. Smith. Thank you for offering me this precious opportunity to study in UBC and explore the catalysis world together with you. Professor Smith's profound knowledge, professional guidance, and unconditional support have inspired me a lot during my whole PhD study and make me grow into an independent researcher. His great personality and wisdom also positively influence me a lot. I would follow his advice in my future career and life.

Next, I would like to thank my committee members Professor Naoko Ellis from the Department of Chemical and Biological Engineering and Professor Keng C. Chou from the Department of Chemistry at UBC for their valuable comments and kindly support in the completion of this work. Prof. Ellis has kindly granted me access to use her laboratory tubular furnace for petroleum coke activation, which helped me a lot at the initial of my study period. Prof. Chou has provided me valuable points every time on our annual committee meeting, which encourage me to thinking from a new point of view. My doctoral study has been made much easier under your help.

Furthermore, I would like to acknowledge the financial support provided by the Natural Sciences and Engineering Research Council of Canada (NSERC) and SHELL Canada. I am also grateful to the University of British Columbia (UBC) for a four-year fellowship award and the collaboration with the University of Calgary (UC).

Moreover, I would like to thank all individuals who have generously and kindly helped me with during my study with their expertise: Dr. Ken Wong (UBC) and Dr. Philip Kubik (SFU) for XPS analysis and training; Dr. John Kim for TOF-SIMS measurements; Dr. Xin Zhang (SFU) for HRTEM analysis and training; Lan Kato for XRD training; Maureen Soon for ICP measurement. I am also grateful to all CHBE office staffs (Marlene Chow, Amber Lee, Lori Tanaka, Michelle Pang, Kristi Chow, William Wijaya etc.) and technical support personnel (Richard Ryoo, Miles Garcia, Serge Milaire, Doug Yuen, Ken Wong, Richard Zhang etc.) for their assistants. Besides, I wish to thank all CHBE Catalysis group members (Shida Liu, Dr. Ross Kukard, Dr. Pooneh Ghasvareh, Chujie Zhu, Alex Imbault, Lucie Solnickova, Rubenthiran Govindarajan, Dr. Mina Alyani, Lingxiu Zhu, Xu Zhao, Yanuar Philip Wijaya, Dr. Ali Alzaid, Majed Alamoudi, Hamad Almohamadi, Abdullah Althobaity, Dr. Rahman Gholami Shahrestani) and visiting scholars (Andreas Geiger, Xin Wang, Yunhua Li, Patrick Neumann and Rubenhran Govindarajan), who helped and supported me with within the past four years.

Last but not least, a special big thank you to my husband, partner, and best friend, Shida Liu, for all the encouragement, supporting and caring during the journey of my PhD life. Without him, I couldn't get this far. Also, I like to express my gratitude to my beloved parents for their loving consideration and great confidence in me all the time.

To my beloved parents

and

my husband, Shida

Chapter 1: Introduction

1.1 Background

1.1.1 Synthesis Methods of Molybdenum Carbide (Mo₂C) Catalysts

Transition metal carbide catalysts, such as W₂C, first reported by Levy and Boudart [1], are formed when interstitial C atoms are incorporated into the lattice of transition metals (Mo, Fe, or W) [2]. The presence of C may change the electron distribution of tungsten, making it more like platinum. In Levy and Boudart's study, the Pt-like behavior of W₂C was demonstrated for three reactions: (1) $\text{H}_2 + \text{O}_2 \rightarrow \text{H}_2\text{O}$ at room temperature, (2) H₂ reduction of WO₃ with water, and (3) isomerization of 2, 2-dimethylpropane to 2-methylbutane. Following the discovery by Levy and Boudart [1], metal carbide catalysts have been widely studied. The low cost of Mo compared with noble metals is another advantage. Among metal carbides, molybdenum carbide (Mo₂C) shows better catalytic activity and selectivity for hydrogenation [3]. Studies focused on Mo₂C as catalyst for isomerization [4, 5], ammonium decomposition [6], the water gas shift reaction (WGS) [7, 8], various electrocatalytic reactions [9], and for hydrotreating [3, 10, 11]. For example, Bouchy et al. [5] pointed out the high selectivity of alkane isomerization on Mo oxycarbide and a detailed explanation of the linkage between Mo oxycarbide structure and catalytic performance was reported. Also, for NH₃ decomposition, Mo₂C has shown a high H₂ production rate compared to other Mo-based catalysts [6]. Sabnis et al. [7] reported a high WGS reaction rate on Pt/Mo₂C catalyst because of the synergistic interaction between Pt-Mo alloy and Mo₂C domains. The study on Mo₂C was also extended to electrocatalysis due to the low cost and less attenuation in acid solution as presented by Chen et al. [9] for the hydrogen evolution reaction. Mo₂C can also be used as a catalyst support [12, 13].

The conventional method of preparing metal carbides is by temperature-programmed reduction of a metal oxide precursor employing a mixture of a hydrocarbon gas (CH_4 , C_2H_6 , C_4H_{10} , C_6H_6 etc.) and hydrogen [14-18]. However, polymeric carbon, a by-product of the hydrocarbon reactions, may contaminate the carbide surface and block active sites, while the high temperature reduction (up to $927\text{ }^\circ\text{C}$) typically yields bulk phase carbides with low intrinsic surface area. Solid carbon can also be used as the carbon source, as reported by Jongorius et al. [19]; wherein, a carbon supported Mo precursor was used for Mo_2C synthesis in N_2 at temperatures $\geq 1000\text{ }^\circ\text{C}$. However, the high temperature treatment can impact the carbon support, decreasing surface area and collapsing pores. An alternative preparation method uses carbothermal hydrogen reduction (CHR), employing a carbon support and pure H_2 to generate the metal carbide at a reduction temperature of $700 \sim 800\text{ }^\circ\text{C}$. This method yields nanoparticles of Mo_2C , as first demonstrated by Mordenti et al. [20]. Similar results were reported by Liang et al. [21]. Thus, CHR is a relatively facile method to synthesize carbon supported Mo_2C catalysts. This carbothermal hydrogen reduction (CHR) synthesis of Mo_2C that uses the solid carbon support as the carburization agent, is more facile than conventional TPR methods using gas phase hydrocarbons. The present study is focused on the synthesis of Mo_2C catalysts using the CHR method with the goal of improving the catalyst properties and hence activity. The study also emphasizes the use of different carbons as support material, especially petroleum coke.

The catalytic properties of Mo_2C are closely related to the surface state of active sites as affected by the carburization conditions and preparation methods. Several parameters such as metal loading, heating rate, carburization atmosphere and temperature can be adjusted to impact the carburization process [22-25]. As reported by Frank et al.[24], Mo loading and carburization

temperature affected the structure of the synthesized catalysts, which in turn impacted their performance in steam reforming of methanol.

Metal promoters can also be introduced to the CHR synthesis process to increase the Mo₂C dispersion by reducing the temperature required for the formation of the metal carbide. Liang et al. [26] reported that the presence of Co decreased the CHR temperature for Mo₂C formation to 600 °C, at a Co/Mo molar ratio of 1.0. They concluded that the Co increased the formation of CH_x species during CHR, facilitating carburization of the Mo. Similar effects have been reported in the synthesis of W₂C by CHR using Ni as the promoter [27, 28]. The presence of the 2nd metal has also been shown to provide synergistic effects in the case of Co doped Mo₂C catalyst where the chemoselective synthesis of various arylamines from their corresponding nitroarenes was used as the probe reaction, with the Co-Mo₂C/AC catalyst having significantly higher activity than the Mo₂C/AC alone [29]. Moreover, the bimetallic carbides formed in the presence of Mo and other transition metals [30, 31] such as Fe, Co and Ni, show effective catalytic activity in hydrotreating reactions. In the present study, Ni promotion of a Mo₂C catalyst supported on carbon is reported, emphasizing the effect of the promoter on the properties of the catalyst and the resulting activity so as to build catalyst property activity relationships.

1.1.2 Carbon Supported Catalysts and their Application in Hydrotreating Reaction

1.1.2.1 Hydrotreating Technology

Hydrotreating is an oil refining technology where the feedstock is thermally treated under H₂ environment at a temperature of 300 ~ 450 °C and pressure of 0.7 ~ 15 MPa in the presence of a hydrogenation catalyst. Usually, there are two objectives of hydrotreating. One is to remove

heteroatoms (S, N and O) and metals (V or Ni etc.); the other is to stabilize the reactive fragments by terminating many coke-formation reactions in hydrocracking and saturating aromatic compounds. The oil quality can be improved after hydrotreating without significantly changing the boiling range, thus it is often referred to as a nondestructive hydrogenation.

1.1.2.2 Carbon Supported Catalysts in Hydrodesulphurization (HDS) and Hydrodenitrogenation (HDN)

Hydrodesulphurization (HDS) and hydrodenitrogenation (HDN) are effective catalytic chemical processes that removes S and N from crude oil by reaction with H_2 [32]. Among these two reactions, HDS is usually the main concern of refineries since the concentration of N (< 1 wt%) is relatively low compared to S (0.1~5.0 wt%) in real feedstocks. The aim of HDS is to improve the quality of the product for light feedstocks with S concentrations of ~ 100 ppm to 1 wt%; whereas, for heavy residue, with S content 4x's that of conventional oil, HDS is accompanied by a high degree of hydrocracking with 70 ~ 90% of the S removed. The produced liquid products can be used for other refining operations.

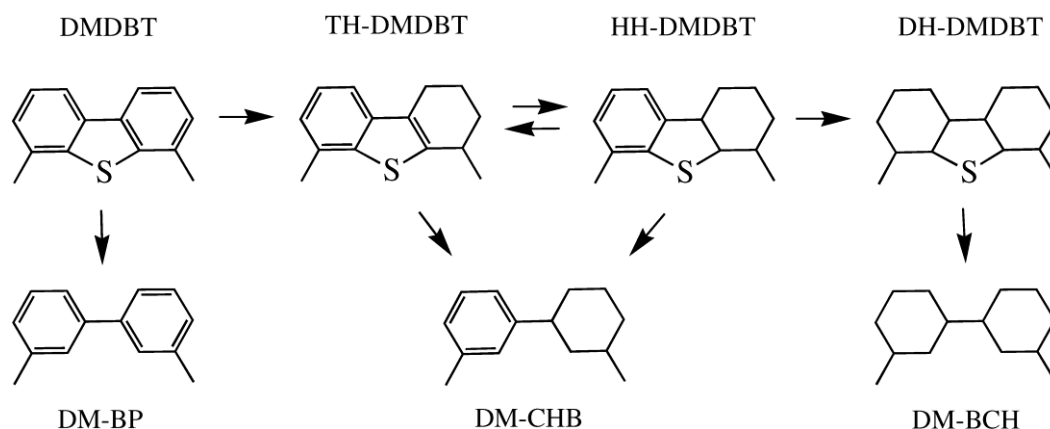


Figure 1.1 Reaction network of hydrodesulfurization (HDS) of dimethyldibenzothiophene (DMDBT) [33].

(Copyright © 2007, Elsevier Inc., reproduced with permission)

Dibenzothiophenes (DBT) and 4, 6-dimethyldibenzothiophene (4, 6-DMDBT) have commonly been used as probe molecules to test the reactivity of HDS catalysts [33-36]. Usually, the HDS reaction occurs in parallel: (I) Direct desulfurization (DDS): which yields biphenyl (BPh) and dimethylbiphenyl (DMBP) as the main products; (II) Hydrogenation (HYD): which gives rise to hydrogenation products tetrahydro- or hexahydro-intermediates followed by desulphurization to cyclohexylbenzenes or bicyclohexyls (Figure 1.1). However, the contribution to the HDS of these two routes is totally different. For 4, 6-DMDBT, HDS usually occurs through the HYD route; whereas the DBT is more likely to convert through the DDS pathway. Also, because of the steric hindrance of alkyl groups, the reactivity of 4, 6-DMDBT is usually less than that of the DBT [36]. Similar to DBT, carbazole (CBZ) is a refractory N compound in HDN and this reaction usually occurs by hydrogenation of the aromatic ring prior to N removal [37].

Sulfided Co(Ni)Mo/Alumina catalysts are commonly used commercial catalysts for HDS and HDN, prepared by impregnation of alumina with metal salts that are subsequently converted to metal sulphides by heat treatment in the presence of a S source such as dimethyldisulphide (DMDS) or H₂S. However, the results of intensive research [38, 39] showed that the metal-aluminum oxide complexes formed after impregnation and calcination are quite stable and may not be sulfided at all. Hence, catalysts prepared on carbon supports have received much attention as a potential commercial replacement with better metal sulphide formation during their preparation.

Carbon as a non-oxide support has several desirable properties, including high surface area, adjustable pore volume and size and also reduced coking propensity. Furthermore, the interaction between the C support and the active metal is weak and the recovery of active metals from spent catalysts could be more straightforward by burn off of the carbon. A study from Sakanishi et al. [40] demonstrated that the activity of NiMoS/C is higher than the commercial NiMoS prepared on alumina in the temperature range of 340 ~ 380 °C. The DDS pathway was found to dominate in this temperature range, while the HYD route was preferred when temperature was lower than 340 °C. A similar phenomenon was also reported by Farag et al. [41, 42] in which carbon and alumina supported CoMoS catalysts were compared for the HDS of DBT and 4, 6-DMDBT. The two supported catalysts showed similar selectivity but a significant difference in catalytic activity. In HDN, different transition metal sulfides supported on carbon have been extensively studied by using quinoline as reactant at 380 °C and 5.5 MPa as reported by Prins et al. [43] The authors reported that high hydrogenation ability of the catalyst corresponded to high quinoline conversion.

Apart from traditional hydrotreating catalysts of sulfided Co(Ni)Mo, the application of Mo₂C in HDS and HDN has attracted a lot of attention because of the noble metal-like behavior of the Mo₂C [44] and its ability to resist sintering at high temperature [45]. Molybdenum carbide (Mo₂C) has been shown to have 5x's the activity of conventional NiMoS/Al₂O₃ and MoS₂/Al₂O₃ catalysts for the hydrotreating of a coal-derived gas oil, based on the number of active sites measured by CO uptake [3]. Park et al. [46] reported that supported Mo₂C possess a higher activity than unsupported Mo₂C and pointed out that unlike MoS₂, Mo₂C was more stable in initial reactivity, which can be attributed to a weakly acidic surface. Moreover, Costa et al. [47] studied the performance of alumina supported Mo₂C for 4, 6-DMDBT in deep HDS reaction. The results indicated that the selectivity of DDS to HYD is higher than conventional CoMoS/Al₂O₃ or NiMoS/Al₂O₃ catalysts, indicating that the DDS route is the preferred pathway. Hence, the required H₂ amount was less for Mo₂C than that of sulfided Mo catalysts. Hynaux et al. [48] reported on HNO₃ functionalized carbon black supported Mo₂C. The prepared Mo₂C/C had a CO uptake of 317 μmol/g, which is much higher than Mo₂C/alumina of 40 μmol/g as reported by Costa et al. [49]. The increased activities were likely a result of the higher dispersion of molybdenum carbide on carbon, compared to the alumina. The performance of Mo₂C catalyst has also been tested in several HDN reactions [50, 51]. As reported by Thompson et al. [50], the synthesized bulk Mo₂C catalyst has shown a higher activity in pyridine HDN compare to the commercial CoMo and NiMo sulfides. Also, a detailed kinetic study of carbazole HDN on Mo₂C was conducted by Szymanska et al. [51], that pointed out the difference from a commercial catalyst (biphenyl was detected).

1.1.2.3 Carbon Supported Catalysts in Hydrodeoxygenation (HDO)

Bio-oils, derived from the fast pyrolysis woody biomass (i.e. thermal cracking in the absence of O₂ at 400- 600 °C and short residence time of the order of 1 second), are a promising alternative to fossil fuels since GHG emissions from bio-oils are 77 ~ 99% less than from fossil fuels [52]. Despite the benefits of bio-oil, the presence of high concentrations of oxygen in the form of furans, phenols, acids, and alcohols is problematic (Table 1.1) [53-55]. The oxygenated compounds are responsible for the instability, high viscosity, and high acidity of bio-oils which make them unsuitable for use without upgrading. Thus, hydrodeoxygenation (HDO) is becoming an important step in bio-oil upgrading [56].

Table 1.1 Comparison between bio-oil and crude oil [55].

	Bio-oil	Crude oil
Water (wt%)	15-30	0.1
pH	2.8-3.8	—
ρ (kg/l)	1.05-1.25	0.86
$\mu_{50^\circ\text{C}}$ (cP)	40-100	180
HHV (MJ/kg)	16-19	44
C (wt%)	55-65	83-86
O (wt%)	28-40	< 1
H (wt%)	5-7	11-14
S (wt%)	< 0.05	< 4
N (wt%)	< 0.4	< 1
Ash (wt%)	< 0.2	0.1

The aim of HDO is to remove the excess amount of O contained in bio-oils under H₂ atmosphere without affecting the boiling range of the oil. The choice of catalyst is crucial for HDO.

NiMoS/Al₂O₃ and CoMoS/Al₂O₃ were considered first, since they are conventional hydrotreating catalysts used in industry [36, 57]. They have been deemed rational choices for the HDO [58]. However, alumina supported catalysts have high coke yields caused by thermal instability of alumina due to the presence of large amounts of water in bio-oil. In addition, because of the acidity of the support, the HDO selectivity is affected by isomerization reactions that lead to a broad product distribution [59]. Furthermore, the stability of the sulfide catalysts is likely to be reduced due to the absence of S in the bio-oil. Consequently, carbon supported metal catalysts [60, 61] such as Mo, W, Ni and Co [62, 63], and Pd/C, Pt/C, Ru/C [64] have been considered because of the inert support and better water tolerance. Although the carbon support may decrease coking propensity during reaction [62, 65], there remains a need for less expensive catalysts with high HDO activity and low coke yield.

Transition metal carbides have received considerable attention because they have catalytic properties similar to noble metals [2, 14, 58, 66-68]. Mo₂C catalysts have been shown to have high selectivities and activities for HDO, and most studies have focused on the HDO of phenolic model compounds, since these are known to be the most refractory species present in bio-oil. For example, in the HDO of guaiacol at 350 °C and 5.5 MPa H₂, Mo₂C catalysts have high selectivity to phenol (45%) and methylated phenols (13%) since removal of the methoxy group (Ar-OCH₃ bond strength 376 kJ/mol) is much more facile than the removal of the phenolic group (Ar-OH bond strength 456 kJ/mol) [19]. Consequently, Lee et al. [69] reported the HDO of anisole at 147 °C on unsupported Mo₂C catalysts, with > 90% selectivity to benzene. The HDO of mono-oxygenated 4-methylphenol on related Mo catalysts such as MoP and NiMoP occurs at higher temperature (up to 375 °C and 4.4 MPa) yielding toluene and hydrogenated products such

as 4-methyl cyclohexene and 4-methyl cyclohexane, confirming that hydrogenation of the aryl ring also occurs under these more severe reaction conditions. Note that assessing HDO catalysts using the more refractory mono-oxygenated phenols is important because hydrogen consumption during HDO needs to be minimized and the conditions at which O removal occurs without over hydrogenation, needs to be determined for these refractory compounds. Furthermore, phenols are more likely to cleave C-O bonds without consuming significant amounts of H₂. As reported by Ren et al. [70], C-O bond scission is much easier than C-C bond cleavage on Mo₂C, resulting in less H₂ consumption compared to precious metal catalysts. Also, the consistency of DFT and experimental data demonstrated that the activation barrier of C-O scission is less than for the C-C bond scission on Mo₂C catalysts.

1.1.3 Activation Methods of Carbonaceous Materials

Raw petroleum coke is a non-porous material and consequently, an activation process seems necessary if we want to use it as a high surface area catalyst support. Therefore, different activation methods for carbonaceous materials are reviewed here.

1.1.3.1 Physical Activation

Physical activation [71] of carbonaceous materials is a two-step pyrolysis/activation method in which the material is first carbonized under inert atmosphere to order the carbon structure and create some initial pores. Following pyrolysis, the interior of the coke particle is activated at > 800 °C in the presence of H₂O, CO₂ or a mixture of them in order to develop a more porous structure with high surface area (See Eq.1-1 and 1-2 [72]). This treatment also influences the surface chemistry by adding functional groups.



DiPanfilo and Egiebor [73] investigated steam activation of fluid coke and showed that a maximum SA (surface area) and PV (pore volume) of 318 m²/g and 0.24 cm³/g, respectively, can develop after the mass burn-off reaches > 50 wt.%. The mass burn-off was mainly from the interior of the particle, thus the particle size distribution remained almost the same or slightly larger than the raw material. The CO₂ activation of delayed petcoke was studied by Karimi et al. [74] who reported a maximum SA of 646 m²/g but with a mass burn-off of ~ 80% and an activation time of 12 h. Small et al. [75] studied the properties of two cokes by varying the activation atmospheres. The results indicated that the mixture of CO₂ with H₂O (0.5 mL/min) is the most effective activation atmosphere, which produced activated delayed petcoke with a SA of 578 m²/g and PV of 0.32 cm³/g, with a V_{meso}/V_{micro} ratio of 1:1. The mass burn-off at this condition was 60%. The authors also noted that the structure pattern of the raw petcoke affects the activation process, reflected in the different gasification rates between delayed and fluid coke. The same phenomenon was also observed by Wu et al. [76], using steam activation. Their results showed different SA of 800 m²/g and 500 m²/g, respectively, for two petcoke samples derived from different origins.

All of these studies indicate that physical activation of petcoke can generate activated carbon that has the possibility to be used as a catalyst support. However, the maximum SA and PV reported

to date were in the lower range when compared with commercial activated carbon as listed in Table 1.2.

1.1.3.2 Chemical Activation

Compared with physical activation, chemical activation has more advantages, including relatively low activation temperature (450 ~ 900 °C), short activation time, highly developed porosity and low mineral content of the resulting petcoke. In chemical activation, the carbon precursor is impregnated with activating agents by a heat treatment in the absence of air. Unlike physical activation, the two steps of carbonization and activation occur simultaneously. The porosity of carbon is affected by several operating variables, such as heating temperature and soaking time. Also, the activating agents can influence the pyrolytic decomposition process. KOH has been reported to be the most widely used alkaline metal compound in petcoke activation by several authors [77-79].

Zhang et al. [78] reported a method of using KOH as reagent for the preparation of adsorbents from petcoke. KOH was chosen as activating agent and mixed with the petcoke. The results indicated that the organic S in petcoke has a high reactivity, and the S could be removed in the temperature range 550 ~ 750 °C during activation. About 23 ~ 33% of the total S present in the petcoke was captured by the K, and transformed into K_2SO_4 and K_2SO_3 . Lee and Choi's study [77] reported that the S removal reached 99.5% at 550 °C when alkali metals were used to treat high S petroleum cokes, consistent with Zhang et al.'s result. Lee and Choi pointed out that the surface area can be developed during the desulphurization process, with a considerable increase in surface area until S removal exceeds 98%. Also, the results showed a better performance for

KOH than NaOH for petcoke activation as illustrated by the improved surface area. Furthermore, the particle size of alkali treated petcoke decreased to about half that of the raw coke, and most particles collapsed after activation, as observed by scanning electron microscopy (SEM). The different mechanisms between KOH and NaOH activation were investigated by Piñero and coworkers [80] based on multiwalled carbon nanotubes (MWNTs). The results indicated that KOH can effectively activate the carbon precursor by the intercalation of metallic K, especially when the carbon precursor has a high crystallinity, while Na is only effective for disordered materials.

Chemical activation under atmospheres other than N₂ have also been studied. Xiao et al. [79] used a mixture of N₂ and H₂ (vol. ratio = 7:3) and enhanced the activation process with KOH by increasing the concentration of -CH- and -CH₂- species and removing surface heteroatoms (N, S, O). The presence of H₂ increased the yield of metallic K, which further improved intercalation in the carbon precursor. The results showed that both the SA and PV were developed. Moreover, Wu et al. [76] reported the combination of KOH and steam activation for petcoke activation. The results showed that the SA of petcoke can reach > 3000 m²/g after 30 min in the presence of steam and KOH at 800 °C, but at the expense of less than 30 wt.% yield.

Unlike physical activation, chemical methods present an ability to create a relatively high surface area petcoke (Table 1.2). However, most of the developed surface area resides in the microporous structure of the petcoke, which is undesirable for catalyst support use, especially for reactions with large molecules. Therefore, metal catalytic activation was considered to modify the pore structure for mesopore development.

Table 1.2: Different thermal activation methods for the development of carbon material derived from petroleum coke.

Author	Carbon precursor	Reagents	Activation condition			Textural properties of activated sample			Reference
			Temperature (°C)	Time (h)	Atmosphere	SA (m ² /g)	PV (cm ³ /g)	Burn-off (%)	
DiPanfilo & Egiebor	Fluid coke (38-841 μm)	H ₂ O (5.0 g/h)	850	6	N ₂	318	0.24	~50	[73]
Karimi et al.	Delayed coke (45-90 μm)	CO ₂	900	12	CO ₂ (150 mL/min)	646	--	80	[74]
Small & Hashisho	Delayed coke (75-150 μm)	CO ₂ +Steam (0.3-0.5 mL/min)	900	6	CO ₂	578	0.32 (V _{meso} =0.15)	51-60	[75]
	Fluid coke (75-150 μm)					533	0.31 (V _{meso} =0.16)		
Wu et al.	Petcoke	KOH(2:1)+Steam	800	0.42	N ₂	2500-3000	Ratio of Meso:Micro=1:1	70-75	[76]
Zhang et al.	High S petcoke (124-150 μm)	KOH (2:1)	850	1	N ₂ (100 mL/min)	1281	0.72	30.6	[78]
		KOH (3:1)				2111	1.23	43.2	
Lee & Choi	Delayed coke	NaOH (4:1) KOH (4:1)	550	1-2	N ₂	1350 1980	0.60 (V _{meso} =0.16)	--	[77]
Xiao et al.	Petcoke (<150 μm)	KOH (2:1)	780	1	N ₂ :H ₂ =7:3 (140 mL/min)	2477	1.11 (V _{meso} =0.19)	59	[79]

1.1.3.3 Catalytic Activation by Metals

As mentioned in Wu's report [76], the Ni and Cr originally present in petcoke can act as a catalyst to facilitate activation and pore development. Therefore, the effects of different catalysts on carbon activation for porosity development have been studied.

Transition metals are commonly used for carbon activation. Tomita et al. [81] reported that the presence of Ni accelerates the steam gasification of coal mainly by pitting holes into the char. SEM clearly records the morphology changes by Ni during gasification. However, no specific data on surface area or pore volume were reported by Tomita et al. [81]. Oya et al. [82] compared steam activation of resin-derived carbon fiber with and without Co. The results presented a noticeable development of mesopores in samples containing Co. At 800 °C, the mesopore volume of carbon fiber increased from 0.03 to 0.34 cm³/g at similar mass burn-off, while the surface area of the non-catalyzed fiber was much higher owing to the large presence of micropores. Liu et al. [83] investigated the difference between Fe catalyzed activation with H₂O versus CO₂. The results showed that without catalyst, the obtained pitch-based carbon was mainly microporous, while with the help of the catalytic reaction, the average pore size distribution was 2 ~ 4 nm and 10 nm under CO₂ and steam, respectively. The mesoporosity from CO₂ activation was also higher than that with steam.

The use of Ca in the development of wide pores under steam or CO₂ atmosphere was studied by Cazorla-Amoros et al. [84]. The results indicated that the V_{meso} of the treated carbon increased from ~ 0.20 cm³/g to ~ 0.70 cm³/g for CO₂, and from ~ 0.25 cm³/g to ~ 0.50 cm³/g for steam, indicating that the catalytic effect of Ca in CO₂ activation played a much bigger role than that of

steam activation. Leboda et al. [85] reported that the ratio of micropore to mesopore volume increased with increased mass burn-off under steam activation without catalyst, while the presence of Ca led to the opposite effect, indicating that increased pore volume by catalytic treatment of Ca is mainly aimed at mesopore development. The improvement of mesopore surface area from 108 to 620 m²/g in the presence of Ca, with a limited increase from 197 to 270 m²/g for the non-catalyzed reaction points to a very significant effect of the Ca. Also, the presence of Ca increased the reaction rate by decreasing the activation energy of carbon gasification from 185 kJ/mol to 164 kJ/mol [85].

The use of rare earth metals, like Cerium (Ce) [86] and Yttrium (Y) [87], was also studied. Although cerium oxide is a seldom used catalyst for carbon gasification, Shen et al.'s research [86] reported CeO as a catalyst for the steam activation of activated carbon. The results showed that CeO was able to increase the mesopore volume when the temperature was < 740 °C and the distribution of pores was mainly between 4 ~ 10 nm. Li et al.' [88] also reported that V_{meso} increased from 0.03 cm³/g to 0.31 cm³/g, while the SA remained at the same level when using Ce. The pores were mainly distributed at 4 nm and 7 nm. The obtained data clearly indicate that the Ce catalyst affects the porosity of the carbon precursor the most. In a subsequent study by Shen et al. [89], metal oxides of Y and Ce were combined for steam activation. They reported that the Y and Ce oxides had a synergistic effect on mesopore development at temperatures below 740 °C.

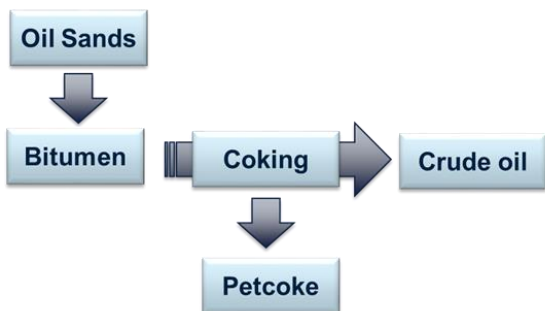
A further increase in the pore size of activated carbon materials can also be achieved by metal (Ni, Pt, Ir, Ru and Fe) catalysed carbon hydrogenation reactions [90-94]. Studies suggest that the

hydrogenation of the carbon occurs through a sequence of steps that include dissolution of carbon into the metal at the carbon/metal interface, diffusion of carbon through the metal particle, and reaction of the carbon with dissociated hydrogen on the metal/gas interface [90, 91, 93, 94]. Two studies have concluded that hydrogenation of the carbon at the gas/metal interface is the rate determining step of the overall carbon hydrogenation reaction [94, 95].

To summarize, catalytic species show great potential to benefit the activation of petcoke as they increase the reaction rate and also change the pore size distribution. The development of selective porosity (mainly mesopores) is of interest to attain an optimum carbon material for application in catalysis.

1.1.3.4 Petroleum Coke

Petroleum coke (petcoke) is a by-product of oil refining generated during thermal coking processes. Petcoke consists mostly of carbon (Figure 1.2 (a)) [96]. In the context of upgrading bitumen derived from the Canadian oilsands, there are two coking processes based on different reactors and operating conditions, where two types of coke can be produced: fluid coke and delayed coke. Both types of coke have similar chemical properties with a S content of ~7 wt.%, with 95% of the S present in organic molecules, and a similar content of mineral matter [97, 98]. Delayed coke derived from oil sands bitumen upgrading, supplied by Suncor Energy Inc., Calgary, Alberta, Canada and shown in Figure 1.2 (b) was used in this study. The component analysis of the raw petcoke is listed in Table 1.3 and other measured properties of the raw petcoke are reported in Appendix A.1.



(a) Formation of petroleum coke during oil refining

(b) Physical appearance of petroleum coke

Figure 1.2: (a) Petroleum coke generation process; (b) physical appearance of raw petcoke.

Table 1.3: Proximate, ultimate analysis and N₂ specific surface area of delayed petroleum coke [99].

(Copyright © 2013, Wiley Online Library, reproduced with permission)

Parameter	Delayed petroleum coke
<i>Proximate analysis (wt.%)</i>	
Moisture	0.3
Volatile matter	9.4
Fixed carbon	87.1
Ash	3.2
<i>Ultimate analysis (wt.%)</i>	
C	84.3
H	3.4
N	1.8
S	6.7
O ^a	0.6
S _{BET} (m ² /g)	0.5

Note: Particle size of delayed petroleum coke is 90~150 μm.
 O content was calculated by difference: O = 100 - (C+H+N+S+ash)

Significant efforts have been made toward coke utilization in a wide range of technologies. One application is through combustion and gasification of oil sands coke for power generation or synthesis gas production [97]. Also, petcoke is a potential material to produce electrodes,

adsorbents, and catalyst supports [78, 100, 101]. However, the high sulfur content and low reactivity have limited its application in energy generation [102]. The aim of present study is to modify petcoke into a carbon support that could be used in catalysis.

1.1.4 Summary

From the above introduction, molybdenum carbide synthesis methods were reviewed, pointing out the advantages of carbothermal hydrogen reduction (CHR) for Mo₂C/C catalyst synthesis. However, there is no research to clearly explain the process of Mo₂C active site formation, and also no study focused on the simultaneous C hydrogenation. To address this knowledge gap, a more detailed study of Mo₂C/C catalyst formation is required to provide insight into CHR so that the synthesis can be controlled to yield desired products.

Also, it is clear that the properties of the raw petcoke will have an impact on the properties of the activated petcoke. Three conventional carbon activation methods have been described although none are able to produce mesoporous carbon in high yield. Consequently, new activation methods need to be developed to enhance yield of mesoporous carbons for applications to catalysts.

Finally, the application of carbon supported catalysts in hydrotreating reactions was reviewed and the potential of Mo₂C/C catalysts was described. The link between Mo₂C catalyst properties and catalytic activity in HDS and HDO needs to be better understood. In the present work, a focus on the dynamic transition of Mo₂C/C catalysts in the presence of S, O and N has been examined so that the stability of these catalysts to real feedstocks can be better understood.

1.2 Objectives of the Thesis

The overall objective of the present study is to develop Mo₂C/carbon catalysts utilizing an activated petroleum coke as the support, especially aimed at Mo₂C mesoporous carbon supported catalysts for hydrotreating reactions. Several tasks were identified to meet this objective.

- Determine the viability of Mo₂C and Ni-Mo₂C catalyst synthesis by CHR using activated charcoal (AC) as the carbon source. In the first phase of the study, AC was used as the carbon source since methods of activation of the raw petcoke were under development. Quantify the catalyst activity and selectivity through the analysis of the reaction kinetics of the HDO and HDS of model reactants. Finally, relate the measured reaction kinetics to the catalyst properties so as to build catalyst activity property relationships for these catalysts.
- Understand and develop methods of mesoporous carbon formation from the raw petcoke. Determine the mechanism of carbon and Mo transformation during the synthesis of Mo₂C on mesoporous activated petcoke (APC) so that Mo₂C/APC catalyst properties can be controlled during synthesis.
- To investigate the effect of different heteroatoms (S, O and N) on Mo₂C/APC catalysts during hydrotreating, with the objective of assessing catalyst stability during reaction and performance of the catalyst with real feedstocks.

1.3 Approach

The approaches to achieve the objectives of this study were primarily experimental and are described as follows:

- 1) Investigate by experiment, the synthesis, characterization and testing of AC supported Mo_2C and Ni promoted Mo_2C (Ni- Mo_2C) catalysts. The prepared catalysts will be tested for the HDO and HDS reactions using the model reactants of 4-methylphenol and dibenzothiophene, respectively. The catalyst tests will be conducted in an autoclave batch reactor. Kinetic analysis is used to link the catalyst properties to catalyst performance.
- 2) Convert raw petcoke into a mesoporous carbon material via a two-step sequential method of thermochemical and catalytic activation (CHR-carbothermal hydrogen reduction) treatment. Several characterization methods will be applied to determine the properties of the obtained catalysts. Additionally, the mechanism of the mesoporous structure development and Mo species transformation will be investigated. The properties of the $\text{Mo}_2\text{C}/\text{APC}$ catalysts will also be determined and assessed together with the activity data for the HDO of 4-methylphenol to determine the impact of petcoke properties on the catalyst activity.
- 3) Explore the effect of different heteroatoms (S, O and N) on Mo_2C catalysts in a continuous flow fixed bed reactor. The particle size effect of Mo_2C catalysts in the presence of S will also be determined by combining experimental and theoretical methods. A deactivation model will also be developed.

1.4 Outline of the Dissertation

This dissertation is presented in seven chapters, as described below. The study conducted in Chapters 2 and 3 was based on activated charcoal (AC) as the starting point to test the viability of C supported (Ni)-Mo₂C catalysts preparation. At the same time, a study of petcoke activation and the corresponding Mo₂C catalyst synthesis was conducted as reported in Chapter 4. Chapters 5 and 6 describe further studies of Mo₂C/APC catalysts focusing on the effect of different heteroatoms. Figure 1.3 illustrates the scope of the contents of the dissertation.

Chapter 1: Provides a brief introduction of Mo₂C catalyst synthesis, hydrotreating technologies, petroleum coke, different activation methods, and the application of carbon supported catalysts. A brief summary is presented that identifies the knowledge gaps addressed in the present study. Also, the research objectives and research approach are described.

Chapter 2: Reports the catalytic performance of Mo₂C/AC catalysts in HDO reaction of 4-methylphenol. A kinetic study was conducted to compare Mo₂C catalyst prepared by different CHRs.

Chapter 3: Explores the application of synthesized Mo₂C/AC and Ni-Mo₂C/AC catalysts in HDS reaction of dibenzothiophene. The catalysts stability is also discussed. The deactivation of Ni-Mo₂C/AC was firstly identified and the properties of the used catalyst were analysed.

Chapter 4: Presents the mesoporous carbon development and Mo transformation during the synthesis of Mo₂C/APC catalysts by carbothermal hydrogen reduction. A comparison between Mo₂C/APC and Mo₂C/AC catalyst was conducted in HDO of 4-methylphenol.

Chapter 5: Focuses on studying the S effect on Mo₂C/APC catalysts with various particle sizes by combining experimental and DFT calculations.

Chapter 6: Extends the study to the effect of other heteroatoms (O and N) on Mo₂C/APC catalysts with various particle sizes.

Chapter 7: Summarizes the conclusions of previous chapters and provide the recommendations for future work.

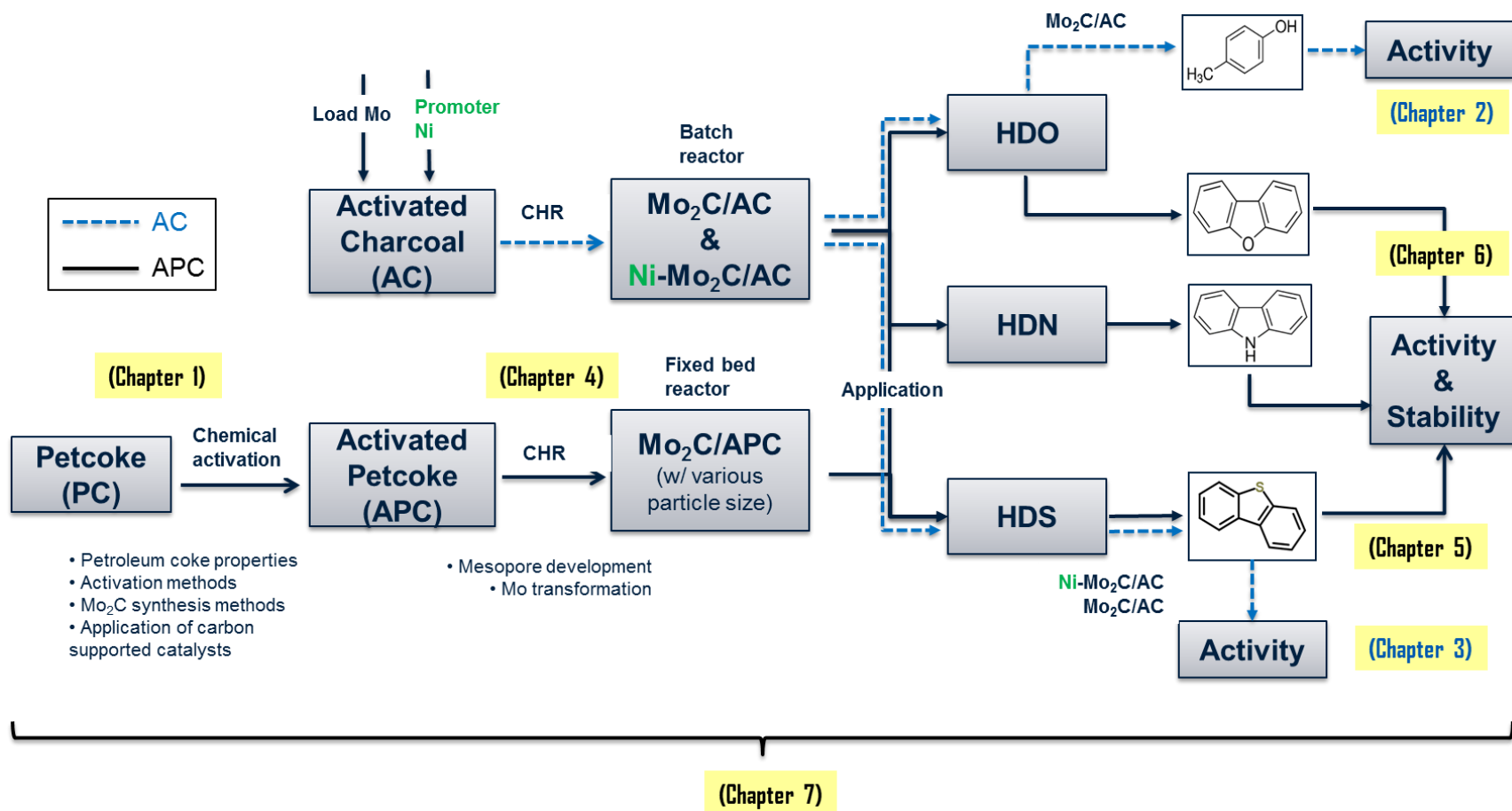


Figure 1.3: Schematic illustration of carbon supported Mo_2C catalysts in the application of hydrotreating reactions.

Chapter 2: Synthesis of Mo₂C/AC Catalysts and the Application in HDO of 4-methylphenol ¹

2.1 Introduction

Bio-oil as a potential alternative fuel has attracted significant attention recently. As noted in Chapter 1, Mo₂C catalysts show promise for HDO reactions due to their Pt-like behaviour of the Mo₂C. Thus, HDO was chosen firstly to test the activity of the synthesized Mo₂C/AC catalysts. However, one important issue with respect to Mo₂C catalysts for HDO is the role of O and its impact on the catalyst, given that Mo₂C is highly oxophilic [66, 69] and that MoO₃ and MoO₂ are active for the HDO of 4-methylphenol [103]. Choi et al. [66] reported the synthesis of unsupported Mo₂C with CH₄/H₂ gas mixture by varying the reaction temperature and CH₄ concentration. The degree of carburization was shown to influence the number and quality of noble metal-like sites of Mo₂C, which can be quantified by CO chemisorption [66, 69]. Increased noble-metal like behaviour occurs with increased carbidic carbon content and reduced residual oxygen content of the Mo lattice [66]. The reactive characteristics of Mo₂C also change upon O adsorption, with reduced hydrogenation activity reported in the presence of O. Lee et al. [69] reported that the high deoxygenation selectivity (> 90%) and low hydrogenation selectivity of Mo₂C for anisole HDO could be ascribed to O adsorption on the Mo₂C during reaction. Hence, O content of the catalyst is critical in determining the Mo₂C catalyst activity and selectivity.

¹ A version of this chapter has been published: H. Wang, S. Liu., and K. J. Smith, "Synthesis and Hydrodeoxygenation Activity of Carbon Supported Molybdenum Carbide and Oxycarbide Catalysts," *Energy & Fuels* (2016) 30(7): 6039-6049.

Note that a commercial activated carbon (AC) was selected for this first attempt to synthesize Mo_2C from a solid carbon source, since it was readily available and the methods used to activate the raw petcoke were not yet developed. In this chapter, CHR at relatively low temperature (600 ~ 800 °C) has been used to prepare the Mo_2C supported on AC. The transformation of the ammonium heptamolybdate tetrahydrate (AHM, $(\text{NH}_4)_6\text{Mo}_7\text{O}_{24}\cdot 4\text{H}_2\text{O}$) to Mo_2C during CHR is examined. At the chosen conditions the resulting catalysts are shown to contain both Mo_2C and MoO_xC_y species and the impact of the residual O on the catalyst activity and selectivity is reported. The catalysts have been evaluated for the HDO of 4-methylphenol (4-MP), a representative phenol and among the most refractory compounds present in bio-oil [104]. Although several other studies have examined di-oxygenated compounds such as 2-methoxyphenol, the choice of 4-methylphenol allows one to focus on the ability of the catalyst to break the stronger Ar-OH bond (versus the much weaker Ar-OCH₃ bond [19, 105]) and hydrogenate the aryl ring. The kinetics of these competing reactions as a function of the O content of the catalyst is reported.

2.2 Experimental

2.2.1 Materials

A commercial activated charcoal (Darco, 100 mesh, 1025 m²/g, pore volume: 0.85 cm³/g), denoted as AC, was used as the carbon support. The elemental composition (wt%) of the AC is: C: 84.34 %, H: 0.19 %, N: 1.3%; S: 0.18%; Ash 12.71 %. (Ash and S analyses were performed at ACL Laboratories by methods similar to ASTM 3177 and ASTM D5142, respectively).

Ammonium heptamolybdate tetrahydrate (AHM; $(\text{NH}_4)_6\text{Mo}_7\text{O}_{24}\cdot 4\text{H}_2\text{O}$) was used as the Mo precursor. Decalin (Aldrich, 99%) and p-Cresol (Aldrich, 99%) (also known as 4-methylphenol) were used as received as reaction solvent and model reactant, respectively.

2.2.2 Catalyst Preparation

The commercial AC was dried at 110 °C for 3 ~ 4 h to remove moisture prior to use. The procedure for preparing the catalyst precursor by wetness impregnation followed Liang et al. [21] with some minor modifications. Ammonium heptamolybdate (AHM) was dissolved in ultra-pure water and added to the dried AC support dropwise (the mass ratio of solution: AC is 5:1) to give a nominal loading of 5 or 10 wt% of Mo. The AHM impregnated AC precursor was equilibrated in an ultrasonic bath for 1 h at room temperature and then transferred to a round bottom flask and vacuum evaporated using a rotary evaporator to remove the water. Finally, the AHM/AC precursor was dried at 110 °C overnight. The precursors are referred to as 5% or 10% AHM/AC. The calculation details associated with obtaining the required Mo loading, are provided in Appendix A.2 (I).

The $\text{Mo}_2\text{C}/\text{AC}$ catalyst was prepared by CHR of the AHM/AC precursor in a H_2 flow of 100 mL (STP)/min. Approximately 0.9 g of the AHM/AC precursor was loaded into a U-tube and held in place with SiC placed on top of the precursor. The temperature was then increased at a rate of 1 °C/min from room temperature to the final reduction temperature (chosen in the range 600 to 800 °C) and held at the final temperature for 90 min. Subsequently the sample was quenched to room temperature under N_2 to obtain the fresh catalyst that was placed in de-gassed acetone without air exposure, for storage. The catalyst is designated as 5% or 10% Mo/AC-X, where X represents

the reduction temperature. Further details on the catalyst preparation are given in Appendix A.2 (III).

2.2.3 Catalyst Characterization

2.2.3.1 N₂ Adsorption and Desorption

The specific surface area (S_{BET}), pore volume and pore size distribution of the catalysts were determined from N₂ adsorption-desorption isotherms measured at -196 °C using a Micromeritics ASAP 2020 analyzer. The measurements were made immediately after catalyst synthesis with the samples transferred with minimal air exposure to a sample holder and degassed at 200 °C under vacuum (100 μm Hg) for 4 h. The specific surface area was calculated from the measured N₂ isotherm using the Brunauer-Emmett-Teller (BET) equation applied in the relative pressure range (P/P_0) of 0.01 ~ 0.20. The total pore volume (V_{total}) was obtained from the N₂ uptake at a relative pressure of $P/P_0 = 0.99$. The average pore diameter is given by $4V_{\text{total}}/S_{\text{BET}}$. (See Appendix B.1 for details of the relative theory and calculation)

2.2.3.2 X-ray Diffraction (XRD)

Powder X-ray diffraction (XRD) patterns were recorded on a Bruker D8 Focus (0-20, LynxEye detector) diffractometer with Co K α ($\lambda=1.789 \text{ \AA}$) radiation operating at 35 kV and 40 mA. In this measurement, the samples were passivated at room temperature prior to the tests. In one case, a fresh sample was analysed without passivation and the XRD pattern was the same as that obtained for the passivated sample, confirming that the air exposure during analysis did not affect the bulk properties of the catalysts and identification of the crystallite structure. (See Appendix B.2 for the calculation details of crystallite size)

2.2.3.3 X-ray Photoelectron Spectroscopy (XPS)

A Leybold Max200 X-ray photoelectron spectrometer was used for relative abundance and chemical state determination of the surface components of the catalysts. Mg K α was used as the photon source generated at 1253.6 eV. The pass energy was set at 192 eV for the survey scan and 48 eV for the narrow scan. The vacuum pressure was set at 2×10^{-9} torr. The C1s peak at 284.5 eV was taken as reference to calculate binding energies and account for charging effects.

Deconvolution of the XPS profiles was done using XPSPEAK41 software. Experimental peaks were decomposed through mixed Gaussian-Lorentzian functions (80%-20%) after Shirley background subtraction. The XPS catalyst sample was pressed onto adhesive tape and placed on the sample holder under ambient conditions prior to being transferred to the vacuum chamber. Exposure of the samples to ambient air during the preparation was minimized to less than 2 minutes. (See Appendix B.3 for details)

2.2.3.4 CO Chemisorption

The CO uptake of the catalysts was measured using a Micromeritics AutoChem II 2920 unit using pulsed chemisorption at 35 °C. Preparation of the catalyst was done in-situ in the unit by passing 50 mL(STP)/min of 9.5 mol% H₂/Ar while heating to the final temperature at 1°C/min, and maintaining the final temperature for 90 min. The Mo₂C/AC was then flushed in He at 400 °C for 4 h and then cooled to room temperature. Next, 0.5 mL pulses of CO were injected into a flow of He (50 mL(STP)/min) and the CO uptake by the catalyst was measured using a TCD. CO pulses were repeatedly injected until no further CO uptake was observed after consecutive injections. Following this measurement the catalyst was cooled to room temperature and

passivated in 1 % O₂ in N₂ for 2 h. The CO uptake measurement was then repeated on the passivated sample. Prior to the measurement, the sample was pretreated to remove the passivation layer by passing 50 mL(STP)/min of 9.5 mol% H₂/Ar while heating to 400 °C at 10 °C/min, and maintaining the final temperature for 2 h. The flow was then switched to He (50 mL(STP)/min) at 400 °C for 4 h in order to remove the adsorbed species. After cooling in a He flow, 0.5 mL pulses of CO were injected into a flow of He (50 mL(STP)/min) and the CO uptake was measured using a TCD as before. (See Appendix B.4 for details)

2.2.3.5 O Content Analysis

A Perkin-Elmer 2400 series II CHNS/O analyzer, operated in O mode and a pyrolysis temperature of 1000 °C, was used to determine the O content of the catalysts prepared by CHR. The acquired oxygen amounts were used to estimate the O content in MoO_xC_y.

2.2.3.6 Transmission Electron Microscopy (TEM)

Transmission electron microscope (TEM) images were generated using a (JEOL) JEM 200 scanning transmission electron microscope operating at 200 kV. Samples were prepared by dispersing them in ethanol and sonicating for 15 min, before placing a drop of liquid on a holey-carbon grid and evaporating for 2 ~ 3 minutes in a vacuum chamber.

2.2.4 Hydrodeoxygenation of 4-methylphenol

The HDO of 4-MP was carried out in a 300 mL stirred-batch reactor (Autoclave Engineers) to assess the catalytic activity of the fresh catalyst prepared at different reduction temperatures. The reactor was operated at 4.3 MPa H₂ and a mixing speed of 1000 rpm. For the catalytic kinetic

study, 10%Mo/AC-600, 10%Mo/AC-650, and 10%Mo/AC-700 were tested at 325, 350 and 375 °C, respectively, with the same final pressure of 4.3 MPa at each reaction temperature. In each case, 3.1 wt% 4-MP was dissolved in 100 mL decalin, to mimic the phenol content of a biomass-derived fast pyrolysis oil, and the catalyst mass was adjusted to ensure a constant Mo/4-MP mass ratio of 0.026 g_{Mo}/g_{4-MP} (See Appendix C.1, Table C.1 for feed calculation). Although the decalin is expected to be inert under the chosen reaction conditions, there is the possibility that decalin can act as an H-donor and/or undergo cracking/isomerization reactions. Experimental analysis of the liquid product showed some cis-decalin/trans-decalin interconversion, but no other significant reactions of decalin occurred. The fresh catalyst was transferred to the liquid reactant in a glove bag under an Ar flow. Before reaction, the reactor was purged with N₂ and flushed in ultra-high purity H₂ (UHP-H₂).

In order to exclude the effect of the reactor heat up period from the catalyst activity assessment, a liquid sample was withdrawn from the reactor and analyzed once the reactor reached the desired temperature, and this concentration is regarded as the concentration at t = 0 min. The H₂ pressure, stirrer speed, system and heating jacket temperatures were continuously monitored during each experiment. The identification and quantitative analysis of the products were achieved using a Shimadzu (QP-2010-S) GC/MS analysis with a Restek RTX5 30 m × 0.25 mm capillary column based on an external calibration method.

2.3 Results

2.3.1 Catalyst Characterization

2.3.1.1 Textural Properties by BET Analysis and Carbon Loss during CHR

Table 2.1 shows that the catalyst BET surface area decreases with increasing CHR temperature, with a significantly higher decrease between 650 and 700 °C compared to other temperatures.

During catalyst preparation by CHR, some portion of the AC is consumed as a consequence of carbon - H₂ reactions ($x\text{C} + 1/2y\text{H}_2 \rightarrow \text{C}_x\text{H}_y$) and conversion of the Mo precursor to Mo₂C.

Table 2.1: Textural properties of Mo-based catalysts prepared by CHR method at different temperatures.

Sample	S _{BET} (m ² /g)	V _{total} ^a (m ³ /g)	V _{micro} ^b (m ³ /g)	V _{meso} ^c (m ³ /g)	Average pore size ^d (nm)
Activated charcoal	1025	0.85	0.23	0.62	3.3
5% AHM/AC	910	0.79	0.19	0.60	3.5
10% AHM/AC	781	0.71	0.16	0.55	3.6
5% Mo/AC-750	955	0.92	0.15	0.77	3.9
10% Mo/AC-600	890	0.77	0.17	0.60	3.5
10% Mo/AC-650	845	0.76	0.14	0.62	3.6
10% Mo/AC-675	669	0.67	0.08	0.59	3.7
10% Mo/AC-700	655	0.61	0.10	0.51	4.0
10% Mo/AC-750	522	0.54	0.07	0.47	4.1
10% Mo/AC-800	283	0.35	0.03	0.32	4.9

^a V_{total} was obtained from N₂ uptake at P/P₀= 0.99;

^b V_{micro} was obtained by t-plot method;

^c V_{meso} was calculated by V_{total}-V_{micro}.

^d The average pore size was calculated by cylindrical model and the equation is as follows:

$$\text{Average pore size} = \frac{4V_{\text{Total}}}{S_{\text{BET}}}$$

Increasing CHR temperature increases the carbon loss from the AC, as shown by the burn-off mass loss reported in Table 2.2. For 10%Mo/AC-700 catalyst, approximately 44 (± 2) wt% of the dried precursor mass is lost during reduction, leaving 17.8 wt% Mo supported on the carbon. Since higher temperature removes more carbon, a higher concentration of C_xH_y in the reduction gas results, which increases the possibility of O replacement by C in the Mo precursor. Also, the Mo may facilitate carbon loss during reduction, although temperature plays a much more important role than the Mo:C ratio in the formation Mo_2C , at least when the amount of Mo is in the range of 5 ~ 10 wt%. For example, the catalyst prepared using the 5%AHM/AC precursor has 50 (± 2)% carbon burn-off at 750 °C (resulting in a Mo:C mass ratio of $\approx 0.11:1$, Table 2.2); whereas, the catalyst prepared using the 10%AHM/AC precursor at 750 °C has a 60 (± 2) wt% carbon burn-off (mass ratio of Mo:C ratio $\approx 0.30:1$, Table 2.2). Even though the ratio of Mo:C in the former catalyst is 3x's lower than in the latter case, the crystallite size of Mo_2C for both catalysts is similar at ~ 15 nm, as shown in Table 2.2. Hence we conclude that the Mo:C ratio has a negligible effect on the formation of Mo_2C compared with the H_2 reduction temperature. The most obvious illustration of this point is shown by the 5%Mo/AC-750 and 10%Mo/AC-650 catalysts that have similar Mo:C mass ratio of $\sim 0.1:1$, but the crystallite size is much larger (~ 15 nm) for the 5%Mo/AC-750 than the 10%Mo/AC-650 (~ 5 nm).

Table 2.2: The crystallite and particle size of Mo/AC prepared at different temperatures.

Catalyst	Crystallite size ^a nm	Particle/cluster size ^b nm	Burn-off ^c wt%	Mo loading ^d wt%	Mass ratio of Mo:C
5% Mo/AC-750	14, 15, 15	N/A	50	10.0	0.11:1
10% Mo/AC-600	—, —, — ^e	— ^f	11	11.2	0.12:1
10% Mo/AC-650	—, —, — ^e	4~6	21	12.7	0.15:1
10% Mo/AC-675	12, 12, 11	2~4, 10~12	34	15.2	0.18:1
10% Mo/AC-700	15, 15, 12	10~15	44	17.8	0.21:1
10% Mo/AC-750	16, 15, 14	16~21	60	25.0	0.30:1
10% Mo/AC-800	21, 19, 18	—, —, — ^g	62	26.3	0.36:1

^a It was calculated by Scherrer equation, representing crystallite sizes corresponding to (100), (002) and (101) planes, respectively;

^b It was obtained from TEM;

^c Burnoff mass (%) = $\frac{m_{\text{before CHR}} - m_{\text{after CHR}}}{m_{\text{before CHR}}}$; standard deviation is around $\pm 2\%$;

^d It was calculated by considering the carbon loss during CHR;

^e Data were not available since there are no peaks observed from XRD;

^f Data were not available due to the amorphous structure of the sample;

^g Data were not available due to the agglomeration of the sample.

2.3.1.2 XRD Analysis

Figure. 2.1 shows that the hexagonal close packed (hcp) phase of β -Mo₂C (PDF card # 00-035-0787) was successfully prepared by CHR of the 10% AHM/AC precursor reduced at different temperatures, with diffraction peaks of β -Mo₂C clearly visible at $2\theta = 40.11^\circ, 44.40^\circ, 46.07^\circ, 61.35^\circ, 72.87^\circ, 82.97^\circ, 86.58^\circ$ and 89.51° and no other bulk phase of MoO_x present. Peaks corresponding to the presence of SiO₂ (PDF card # 00-046-1045) in the AC (17.1 wt% ash) were

also present, and increased in intensity with increased reduction temperature, a consequence of increased C loss at the higher CHR temperatures.

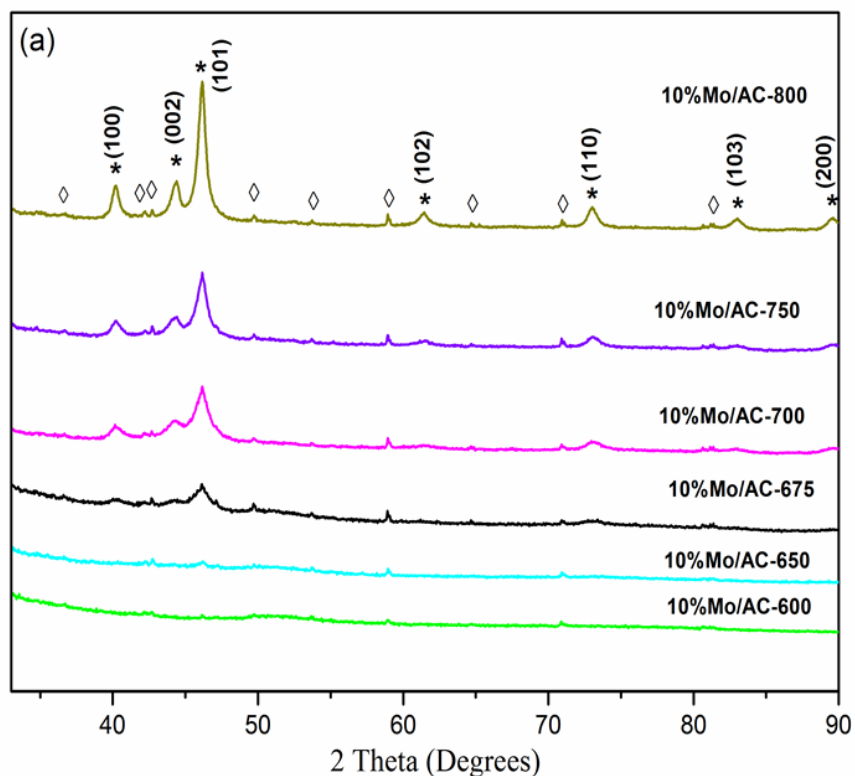


Figure 2.1: XRD patterns of 10% Mo/AC catalysts prepared at different CHR temperatures under H₂ ((\diamond) SiO₂; (*) β -Mo₂C).

Table 2.2 summarizes the β -Mo₂C crystallite size calculated from Scherrer's equation, showing that the crystallite size increased with increasing CHR temperature and suggesting that higher temperature causes sintering of the β -Mo₂C particles. Table 2.2 also shows reasonable agreement between the crystallite size determined by XRD and the cluster size determined by TEM, except for the 10%Mo/AC-650 catalyst, due to the inability of XRD to accurately determine crystallite size of ≤ 5 nm and for the 10%Mo/AC-800 catalyst, since it is difficult to measure the particle

size in TEM when the clusters agglomerate. Agglomeration of the β -Mo₂C is also demonstrated by the decreased BET surface area and pore volume shown in Table 2.1 for the same catalysts.

2.3.1.3 XPS, O Analysis and CO Uptake

Although XRD analysis confirms the presence of β -Mo₂C, the presence of amorphous forms of MoO_xC_y or MoO_x cannot be determined by XRD. Hence, XPS and O analysis were used to identify the presence of carbide and oxycarbide surface species and to determine the surface composition of the catalysts. Since all the samples were supported on carbon, it is not possible to obtain useful information from C 1s peaks. Consequently the XPS analysis focused on the Mo 3d spectra that consist of two peaks, because of spin-orbit (j-j) coupling, assigned to Mo3d_{5/2} and Mo3d_{3/2} and that are separated by 3.1 eV with a peak area ratio of 3:2 [106, 107].

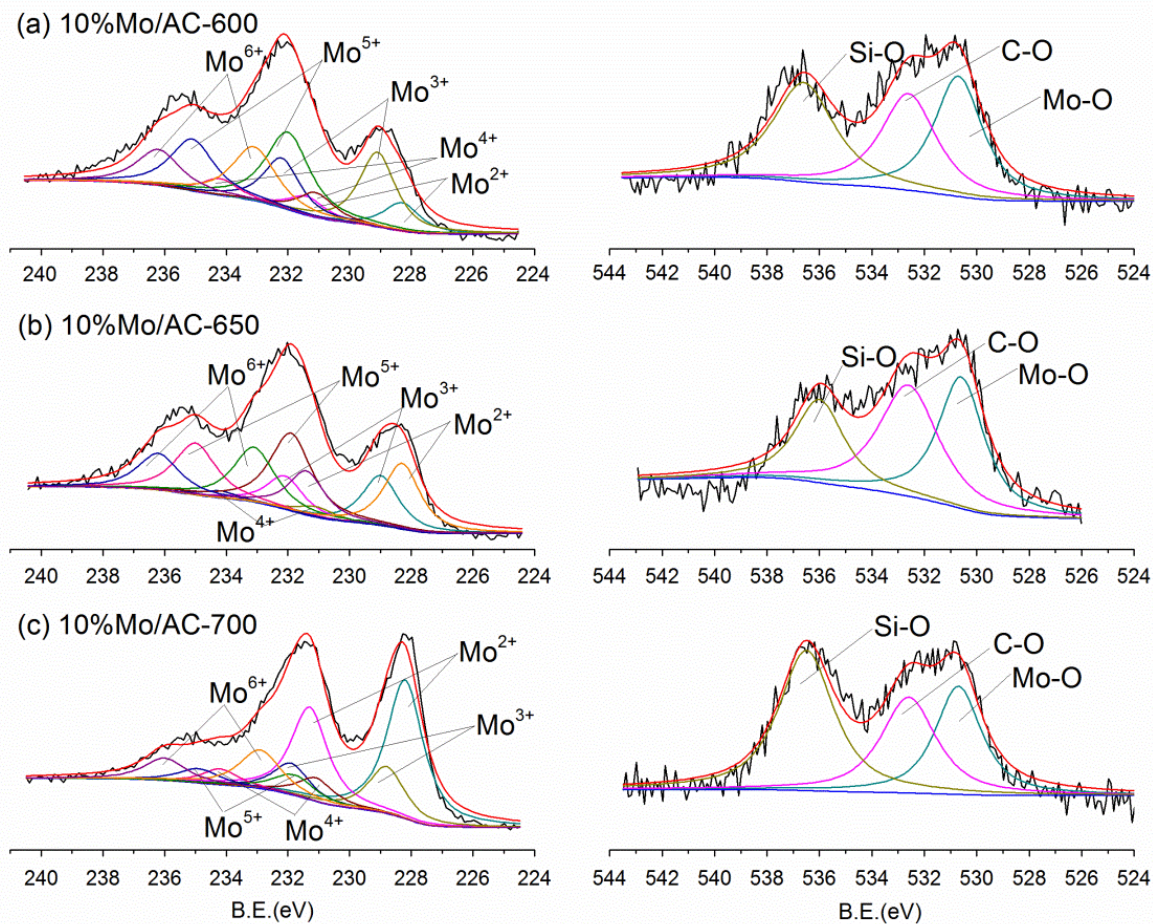


Figure 2.2: XPS narrow scan spectra deconvolution of Mo 3d and O1s for fresh 10% Mo/AC catalysts prepared at different temperatures: (a)10%Mo/AC-600; (b)10%Mo/AC-650; and (c)10%Mo/AC-700.

The measured spectra (Figure 2.2) show no evidence of zero-valent Mo species (B.E. = 227.8 eV [108]) in the synthesized catalysts. Results of curve fitting applied to the linked doublets to decompose the Mo 3d spectra into five different Mo species with B.E. in the range of 228.0 eV to 232.4 eV, are summarized in Table 2.3. Using the approach reported by Izhar et al. [109] and Oshikawa et al. [110] to analyse the Mo 3d spectra, the Mo3d_{5/2} at B.E.= 228.4 eV with FWHM of 1.4 eV is assigned to a carbide phase. The Mo 3d_{5/2} spectra is fitted by Mo³⁺ at 229.0 eV, Mo⁴⁺ at 231.1eV, Mo⁵⁺ at 231.9 eV, and Mo⁶⁺ at 233.1 eV, with FWHM of 1.4 eV, 1.4 eV, 1.4 eV, 1.6

eV and 1.7 eV, respectively. These B.E.s are associated with MoO_xC_y . There are several reasons why the MoO_xC_y has a wide range of Mo 3d B.E.s. Firstly, there is no visible peak for MoO_3 in the XRD, yet Mo^{6+} and Mo^{5+} species are identified by XPS after MoO_3 reduction, indicating that surface vacancies are generated. Depending on the nature and composition of the reducing gas, either MoO_2 or MoO_xC_y forms [111]. In the present study, the CH_4 formed during CHR is able to partially fill the vacancies and stop the transformation from MoO_3 to MoO_2 , leaving Mo in a relatively stable phase with relatively high valence. However, Mo^{4+} does exist suggesting the possibility of MoO_2 , yet the amount is below the detection limit of the XRD. In this study all Mo^{4+} have been assigned to MoO_xC_y in order to simplify the analysis. In the absence of CH_4 , the MoO_3 will be reduced directly to MoO_2 as shown by the XRD patterns of the same AHM/AC precursor treated in Ar (Appendix E, Figure E.1). There is no obvious MoO_2 peak in the XRD either, yet Mo^{4+} , and Mo^{2+} to Mo^{4+} assigned to MoO_xC_y are present in the XPS. Puello-Polo and Breto [31] conclude similarly, although they proposed that the B.E.s from 229.3 eV~230.4 eV to be Mo^{4+} and the FWHM is larger than that observed in the present study.

Table 2.3: XPS analysis of Mo (3d) of 10% Mo/AC catalysts prepared at different CHR temperatures.

Catalyst	B.E. (eV) of Mo 3d _{5/2}					Composition (mol. %)				
	Mo ²⁺	Mo ³⁺	Mo ⁴⁺	Mo ⁵⁺	Mo ⁶⁺	Mo ²⁺	Mo ³⁺	Mo ⁴⁺	Mo ⁵⁺	Mo ⁶⁺
10%Mo/AC-600	228.3	229.1	231.1	232.0	233.1	9.94	25.96	8.65	32.71	22.75
10%Mo/AC-650	228.3	229.0	231.1	231.9	233.1	23.69	18.01	3.79	31.96	22.55
10%Mo/AC-700	228.2	228.8	231.1	231.8	232.9	50.47	17.07	8.56	8.70	15.19

O analysis was used to determine the O content of the Mo oxycarbide species present in the catalysts after CHR by accounting for the O content of the AC (without Mo) after CHR.

Although there are a few minutes exposure to air due to the sample transfer and preparation, it does not significantly affect the comparison between the samples. The O signal is mainly contributed to by the oxycarbide present in the catalyst samples. The measured O content (Appendix C.2, Table C.4) assigned to MoO_xC_y was combined with the Mo valence states determined by XPS, to estimate the ratio between oxygen and carbon in the MoO_xC_y , as shown in Table 2.4. The calculation (see Appendix C.2) assumes that the C has -4 valence, that the CHR at these temperatures does not reduce the SiO_2 present in the AC and that the O is uniformly distributed in the bulk and surface of the catalyst. The formula of the MoO_xC_y reported in Table 2.4 represents the average composition of all the MoO_xC_y surface species present in the sample, and excludes the surface content of Mo_2C . The data show that as the CHR temperature increases the O content of the MoO_xC_y decreases and the Mo_2C content of the catalyst increases. At a CHR of 700 °C, the Mo is distributed approximately equally between Mo_2C and MoO_xC_y . The O1s XPS spectra (Figure 2.2) also confirm the presence of multi-oxidation states of Mo. From the report of Delporte et al. [106], the O1s peak at 532.7 eV with FWHM 2.5 eV is attributed to O atoms in carbonate species. The O1s binding energy for Mo-O species present in MoO_xC_y appears at 530.7 eV with FWHM 2.1 eV. Another O peak at 536.5 eV is assigned to Si-O, and although the position of this peak should be at 532.8 eV, due to charging it occurs at 536.5 eV.

Table 2.4: The calculated formulas of Mo oxycarbide with different CHR temperatures and the CO uptake measurements

Catalyst	O content	Formula	Mo distribution		CO uptake	
	from		Mo ₂ C	MoO _x C _y	Fresh	Passivated
	MoO _x C _y ^a		Mo mol%		μmol/gMo	
	wt%					
10% Mo/AC-600	2.59	MoO _{1.64} C _{0.33}	9.9	90.1	147	94
10% Mo/AC-650	1.76	MoO _{1.16} C _{0.61}	23.7	76.3	186	98
10% Mo/AC-700	1.00	MoO _{0.83} C _{0.90}	50.5	49.5	156	58

^a. O content from MoO_xC_y = Total O amount in samples – O amount from AC support; see Appendix C.2.

The CO uptake data reported in Table 2.4 also show an increase with increased CHR temperature and hence Mo₂C content, however, at a CHR of 700 °C the CO uptake decreases, presumably a consequence of the larger Mo₂C particles at this temperature, as identified by XRD and reported in Table 2.2.

2.3.1.4 TEM Analysis

TEM micrographs of the catalysts reduced at different temperatures are presented in Figure 2.3. At a reduction temperature of 650 °C, the TEM micrograph shows that there is no clear boundary between carbide particles and the carbon support. However, careful observation of Figure 2.3 (b) shows the characteristic slabs of β-Mo₂C with an interplanar distance of 0.228 nm. At 675 °C, the Mo carbide is clearly identified with a bi-modal size distribution, namely the coexistence of small particles of 2 ~ 4 nm and 10 ~ 12 nm as shown in Figure 2.3 (c). However, distinct fringes of graphitic structures are also observed in this sample, indicating the generation of carbon

filaments. Above 675 °C, the crystallization of the Mo₂C increases as does agglomeration of the nanoparticles. At a reduction temperature of 700 °C, an enlarged image of this sample yields a d-spacing of 0.228 nm, corresponding to the (101) plane of Mo₂C and more layers are observed indicating more crystalline Mo₂C in this catalyst.

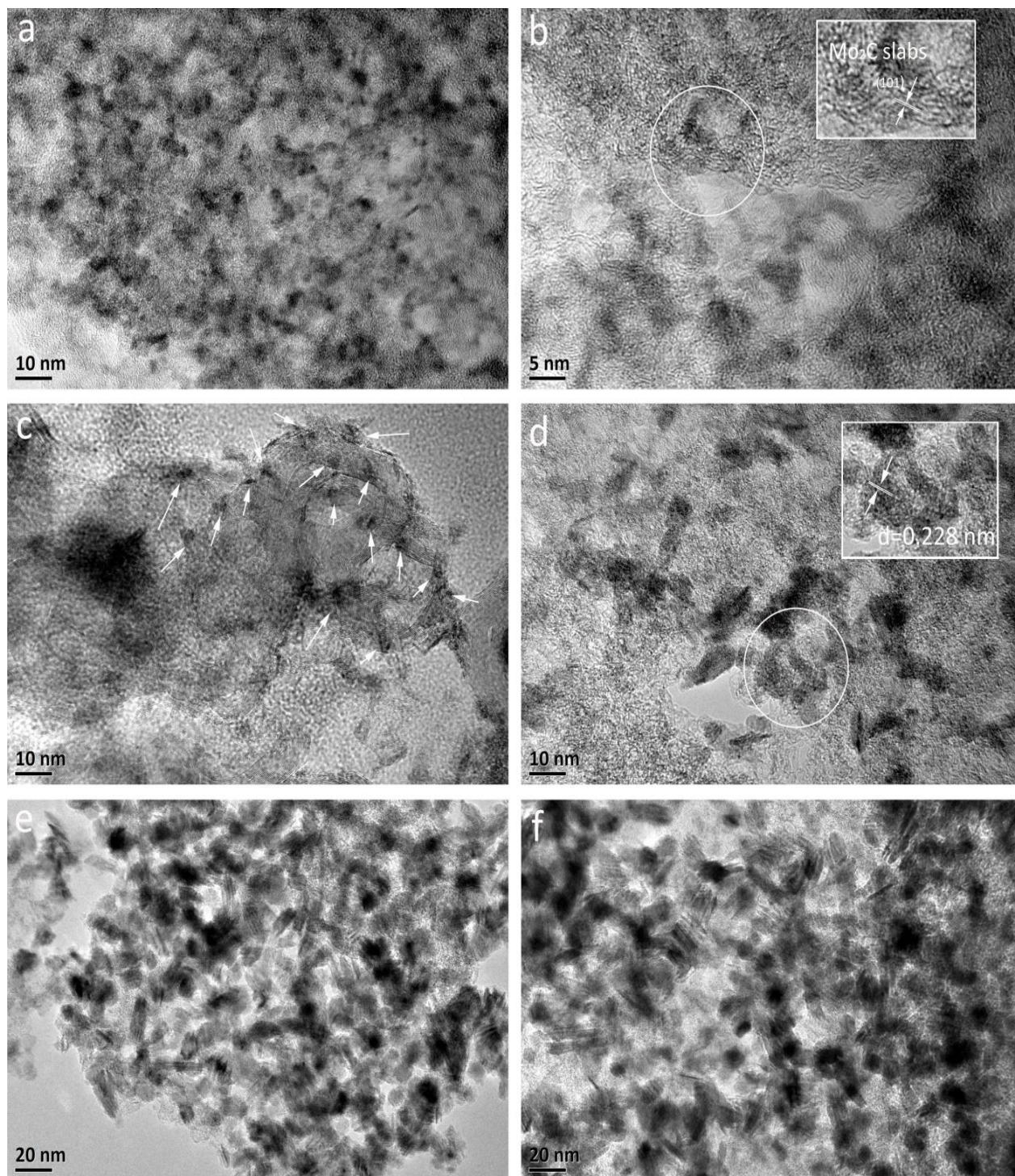


Figure 2.3: TEM images of 10%Mo/AC prepared at different reduction temperatures: (a, b) 10%Mo/AC-650 with insert of lattice fringe d-spacing estimated at 2.28 Å for the (101) plane; (c) 10% Mo/AC-675; (d) 10% Mo/AC-700; (e) 10% Mo/AC-750; and (f) 10% Mo/AC-800.

2.3.2 Catalytic Performance in HDO of 4-MP

4-Methylphenol was chosen as model reactant to determine the activity of the prepared catalysts. The results of the activity tests at different reaction temperatures for catalysts prepared at different CHR temperatures are shown in Figure 2.4. The main products of 4-MP HDO at 350°C and 4.3 MPa H₂ are toluene, methylcyclohexane, 1-methylcyclohexene and 4-methylcyclohexene. The primary product is toluene which is produced by Ar-OH bond hydrogenolysis or direct deoxygenation (DDO). Hydrogenated products result from ring hydrogenation and rapid dehydration to produce 4-methylcyclohexene which is rapidly hydrogenated to methylcyclohexane (the hydrogenation route or HYD). The distribution of hydrogenated products is illustrated in Appendix E.1, Figure E.2 that shows that most of the HYD product consists of methylcyclohexane and 4-methylcyclohexene, with the latter product decreasing with increasing reaction time. For clarity of discussion, the total hydrogenated product concentration (HYD) is reported in Figure 2.4, which shows that the 4-MP conversion for 10% Mo/AC-650 is almost the same as that for the 10%Mo/AC-600, especially at low reaction temperatures. However, when the CHR temperature is 700 °C, agglomeration of Mo₂C reduces the catalyst activity.

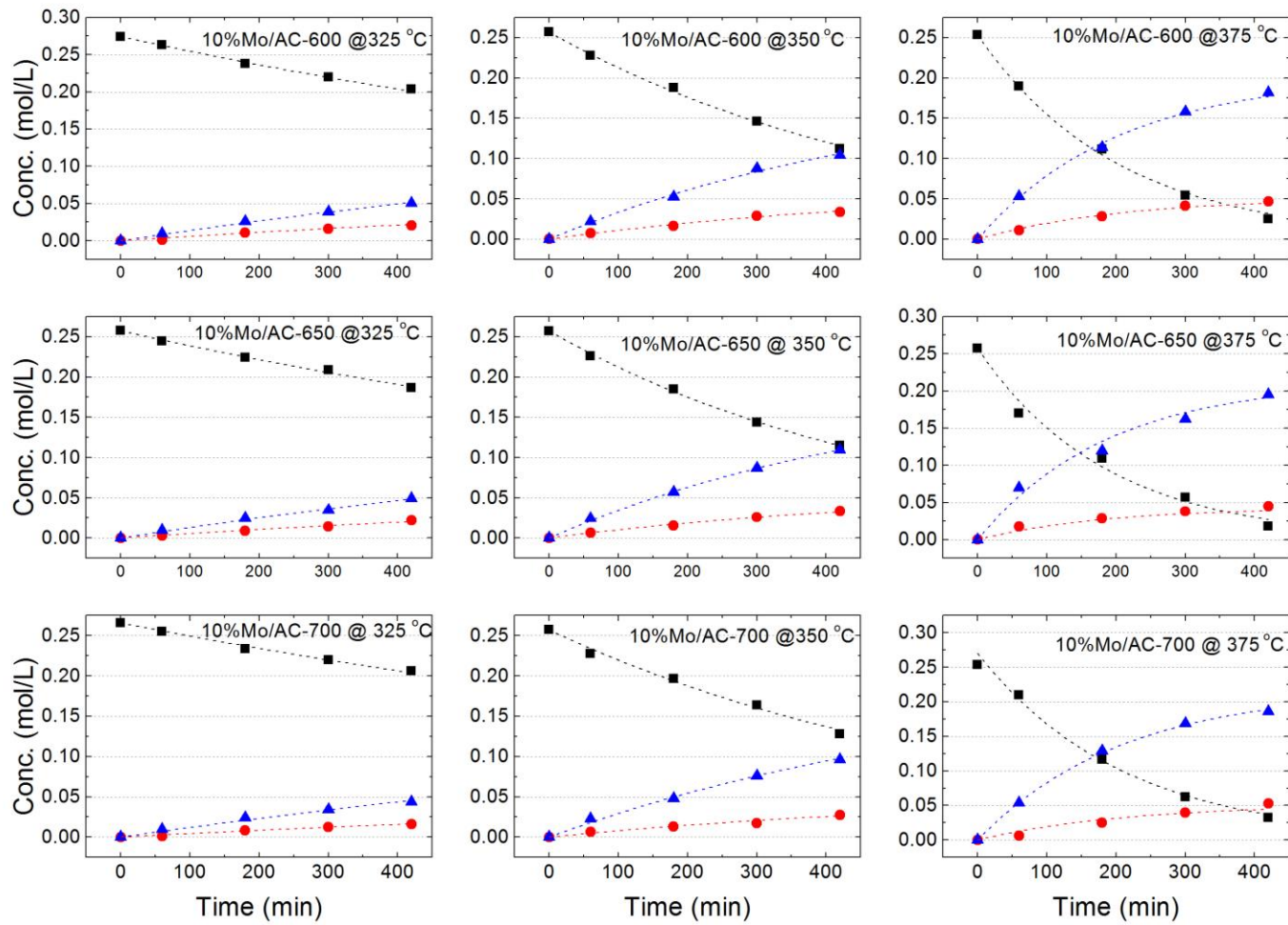


Figure 2.4: Experimental and model concentration data versus reaction time of different catalysts at different reaction temperatures: 4-methylphenol

(■), DDO product (▲), HYD product (●), kinetic model fit (--).

The kinetics of the reaction were determined for the 10%Mo/AC-600, 10%Mo/AC-650, 10%Mo/AC-700 catalysts operated at 325, 350 and 375 °C. Similar to results reported previously on other Mo-based catalysts for the HDO of 4-MP at high temperatures (325 ~ 375 °C) [103], the pseudo 1st-order rate equations for the DDO and HYD parallel reaction paths shown in Figure 2.5 were fitted to the data of Figure 2.4. Accordingly, the rate equation for the DDO is written as $r_{DDO} = (k_{DDO}^T + k_{DDO}C_{cat})C_{4-MP}$ and for the HYD $r_{HYD} = (k_{HYD}^T + k_{HYD}C_{cat})C_{4-MP}$ where k_{DDO}^T and k_{HYD}^T (min⁻¹) are the 1st-order rate constants of the thermal reaction (without catalyst) (See calculation details in Appendix E.1, Table E.1), C_{cat} is the catalyst concentration in the reaction (g_{Mo}/mL) and k_{DDO} and k_{HYD} (mL/(g_{Mo}.min)) are the 1st-order rate constants of the catalytic reaction. Since the two reaction pathways proceed in parallel, according to Whiffen and Smith [112], the DDO/HYD selectivity ratio has been calculated as $S_{DDO/HYD} = k_{DDO}/k_{HYD}$.

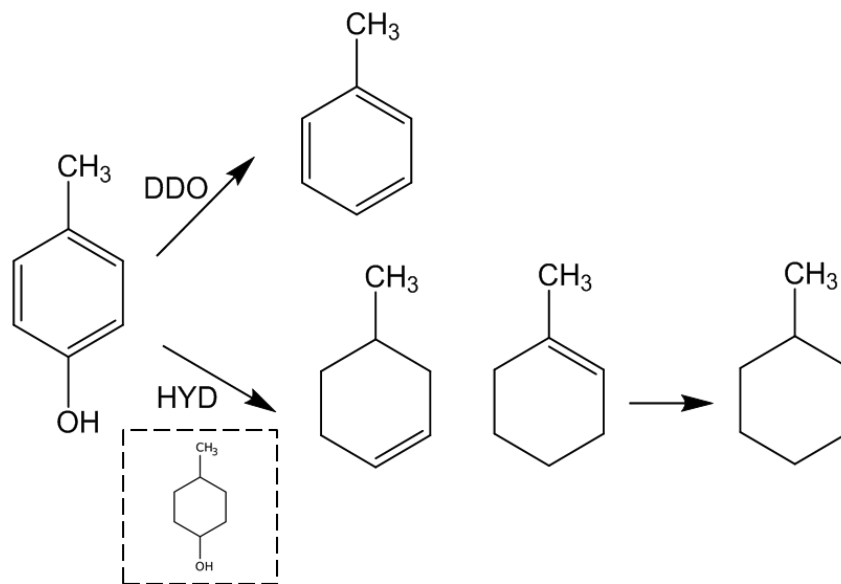


Figure 2.5: Simplified kinetic steps of 4-methylphenol HDO showing 1st-order reaction paths for DDO and HYD over all Mo₂C catalysts prepared at various CHR temperatures. (The product presented in the dashed box is an intermediate-product)

The rate equations were incorporated into the batch reactor design equation and the parameter values estimated using a Levenberg-Marquardt non-linear regression methodology (See details in Appendix D.1). The rate constants for the thermal reactions (k_{DDO}^T and k_{HYD}^T) were estimated from a series of experiments done without catalyst, and the estimated values are reported in Appendix E.1, Table E.3. The estimated values of the catalytic rate constants (k_{DDO} and k_{HYD}) are reported in Table 2.5 and the DDO/HYD selectivity ratio $S_{DDO/HYD}$ is reported in Table 2.6. Comparison of the rate constants (on a per gram Mo basis) indicates that 10% Mo/AC-650 had the highest activity among the catalysts and that on all catalysts the DDO rate is significantly greater than the HYD rate. The data also show that the reaction temperature has a significant influence on the reaction rate as well and this impact is greater on the DDO route than the HYD. For example, the DDO rate increased 2 times as the reaction temperature increased from 325 °C to 350 °C, and ~3 times as the temperature increased from 350 °C to 375 °C. The data of Table 2.6 suggest a small increase in DDO selectivity with CHR temperature, although at higher reaction temperature there is a significant error associated with the calculated selectivity ratio. Note that the selectivity to toluene is high for the synthesized Mo₂C of Table 2.5, which implies that the DDO reaction pathway is dominant and the removal of O from 4-MP occurs prior to ring saturation. The DDO selectivity of the as-synthesized catalyst is much higher than that reported on unsupported MoO₂ [103], MoS₂ [103, 113], MoP [103], sulfided CoMo/Al₂O₃ [114] and precious metal catalysts [115]. Wandas et al. [114] reported on the HDO of cresol over CoMo/Al₂O₃ and showed that the DDO/ HYD selectivity ratio was less than 0.25.

Table 2.5: Kinetic rate constants of catalysts prepared at different CHR temperatures at different reaction temperatures.

Temperature, °C	325		350		375	
Catalyst	k_{DDO}	k_{HYD}	k_{DDO}	k_{HYD}	k_{DDO}	k_{HYD}
	mL/(g _{Mo} .min)		mL/(g _{Mo} .min)		mL/(g _{Mo} .min)	
10% Mo/AC-600	0.514±0.050 ^a	0.201±0.046	1.256±0.122	0.433±0.110	3.525±0.188	0.812±0.170
10% Mo/AC-650	0.521±0.052	0.202±0.052	1.331±0.080	0.393±0.072	4.089±0.742	0.836±0.492
10% Mo/AC-700	0.436±0.058	0.129±0.058	0.996±0.118	0.248±0.110	3.519±0.680	0.577±0.468

^a 95% CI estimated as 2×(Std. Dev.)

Table 2.6: 4-MP HDO conversion and product selectivity at different reaction temperatures for Mo₂C catalysts prepared at different CHR temperatures.

Reaction Temperature, °C	325		350		375	
Catalyst	X _{4-MP}	S _{DDO/HYD}	X _{4-MP}	S _{DDO/HYD}	X _{4-MP}	S _{DDO/HYD}
10% Mo/AC-600	25.9 ^a	2.55 ± 0.68 ^b	56.5	2.90 ± 0.80	90.2	4.34 ± 0.94
10% Mo/AC-650	27.5	2.58 ± 0.72	55.3	3.39 ± 0.66	93.2	4.89 ± 3.02
10% Mo/AC-700	22.6	3.34 ± 1.56	50.2	4.02 ± 1.86	87.4	6.09 ± 5.08

^a This value was the conversion of 4-MP after a reaction time of 420 min.

^b 95% CI estimated as 2×(Std. Dev.).

The apparent activation energies (E_{DDO} and E_{HYD}) and pre-exponential factors, as per the equations $k_{DDO} = k_{DDO}^o e^{\frac{-E_{DDO}}{R}(\frac{1}{T} - \frac{1}{T_o})}$ and $k_{HYD} = k_{HYD}^o e^{\frac{-E_{HYD}}{R}(\frac{1}{T} - \frac{1}{T_o})}$ where T_o is the centre temperature (350 °C), were determined from Arrhenius plots of the rate constants (Table 2.7 and Figure E.3). The DDO apparent activation energy (~125 kJ/mol) is significantly greater than that of the HYD route (~89 kJ/mol) and the values are invariant over the 3 catalysts prepared at different CHR reduction temperatures, despite the change in Mo_2C and MoO_xC_y content of the catalysts. Finally we note that the activity of the 10%Mo/AC-650 catalyst for the HDO of 4-MP is lower than that reported for MoO_3 but better than MoP, MoO_2 , MoS_2 [103], measured at the same conditions, as those shown in Table 2.8 and reported per gram of Mo.

Table 2.7: Pre-exponential factors and apparent activation energies extracted from 1st-order rate constants for the DDO and HYD of 4-MP over Mo_2C catalysts prepared at different CHR temperatures.

Catalyst	HYD		DDO	
	k_{HYD}^o	E_a	k_{DDO}^o	E_a
	mL/(g _{Mo} .min)	kJ/mol	$\times 10^{-3}$ mL/(g _{Mo} .min)	kJ/mol
10%Mo/AC-600	0.420±0.014 ^a	89.8±5.4	1.358±0.128	126.1±14.2
10%Mo/AC-650	0.399±0.024	86.2±12.8	1.367±0.150	124.5±26.2
10%Mo/AC-700	0.261±0.032	90.9±22.2	1.103±0.286	125.0±50.0

^a – 95% CI estimated as 2×(Std. Dev.).

Table 2.8: Kinetic rate constants for the conversion of 4-MP over different Mo-based catalysts at 350 °C.

Catalysts	k (mL/(min.g _{Mo}))
MoS ₂ unsupported [103]	0.47
MoO ₂ unsupported [103]	0.55
MoP unsupported [103]	1.64
MoO ₃ unsupported [103]	3.78
10%Mo/AC-650 ^a	1.72
10%Mo/AC-600 ^a	1.69
10%Mo/AC-700 ^a	1.24

^a k was calculated by formula: $k = k_{DDO} + k_{HYD}$ as reported in Table 2.5.

2.4 Discussion

The catalysts prepared from AHM/AC precursors by CHR at relatively low temperature (600 ~ 800 °C) are mixtures of Mo₂C and MoO_xC_y. The appearance of Mo₂C in the XRD (Figure 2.1) first occurs at a reduction temperature of 650 °C, where a weak peak at $2\theta = 46.07^\circ$ occurs, indexed to the (101) plane of β -Mo₂C. From the trend in diffraction peak intensities, one concludes that the β -Mo₂C is poorly crystallized but highly dispersed at this temperature. As the reduction temperature increases, the diffraction peak intensities of β -Mo₂C increase, a consequence of both increased β -Mo₂C concentration and increased crystallinity.

The TEM results are consistent with the XRD results. The catalyst prepared at a CHR temperature of 650 °C has a weak diffraction pattern (Figure 2.1) and the TEM micrograph of the same sample (Figure 2.3 (a)) shows that there is no clear boundary between Mo₂C particles and

the carbon support, indicative of the low crystallinity of the sample and suggesting that some of the Mo remains in an amorphous oxycarbide phase at this temperature. Analysis of the TEM micrographs reveals that the β - Mo_2C particle diameters range from 4 ~ 6 nm, indicating a high dispersion on the carbon support. Figure 2.3 (c) shows that carbon filaments are formed around the Mo_2C particles (indicated by white arrows). Yoshida et al. [116] found that iron carbide converts C_2H_2 into CNTs at 600 °C and CH_4/H_2 mixtures have been used in CNT synthesis on Fe and Fe-Co catalysts [117, 118]. Under the reduction conditions of the present study, the AC is converted to CH_4 and other hydrocarbons in the presence of the added H_2 , and this gas likely generates carbon filaments over the Mo_2C . The formed graphite layers could extend and bend along the facets of the Mo-carbide, and thus cover the Mo-carbide particle leading to lower activity. At a reduction temperature of 700 °C, the average particle size of the lamellate-like structure is 10 ~ 15 nm, which is larger than that formed at 650 °C and in good agreement with the XRD analysis showing the same trend. The TEM micrograph also shows that some slabs overlap with each other, suggestive of some agglomeration at 700 °C. When the CHR temperature rises to 750 or 800 °C, the agglomeration is severe. The average size for the isolated particle is 16 ~ 21 nm at 750 °C (Figure 2.3 (e)). As shown in Figure 2.3 (f), the increased temperature results in severe agglomeration with the particle size at 800 °C difficult to measure.

Aside from the unclear boundary shown in the TEM at 650 °C, the XPS results shown in Figure 2.2 and Table 2.3 indicate the existence of MoO_xC_y . Deconvolution of the XPS narrow scan spectra finds that all three samples prepared at 600, 650 and 700 °C have Mo_2C and MoO_xC_y phases present. Different reduction temperatures influence the relative abundance of each Mo species. As the reduction temperature increases, the amount of Mo_2C increases accompanied by

a decrease in MoO_xC_y (Table 2.4). At a reduction temperature of 700 °C, the carbide phase accounts for 50 % of all Mo species. The composition of different Mo states listed in Table 2.3 shows clearly the transition from MoO_xC_y to Mo_2C . The Mo 3d spectra of Figure 2.2 (a), (b) and (c) show a shift from high B.E. to low B.E. At high temperature, carbon diffusion into the Mo is more likely, while the carbon may also modify the electronic properties of the surface Mo species to increase the reaction between the H_2 and carbon, leading to the higher mass burn-off observed with increased temperature. The formula in Table 2.4 indicates that more C is introduced into the MoO_xC_y structure as the reduction temperature increases. In conclusion, MoO_3 gradually converts through high valence states (Mo^{5+} and Mo^{6+}) of MoO_xC_y to lower valence states (Mo^{4+} and Mo^{3+}), finally forming the Mo_2C . A similar transformation process has been observed by Choi and Thompson [107]. However, further increases in CHR temperature results in agglomeration and carbon deposition that deactivates the catalyst. Thus there is a narrow CHR temperature range that yields the most active catalyst, even though the resulting catalyst has a surface composed of both Mo_2C and MoO_xC_y .

The analysis of the 4-MP HDO reaction kinetics shows very similar values for both k_{DDO} and k_{HYD} on the 10% Mo/AC-650 and the 10% Mo/AC-600 at low temperature, indicating that both Mo_2C and MoO_xC_y function as active sites for HDO. Reduction at 700 °C results in Mo_2C agglomeration and the formation of filaments that lead to reduced activity. However, the catalyst prepared at higher reduction temperature has a marginally higher DDO selectivity, suggesting that the Mo_2C has higher DDO selectivity than the MoO_xC_y . A similar phenomenon has been reported by Ren et al. [70], indicating that the dominant products of biomass-derived oxygenates from Mo_2C contain unsaturated products and the strong oxygen binding energy on Mo_2C

promotes the scission of C=O/C-O bonds. The O occupied Mo₂C surface (denoted as MoO_xC_y), also has the ability to dissociate hydrogen to form hydroxyl, followed by reaction with another hydroxyl to form water and O vacancies. The DDO route of HDO usually occurs by the absorption of the reactant through O atoms [119]. The formation process of Mo₂C and MoO_xC_y suggests that there might be many vacancies on the catalyst that were originally occupied by O. The catalysts are extremely sensitive to oxygen indicating that the interactions between oxygen atoms and active sites should be facile. Lee et al. [69] reported that high DDO selectivity is due to the suppression of catalyst hydrogenation activity by the presence of O-containing species from the reactants changing the surface properties of Mo₂C. Liu et al. [120] also indicate the possibility of changing the selectivity of transition metal carbides by O₂ treatment.

Table 2.9: XPS Analysis of Mo 3d for 10% Mo/AC-650 catalyst after reaction.

Catalyst	B.E. (eV) of Mo 3d _{5/2}					Composition (mol.%)				
	Mo ²⁺	Mo ³⁺	Mo ⁴⁺	Mo ⁵⁺	Mo ⁶⁺	Mo ²⁺	Mo ³⁺	Mo ⁴⁺	Mo ⁵⁺	Mo ⁶⁺
10%Mo/AC-650	228.3	229.0	231.1	231.9	233.1	23.69	18.01	3.79	31.96	22.55
After 1 h	228.4	229.2	230.6	232.1	233.2	13.12	20.08	17.80	34.47	14.53
After 5 h	228.4	229.2	230.6	232.1	233.2	12.69	20.66	16.93	35.16	14.56

The catalysts of the present study are also seen to be very sensitive to O, even though after CHR the Mo is present as both Mo₂C and MoO_xC_y. Table 2.9 reports a marked increase in the Mo⁴⁺ and Mo⁵⁺ surface species and a reduction in Mo²⁺, as estimated from the XPS analysis, after 1 hour reaction compared to the fresh catalyst. After a further 5 h reaction, there is no further change in composition of the Mo species. The sensitivity is further illustrated by the CO uptake data that show a significant drop in uptake after passivation, compared to the un-passivated

catalysts (Table 2.4). Nonetheless, several authors have reported that CO uptake is a valid measure of the metallic-like sites of the Mo₂C catalysts [66, 69] and the data of Table 2.4 show CO uptake increases with increased Mo₂C content, but at a CHR of 700°C, CO uptake decreases, likely because of Mo₂C agglomeration identified by TEM and XRD analysis.

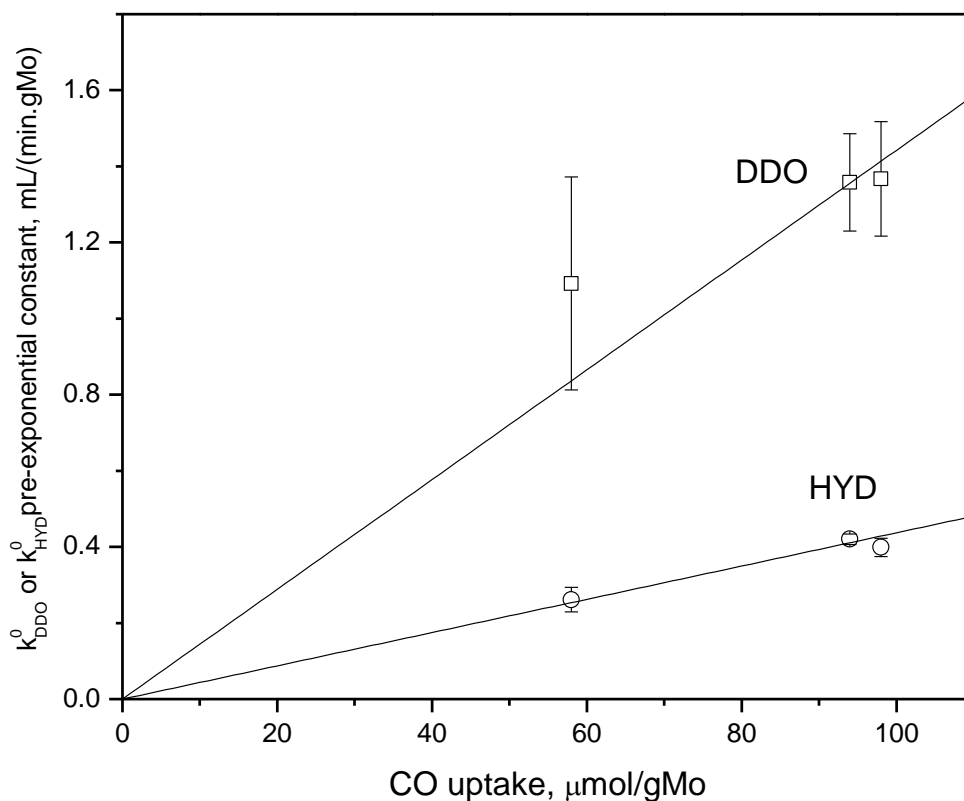


Figure 2.6: 1st-order pre-exponential constant for DDO and HYD over all Mo₂C catalysts prepared at various CHR temperatures. (The error bar reflects the calculated 95% CI)

The apparent activation energy determined from the kinetic analysis shows that both the DDO and HYD reaction pathways are unchanged as the CHR temperature increases. Table 2.7 reports the pre-exponential values for the 1st-order rate constants of the catalysts on a per gram Mo basis.

These values are plotted as a function of the CO uptake (following passivation and re-reduction) in Figure 2.6 and show a reasonable linear correlation for both the DDO and HYD reactions. The fact that HYD pre-exponential rate constant falls on the straight line indicates that the corresponding catalytic reaction is not structure sensitive, since the data were obtained on catalysts of varying Mo₂C size. Similarly, the values of the DDO pre-exponential rate constant suggest a linear correlation with CO uptake, from which one concludes that the DDO route is not structure sensitive either. Note that the correlation of the DDO rate constant shows significant more deviation from the linear correlation than the data of the HYD route. However, taking account of the error associated with the rate constant estimates, one concludes that the linear correlation is statistically valid. The rate constant for the sample prepared at a CHR of 700°C shows some deviation that may indicate structure sensitivity of this reaction, since the Mo₂C particle size was significantly higher for this catalyst (~15 nm) compared to the others of Figure 2.6. The slopes of the lines in Figure 2.6 allow the TOF of the reactions to be calculated based on the kinetic parameters. For the 10%Mo₂C-650 sample at 350°C the TOF for the DDO of 4-MP is $6.4 \times 10^{-2} \text{ s}^{-1}$ and for HYD a value of $1.9 \times 10^{-2} \text{ s}^{-1}$ is obtained. These values are about 2 orders of magnitude greater than the values reported for the HDO of anisole at 150 °C [69], but extrapolating to 325°C yields a TOF of about $1.8 \times 10^{-1} \text{ s}^{-1}$, reflecting a more facile Ar-OCH₃ bond compared to the Ar-OH bond.

The fact that the kinetics of the reactions are not strong functions of the CHR reduction temperature and hence relative content of Mo₂C versus MoO_xC_y, suggests that the active site of the catalyst is determined by the state of the catalyst under reaction conditions, wherein O

adsorption and/or exchange with the catalyst likely occurs, as indicated by the XPS data of Table 2.9 and the CO uptake measurements of the fresh versus passivated catalysts. The resulting active sites can occur on both Mo_2C and MoO_xC_y during the HDO reaction. The data of Table 2.8 also illustrate that the Mo-oxides are active for 4-MP HDO and as noted elsewhere, electrophilic co-ordinatively unsaturated sites present on MoO_3 and MoO_2 under reaction conditions, result in a high selectivity for C-O hydrogenolysis or DDO [103]. Previous studies have also concluded that oxygen-containing species change the surface properties of the Mo_2C during HDO [121]. Lee et al. [69] reported that the presence of D_2O suppresses the hydrogenation ability of Mo_2C significantly and this change is irreversible suggesting that the loss in activity is not due to competitive adsorption. Liu and coworkers [120] also report the possibility of changing the selectivity of transition metal carbides by O_2 treatment.

2.5 Conclusions

Molybdenum carbide supported on AC has been synthesized by carbothermal hydrogen reduction. MoO_3 transforms from high valence states such as Mo^{5+} and Mo^{6+} in MoO_xC_y , to lower valence states Mo^{4+} and Mo^{3+} , and finally to Mo_2C . The degree of crystallization of β - Mo_2C increases and the oxygen in MoO_xC_y decreases with increased CHR temperature. Increasing CHR temperature also increases the C burn-off rate above 650 °C, and at 675 °C some graphitic structures are formed as a consequence of catalytic reactions with the formed β - Mo_2C and these are detrimental for catalysis. When the CHR temperature reaches 700 °C, agglomeration occurs, decreasing the catalyst activity further. Although the activity of the $\text{Mo}_2\text{C}/\text{MoO}_x\text{C}_y$ prepared at optimum temperature (650 °C) is lower than MoO_3 , it is higher than MoS_2 , MoO_2 and MoP , and the catalyst has higher DDO selectivity. Kinetic analysis shows the

DDO activation energy to be significantly higher than the HYD value, and the rate constants per gram Mo are well correlated to the CO uptake data, regardless of the Mo₂C content of the catalyst.

Chapter 3: Preparation of Mo₂C/AC and Ni-Mo₂C/AC Catalysts and their Stability in HDS of Dibenzothiophene ²

3.1 Introduction

In traditional crude oil upgrading, hydrodesulphurization (HDS) is an important oil refining process to improve the oil quality [122, 123]. Unlike bio-oil, there is not much O contained (< 1 wt%) conventional crude oils ; while the S content is usually high (> 4wt%). Thus, in this chapter, HDS has been used as the probe reaction to test the catalytic activity of Mo₂C/AC and Ni-Mo₂C/AC catalysts. However, one of the difficulties encountered when applying Mo₂C catalysts for HDS is that they are unstable because of surface sulfidation, even in the presence of low concentrations of S (< 0.1 wt%). Aegerter et al. [124] proposed that a thin layer of highly dispersed MoS₂ is formed on the surface of Mo₂C or Mo₂N particles during thiophene HDS, as evidenced by IR and TPD-CO measurement of the catalysts. The authors proposed that Mo₂C and Mo₂N particles serve as rigid substrates for a sulfided Mo phase, exposing a large number of co-ordinatively unsaturated Mo sites (CUSs), which results in increased activity of the catalyst (by 50%), compared to a conventional MoS₂ catalyst. Oyama et al. [125] suggested the formation of a Mo-carbosulfide active site to explain product selectivities observed during the simultaneous conversion of sulfur, oxygen and aromatic compounds over Mo₂C, compared to the product selectivities measured with a single reactant, especially for the case of cumene hydrogenation. In another study, Brito and coworkers [126] presulfided a NiMo carbide catalyst prior to HDS and claimed that a Ni-Mo-S phase was responsible for the measured HDS activity.

² A version of this chapter has been published:

H. Wang, S. Liu., R. Govindarajan, and K. J. Smith, "Preparation of Ni-Mo₂C/carbon catalysts and their stability in the HDS of dibenzothiophene," *Applied Catalysis A: General* (2017) 539(5): 114-127.

Jin et al. [127] reported on NiMo carbide and Mo₂C catalyst performance for the HDS of dibenzothiophene (DBT) and pointed out that Ni addition increased the Mo₂C activity by 57 %, although there was no conclusion drawn regarding the effect of S on the metal carbides during HDS. The transformation of Ni-Mo₂C catalysts in the presence of S-compounds remains somewhat unclear and the application of these catalysts for HDS in high S concentrations (as is the case for gas oils derived from residue oils, for example) has not been reported.

The present chapter reports on the CHR synthesis of Ni-Mo₂C catalysts supported on activated charcoal (AC) and their application to the HDS of DBT at high S concentrations (~ 3500 ppmw) that mimic the S content of heavy oil [32]. New data are reported that capture the effect of Ni content on the formation of the Ni-Mo₂C catalysts and their resulting HDS catalytic activities. In particular, the changes in catalyst morphology that occur during reaction, with the formation of a core-shell Mo₂C-MoS₂ structure, is reported for the first time. The structural changes are related to the stability of the Ni-Mo₂C/AC and the Mo₂C/AC catalysts. Note that the catalysts reported in this chapter were prepared on a commercial activated charcoal rather than the petcoke used in the following Chapters 4 ~ 6. At the time that this study was completed, activated petcoke samples were not yet available. The commercial activated carbon was chosen as a suitable support since it removed any potential impacts of petcoke variability on the comparison between the Mo₂C and Ni-Mo₂C catalysts.

3.2 Experimental

3.2.1 Catalyst Preparation

Activated charcoal was impregnated with a solution of ammonium heptamolybdate (AHM) in acetone (10 %) and H₂O (90 %) and rotary evaporated under vacuum to remove all the solution. The resulting solid was aged in air for 4 h before drying at 110 °C overnight to yield the precursor. The precursor was then calcined in N₂ at 300 °C for 5 h to obtain the oxide states of Mo. The calcined precursor (ca. 1.8 g) was placed in a U-tube reactor and subsequently converted to the Mo₂C/AC catalyst by CHR in a continuous H₂ flow (200 mL (STP)/min), while increasing temperature from room temperature to 500 °C at 10 °C /min, followed by increasing temperature at 1 °C/min to 650 °C and holding the final temperature for 90 min before quenching to room temperature in N₂ [128]. This catalyst (designated as 10%Mo₂C/AC-650) was compared with Ni-Mo₂C/AC catalysts, prepared similarly but with successive impregnations of the AC with solutions of AHM and Ni(NO₃)₂, respectively, to obtain precursors with different Ni:Mo ratios. After calcination, the precursors were converted to Ni-Mo₂C/AC by CHR as described above but with final reduction temperatures of 550 or 600 °C. The resulting Ni-Mo₂C catalysts with different Ni:Mo ratio (from 0.02 ~ 0.76) are designated as Ni_xMo₂C-y, where x represents the Ni:Mo atomic ratio and y represents the reduction temperature (°C) (See details in Appendix A.2). The 10% Mo₂C/AC-650 and Ni-Mo₂C/AC catalysts, assessed in a batch reactor to determine reaction kinetics, were loaded into the reactor without passivation. The catalysts were transferred from the preparation U-tube reactor to the batch reactor in a glove bag under a N₂ blanket to ensure minimal air exposure.

For the catalyst stability tests conducted in a trickle-bed reactor and for the characterization of the fresh catalysts (XRD, BET), the catalyst samples were first passivated in a flow of 1 vol % O₂/N₂ at room temperature for 2 h prior to the analysis and a mild pre-reduction of the passivated catalysts was done prior to the reaction test. Carbon supported MoS₂ (MoS₂/AC) was also used herein as a reference to compare with the used Ni-Mo₂C/AC catalysts. The MoS₂/AC precursor was prepared similarly to the Mo₂C/AC precursor followed by ex-situ presulfiding in a 100 mL decalin for 3 h at 350 °C under approximately 10 vol% H₂S/H₂ generated from CS₂ (See details in Appendix C.3).

3.2.2 Catalyst Characterization

3.2.2.1 Elemental Analysis

(1) CHNS analysis

The adsorbed S on the used catalysts was determined using a Perkin-Elmer 2400 series II CHNS/O Analyzer. The combustion temperature was set at 975 °C.

(2) ICP-OES analysis

Elemental analysis of the catalysts was conducted by inductively coupled plasma optical emission spectroscopy (ICP-OES). All samples were digested in aqua regia to extract the Mo from the carbon support. After metal extraction, the solution was filtered to remove undissolved C residue from the solution before evaporation to remove all aqua regia by heating the sample to 150 °C. Finally, the concentration of all samples was adjusted to the range of 1 ~ 50 ppm in 2 vol% HNO₃. An internal standard method based on In was used to quantify the ICP-OES analysis.

3.2.2.2 N₂ Adsorption and Desorption

The Brunnauer-Emmett-Teller (BET) surface area, pore volume and pore size of the calcined Ni-Mo₂C precursors, passivated Ni-Mo₂C and used catalysts (following HDS reaction) were determined from N₂ adsorption/desorption isotherms measured at -196 °C using a Micromeritics ASAP 2020 analyzer. The used catalysts were washed with acetone several times before analysis to remove the decalin solvent used in the reaction. (See Chapter 2 and Appendix B.1 for Details of the relative theory and calculation)

3.2.2.3 X-ray Diffraction (XRD)

The XRD of the fresh and used catalysts was compared to identify bulk phase changes of the catalysts during reaction. A Bruker D8 Focus (0-20, LynxEye detector) diffractometer was used for the analyses. (See Chapter 2 and Appendix B.2 for details)

3.2.2.4 X-ray Photoelectron Spectroscopy (XPS)

The details of XPS analysis were described in Chapter 2. Deconvolution of the XPS profiles was done using XPSPEAK41 software. Experimental peaks were decomposed through mixed Gaussian-Lorentzian functions (80% - 20%) after Shirley background subtraction. (See Appendix B.3 for details)

3.2.2.5 Transmission Electron Microscopy (TEM)

Transmission electron microscope (TEM) images of the supported catalysts were generated using a (JEOL) JEM 2200FS electron microscope operated at 200 kV, with a 1.9 Å point-to-

point resolution. Used catalysts were analyzed to identify the particle size distribution and characteristic slabs of the synthesized/formed species. The samples were prepared by dispersion in ethanol and then sonicated for several minutes. A drop of the suspension was placed on a 230 mesh copper grid coated with Formvar-Carbon film and then dried in a vacuum chamber. The clusters/particles identified in the TEM images were measured and counted to yield a size distribution that was fitted to a lognormal distribution to determine the average size of the cluster/particle. The number of formed MoS₂ layers was also counted based on the TEM images and the stacking degree (N) of MoS₂ was calculated as Eq. 3-1.

$$N = \frac{\sum_{i=1..t} n_i N_i}{\sum_{i=1..t} n_i} \quad (\text{Eq. 3-1})$$

where n_i is the number of stacks with N_i layers. (See Appendix C.4 for details)

3.2.2.6 Time of Flight Secondary Ion Mass Spectroscopy (TOF-SIMS)

A time of flight secondary ion mass spectrometer (TOF-SIMS; a PHI TRIFT V instrument) was used in the static SIMS mode to analyse the used catalysts and to identify changes in catalyst surface properties (with or without Ni as a promoter) following the HDS reaction. TOF-SIMS yields both elemental and molecular ions, and hence it can provide detailed information on the upper layer of the used catalysts. The catalyst samples were sputtered by a primary ion beam of Au⁺ before the spectra were collected in negative mode. For each analysis the delivered ion dose was 6.3×10^{11} ion/cm², and the total sputtering time for each spectrum was approximately 1800 s. The detected mass range was within 0 ~ 1850 amu and triplicate spectra were collected at three different points across the prepared samples with a raster size of 400.0 μm × 400.0 μm as representative sample areas. The obtained spectrum is shown in Appendix E.2, Figure E.10 for the used Ni_{0.19}Mo₂C/AC-550 catalyst.

3.2.3 Catalyst Activity Tests

The HDS of dibenzothiophene (DBT) was carried out in a 300 mL stirred-batch reactor (Autoclave Engineers) to assess the catalytic activities of the as-prepared Ni-Mo₂C/AC fresh catalysts with different Ni:Mo ratios (Ni:Mo = 0 ~ 0.76). The experiments were operated at 350 °C with an initial H₂ pressure of 2.1 MPa with ca. 2.0 wt% of DBT (0.35 wt% S) as the reactant in 100 mL decalin. Dissolution of DBT in decalin was assisted by sonication, which also removed dissolved air from the prepared liquid feed (Feed preparation is reported Appendix C.1, Table C.2). The catalyst was added to obtain 0.13 ~ 0.14 g_{metal}/100 mL liquid in the slurry. The fresh catalyst and O-free reactant liquid were placed in the reactor sequentially, under a N₂ blanket using a glove bag. The reactor was then sealed and flushed with N₂ to remove residual air from the reactor. After a leak test, ultra-high purity H₂ was used to first flush and then fill and pressurize the reactor to the desired level, following which the reactor was heated to a pre-determined temperature within 35 mins. After the reaction period (up to 5 h) the reactor was cooled to room temperature and de-pressurized. Liquid samples were recovered periodically during the reaction and analyzed using a Shimadzu (QP-2010-S) GC/MS and RTX5 30 m × 0.25 mm capillary column based on an internal calibration method. The internal standard used in this study was diphenylmethane (DPM) (see Appendix C.1 for details). Overall, the activity data reported herein were measured with a carbon balance ≥ 94% and several experiments were repeated to quantify the error in the activity data (See details in Appendices F.1, F.3 and F.4). Both external and internal mass transfer effects were shown to be minimal at the chosen reaction conditions and details of these calculations are presented in Appendix G.5 Table G.7.

A fixed bed reactor (length 50 cm, hot zone 30 cm with an internal diameter of 8.64 mm) operated in a down-flow mode was also used to compare the stability of the $\text{Ni}_{0.19}\text{Mo}_2\text{C}/\text{AC}-600$ and 10 % $\text{Mo}_2\text{C}/\text{AC}-650$ catalysts. The schematic of the reactor system is shown in Figure 3.1.

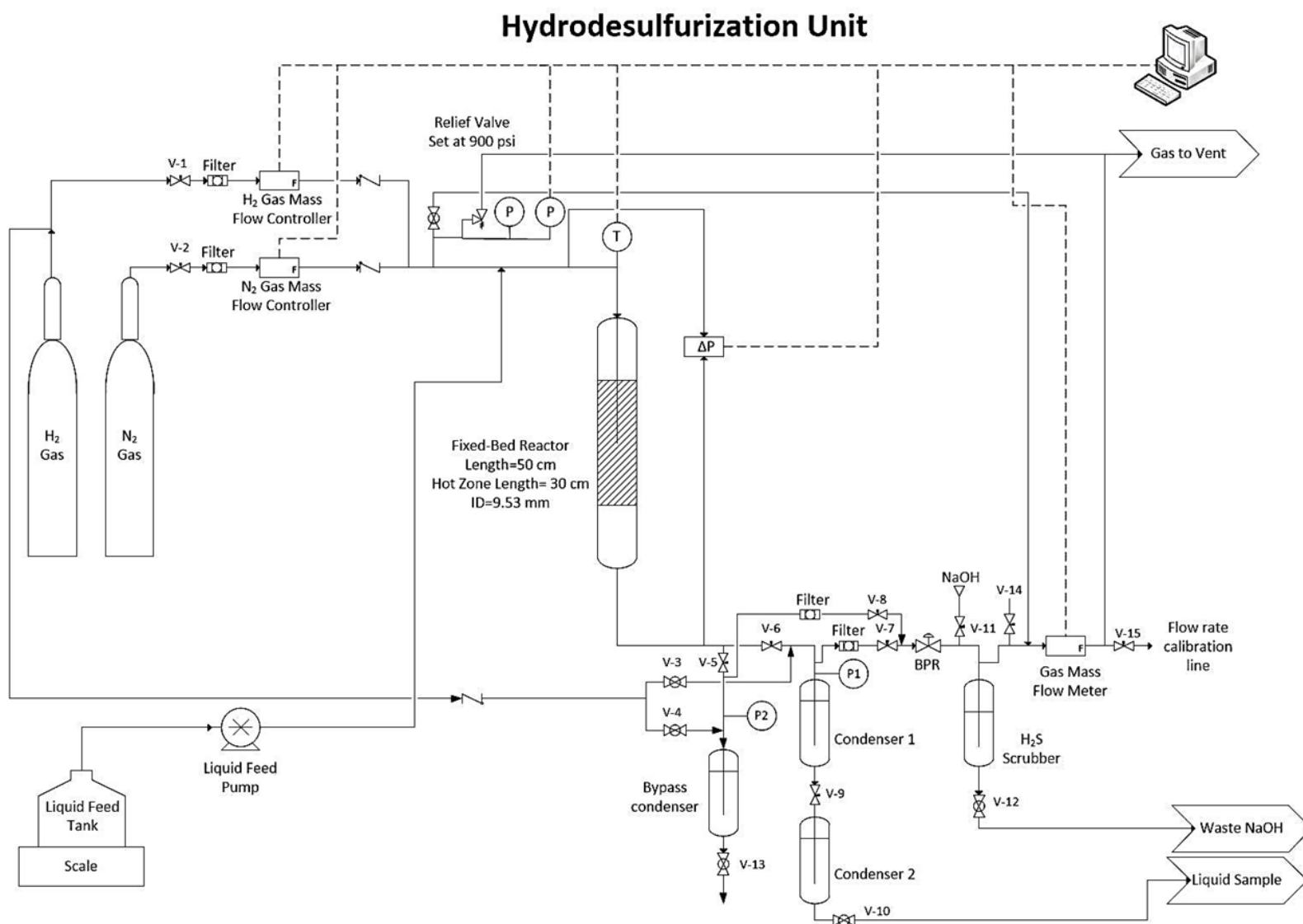


Figure 3.1: Schematic diagram of high pressure fixed-bed reactor for HDS of DBT.

The experiments were operated at 310 °C at a constant pressure of 4.1 MPa. The liquid feed, consisting of ca. 2.0 wt% DBT in decalin, was fed to the reactor by means of a high-pressure piston pump (Gilson model 307). The H₂ flow was controlled by a mass flow controller (Brooks 5850TR). All the experiments were operated with a H₂/feed volumetric ratio of 600 and a liquid-hourly space velocity (LHSV) of 8 h⁻¹. The liquid product was collected periodically from a condenser placed after the reactor exit and held at room temperature. Finally, the liquid samples were analyzed using gas chromatography (Shimadzu GC) by a capillary column (SHRXL-5MS, 15 m x 0.25 mm x 0.25 μm) and a FID detector. Before performing the activity test, the passivated catalyst (ca. 0.77 g, 2.5 mL) was activated in-situ under H₂ flow at 400 °C for 2 h to remove the passivation layer from the catalyst surface.

3.3 Results

3.3.1 Fresh Catalysts Characterization

XRD analysis of the calcined Ni-Mo₂C/AC catalyst precursors showed an amorphous structure, indicating a high dispersion of metals on the support (Appendix E.2, Figure E.4). Figure 3.2 presents the XRD patterns of the Ni-Mo₂C/AC catalysts with Ni:Mo ratios of 0 ~ 0.76, and prepared at different CHR temperatures (Figure 3.2 (a): 550 °C; Figure 3.2 (b): 600 °C). Included at the top of both Figures are the spectra for 10%Mo₂C/AC-750, the unpromoted Mo₂C prepared at a reduction temperature of 750 °C to show the positions of β-Mo₂C (PDF card # 00-035-0787). Mo₂C is detected in all the diffractograms of Figure 3.2, with diffraction peaks at 2θ = 40.12°, 44.21°, 46.14°, 61.35°, 72.87°, 82.97°, 86.58° and 89.51° and no other bulk phases of MoO_x present in the samples. At a reduction temperature of 550 °C, the peak intensities of Mo₂C

increased with increased Ni:Mo ratio in the range of 0.02 ~ 0.44 and the same phenomenon occurred at a reduction temperature of 600 °C, but for a narrower Ni:Mo ratio of 0.02 ~ 0.19. Figure 3.2 (b) shows that when Ni:Mo ratio is > 0.19, the intensities of the Mo₂C reflections do not increase, however other phases are detected. The peaks at 51.28 ° and 60.23 ° are assigned to metallic Ni (PDF card # 00-004-0850) and the separation of Ni from the Mo₂C can be observed when the Ni:Mo ratio is > 0.38 at both reduction temperatures of 550 °C and 600 °C. A clear phase separation of Ni from the Mo₂C was also reported by Puello-Polo et al. [31] and Santillán et al. [30] when synthesizing the catalysts using the same metal salts as those used herein. The Ni-Mo bimetallic carbide (Ni₆Mo₆C₂, PDF card # 01-089-4883) was detected with diffraction angles $2\theta = 47.76^\circ$, 50.51° and 53.40° when the Ni:Mo ratio reached 0.38 at both reduction temperatures, whereas nickel carbide was not detected in any of the samples.

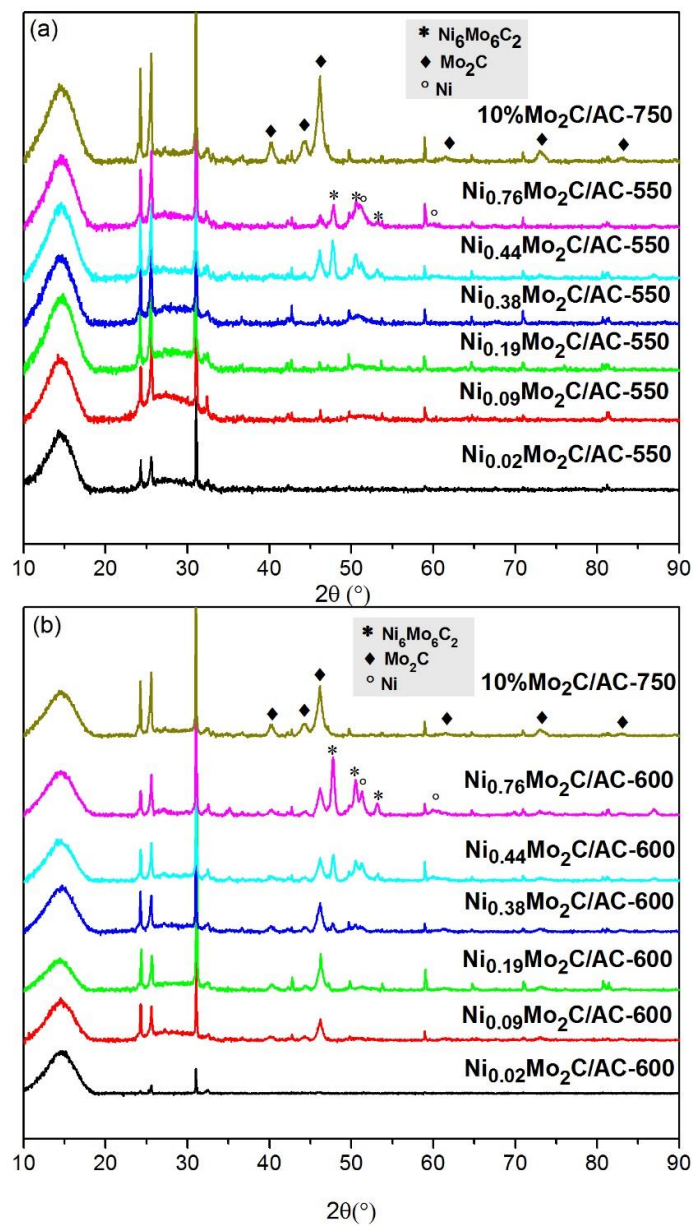


Figure 3.2: XRD patterns of Ni-Mo₂C/AC catalysts with different ratios of Ni:Mo (0 ~ 0.76) prepared at different reduction temperatures: (a) Reduced at 550 °C; (b) Reduced at 600 °C. (◆) Mo₂C; (○) Ni; (*)

Ni₆Mo₆C₂.

Analysis of the XRD data for the Ni_xMo₂C/AC-600 catalysts (0 ≤ x ≤ 0.19) yields a small decrease in the Mo₂C lattice parameters with increased Ni content (Table 3.1). The diffraction angles also shifted to higher diffraction angles for the Ni_{0.19}Mo₂C/AC-600 compared to the unmodified catalyst (10%Mo₂C/AC-750), implying some incorporation of Ni into the β-Mo₂C crystal structure. The presence of Ni means that some of the Ni may substitute Mo atoms in the crystal structure randomly. Thus, the crystallite strain will be changed, leading to a change in the lattice parameters. Similar phenomena have been reported elsewhere [129, 130]. Thus, the interaction between Ni and Mo₂C occurs at low Ni loadings. The lattice parameters at higher Ni contents were not determined because of Ni phase separation and the crystallite sizes were not calculated from the XRD data because small particles of Mo₂C are air sensitive and re-oxidize during analysis.

Table 3.1: XRD analysis of Ni_xMo₂C/AC-600 catalysts and Mo₂C/AC-750 catalyst.

Catalyst	Phases	Diffraction peaks, 2θ			Lattice parameters ^a (Å)	
		Mo ₂ C			a/b	c
		100	200	101		
10%Mo ₂ C/AC-750	β-Mo ₂ C	40.23	44.30	46.14	3.0050	4.7633
Ni _{0.09} MoC/AC-600	β-Mo ₂ C	40.25	44.23	46.18	3.0032	4.7563
Ni _{0.19} MoC/AC-600	β-Mo ₂ C	40.30	44.41	46.26	3.0000	4.7402

a. The lattice parameters were calculated by Eq.B-4 (Appendix B.2).

The measured Ni:Mo ratios of the catalysts are reported in Table 3.2. The carbon loss (mass burn-off) from the AC support that occurred during CHR (as shown in the last two columns in Table 3.2) increased with increased Ni:Mo ratio and increased reduction temperature.

Table 3.2: Catalyst composition of fresh Mo₂C/AC-650 and Ni-Mo₂C/AC catalysts.

Ni:Mo ^a	Metal content (wt%)				Mass burn off ^b	
	550 °C		600 °C		550 °C	600 °C
	Ni	Mo	Ni	Mo		
0.02	0.12	8.60	0.13	9.41	5	14
0.09	0.49	8.49	0.53	9.26	9	17
0.19	1.01	8.52	1.22	10.35	18	33
0.38	2.06	8.90	2.43	10.52	19	34
0.44	2.90	10.77	3.89	14.43	25	47
0.76	4.78	10.26	6.26	13.44	28	48

^a. These values were measured by ICP-OES.

^b. Mass burn-off (%) was calculated by the mass difference before and after CHR divided by the mass before CHR, error $\pm 2\%$.

During CHR, the AC support reacts with the H₂, mostly forming CH₄, as determined by GC-FID analysis of the product gases (Figure 3.3). The maximum concentration of CH₄ in the product gas from the CHR was ~ 2.0 mol% at 650 °C for the unpromoted Mo₂C (Figure 3.3 (a)); whereas, in the presence of Ni, the CH₄ concentration was significantly higher (up to ~ 6 mol%), even at 600 °C. Figure 3.3 (b) shows that the maximum in the CH₄ content of the CHR product gas increased with increased Ni content. Furthermore, the CH₄ formation profiles are different between the unpromoted and Ni promoted Mo₂C. In the former case, the CH₄ content doubles every 50 °C in the temperature interval 550 °C \sim 650 °C and remains approximately constant during the hold period; whereas, for the Ni-Mo₂C precursors, the CH₄ concentration decreases significantly above the highest reduction temperature of 600 °C. The mass burn-off (carbon loss) for the Mo₂C/AC-650 catalyst was ~ 18 wt%, similar to the Ni_{0.19}Mo₂C/AC-550 (reduced at 550 °C), clearly indicating that the presence of Ni accelerates the carbon loss at low temperature,

which reduces the carburization time required for the Mo precursor. Also note that the mass burn-off is well correlated with CH_4 formation during CHR (Figure 3.4).

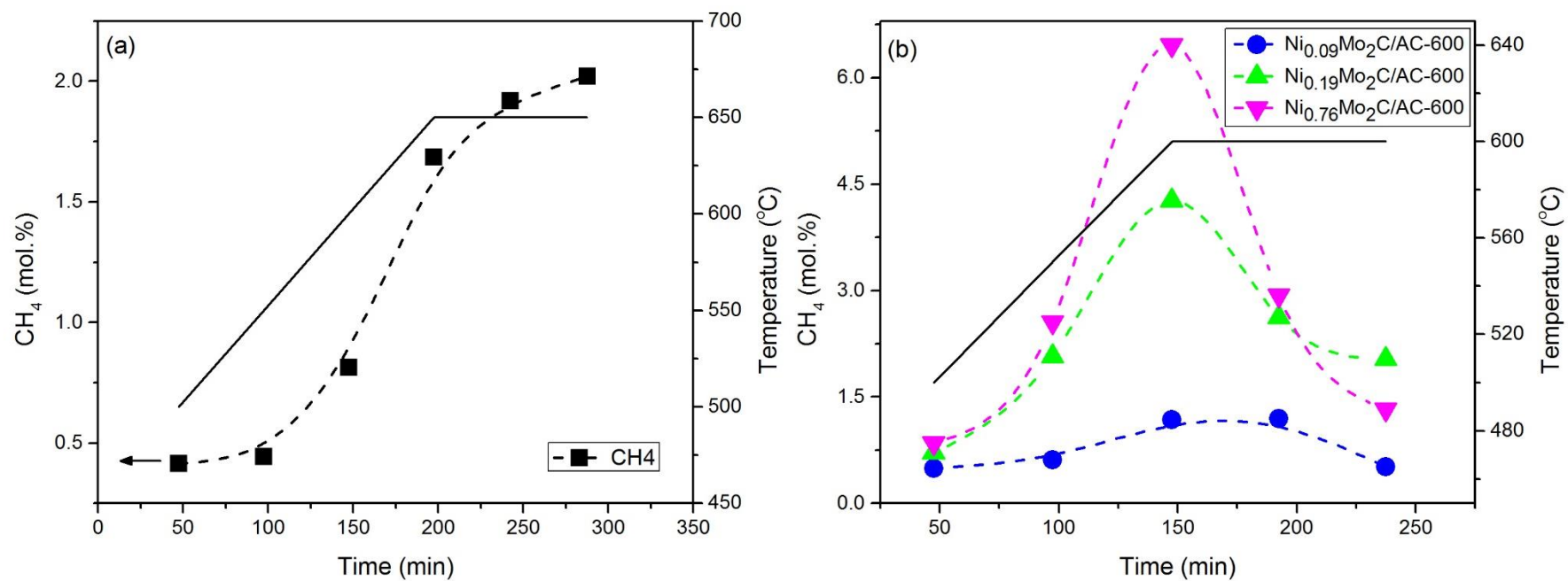


Figure 3.3: Profile of detected CH₄ (mol%) during carbothermal hydrogen reduction of the catalyst generation: (a) Mo₂C/AC-650 (■); (b) Ni-Mo₂C/AC with different ratios of Ni:Mo ((●) Ni_{0.09}Mo₂C/AC-600; (▲) Ni_{0.19}Mo₂C/AC-600; (▼)Ni_{0.76}Mo₂C/AC-600).

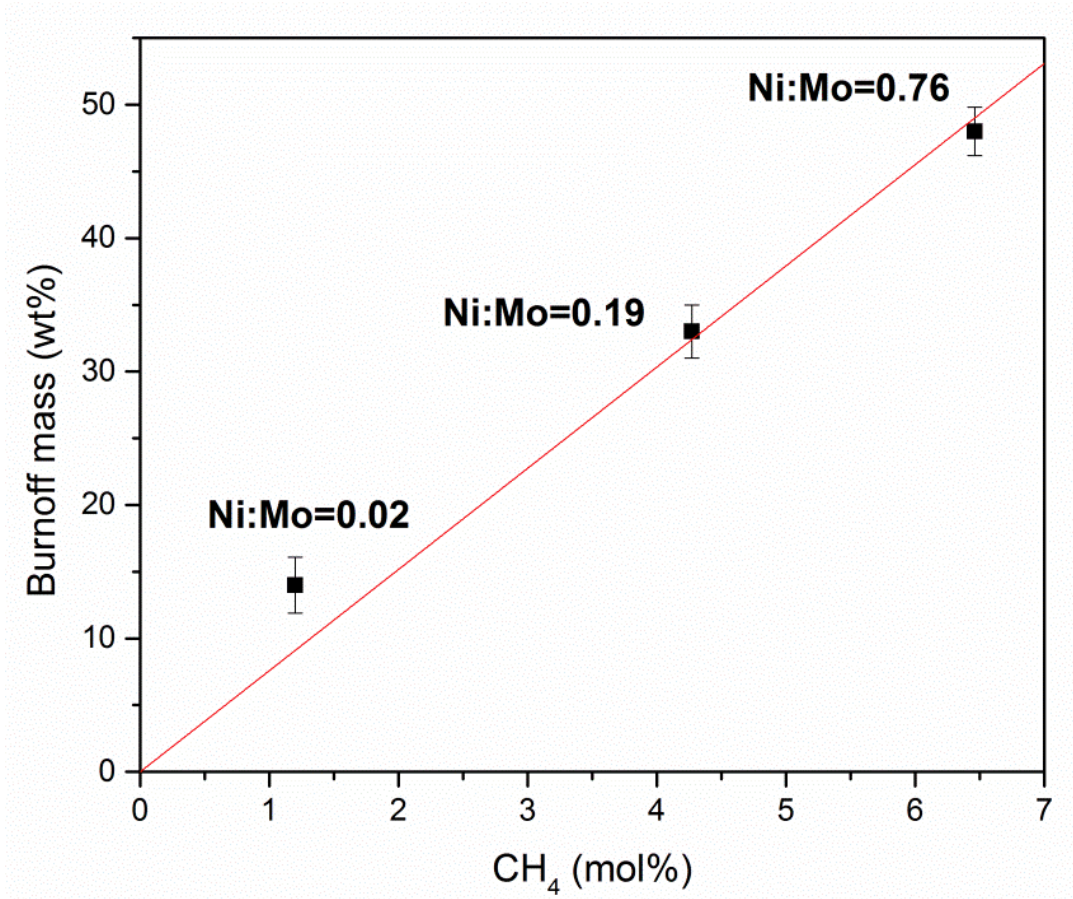


Figure 3.4: A correlation between mass burn-off (wt%) and formed CH₄ (mol%) during CHR process. The solid line represents the correlation equation: Mass burn-off (wt%) = 7.5847 × CH₄ (mol%), Std.Dev.= 0.4055. (R²=0.9918)

After CHR, the shape of the N₂ adsorption isotherms were similar to the AC support for all prepared catalysts with a H3 type hysteresis loop (Appendix E.2, Figure E.5). Also, it found that the hysteresis loop spanned P/Po = 0.4~1.0, suggesting a wider distribution of the pore size. The surface area of the catalysts prepared at a CHR temperature of 550 °C did not show a significant change with increased Ni content; whereas, at 600 °C, the surface area decreased with increased Ni content (Table 3.3 and Appendix E.2-Figure E.6). Moreover, both catalysts showed a general

trend of increased pore size with increased Ni content and the increase was due to an increase in mesopore volume (Appendix E.2, Figure E.6).

Table 3.3: Physical properties of fresh and used Ni-Mo₂C/AC catalysts prepared at reduction temperatures of 550 °C and 600 °C.

Ni:Mo	Surface area (m ² /g)				Ave. pore size (nm)				V _{meso} /V _{total} (%)			
	Fresh		Used		Fresh		Used		Fresh		Used	
	550	600	550	600	550	600	550	600	550	600	550	600
0.00 ^a	911	467	911	467	3.70	4.70	3.70	4.70	83	93	83	93
0.02	778	406	887	450	3.58	4.90	3.75	4.90	76	95	80	94
0.09	815	436	774	472	3.67	4.90	4.46	5.50	81	95	85	98
0.19	721	403	701	409	3.88	5.10	5.10	7.10	83	97	90	100
0.38	763	446	650	380	3.86	5.40	6.12	7.50	84	95	93	100
0.44	774	349	647	369	4.50	5.60	6.30	9.00	88	97	95	100
0.76	806	385	525	206	4.70	6.20	6.87	9.40	89	100	98	100

^a. This is the unpromoted Mo₂C/AC-650 catalyst.

3.3.2 Catalysts Characterization after HDS Reaction

All the catalysts were characterized after the HDS reaction to identify potential changes in the catalyst chemical and physical properties. In addition, the MoS₂/AC catalyst properties are reported here as a comparator for the used Ni-Mo₂C/AC catalyst properties. The catalysts were separated by high speed centrifuge from the slurry recovered from the batch reactor. The solid fraction was then washed in acetone and dried overnight under a N₂ blanket in a glove bag. Prior to XPS and TEM analysis, the dried samples were degassed in vacuum at 200 °C for 4 h. The transfer of the samples to the vacuum chamber (XPS, TEM) was done within 5 min to minimize exposure to air.

3.3.2.1 XRD and BET Analysis

As shown in Figure 3.5, the XRD analysis of the used catalysts showed no change in the Mo_2C bulk structure after reaction, indicating that the Mo_2C crystallites are resistant to bulk sulfidation under the chosen reaction conditions, consistent with the observation made by Aegerter et al. [124]. There were no peaks that could be assigned to S compounds in the XRD pattern of the used catalysts either.

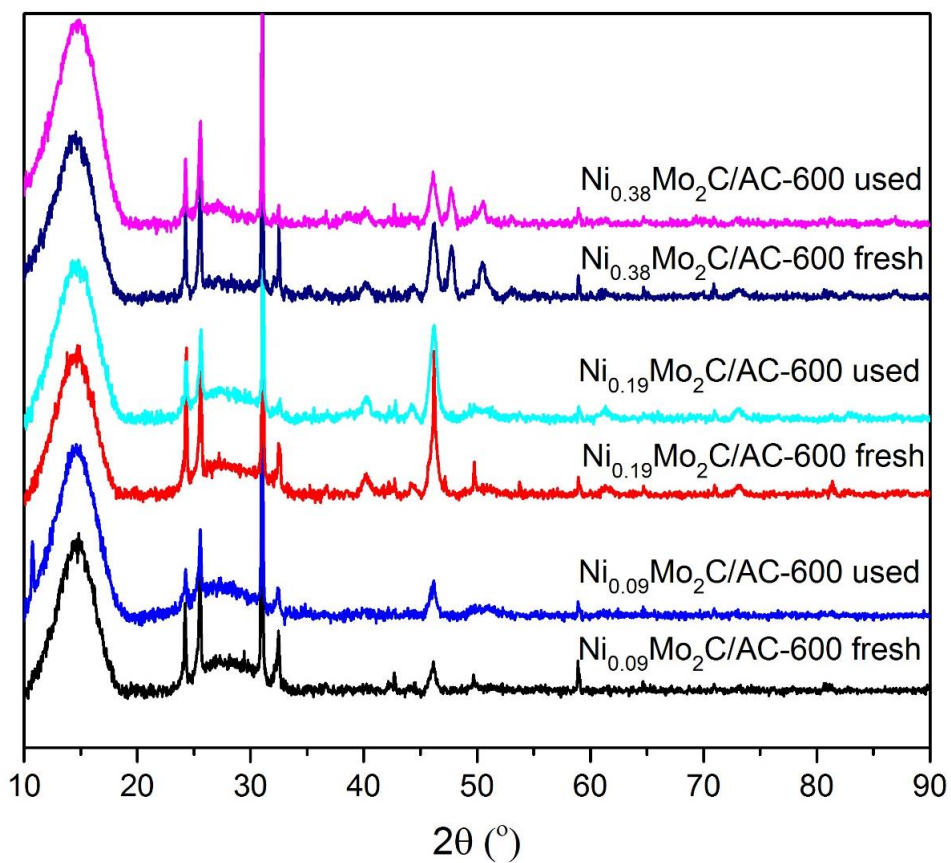


Figure 3.5: X-ray diffraction patterns for fresh and used Ni- $\text{Mo}_2\text{C}/\text{AC}$ catalysts.

The BET analysis data (Table 3.3) generally indicate that after the HDS reaction, there was a significant loss in catalyst surface area, whereas the average pore size and mesopore volume fraction increased, implying that mostly micropores were blocked during reaction.

3.3.2.2 XPS and CHNS Analysis

The effect of increased Ni:Mo ratio on the XPS spectra of the used catalysts is shown in Table 3.4 and Figure 3.6. The elemental surface compositions clearly show the presence of S on the catalyst surface after the HDS of DBT, consistent with data reported by Sajkowski and Oyama [3]. As illustrated in Table 3.4, the used Ni-Mo₂C catalysts reduced at 550 °C have higher S content than the same catalysts reduced at 600 °C. In addition, the Ni-Mo₂C catalysts all have higher S content after reaction than the Mo₂C catalyst with no Ni addition.

Table 3.4: XPS and CHNS analysis of used (Ni)-Mo₂C/AC catalysts with different Ni:Mo ratios and different reduction temperatures.

Used catalyst ^a	S, At% ^b	Mo, At% ^b	O, At% ^b	C, At% ^b	S/Mo atomic ratio, %	S ^c , wt%	S ^d , wt%
10%Mo ₂ C/AC-650	0.43	0.82	4.43	94.32	0.53	1.07	2.00
Ni _{0.19} Mo ₂ C/AC-550	0.90	0.64	3.68	94.78	1.41	2.23	3.24
Ni _{0.44} Mo ₂ C/AC-550	1.10	0.52	5.06	93.32	2.12	2.75	3.84
Ni _{0.19} Mo ₂ C/AC-600	0.67	0.68	4.99	93.67	0.99	1.65	2.22
Ni _{0.44} Mo ₂ C/AC-600	0.97	0.76	4.40	93.87	1.28	2.39	2.85

^a All of these used catalysts listed were recovered following 5 h HDS of DBT in the batch reactor;

^b These values were measured by XPS and being normalized;

^c It indicated the amount of surface adsorbed S wt% based on XPS measurement;

^d It indicated the amount of bulk phase S wt% based on CHNS analyzer.

Apart from a clear increase in S content on the catalyst surface with increased Ni addition, the Mo3d XPS spectra of Figure 3.6 (a) and (c) show an obvious shift from lower B.E. to higher B.E. as Ni content increases, indicative of the formation of Mo-S surface species. The Mo3d shift to higher B.E. on the Ni-Mo₂C is greater than that of the Mo₂C/AC, indicating more sulfidation of the Mo in the presence of the Ni. The presence of Ni likely increased the S adsorption on metal sites, such that the S content of the used catalysts increased with increased Ni addition.

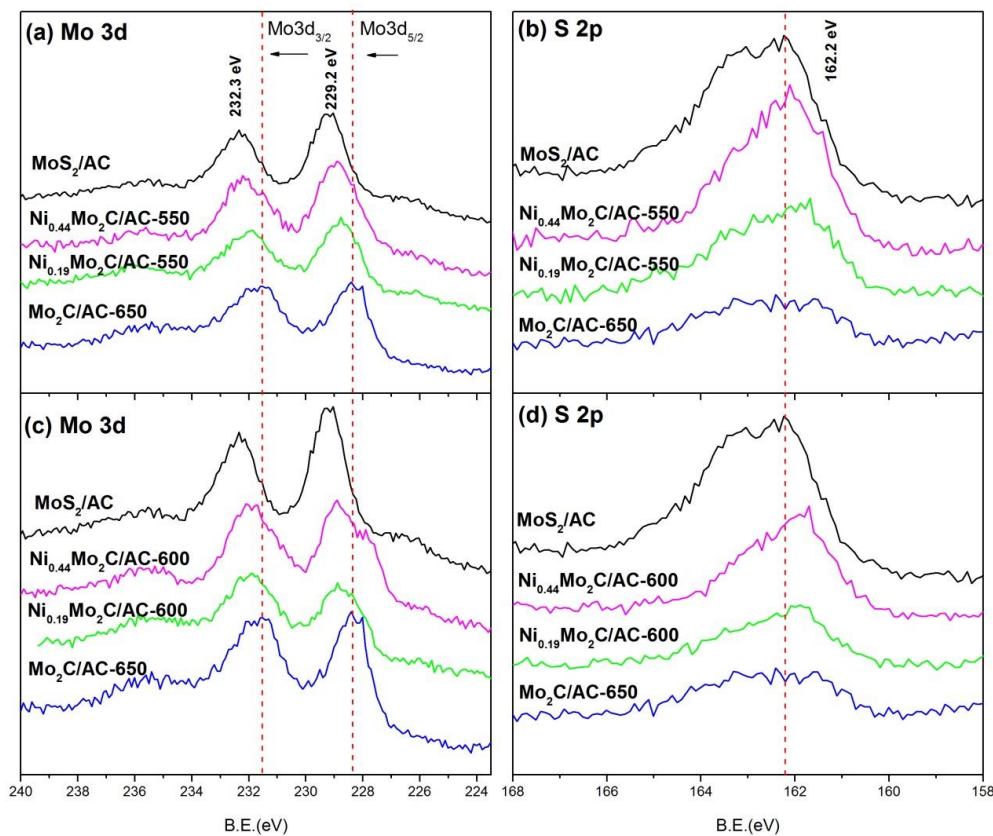


Figure 3.6: XPS narrow scan spectra of used MoS₂/AC, Mo₂C/AC and Ni_xMo₂C/AC-y catalysts: (a, c) Mo 3d; (b, d) S 2p. (The dashed lines in (a, c) indicate the position of Mo²⁺ species from Mo₂C; the dashed lines in (b, d) indicate the position of S²⁻ species from MoS₂.)

Figure 3.7 compares the Mo 3d and S 2p XPS spectra of the $\text{Ni}_{0.19}\text{Mo}_2\text{C}/\text{AC}-550$ catalyst after reaction for different periods to that of the MoS_2/AC catalyst. The S 2p peak at B.E. = 162.2 eV confirms the presence of Mo-S surface species, consistent with the results from the Mo 3d spectra. In addition, it is noted that the Mo 3d B.E. of the Ni-Mo₂C catalyst surface is relatively stable after 1 h of reaction and clearly different from that of the MoS_2/AC surface as shown in Figure 3.7.

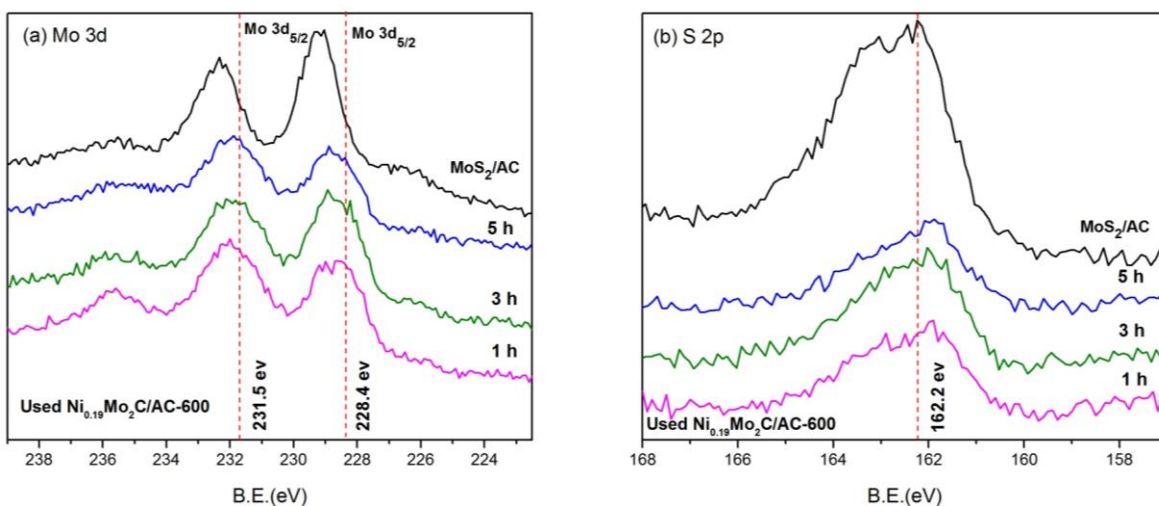


Figure 3.7: XPS narrow scan spectra of used $\text{Ni}_{0.19}\text{Mo}_2\text{C}/\text{AC}-550$ catalyst after HDS reaction for different reaction periods. (a) Mo 3d; (b) S 2p.

Table 3.5 also shows that the S species accumulate during reaction since the S content (i.e. the atomic ratio of S to Mo or S wt%) increased with increased reaction time for all catalysts. The S content (wt%) measured by CHNS and reported in the last column of Table 3.5, does not show a clear difference between the two catalysts. However, the S wt% calculated based on the XPS

data give clear differences between these two catalysts, showing a strong ability of S adsorption in the presence of Ni. For the 10%Mo₂C/AC-650 catalyst, the S:Mo ratio is 0.30 after 1 h of HDS, whereas for the Ni-Mo₂C it is 0.69, indicating a faster sulfidation of the Ni-Mo₂C catalyst at the beginning.

Table 3.5: XPS and CHNS analysis of used catalysts ($\text{Mo}_2\text{C}/\text{AC}-650$ and $\text{Ni}_{0.19}\text{Mo}_2\text{C}/\text{AC}-600$) after HDS reaction in the batch reactor for different reaction periods.

Used catalyst	Reaction time (h)	S, At% ^a	Mo, At% ^a	O, At% ^a	C, At%	S/Mo atomic ratio, %	S ^b , wt%	S ^c , wt%
$10\%\text{Mo}_2\text{C}/\text{AC}-650$	1	0.20	0.68	3.73	95.39	0.30	0.51	1.33
	3	0.30	0.70	4.08	94.92	0.43	0.75	1.47
	5	0.40	0.69	4.44	94.47	0.59	1.01	2.00
$\text{Ni}_{0.19}\text{Mo}_2\text{C}/\text{AC}-600$	1	0.47	0.68	4.01	94.83	0.69	1.18	1.40
	3	0.58	0.68	3.41	95.33	0.87	1.46	1.83
	5	0.67	0.68	4.99	93.67	0.99	1.65	2.22

^a These values reported here were measured by XPS and being normalized;

^b It indicated the amount of surface absorbed S wt% based on XPS measurement;

^c It indicated the amount of bulk phase S wt% based on CHNS analysis.

3.3.2.3 TOF-SIMS Analysis

The negative ion mass spectrum of Mo, sulfur or oxysulfide (oxide) spectra were recorded during sputtering from a catalyst sample area of $400.0 \times 400.0 \mu\text{m}$. Several interesting Mo characteristic fragments containing O, S or both were detected in the used catalysts, such as MoS^- or MoO_2 ($m/z=128$), MoOS^- or MoO_3 ($m/z=144$), MoO_2S^- or MoS_2 ($m/z=160$), MoO_3S^- ($m/z=176$) and MoO_2S_2 ($m/z=192$). The presence of sulfur indicates that the surface of the catalyst has been changed during the HDS reaction with the formation of Mo-O-S or Mo-S bonds on the catalyst surface. In order to eliminate possible variations between samples, the normalized ion intensity yield (i.e. relative intensity, RI) is used to make comparisons. The distribution of identified Mo oxysulfide species (MoO_xS_y) is represented by the abundance of each Mo oxysulfide species divided by the abundance of all MoO_xS_y ions (Prime relative intensity, RI'). The identified molecular fragments and their relative abundance are reported in Table 3.6. These data confirm the adsorption of S on the catalyst surface during reaction and indicate that in the presence of Ni, the amount of MoS surface species is almost 2x's higher than that on the unpromoted Mo_2C (Ni:Mo=0), consistent with the XPS analysis results.

Table 3.6: Normalized intensity of selected ions (containing the most abundant isotope ^{32}S) calculated based on TOF-SIMS spectra of used catalysts of 10%Mo₂C/AC-650 and Ni_{0.19}Mo₂C/AC-600.

Calculated parameters	Used catalyst	
	10%Mo ₂ C/AC-650	Ni _{0.19} Mo ₂ C/AC-550
RI (S) ^b (x 10 ⁻²)	1.91 ±0.12 ^a	2.27±0.10
RI (MoO _x S _y) ^c (x 10 ⁻²)	0.13±0.01	0.25±0.01
RI (MoO _x S _y)/RI (S) (%)	6.81±0.68	11.01±0.66
Distribution of Identified MoO _x S _y species (RI') ^d (%)		
RI'(MoS) ^e	13.09±0.87	6.98±0.16
RI'(MoOS) ^f	52.30±0.46	56.07±0.43
RI'(MoO ₂ S or MoS ₂) ^f	24.28±0.45	26.46±0.39
RI'(MoO ₃ S or MoOS ₂) ^f	6.60±0.40	4.45±0.05
RI'(MoO ₂ S ₂ or MoS ₃) ^f	3.72±0.28	6.05±0.17

^a. This value was estimated as standard deviation;

^b. The relative intensity (RI) of total identified S to total ions: $\text{RI}(\text{S}) = \Sigma \text{S}^- / \Sigma \text{I}^+$.

^c. The relative intensity (RI) of total identified MoO_xS_y⁻ to total ions: $\text{RI} = \Sigma \text{MoO}_x\text{S}_y^- / \Sigma \text{I}^+$.

^d. This distribution was based on all the identified MoO_xS_y⁻ species.

^e. Prime relative intensity (RI') of MoS ions to total MoO_xS_y⁻ ions: $\text{RI}' = \text{MoS} / \Sigma \text{MoO}_x\text{S}_y^-$.

^f. All of these were similar to e's calculation by changing numerator.

3.3.2.4 TEM Analysis

The TEM micrographs of the used Ni-Mo₂C/AC catalysts reduced at 600 °C with various Ni:Mo ratios are presented in Figures 3.8 and 3.9. The formation of core-shell like structures is clearly visible, suggesting that a Mo₂C core is surrounded by MoS₂ generated during the HDS reaction. The size of the core-shell structure increases from 9.8 nm to 20.9 nm as Ni content increases, as shown by the lognormal distribution data of Figure 3.8. The Mo₂C-MoS₂ clusters become agglomerated when the Ni:Mo ratio > 0.44. At low Ni content, such as Ni_{0.02}Mo₂C/AC-600, the

contrast between particle and support is low and it is difficult to quantify the particle size from the TEM micrograph. For the 10%Mo₂C/AC-650, the characteristic slabs of MoS₂ are difficult to identify. Note also that the number of MoS₂ layers formed around the Mo₂C core increases with increased Ni content, as reported in Figure 3.9.

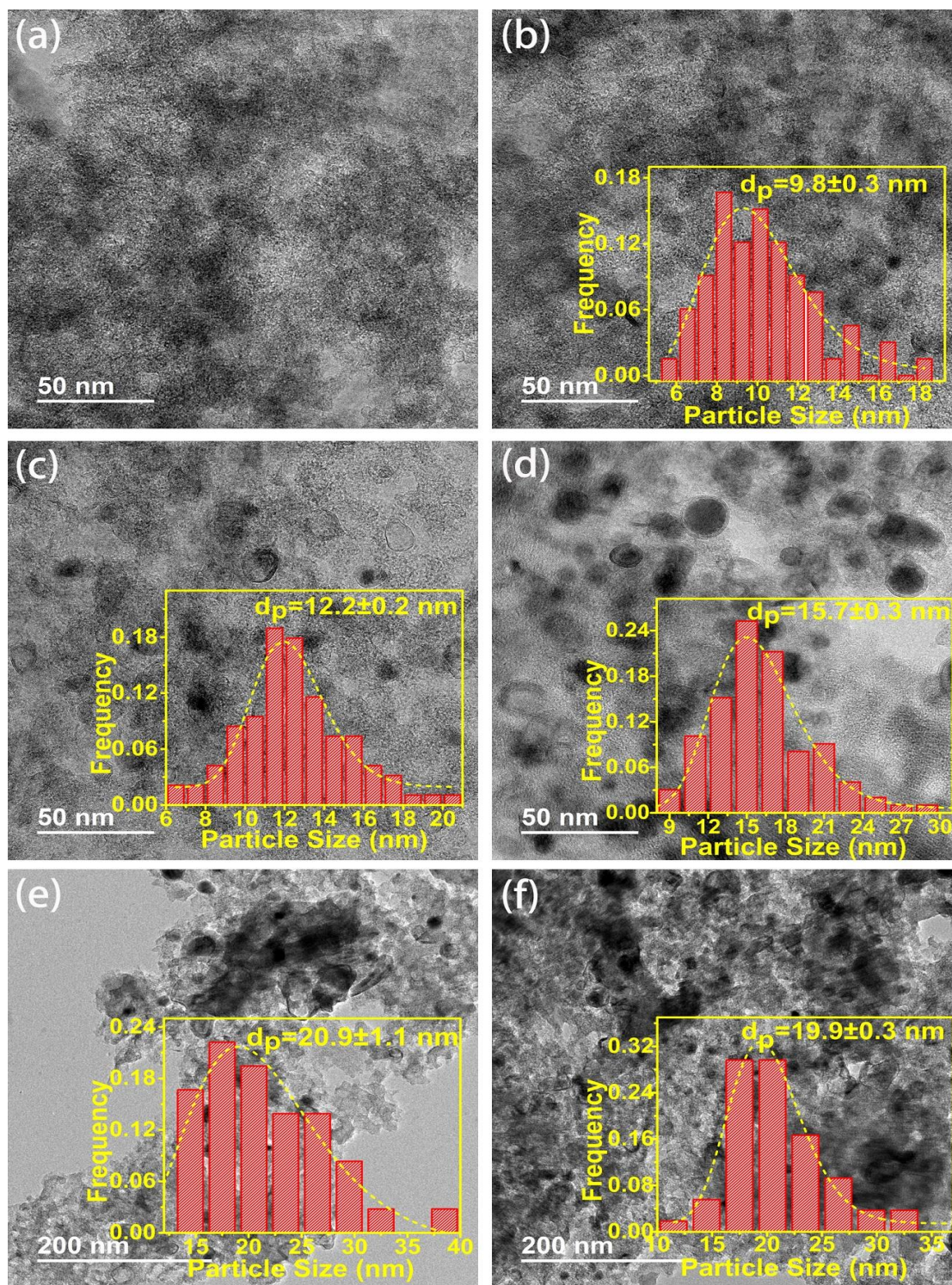
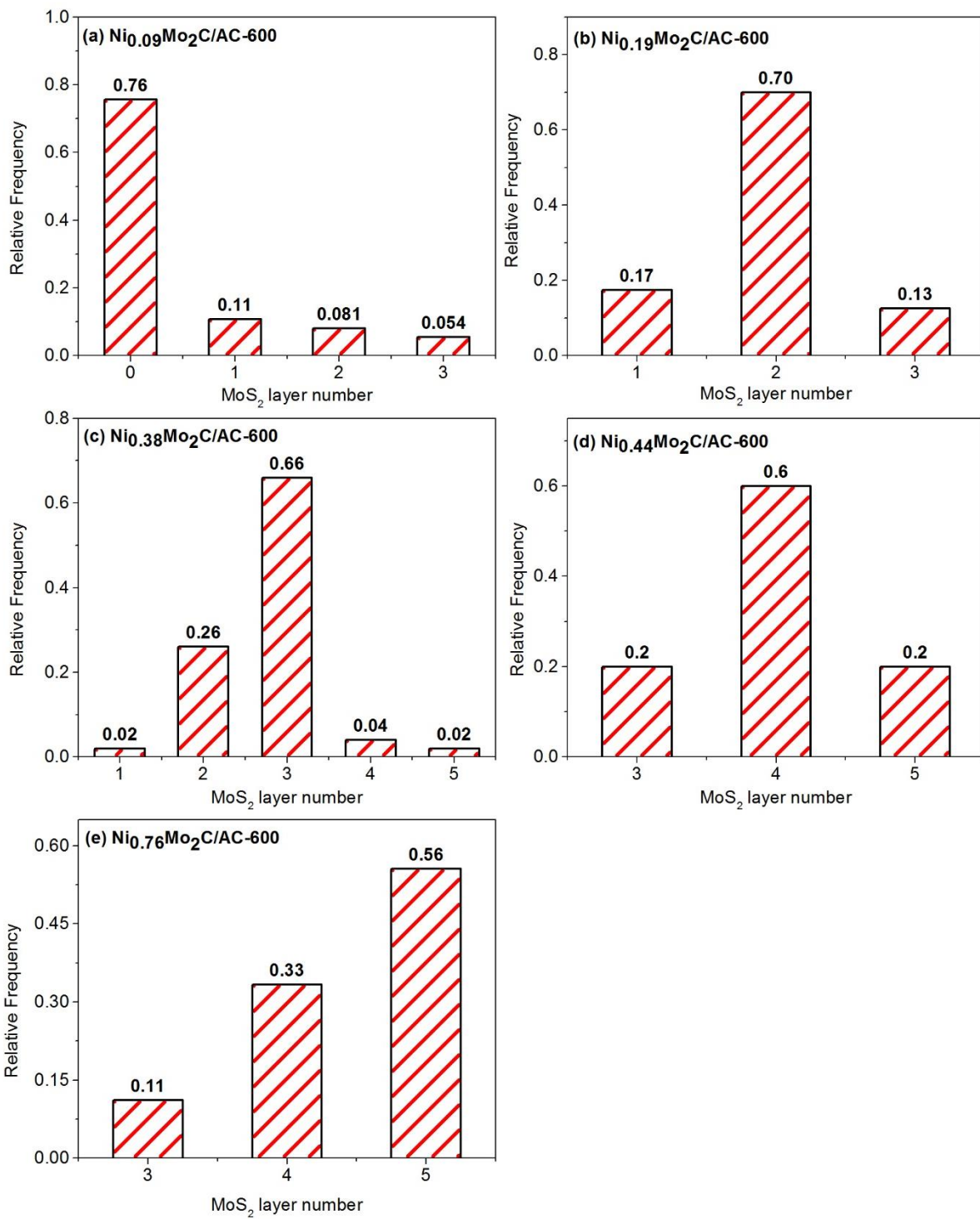


Figure 3.8: TEM images and cluster size distribution of used Ni-Mo₂C/AC catalysts with different Ni contents. (a) Ni_{0.02}Mo₂C/AC-600; (b) Ni_{0.09}Mo₂C/AC-600; (c) Ni_{0.19}Mo₂C/AC-600; (d) Ni_{0.38}Mo₂C/AC-600; (e) Ni_{0.44}Mo₂C/AC-600; and (f) Ni_{0.76}Mo₂C/AC-600.



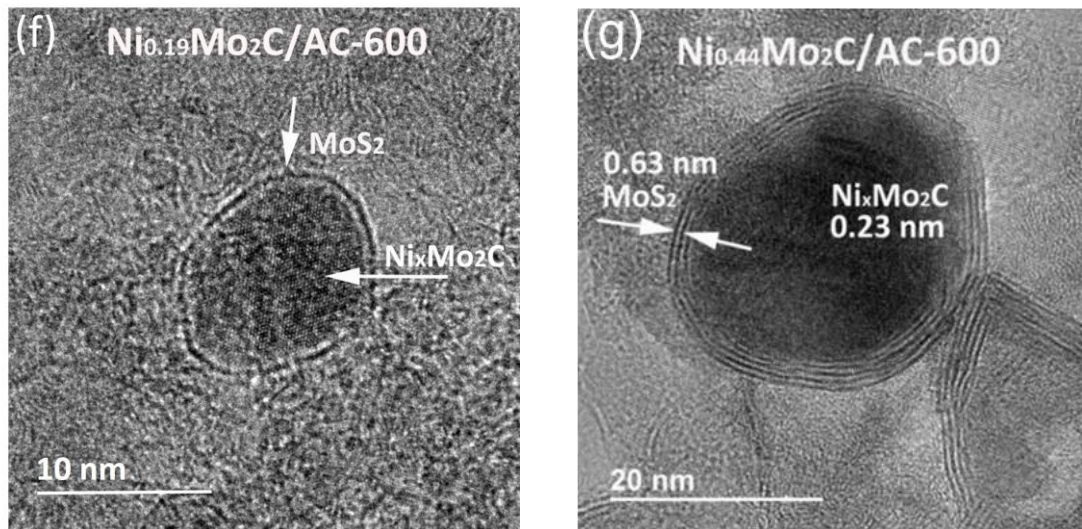


Figure 3.9: Distribution of MoS_2 layer numbers for used catalysts. (a) $Ni_{0.09}Mo_2C/AC-600$; (b) $Ni_{0.19}Mo_2C/AC-600$; (c) $Ni_{0.38}Mo_2C/AC-600$; (d) $Ni_{0.44}Mo_2C/AC-600$; (e) $Ni_{0.76}Mo_2C/AC-600$; (f) Enlarged $Ni_{0.19}Mo_2C/AC-600$; and (g) Enlarged $Ni_{0.44}Mo_2C/AC-600$.

3.3.3 Catalyst Performance in HDS of DBT

Dibenzothiophene (DBT) was chosen as the model reactant to determine the activity of the prepared catalysts. The results of the activity tests at 350 °C for Ni- Mo_2C/AC catalysts, prepared at different reduction temperatures and Ni:Mo ratios are presented in terms of DBT conversion in Table 3.7.

Table 3.7: DBT conversion for (Ni)-Mo₂C/AC catalysts at 350 °C and an initial pressure of 2.1 MPa.

Catalysts	Catalyst weight (g)	Burn off% [g _{cata./} g _{precursor}]	Metal weight in RXN (g)	Conversion ^a (%)	Catalysts	Catalyst weight (g)	Burn off% [g _{cata./} g _{precursor}]	Metal weight in RXN (g)	Conversion ^a (%)
Mo ₂ C/AC-650	1.4029	16.95	0.14	33.67	Mo ₂ C/AC-650	1.4029	16.95	0.14	33.67
Ni _{0.02} Mo ₂ C/AC-550	1.6485	5.17	0.14	41.69	Ni _{0.02} Mo ₂ C/AC-600	1.4920	14.09	0.14	36.79
Ni _{0.09} Mo ₂ C/AC-550	1.5026	8.79	0.13	44.58	Ni _{0.09} Mo ₂ C/AC-600	1.4112	17.13	0.14	35.84
Ni _{0.19} Mo ₂ C/AC-550	1.3144	17.68	0.13	44.34	Ni _{0.19} Mo ₂ C/AC-600	1.1252	33.83	0.13	48.07
Ni _{0.38} Mo ₂ C/AC-550	1.2602	19.10	0.14	50.22	Ni _{0.38} Mo ₂ C/AC-600	1.0326	33.15	0.13	35.52
Ni _{0.44} Mo ₂ C/AC-550	1.2798	25.89	0.18	45.08	Ni _{0.44} Mo ₂ C/AC-600	0.6644	47.63	0.12	31.17
Ni _{0.76} Mo ₂ C/AC-550	1.2081	28.01	0.18	39.58	Ni _{0.76} Mo ₂ C/AC-600	0.6262	48.03	0.12	31.14

a. This conversion was obtained based on HDS reaction of DBT at 350 °C following 5 h.

The mass of catalyst used for each activity measurement varied to account for the AC mass loss during the various CHR conditions; however, the total Mo+Ni mass remained relatively constant ($\sim 0.14 \text{ g}_{\text{metal}}/100 \text{ mL}_{\text{feed}}$) for all experiments. The data of Table 3.7 show that the DBT conversion on Ni-Mo₂C/AC reduced at 550 °C were generally higher than the DBT conversion measured on the unpromoted Mo₂C/AC catalyst and higher than the DBT conversion measured on the Ni-Mo₂C/AC reduced at 600 °C, provided the Ni:Mo ratio is < 0.44 . The data clearly show improved activity of the Mo₂C in the presence of Ni. The conversion over the Ni-Mo₂C/AC-550 catalyst increased with increased Ni content for Ni:Mo ratios of 0 ~ 0.38, but decreased when the ratio increased > 0.38 . The decreased conversion is likely due to the Ni phase separation that occurs at high Ni content and higher carbon loss (burn-off%) above a Ni:Mo ratio of 0.38 that may also decrease Mo dispersion. Similar observations with respect to increased HDS activity of P-doped Ni-Mo₂C/Al₂O₃ catalysts with increased Ni content, were reported by Sundaramurthy et al. [131], using gas oils derived from Athabasca bitumen.

Kinetic analysis of the batch reactor data is complicated by the fact that the Mo₂C-based catalysts undergo sulfidation during reaction and consequently, their activity and selectivity may change with reaction time in the batch reactor. As shown in Table 3.5, the S content of the catalysts (with or without Ni addition) increases with reaction time. However, the difference in the amount of sulfur adsorbed on the 10%Mo₂C/AC-650 and Ni_{0.19}Mo₂C/AC-600 is constant at $\sim 0.27 \text{ At\%}$ independent of reaction time (Table 3.5, column 3). This indicates that Ni has the ability to increase S adsorption but the effect of the Ni occurs rapidly within the 1st hour of reaction. The continued adsorption of S beyond this period is a consequence of the carbon

support. Furthermore, Figure 3.7 shows that there is no visible difference with respect to the Mo oxidation state of the catalyst after the 1st hour of the reaction.

To confirm the stabilization of the catalysts, Figure 3.10 reports the DBT conversion as a function of time-on-stream (TOS) for the Mo₂C and the Ni_{0.19}Mo₂C/AC-600 catalysts measured at 310 °C and 4.1 MPa H₂ pressure and a LHSV of 8 h⁻¹ in the downflow fixed-bed reactor. A rapid decrease in DBT conversion occurs within the first 60 mins of operation beyond which both the DBT conversion and product selectivities stabilize. Continued operation beyond 5000 min showed that the activity of the Ni_{0.19}Mo₂C/AC-600 catalyst remained stable; whereas the DBT conversion over the Mo₂C/AC showed a small decline. Hence, to minimize these catalyst stabilization effects on the kinetic analysis of the batch reactor data, only data collected after 1 h operation are included in the analysis. Hence, the kinetic analysis is performed on the partly sulfided, but stabilized Mo₂C-based catalysts.

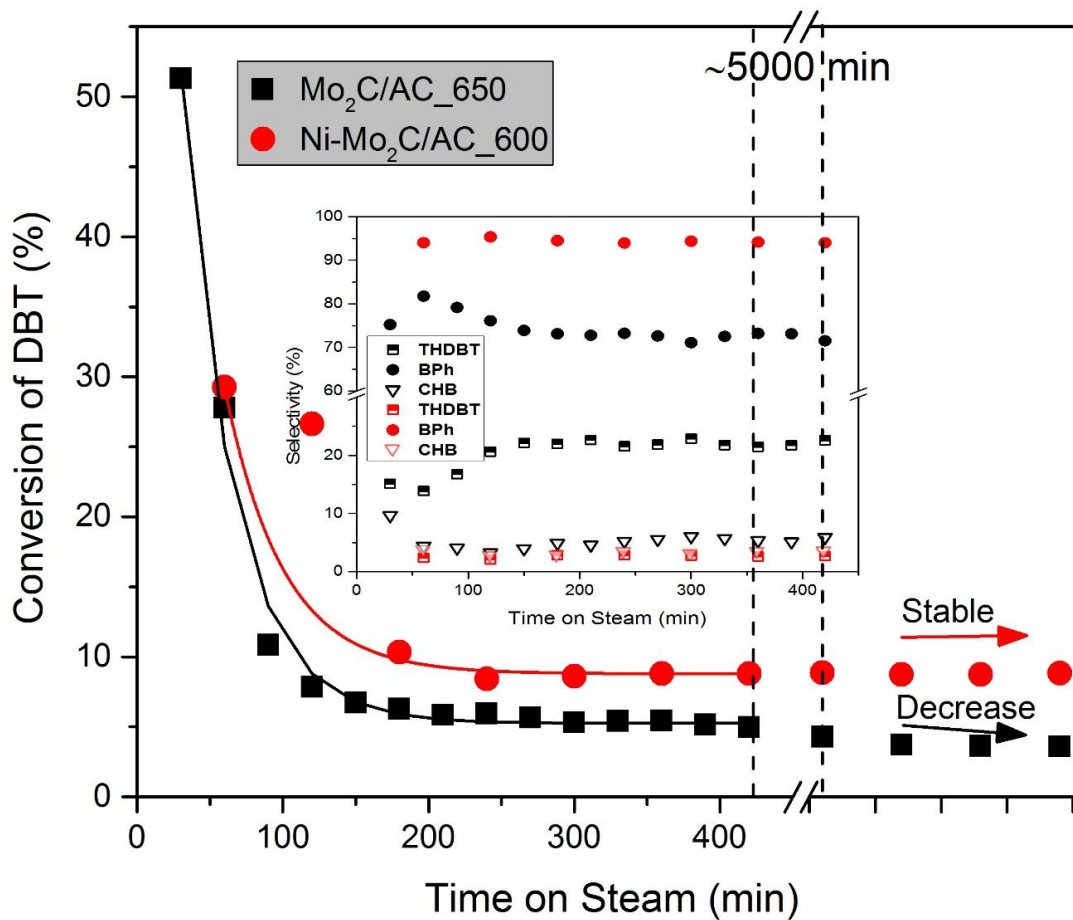


Figure 3.10: DBT conversion and product selectivity versus time on stream for Ni_{0.19}Mo₂C/AC-600 and Mo₂C/AC-650 catalyst, measured in the down flow fixed-bed reactor is at 310 °C, 4.1 MPa, H₂/feed volumetric ratio = 600 and LHSV = 8 h⁻¹.

The kinetics of the HDS of DBT on all the synthesized catalysts were determined assuming 1st-order reactions and a reaction pathway [132] illustrated in Figure 3.11.

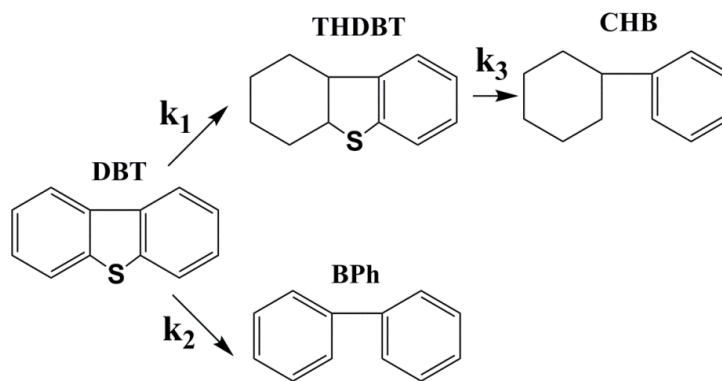


Figure 3.11: Simplified kinetic steps HDS of DBT showing 1st order reaction paths over all Ni-Mo₂C/AC catalysts with different ratios of Ni:Mo and different reduction temperatures.

Direct desulfurization of DBT (the DDS pathway) to form biphenyl (BPh) competes with a hydrogenation pathway (the HYD pathway) in which DBT is converted to 1,2,3,4-tetrahydrodibenzothiophene (THDBT) before S-removal to yield cyclohexylbenzene (CHB). The kinetic parameters of this simplified reaction scheme were estimated using a Levenberg-Marquardt nonlinear regression methodology to solve the relevant ODEs (Eq. 3-2 to 3-5) as below.

$$\frac{dC_{DBT}}{dt} = -k_1 C_{DBT} - k_2 C_{DBT} \quad (\text{Eq. 3-2})$$

$$\frac{dC_{THDBT}}{dt} = k_1 C_{DBT} - k_3 C_{THDBT} \quad (\text{Eq. 3-3})$$

$$\frac{dC_{BPh}}{dt} = k_2 C_{DBT} \quad (\text{Eq. 3-4})$$

$$\frac{dC_{CHB}}{dt} = k_3 C_{THDBT} \quad (\text{Eq. 3-5})$$

The 1st-order estimated kinetic rate constants k_j , $j=1-3$, are reported in Table 3.8 and the model fit to the data is shown in Appendix E.2, Figure E.7 and Figure E.8, for the CHR reduction temperatures of 550 °C and 600 °C, respectively, based only on the data obtained after a reaction time > 1 h. The magnitude of the rate constant for the total consumption of DBT ($k_{total}=k_1+k_2$) (Table 3.8) indicates that the Ni_{0.38}Mo₂C/AC-550 and Ni_{0.19}Mo₂C/AC-600 have the highest activity among all the catalysts. Figure 3.12 shows that the rate constants k_1 and k_2 increase with increased Ni addition up to a maximum value and then decrease at high Ni contents. The thermal reactions are neglected since the thermal related conversions are very low (less than 5%).

Table 3.8: Kinetic model parameters estimated for the HDS of DBT after the 1st hour of the reaction in the batch reactor over Ni-Mo₂C/AC catalysts at 350 °C and initial P_{H2}=2.1 MPa.

Ni _x Mo ₂ C/AC-	Kinetic Parameter					Ni _x Mo ₂ C/AC-	Kinetic Parameter				
	(mL /g _{metal} .min)						(mL /g _{metal} .min)				
550	k ₁	k ₂	k ₃ ^b	k _{total} (k ₁ +k ₂)	S _{DDS/HYD} (k ₂ /k ₁)	600	k ₁	k ₂	k ₃	k _{total} (k ₁ +k ₂)	S _{DDS/HYD} (k ₂ /k ₁)
0.02	0.12±0.07 ^a	0.62±0.06	2.21±1.48	0.74±0.13	5.00±2.87	0.02	0.12±0.04	0.54±0.04	1.99±1.32	0.67±0.08	4.40±1.59
0.09	0.16±0.05	0.65±0.05	1.78±1.05	0.81±0.10	4.20±1.48	0.09	0.13±0.04	0.48±0.04	1.89±1.11	0.61±0.08	3.55±1.12
0.19	0.22±0.03	0.79±0.03	4.75±1.13	1.01±0.05	3.58±0.47	0.19	0.28±0.12	0.86±0.11	7.77±7.83	1.14±0.22	3.06±1.33
0.38	0.30±0.12	0.81±0.11	4.84±3.79	1.11±0.23	2.71±1.18	0.38	0.17±0.04	0.55±0.04	4.95±2.81	0.72±0.08	3.22±0.88
0.44	0.24±0.11	0.55±0.10	4.12±3.86	0.79±0.21	2.25±1.10	0.44	0.20±0.10	0.40±0.09	6.25±6.76	0.60±0.19	2.06±1.19
0.76	0.22±0.08	0.41±0.07	3.41±2.80	0.63±0.15	1.89±0.78	0.76	0.18±0.11	0.41±0.09	4.71±6.01	0.59±0.20	2.36±1.54

^a. Estimated standard deviation.

^b. k₃ is determined by the concentration variation of THDBT. When the conversion of THDBT is too fast, the concentration becomes very low and it is difficult to estimate k₃, resulting in a large error in the estimated value of k₃, such that k₃ is not statistically different from zero.

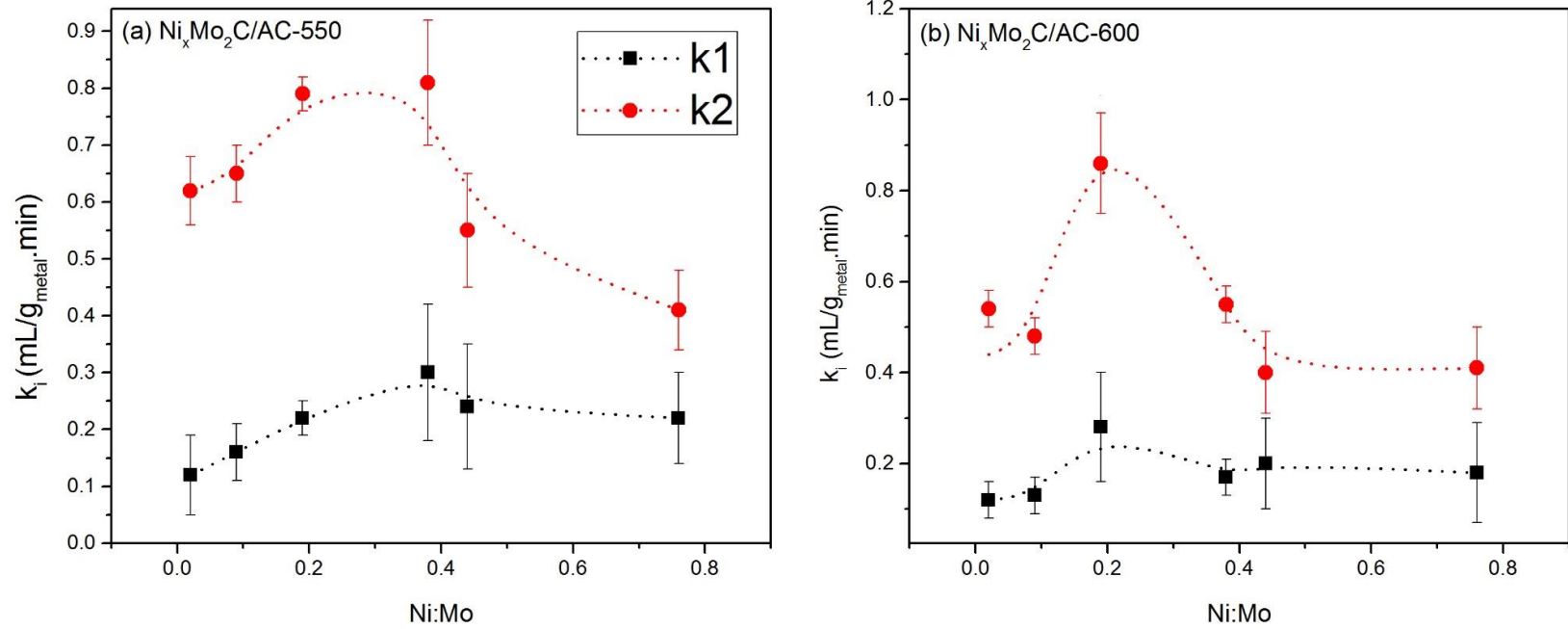


Figure 3.12: Kinetic parameters k_1 , k_2 vs. Ni:Mo ratio of Ni-Mo₂C/AC catalysts: (a) reduced at 550 °C; (b) reduced at 600 °C. (...Trend line)

The catalyst selectivity to the three main products of BPh, THDBT and CHB is illustrated in Figure 3.13. Biphenyl was the main product resulting from direct hydrogenolysis of the C-S bond of DBT, accounting for > 80% of all products of the Mo₂C/AC-650 catalyst, and even higher for the Ni promoted catalysts, as shown from Figures 3.13 (a) and (d). These data imply that the DDS reaction route is dominant and is the preferred route for S removal on these Mo₂C-based catalysts. However, the data of Table 3.8, comparing the relative rates of DDS to HYD and reflected in the value of $S_{\text{DDS}/\text{HYD}} = k_2/k_1$, suggests an increase in HYD selectivity with increased Ni/Mo ratio. The hydrogenated product CHB is mainly formed from the hydrogenation of THDBT and the data show that the presence of Ni increases CHB selectivity (Figure 3.13 (b), (c), (d) and (e)).

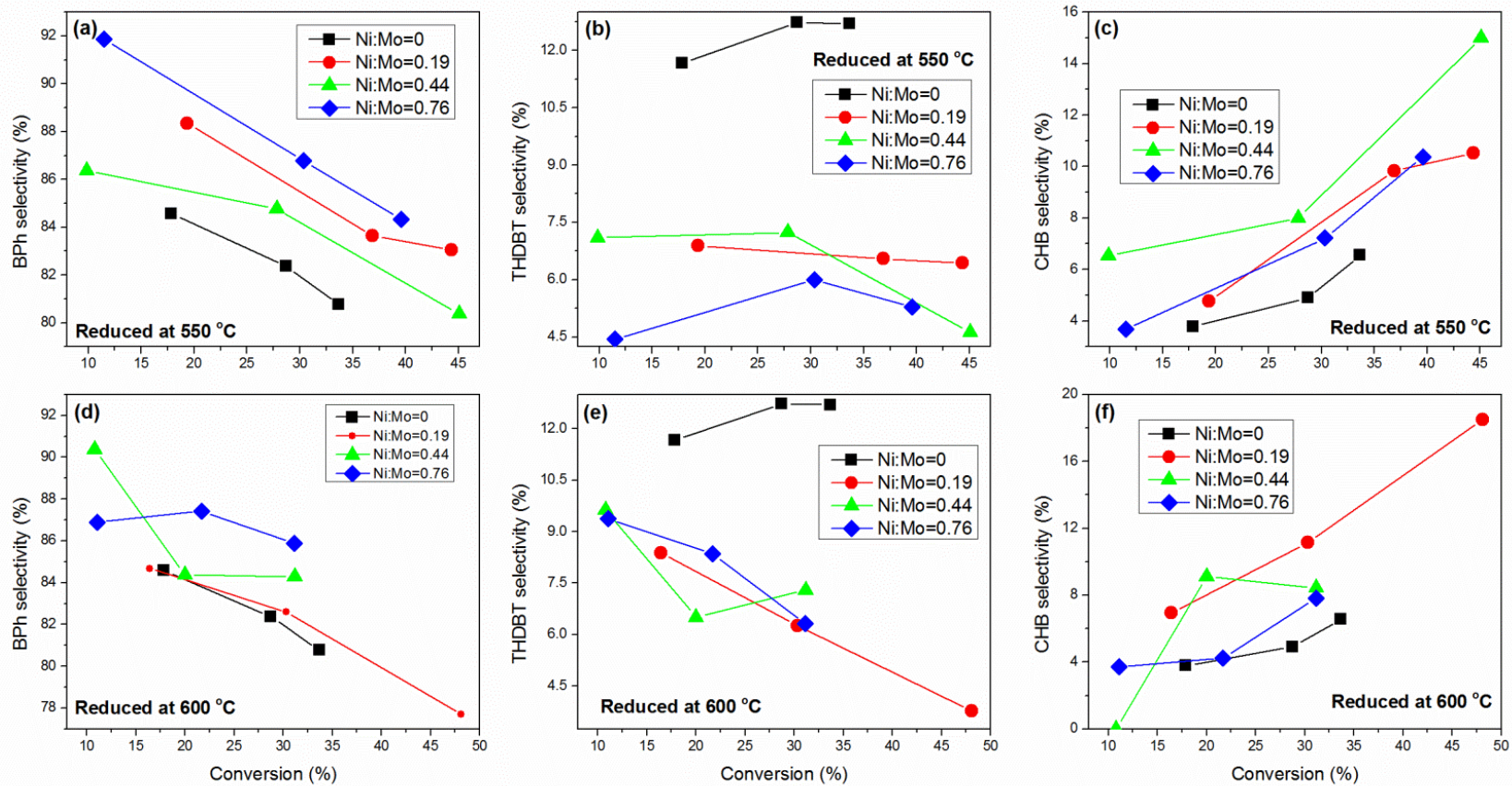


Figure 3.13: The selectivity to biphenyl (BPh), tetrahydro-dibenzothiophene (THDBT) and cyclohydrobenzene (CHB) vs. DBT conversion: (a-c) reduced at 550 °C; (d-e) reduced at 600 °C.

3.4 Discussion

The addition of Ni is shown to decrease the CHR temperature required for Mo₂C formation from the AHM/AC calcined precursor and this observation is in agreement with that reported previously by Liang et al. [26]. In Chapter 2's study [128] the optimized reduction temperature for Mo₂C formation from AHM supported on AC was reported to be 650 °C; whereas, in the present study, Mo₂C formation at significantly lower CHR temperature (550 °C) with Ni addition is demonstrated. Furthermore, the amount of Ni is shown to be critical in terms of the phases generated by CHR and in terms of the catalyst DBT activity. At a reduction temperature of 550 °C, the formation of Mo₂C was confirmed by XRD when the Ni:Mo ratio was low (0.09). Since Ni activates H₂ at relatively low temperature [133, 134], hydrogenation of the carbon to yield CH₄ can occur at low temperature. In addition, by activating H₂ at relatively low temperature, Mo oxide is more readily reduced which makes the subsequent conversion to Mo carbide or oxycarbide more facile. As shown in Figure 3.3, the CH₄ concentration generated in the product gas from CHR of the Ni_{0.19}Mo₂C/AC-600 catalyst is ~ 4x's higher than that of the 10%Mo₂C/AC-650 catalyst when the reduction temperature reaches 600 °C. In general, the concentration of CH₄ generated during CHR increases as the reduction temperature increases and as Ni loading increases. The XRD data show that as the amount of Ni increases, the intensity of the Mo₂C diffraction peaks increases. Figure 3.3 shows that the CH₄ generation rate increases rapidly above about 600 °C and Ni can lower this temperature. Hence, although temperature is the most important factor determining the CH₄ concentration measured during CHR, the Ni:Mo ratio also plays an important role in the reduction. Hence it is concluded that although the presence of Ni decreases the required reduction temperature for carbide formation, temperature remains the key factor in the CHR synthesis of metal carbides. However, higher temperature

results in a higher degree of crystallization and higher carbon loss (burn-off) from the carbon support. The burn-off was 48% for the Ni_{0.76}Mo₂C/AC-600 whereas at 550 °C, the burn-off decreased significantly to only 28%. If different Ni:Mo ratios are compared, the difference in mass loss between Ni:Mo ratios of 0.02 and 0.19 is much larger than the mass loss between 0.19 and 0.76, suggesting that the effectiveness of Ni in increasing the CH₄ concentration is reduced at high Ni concentrations. When the Ni:Mo ratio reaches 0.38 at both 550 and 600 °C, Ni₆Mo₆C₂ species appear in the XRD, indicating that Ni has been incorporated into the Mo₂C structure during the CHR process. When the Ni:Mo ratio is > 0.38, metallic Ni appears. Unlike Mo₂C, the formation of Ni₆Mo₆C₂ and Ni are mostly dependent on Ni content rather than CHR temperature. Thus, the formation of the bimetallic carbide and Ni phase separation appears at the same Ni:Mo ratio despite differences in CHR temperature. Table 3.3 and Figure E.9 show that when the catalyst precursors were reduced at 550 °C, the surface areas were approximately constant at ~ 800 m²/g for different Ni:Mo ratios; whereas, at a CHR temperature of 600 °C, there was a clear decrease in surface area with increased Ni content. The differences are due to the fact that the pore widening process that occurs during CHR, removes some pore walls between micropores causing a loss in surface area at 600 °C; whereas, at 550 °C widening occurs, but since the pores are still developing, the pore walls and the resulting surface area remain intact. In addition, the catalyst pore size increased in the presence of Ni at both CHR temperatures, with most of the micropores of the AC support enlarged into mesopores, which is beneficial for molecular diffusion of large molecules such as DBT.

XRD analysis of the fresh and used catalysts showed that the bulk phase properties of the catalysts were unchanged after reaction with DBT. However, CHNS and XPS analysis both

showed that S was present on the surface of the used catalysts. Note that the measured d-spacing from the TEM is ~ 0.63 nm (Figure 3.9), indicating the formation of MoS_2 species on the used Ni- $\text{Mo}_2\text{C}/\text{AC}$ catalysts [135]. A similar observation was reported by Zhang et al. [136] on a used $\text{Ni}_2\text{Mo}_3\text{N}$ catalyst after hydrogenation in the presence of 100 ppm of thiophene. As shown in Table 3.4 and Figure E.9, the amount of S increased with increased Ni content of the catalyst, suggesting that the Ni enhanced S adsorption on the metal sites. In addition, the TEM results confirmed this conclusion showing an increase in the number of MoS_2 layers with increased Ni content of the catalyst (Figure 3.9). Also note that the catalysts reduced at 550°C had higher S content after use than those reduced at 600°C . These results are consistent with the data obtained by CHNS analysis in which S content of the used catalysts is well correlated with the Ni:Mo ratio. The difference in S content of the catalyst as measured by CHNS (bulk analysis) versus XPS (surface analysis; reported in the last two columns of Table 3.4) can be accounted for by the S adsorbed inside the pores of the carbon support, the carbon “sink effect” proposed by Laine et al. [137]. There is a ~ 1.0 wt% difference between the bulk and surface S content of the Ni- Mo_2C catalysts reduced at 550°C ; whereas, the difference is ~ 0.5 wt% for the Ni- Mo_2C catalysts reduced at 600°C . This difference is caused by the pore structure modification during CHR at different reduction temperatures. Since many micropores are destroyed at higher reduction temperature (600°C), the S adsorption capacity is decreased compared to the catalyst prepared at the lower CHR temperature.

XRD showed that Ni incorporates with Mo species during the CHR process. The calculated lattice parameters of $\beta\text{-Mo}_2\text{C}$ decrease with increased Ni content before phase separation at high Ni content, which implies that smaller Ni atoms randomly substitute for Mo atoms in the metal

carbide crystal structure. A similar conclusion was made by Wan and Leonard [130] in regards to Fe modified Mo_2C . XPS shows that the addition of Ni increased the S adsorption on to the catalyst surface after reaction with DBT. TEM analysis of the used Ni- $\text{Mo}_2\text{C}/\text{AC}-600$ catalysts (Figure 3.8) clearly showed that the Mo_2C particle size increased with Ni content. The catalyst metal carbide particle size is well correlated with Ni:Mo ratio as shown in Figure 3.14.

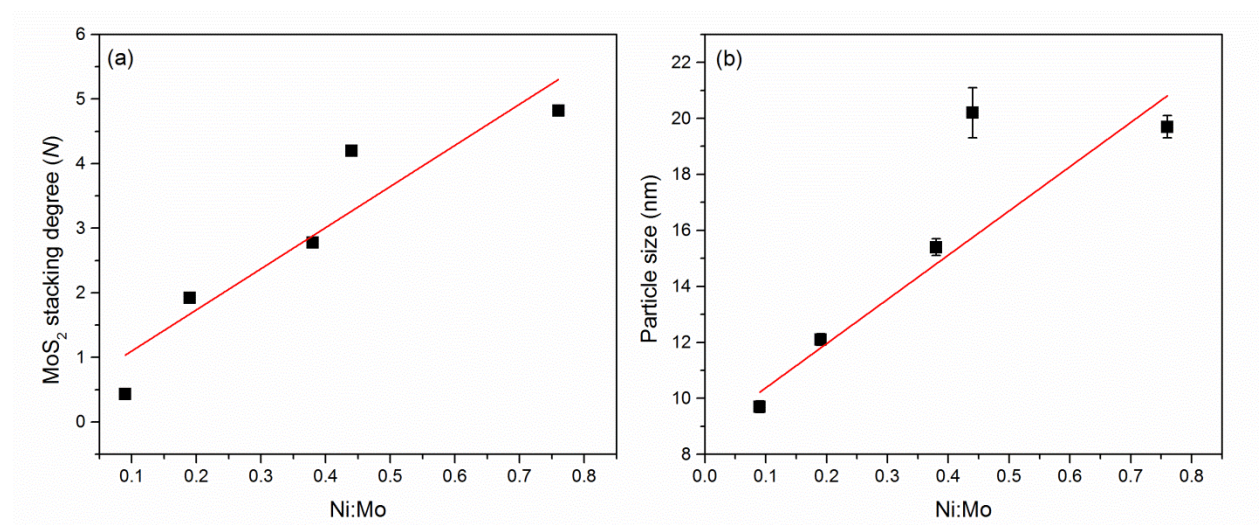
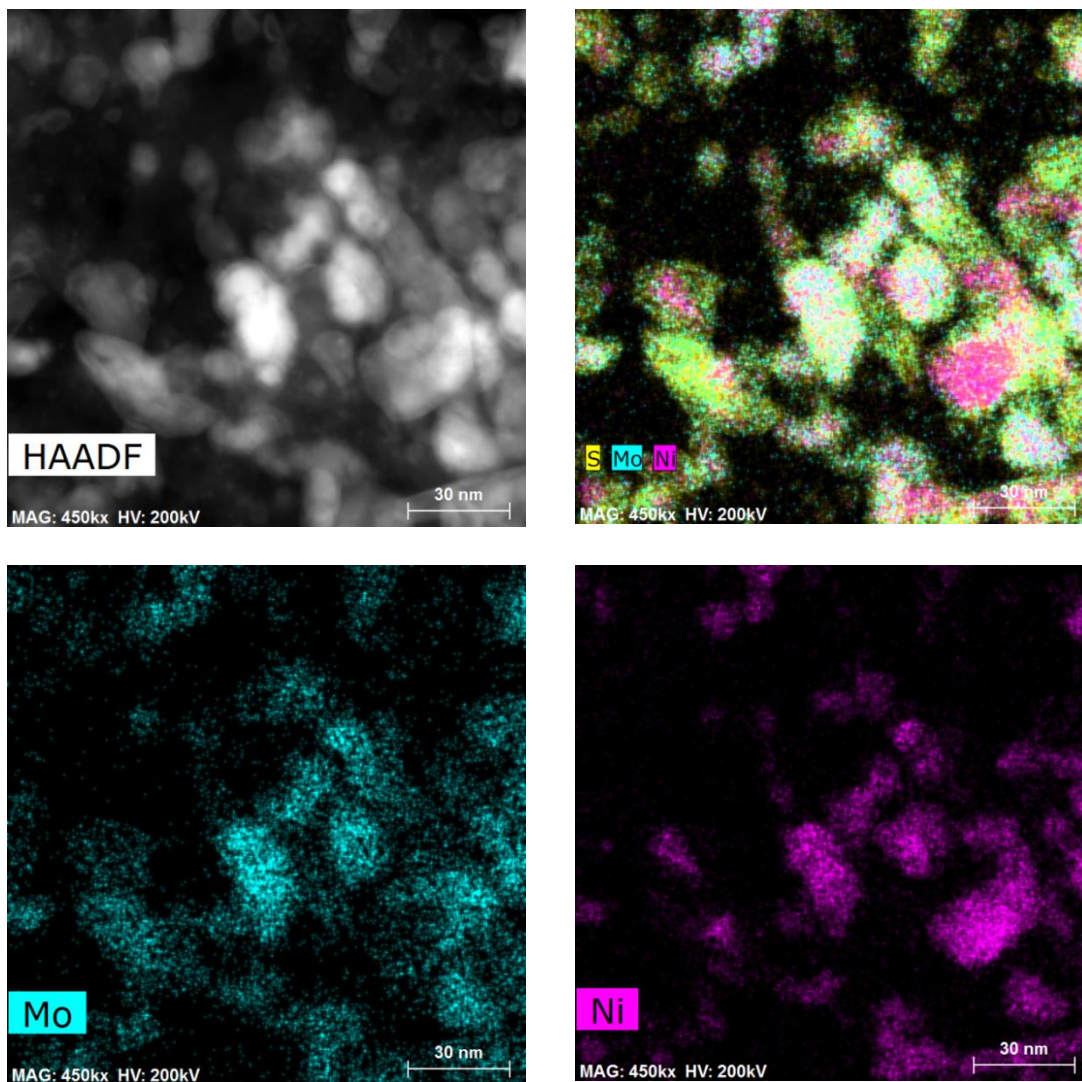


Figure 3.14: The correlation of Ni:Mo ratio to MoS_2 stacking degree (N) (a) and the average particle size (b). — is the fitted line.

Comparing the 10% $\text{Mo}_2\text{C}/\text{AC}-650$ and $\text{Ni}_{0.09}\text{Mo}_2\text{C}/\text{AC}-600$ catalysts with the same burn off shows an increase in particle size from 5 nm for the 10% $\text{Mo}_2\text{C}/\text{AC}-650$ catalyst to 10 nm for the $\text{Ni}_{0.09}\text{Mo}_2\text{C}/\text{AC}-600$ catalyst. Similar results were reported by Yao et al. [138] in their study of a NiMoC catalyst and Leonard and Wan [130] noted that unlike Fe, which decreases the size of Mo_2C particles, Ni will increase the size of Mo_2C . Figure 3.9 also shows that addition of Ni increases the number of MoS_2 layers in the MoS_2 shell that surrounds the Mo_2C of the used

catalyst. Ni increases the stack number of MoS₂ as has also been reported on NiMoS/Al₂O₃ catalysts by Lercher et al. [134]. The STEM mode selected area analysis of the used catalyst shown in Figure 3.15, confirms that the Ni, Mo and S are closely bound in the used catalyst, suggesting that Ni can enhance the S interaction with Mo.



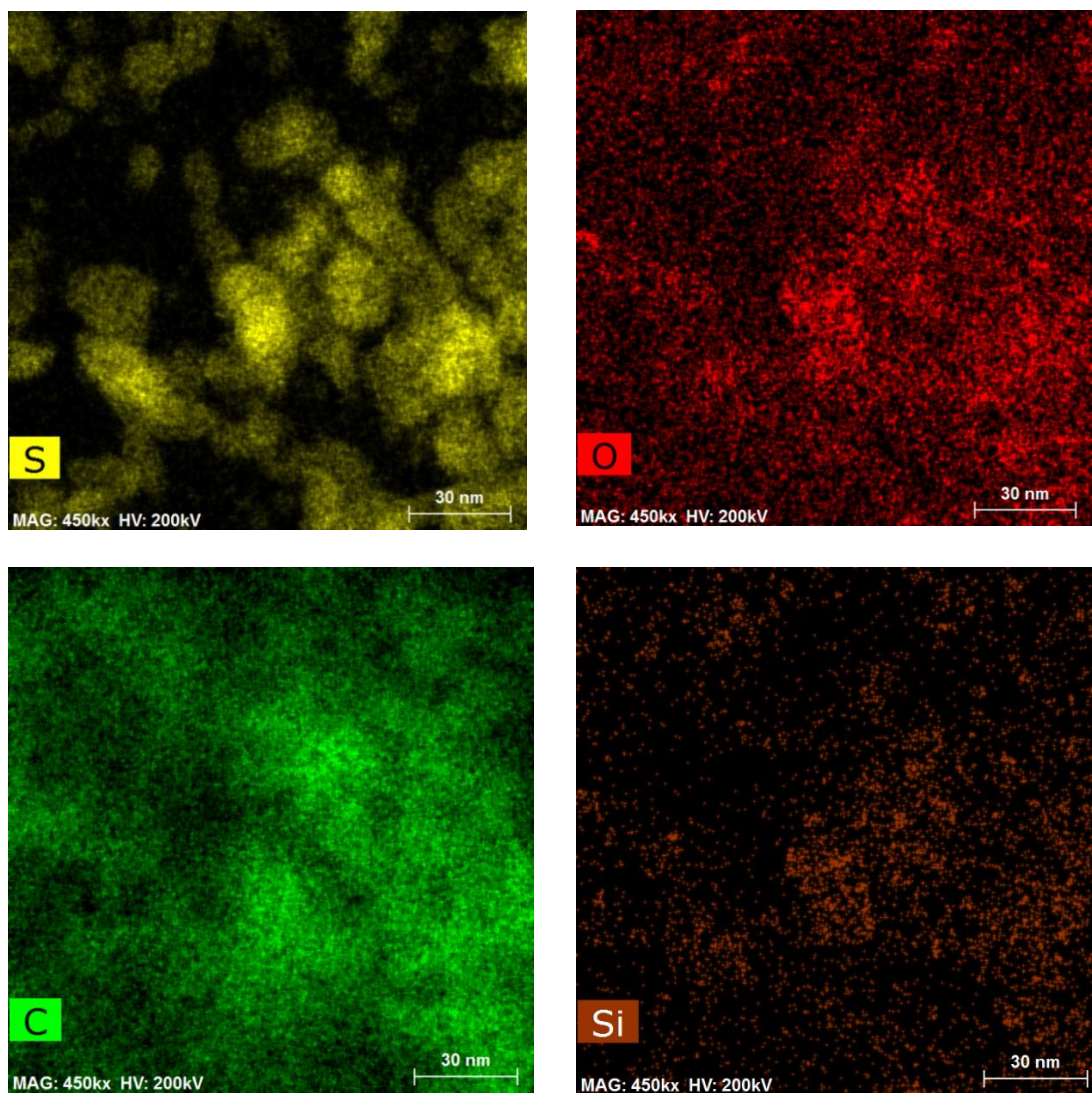


Figure 3.15: High angle annular dark field scanning (HAADF-STEM) image and energy-dispersive X-ray (EDX) elemental mapping of used $\text{Ni}_{0.19}\text{Mo}_2\text{C}/\text{AC}-600$ catalyst for elements Mo, Ni, S, O, C, and Si.

The study reported in this chapter has shown that Ni addition has a significant impact on both the CHR process and the S adsorption by the catalyst during the HDS reaction, and that both depend on the Ni content of the catalyst. During reaction, Ni enhances the adsorption of S by the Mo to form Ni-Mo-S on the outside of the Mo_2C particle, leading to the generation of a core-shell like

structure. None of the characterization data, including the TOF-SIMS analysis, identified the presence of Mo carbo-sulfide structures, as proposed by Oyama et al. [125], and although they were not present as bulk species, we cannot exclude the possibility that they exist on the catalyst surface under reaction conditions.

The data of Table 3.8 and Figure E.7 show that Ni added to the Mo₂C catalyst increases DBT conversion. A trend notable from Table 3.8 and Figure 3.12 is that k_2 , representing catalytic ability to perform DDS, increases to a maximum value with increased Ni content. When the Ni concentration is relatively low, the added Ni is incorporated with Mo species into the final metal carbide phase. Thus, in the HDS of DBT, increased Ni increases the MoS₂ stacking number and according to the ‘rim-edge’ model of Chianelli and Daage [139], a higher stacking number yields higher DDS selectivity. However, when the Ni concentration is above a critical value (Ni:Mo > 0.38), the added Ni is not incorporated into the Ni-Mo carbide phase; on the contrary, more Ni causes phase separation and enlarges the particle size leading to less active sites and eventually lower activity. Also, available surface area is decreased by increased burn-off with increased Ni content, resulting in decreased dispersion of active sites and reduced activity. Moreover, more reduced single phase Ni contributes to the hydrogenation ability of the catalyst and thus, a decrease in $S_{DDS/HYD}$ is observed. Note that the trend of $S_{DDS/HYD}$ versus Ni content at 600 °C is not very clear, due to the loss of surface area along with Ni addition affecting the catalytic performance. For the above reasons, it is found that the best performing catalysts are Ni_{0.38}Mo₂C-550 and Ni_{0.19}Mo₂C-600. They have a total kinetic constant for DBT conversion of 1.11 and 1.14 mL/g_{metal}.min along with a very high $S_{DDS/HYD}$ ratio of 2.7 and 3.1, respectively.

3.5 Conclusions

Ni addition significantly reduces the temperature required for Mo₂C generation by CHR, with the presence of Mo₂C confirmed by XRD at a CHR temperature of 550 °C for a catalyst with a Ni:Mo ratio of 0.09. This CHR temperature is about 100 °C lower than that required to form Mo₂C in the absence of Ni. XRD and XPS show that Ni is incorporated into the Mo₂C structure during the CHR process and TEM showed that increased Ni content increased the Mo₂C particle size. However, for Ni:Mo > 0.38 phase separation occurred, decreasing the catalyst activity and the direct desulfurization selectivity. The Ni also increased the rate of S adsorption during reaction, leading to the formation of Mo₂C-MoS₂ core-shell structures. Increasing Ni content also increased the stack height of the MoS₂ shells, leading to a higher DDS selectivity in the HDS of DBT. The best performing catalysts in the HDS of DBT at 350 °C are Ni_{0.38}Mo₂C/AC-550, with a total kinetic constant of 1.11 mL/g_{metal}.min and $S_{DDS/HYD}$ of 2.7, and Ni_{0.19}Mo₂C/AC-600 with a total kinetic constant of 1.14 mL /g_{metal}.min and $S_{DDS/HYD}$ around 3.1.

Chapter 4: Synthesis of Mesoporous Mo₂C/Carbon Catalysts by Carbothermal Hydrogen Reduction using Petroleum Coke ³

4.1 Introduction

After the successful preparation of Mo₂C from activated charcoal (AC) as reported in Chapters 2 and 3, the study was extended to activated petcoke (APC) as reported in this chapter. A thermochemical activation method was developed, starting with petcoke and using KOH at a temperature of 800 °C to generate pores (> 75% micropores) and a APC surface area of 2028 cm²/g. After the synthesis of the APC, a metal catalyzed carbon hydrogenation was used to further increase the pore size of the APC [77-79, 140-142]. The metal catalyzed method used in the present study is carbothermal hydrogen reduction (CHR), where APC was impregnated with Mo salts, to synthesize Mo₂C catalysts supported on APC at relatively low temperature (< 800 °C) [20, 128]. During CHR the carbon of the support and H₂ are used to convert the Mo-precursor (usually MoO_x) to Mo₂C and although several studies of CHR have been reported [21, 143], the sequence of reaction steps that lead to Mo₂C remains unclear. Direct reaction between MoO_x and carbon occurs at temperatures higher than 900 °C and is therefore only a minor contributor to Mo₂C formation during CHR [19, 21]. CH₄ from the gas phase, generated by hydrogenation of the carbon support (H₂ + C → CH₄), may react with the Mo-precursor to produce Mo₂C, although the reaction requires a significant CH₄ gas phase activity to occur to any significant extent [21, 144]. Furthermore, since dissolution of carbon in metal oxides is orders of

³ A version of this chapter has been published:

H. Wang, S. Liu, B. Liu, V. Montes, J. M. Hill, and K. J. Smith, "Carbon and Mo transformation during the synthesis of mesoporous Mo₂C/carbon catalysts by carbothermal hydrogen reduction," *Journal of Solid State Chemistry* (2017) 258: 818-824.

magnitude less than in metals, diffusion of carbon through the metal oxide and subsequent hydrogenation at the gas/metal oxide interface is unlikely [145].

Consequently, in the present chapter, the conversion processes that occur during CHR were examined to clarify the sequence of reaction steps that lead to Mo₂C. The study reports for the first time that simultaneous hydrogenation of the carbon support during CHR, catalysed by the Mo₂C, yields mesopores (2~50 nm) within the carbon support. Both the effect of the CHR final temperature and the holding time at this temperature, have been examined. The transition of the AHM precursor to Mo₂C and the corresponding changes to the APC morphology that occur during CHR, determined from both characterization data and computational methods, are reported. The Mo species are shown to catalyse the hydrogenation of the carbon support, similar to metals, modifying the pore structure such that Mo₂C supported on activated charcoal, with a high mesopore volume, is obtained. Finally, the catalytic activity of the Mo₂C/APC catalysts is assessed using 4-methylphenol (4-MP) as a model reactant for the hydrodeoxygenation (HDO) reaction to compare with Mo₂C/AC catalysts reported in Chapter 2. The difference between activated petroleum coke (APC) and activated charcoal (AC) supported Mo₂C catalyst was explored.

4.2 Experimental and Computational Methods

4.2.1 Catalyst Preparation

Petcoke, generated by delayed coking, was used as the carbon source (See Appendix A.1 for details of petcoke properties). Thermo-chemical activation of the petcoke was done at 800 °C for 2 h under N₂ flow with a KOH:petcoke mass ratio of 3:1. The petcoke was then wet impregnated

with an AHM solution (9:1 mass ratio of water to acetone with sufficient AHM to yield the 10 wt% Mo/APC precursor; AHM was purchased from Sigma-Aldrich, ACS reagent, 81.0-83.0% MoO₃ basis) and dried at 120 °C to yield the AHM/APC precursor (See Appendix A.2 and A.3 for details of catalyst preparation; Appendix F.2 for repeatability tests of petcoke activation). CHR of the AHM/APC precursor was done in a quartz U-tube reactor with 0.9 g of sample and a 100 mL (STP)/min H₂ flow as the temperature increased at a ramp rate of 1 °C/min from 25 to 500, 550, 600, 650, 700, 750 and 800 °C, respectively (Appendix E.2, Figure A.4 for the illustration of U-tube reactor). The samples are designated as MoTTT_APC where TTT is the final temperature of the CHR. In three cases, the sample was held at the final CHR temperature (600, 650, and 700 °C) for a further 90 min in the H₂ flow and these samples are designated as MoTTT_APC-90.

4.2.2 Catalyst Characterization

Physical and chemical properties of the AHM/APC precursor and the CHR produced Mo₂C/APC catalysts were determined by N₂ adsorption/desorption isotherms (measured using a Micromeritics ASAP 2020 analyzer), X-ray photoelectron spectroscopy (Leybold Max200 XPS), and transmission electron microscopy (Tecnai Osiris TEM). Note that the catalyst samples used for XPS and TEM analysis were transferred from the U-tube reactor into sealed glass vials within a N₂ protected glove bag. The samples were subsequently transferred from the glass vial to the XPS or TEM unit as quickly as possible, limiting exposure to the atmosphere to less than 2 min. The evolved gas from the U-tube reactor during CHR was simultaneously analyzed by an online gas chromatograph using a flame-ionization detector (Shimadzu GC-14B) (See Appendix B.1, B.3 and B.5 for details).

The pore size distribution was determined from the Non-Local Density Functional Theory (NLDFT) analysis of the N₂ isotherm data [146] and the Mo₂C particle size distribution was determined by counting > 100 particles from the TEM micrographs and applying a lognormal distribution to the particle count data. A relatively high loading of 10 wt% Mo was chosen so as to obtain XPS data with high signal intensities and clear information on the transition process of Mo species during the CHR process.

4.2.3 Catalyst Activity Tests

The catalyst activity tests follow those described in Chapter 2 [128]. The reaction was conducted at 350 °C and 4.3 MPa with a stirring speed of 1000 rpm in a batch reactor. The same concentration of 4-methylphenol (3.1 wt%) was used here to make it comparable with Mo₂C/AC catalysts. The obtained Mo₂C/APC catalyst was added to the reactor with minimal air exposure using a glove bag under Ar flow and the catalyst mass was adjusted to ensure a constant Mo/4-MP mass ratio of 0.021 g_{Mo}/g_{4-MP} (calculation details see Appendix C.5, Table C.6). First-order kinetic analysis of the 4-MP conversion versus time data was used to extract the apparent 1st-order rate constant of the HDO reactions and these rate constants were used to compare catalyst activities (See Appendix C.6 and Appendix D.1 for details).

4.2.4 Computational Method

Density functional theory (DFT) calculations were performed to provide insight into the activation of H₂ during the CHR process as the AHM was converted to Mo₂C. The calculations

were completed using the Vienna *ab initio* simulation package (VASP) [147]. The projector-augmented wave method was used to represent core-valence interactions [148, 149]. Valence electrons were described by a plane wave basis with an energy cutoff of 400 eV. The generalized gradient approximation with the Perdew-Burke-Ernzerhof functional was used to model electronic exchange and correlation [150]. The Brillouin zone was sampled at the Gamma point. Optimized structures were obtained by minimizing the forces on each ion until they were less than 0.05 eV/Å. Gaussian smearing with a width of 0.05 eV was used to improve convergence of states near the Fermi level.

The adsorption energy was defined as [151]:

$$E_{\text{ads}} = E_{(\text{adsorbate}+\text{surface})} - E_{(\text{adsorbate})} - E_{(\text{surface})}$$

where $E_{(\text{adsorbate}+\text{surface})}$ is the total energy of the adsorbate interacting with the surface; $E_{(\text{adsorbate})}$ and $E_{(\text{surface})}$ are the energies of the free adsorbate in gas phase and the bare surface, respectively. A negative value corresponds to exothermic adsorption, with a more negative value corresponding to stronger adsorption.

4.3 Results and Discussion

4.3.1 Characterization Results

The previous study [128] of Mo₂C synthesis on AC supports by CHR as described in Chapter 2, reported that during the temperature ramp, H₂ reacts with the C support generating CH₄, while at the same time converting the Mo precursor to Mo₂C. Figure 4.1 shows the CH₄ concentration measured at the reactor exit during CHR of the AHM/APC precursor, to a maximum temperature of 800 °C. From 25 °C to 350 °C there was no measurable quantity of CH₄ produced; whereas, from 350 to 550 °C, the CH₄ concentration slowly increased. From 550 to 700 °C the CH₄

concentration increased exponentially before declining again above 700 °C. CHR of the APC alone (no Mo addition) showed minimal reaction between the APC and the H₂ with < 0.5 % CH₄ in the produced gas at 800 °C. Hence, the presence of Mo species is critical for the generation of most of the CH₄ at these relatively low CHR temperatures.

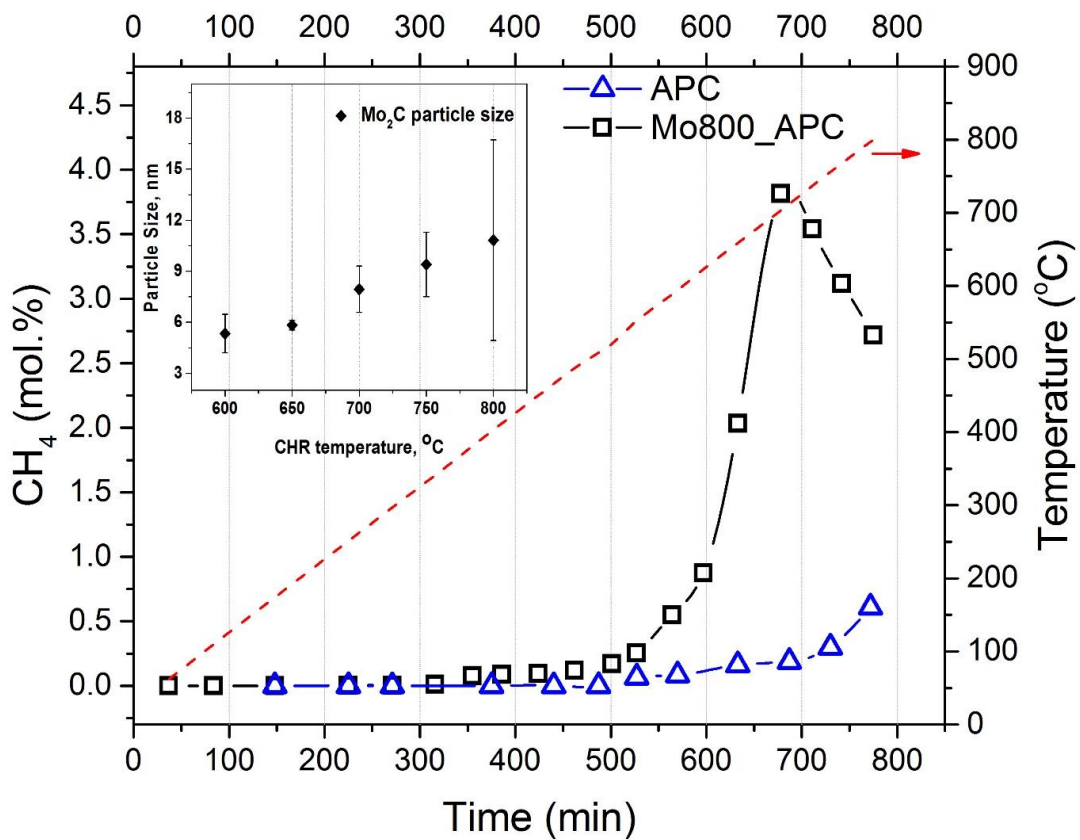


Figure 4.1: The CH₄ concentration (mol%) in the U-tube reactor exit gas measured during CHR of Mo800_APC (□) and APC support (Δ). Inset: Particle size of generated Mo₂C at different CHR temperatures

(◆).

Table 4.1 reports the distribution of Mo species, identified by XPS analysis, present after CHR to final temperatures between 400 and 800 °C. A peak deconvolution of Mo 3d is shown in Appendix E.3, Figure E.11 and E.12. The valence state of Mo decreased from Mo⁶⁺ to Mo²⁺ as the final CHR temperature increased.

Table 4.1: XPS analysis of Mo (3d) for Mo/APC samples prepared at different CHR temperatures.

Activated Samples	Composition (%)		
	Mo ²⁺	Mo ^{3+ ~ 4+}	Mo ^{5+ ~ 6+}
Mo400_APC	0.0 ^a	29.9 ^b	70.1 ^c
Mo500_APC	0.0	47.3	52.7
Mo550_APC	1.7	51.9	46.5
Mo600_APC	10.7	46.5	42.8
Mo650_APC	14.3	36.9	48.8
Mo700_APC	22.3	29.4	48.3
Mo750_APC	38.0	26.4	35.6
Mo800_APC	49.2	20.9	29.9
<i>Holding 90 min at final temperature</i>			
Mo600_APC-90	13.9	30.8	55.3
Mo650_APC-90	15.0	36.9	48.1
Mo700_APC-90	40.9	24.8	34.3

a. The deconvoluted peak position of Mo²⁺ was 228.3 eV.

b. The deconvoluted peak positions of Mo³⁺ and Mo⁴⁺ were 229.1 and 230.3 eV, respectively.

c. The deconvoluted peak positions of Mo⁵⁺ and Mo⁶⁺ were 231.9 and 233.1 eV, respectively.

Furthermore, Figures 4.2, and 4.3, and the inset of Figure 4.1 show that the Mo₂C particle size, as measured by TEM analysis, increased with increased CHR temperature, especially above 650 °C. From 650 to 700 °C, the average particle size increased significantly from 5.8 to 7.9 nm and above 700 °C the particle size increased by ~1.5 nm per 50 °C. The physical properties of the Mo₂C/APC also varied with the CHR temperature as shown in Table 4.2, Figure E.13 and Figure E.14. Between 550 and 800 °C, the mesopore volume increased to 0.34 cm³/g at 750 °C and then decreased to 0.20 cm³/g at 800 °C. The data also show that CHR of the APC alone (no Mo) at

800 °C, resulted in minimal change in both mesopore volume and the catalyst surface area (APC w/o Mo but CHR to 800 °C — Table 4.2).

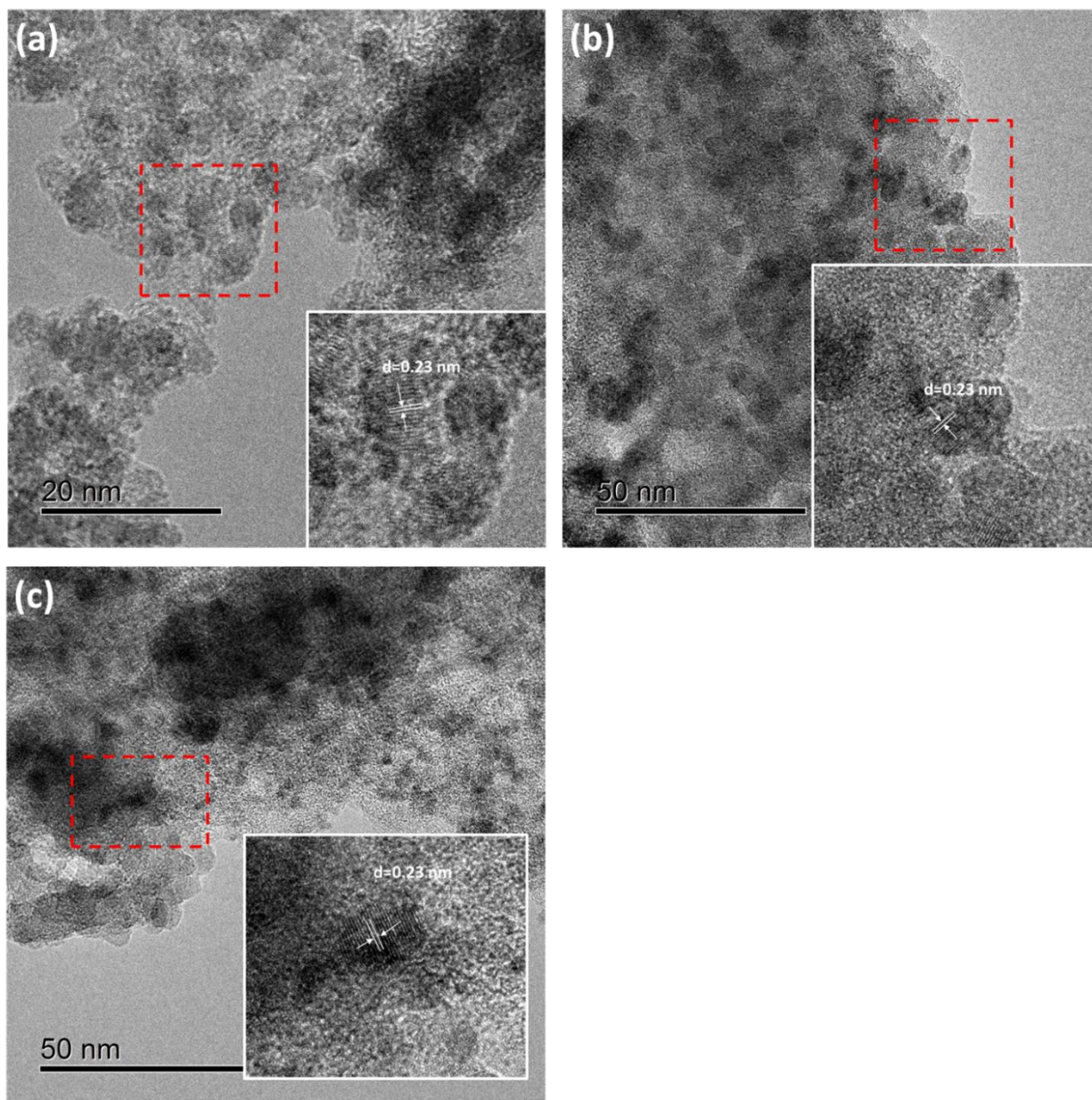


Figure 4.2: TEM graphs of different samples: (a) Mo600_APC; (b) Mo700_APC; and (c) Mo800_APC.

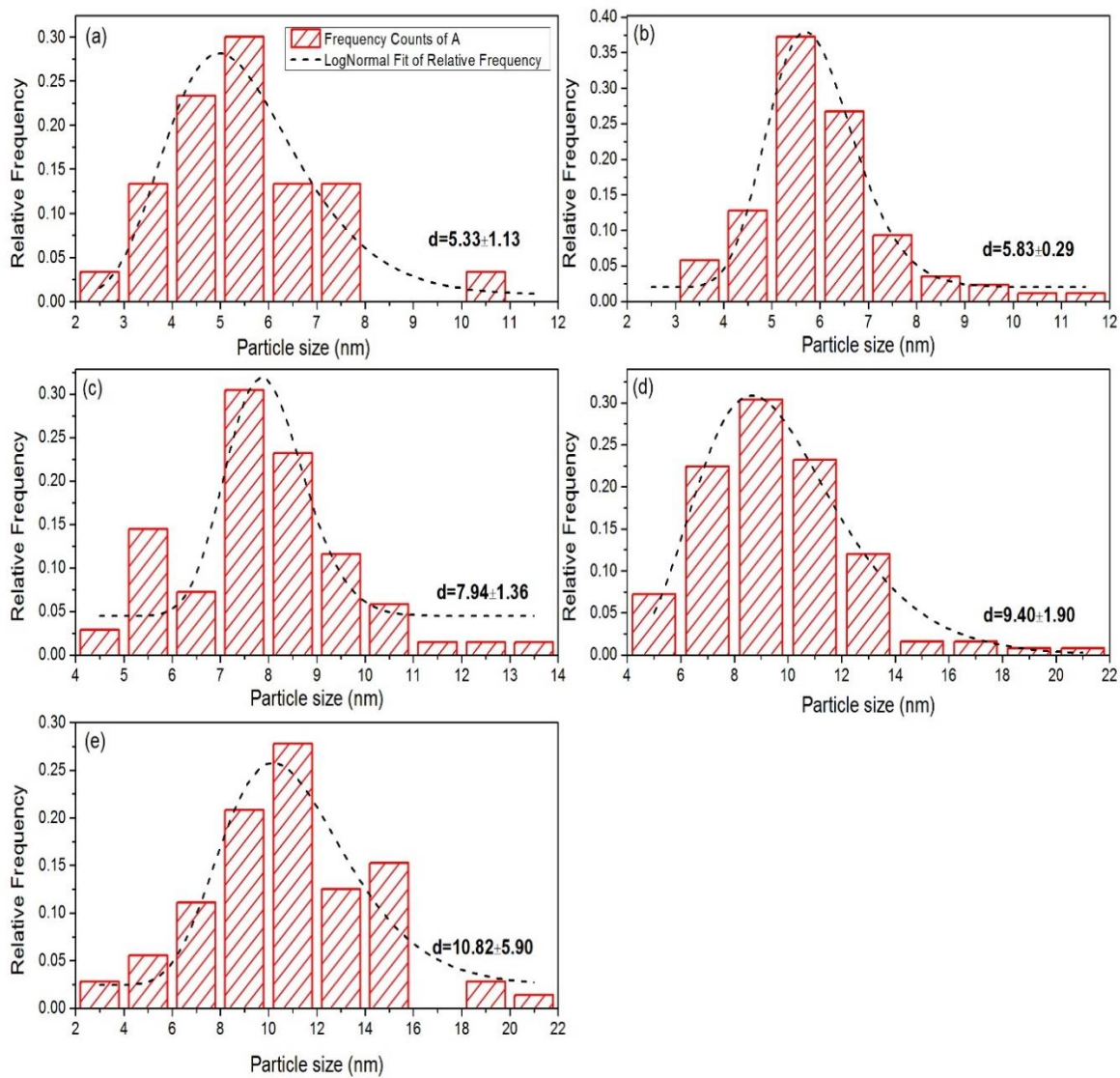


Figure 4.3: Particle size distribution from TEM micrographs and fitted lognormal distribution: (a)

Mo600_APC; (b) Mo650_APC; (c) Mo700_APC; (d) Mo750_APC; and (e) Mo800_APC.

Table 4.2: Physical properties of Mo₂C/APC catalysts produced at different CHR temperatures.

Sample	Surface area (m ² /g)	Pore Volume (cm ³ /g)	Mesopore Volume (cm ³ /g)	Micropore Volume (cm ³ /g)	Mesopore Volume (%)	Yield (%)	Mo loading (%)
<i>Starting Materials</i>							
APC	2028 ^a	0.93	0.12 ^b	0.81 ^b	12.90	66.14 ^d	—
AHM/APC	1520	0.69	0.08	0.61	11.59	—	8.23 ^e
<i>Activated Samples</i>							
APC_w/o Mo ^c	1957	0.91	0.13	0.78	14.29	95.18	8.65 ^f
Mo400_APC	1832	0.80	0.09	0.71	11.25	86.67	9.50
Mo500_APC	1794	0.78	0.09	0.69	11.54	84.52	9.74
Mo550_APC	1763	0.77	0.08	0.69	10.39	85.10	9.67
Mo600_APC	1751	0.78	0.09	0.69	11.54	83.22	9.89
Mo650_APC	1709	0.76	0.09	0.67	11.84	82.35	9.99
Mo700_APC	1613	0.82	0.19	0.63	23.17	69.82	11.79
Mo750_APC	1563	0.91	0.34	0.57	37.36	62.75	13.12
Mo800_APC	1717	0.86	0.20	0.66	23.26	54.99	14.97
Mo600_APC-90	1911	1.02	0.10	0.92	9.94	79.90	10.30
Mo650_APC-90	1759	1.02	0.17	0.84	17.11	64.58	12.74
Mo700_APC-90	1651	1.16	0.42	0.74	36.21	46.33	17.76

a. The specific surface area was calculated from the measured N₂ adsorption isotherm using 2D-NLDFT applied in the P/P₀ range of 0.01~0.30.

- b. The pore volume was reported based on NLDFT method provided by Micromeritics, where mesopore volume is between 2-50 nm and micropore is ≤ 2 nm.
- c. It represented the CHR treated APC at 800 °C without Mo loading.
- d. Yield was calculated by the final mass of the catalyst relative to the initial mass of the precursor.
- e. This value was measured by ICP-MS.
- f. The Mo loading of activated samples calculated as $(8.23\%)/[1-(1-\text{cata. yield after CHR})]$.

The effect of holding the final reaction temperature (600, 650 and 700 °C) for a further 90 min on the properties of the Mo₂C/APC catalyst are summarized in Table 4.1 and 4.2 as well. The XPS data of Table 4.1 and Figure E.12 of Appendix E.3 show that conversion of the Mo-precursor to Mo₂C increased with holding time. Comparing the corresponding samples prepared with no holding time shows that the holding time increased the Mo²⁺ content of the catalysts. In addition, the 90 min holding time increased the extent of carbon hydrogenation, resulting in a lower catalyst yield, and higher total and mesopore volumes (Table 4.2).

4.3.2 Mo Species Transformation

The transformation of Mo species and mesopore development can be grouped into four steps based on different temperature ranges referenced in Figure 4.1:

(I) CHR temperature ≤ 350 °C

Since no detectable CH₄ was produced during CHR between 25 and 350 °C, the main transformation that occurred in this temperature range was the decomposition of AHM to MoO₃. Normally the decomposition of AHM to MoO₃ occurs at temperatures in the range of 310 ~ 350 °C [152]; although, Thomazeau et al. [153] report that the carbon support can increase the AHM decomposition temperature, 350 °C was sufficient to ensure conversion of the AHM to MoO₃.

(II) CHR temperature: 350 ~ 550 °C

Between 350 and 550 °C, the conversion of MoO₃ to MoO_xC_y was initiated (Table 4.1) and the production of CH₄ was apparent as shown in Figure 4.1. A commonly acknowledged theory of the reduction of MoO₃ by hydrogen is that the reduction starts with a hydrogen molecule directly

attacking O atoms [154, 155]. After the initial reaction, O vacancy sites are generated as water is produced. Chen et al. [156] used DFT analysis to show that vacancy sites on MoO₃ enhance the dissociative adsorption of H₂ on the surface. Similar calculations have been reported for NiO by Rodriguez et al. [157], who also concluded that such vacancy sites assist the dissociative adsorption of H₂. Furthermore, in the study by Chen et al. [156], the dissociative adsorption of methyl groups was shown to benefit from vacancy sites. H species can migrate to the carbon support and react, producing CH_x (and CH₄). The CH_x species may also migrate and interact with other vacancy sites, hence replacing oxygen with carbon, yielding the MoO_xC_y.

Alternatively, the produced CH₄ may adsorb on the active sites of the MoO_x, decomposing to hydrogen; and an adsorbed, highly reactive carbon that reduces the MoO_x to yield the MoO_xC_y [144]. The O is removed as H₂O, CO or CO₂, confirmed in the present study from the mass spectrometer analysis of the exit gas from the CHR. However, the generated amounts of these species were too low to be accurately quantified. Consequently, only the main product CH₄ was reported here. Although it is well known that hydrocarbons can facilitate the carburization reaction on Mo oxides [14-18, 66], the relatively low temperature and CH₄ concentration implies a low carbon activity at these conditions, limiting the reaction [144]. The XPS data confirm the gradual conversion of MoO₃ to MoO_xC_y with only 1.7 % Mo₂C on the surface of the catalyst after CHR to 550 °C (Table 4.1). Furthermore, the properties of the Mo₂C/APC do not change significantly from 350 ~ 550 °C (Table 4.2), indicative of the low reactivity of the carbon at these temperatures.

DFT calculations were performed to elucidate the influence of O vacancies and C on the adsorption of H in the transformation of MoO₃ to MoO_xC_y. The adsorption of H on an O vacancy

(-1.21 eV) was stronger than that on a stoichiometric surface of MoO_3 (-1.10 eV), indicating that O vacancy sites promoted the adsorption of hydrogen (Appendix E.3: Figure E.15 and Table E.3). MoO_xC_y also promoted the adsorption of hydrogen with a high binding energy of -2.46 eV, indicating that the interaction between H and C can create more and more vacancy sites through oxygen removal and water formation, consistent with the XPS results shown in Table 4.1. The oxidation state of Mo gradually changed towards lower valency, indicating that more and more vacancy sites were being generated and O was being removed.

(III) CHR temperature: 550 ~ 700 °C

As the CHR temperature increased from 550 to 700 °C, the CH_4 concentration increased rapidly as the transition of MoO_xC_y to Mo_2C occurred. The CH_4 production observed during CHR is a consequence of two processes occurring simultaneously such that the net rate of CH_4 production depends on the rate at which the carbon support is hydrogenated minus the rate at which the CH_4 is consumed by the carburization of the Mo. However, the portion of CH_4 consumed by the Mo precursor was small (< 1%) compared to the total CH_4 produced, so that the measured CH_4 production rate was taken as a measure of the carbon hydrogenation rate. Since, in the absence of Mo there was minimal CH_4 produced during CHR, the rate of carbon hydrogenation is assumed to be determined by the reaction temperature, the concentration of H activated by the Mo and the carbon in contact with the Mo particle or in close proximity to the particle, such that the H is able to interact with the C at the metal/carbon interface or spillover onto the carbon prior to reaction.

The observed rate of carbon hydrogenation during CHR, calculated from the exit CH_4 concentration and exit gas flowrate is well described by the Arrhenius equation in the

temperature range 550 to 700 °C (Figure 4.4; see Appendix C.7 for calculation details). The apparent activation energy for hydrogenation of the APC was determined to be approximately 120 kJ/mol, compared to a value of 105 kJ/mol reported for a Ni impregnated carbon [92]. Note, however, that as the temperature increased from 550 to 700 °C, the concentration of Mo₂C increased and the number and type of sites available for hydrogen activation also increased because of the transition of MoO_xC_y to Mo₂C and the fact that Mo₂C has strong hydrogen activation ability [158]. The fact that the carbon hydrogenation rate follows an Arrhenius dependency, despite these changes in the catalyst, implies that carbon hydrogenation is the slow step of the reaction, whereas hydrogen activation and spillover to the carbon surface are much faster.

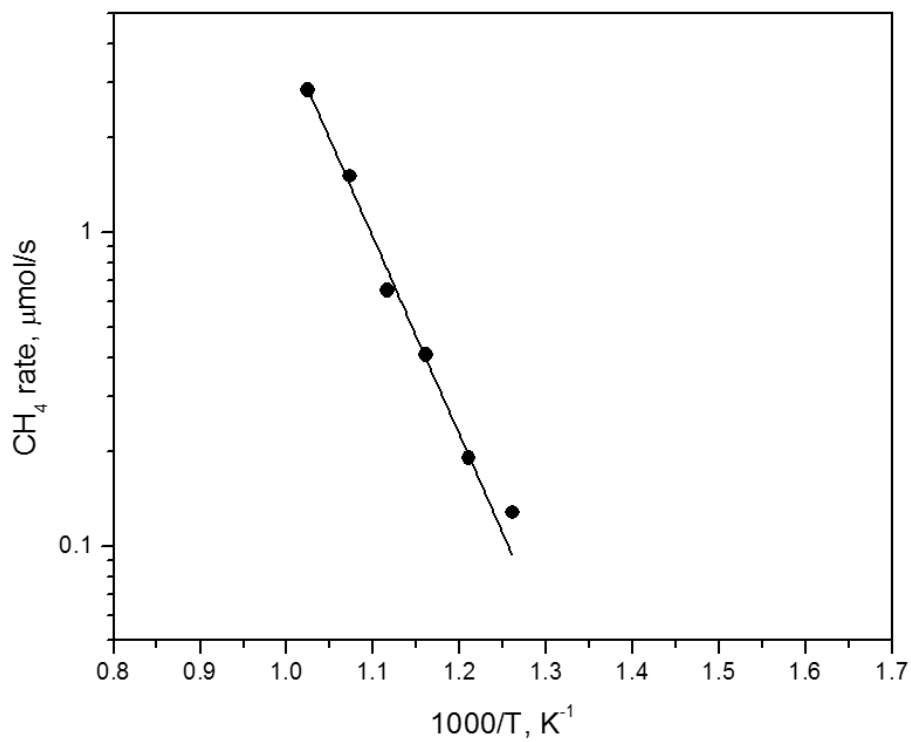


Figure 4.4: Arrhenius plot of temperature dependence in the range of 550~700 °C.

The maximum carbon hydrogenation rate on the Mo₂C/APC catalyst was estimated at 650 °C to be approximately 10¹³ molecules/(cm².s), based on a Mo₂C particle diameter of 5.8 nm.

Comparable values have been reported for Ni hydrogenation of graphite at 800 °C (of the order 10¹⁴ molecules/(cm².s)) [91].

(IV) CHR temperature: > 700 °C

The CH₄ generation rate decreased when the CHR temperature was above 700 °C, even though more Mo₂C was generated at higher temperatures as shown in Table 4.1. The decline in activity can be explained by two phenomena. Firstly, in the catalytic hydrogenation of the APC, highly reactive amorphous carbon will react first so that above 700 °C, the MoO_xC_y and Mo₂C particles are now more likely in contact with less reactive, highly crystalline graphite [92]. Secondly, Figure 4.3 shows that the MoO_xC_y and Mo₂C particles grow significantly larger above 700 °C and hence, the total interfacial area between these particles and the carbon support will decrease, resulting in a reduced rate of carbon hydrogenation. The transition process that occurred with increased temperature can be illustrated as in Figure 4.5.

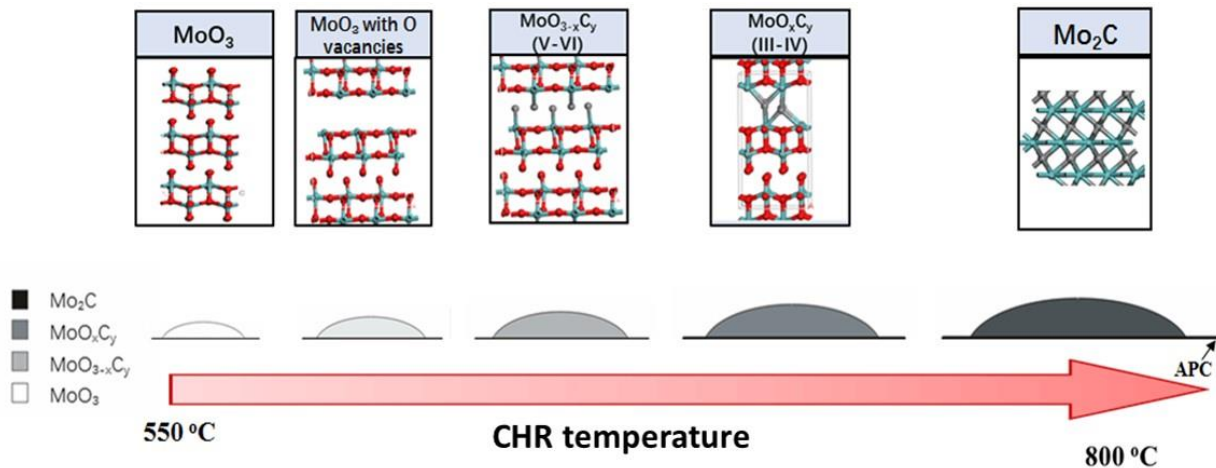


Figure 4.5: Schematic representation of Mo species transformation during CHR process. (Sizes of Mo species particles are not drawn to scale.)

4.3.3 Pore Development during Carbothermal Hydrogen Reduction (CHR)

The data of Table 4.2 show that the Mo_2C and MoO_xC_y had no significant impact on the physical properties of the materials synthesized by CHR at temperatures below $650\text{ }^\circ\text{C}$. The total pore volume remained approximately constant at $0.80\text{ cm}^3/\text{g}$ and the mesopore volume was $0.09\text{ cm}^3/\text{g}$. Above $650\text{ }^\circ\text{C}$, both the total pore volume and the mesopore volume increased significantly, consistent with the rapid increase in carbon hydrogenation as reflected in the rapid increase in the CH_4 concentration in the gas exiting the reactor. The pore development is further illustrated in the pore size distribution plots (Figure 4.6); the number of pores of size between 1.5 and 20 nm increased. With 10 wt% Mo loading at $750\text{ }^\circ\text{C}$, the mesopore volume reached a maximum of $0.34\text{ cm}^3/\text{g}$. Above $750\text{ }^\circ\text{C}$, pore volume decreased, mostly likely a consequence of excessive C removal from the APC that resulted in pore wall collapse. In the absence of the Mo_2C , the data of Table 4.2 show that almost no pore development occurred despite CHR at 800

°C. Hence, the hydrogenation of the carbon support, catalyzed by Mo₂C, showed more pore development potential given suitable reaction conditions, which in this case required temperatures from 650 to 750 °C.

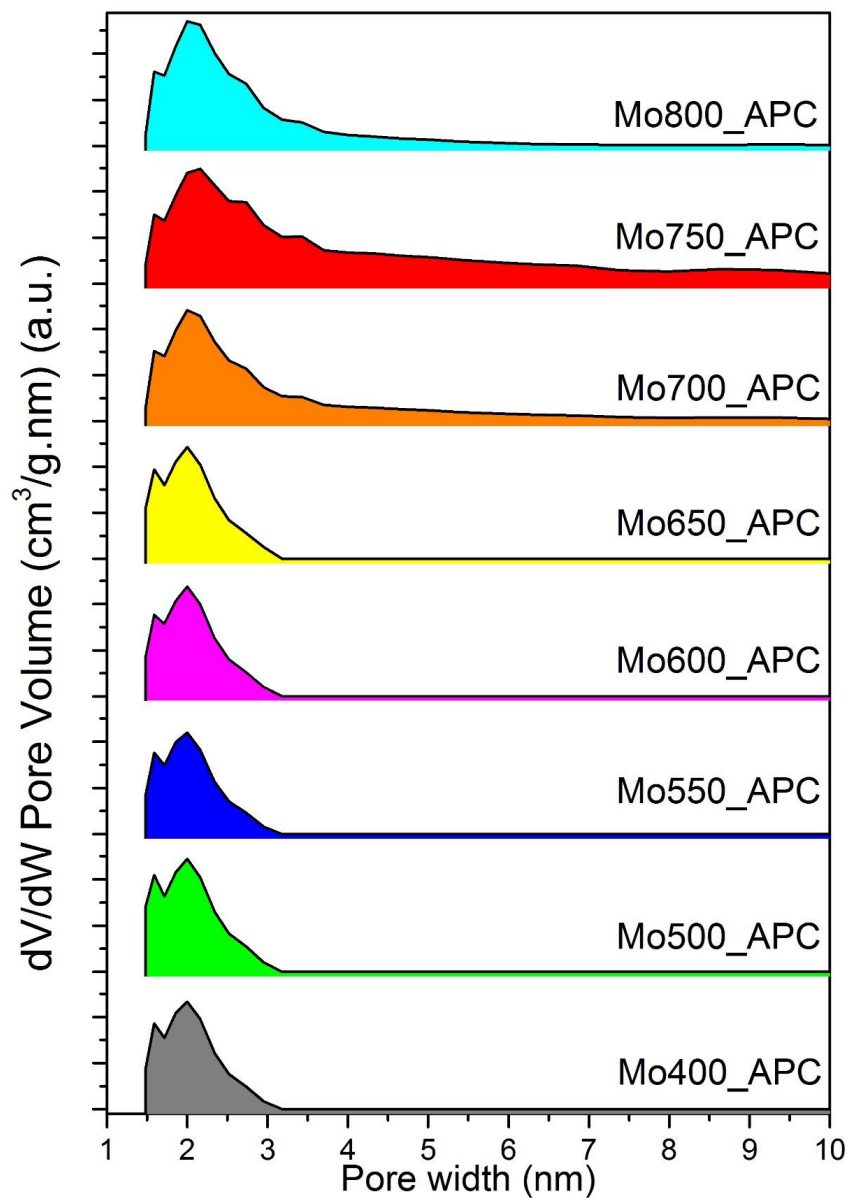


Figure 4.6: Pore size distribution of Mo₂C/APC catalysts prepared at different CHR temperatures calculated from NLDFT model.

Much like the growth in catalyst particles that is observed when metal oxides are used in the metal-catalyzed steam activation of carbons [142], growth of Mo₂C particles during CHR was also observed in this study. The average particle size of the Mo₂C increased from 5.8 ± 0.3 nm after CHR at 650 °C to 9.4 ± 1.9 nm at 750 °C, as determined from the TEM analysis (Figure 4.2). The average Mo₂C particle size was larger than the average pore size of the APC. However, both the pore size distribution and the Mo₂C size distribution data show that small Mo₂C particles could reside within the pores of the APC. As the CHR temperature increased, the Mo₂C particle size increased (Figure 4.3). Hence it is assumed that the pore growth was due to smaller Mo₂C particles within the pores of the APC catalyzing hydrogenation of the pore walls, resulting in increased pore width. Furthermore, growth of the particles as the CHR temperature increased would also result in increased pore size.

4.3.4 Activity Test in HDO of 4-methylphenol

The catalysts of Table 4.1 were assessed for the HDO of 4-MP and the results are reported in Table 4.3 and Figure E.16. The catalysts supported on APC prepared by CHR (Mo₂C/APC) with a 90 min holding time were more active than Mo₂C/AC catalysts as reported in Chapter 2 [103, 128]. In general, the bulk kinetic rate constant of Mo₂C/APC catalyst is > 3x's higher than that of Mo₂C/AC due to the high surface area of APC and different C sources. A relatively high surface area of APC (>1500 m²/g) facilitates the metal dispersion of Mo₂C. Also, due to the high thermal resistance of the APC, the generated pore structure does not collapse easily. Furthermore, increased activity (increase in bulk kinetic rate constant k) was associated with increased mesopore volume (Tables 4.1 and 4.2).

Table 4.3: Bulk kinetic rate constants for the conversion of 4-MP over different Mo-based catalysts at 350 °C.

Catalysts	k (mL/(min.g _{Mo}))
MoP unsupported [103]	1.64
MoO ₃ unsupported [103]	3.78
10Mo%/AC-650 [128]	1.72
Mo600_APC-90	5.62
Mo650_APC-90	6.19
Mo700_APC-90	7.30

4.4 Conclusion

The transition of Mo species during CHR was reported as a function of temperature up to 800 °C. The generation of CH₄ from the APC was critical for the transformation of MoO₃ → MoO_xC_y → Mo₂C and the rate of CH₄ generation increased on Mo₂C. CHR of the Mo-loaded APC had a significant impact on the physical properties of the APC. Mesoporous Mo₂C/APC resulted when CHR was done at temperatures to 750 °C, above which significant Mo₂C sintering and APC pore collapse occurred. A 90 min holding time at the final reduction temperature increased the total pore volume and the mesopore volume fraction of the catalyst. The activity of the Mo₂C/APC catalysts for the HDO of 4-MP was > 3x's higher than that of Mo₂C/AC as reported in Chapter 2, and the activity increased with increased mesoporosity of the carbon support.

Chapter 5: The Effect of S on Mo₂C/APC Catalysts with Various Particle Sizes ⁴

5.1 Introduction

S present in many oil feedstocks has a detrimental effect on noble metal catalysts [98]. Similarly, S has been shown to modify Mo₂C catalysts during reaction [10, 124, 125, 159-161]. The study of Chapter 3 reported the deactivation of Ni-Mo₂C/AC (AC– activated charcoal) catalyst during HDS [160]. However, the transformation of the Ni-Mo₂C in the presence of S occurs rapidly and consequently, the relationship between the changing composition and morphology of the catalyst surface and the catalyst activity remain unclear. Also, the introduction of Ni makes the study of the nature of Mo₂C catalyst during the transformation much more complex. Therefore, this chapter focused on studying the effects of S on Mo₂C/APC catalysts by performing the reactions in a packed-bed reactor so that the dynamics of the transformation could be quantified. The impact of S on Mo₂C catalysts was first reported by Lee and Boudart [10] for the hydrodesulphurization (HDS) of thiophene. Aegerter et al. [124] proposed a model of Mo₂C/Al₂O₃ catalyst after HDS, where a thin layer of MoS₂ covered Mo₂C species, as evidenced by CO-IR spectroscopy. Oyama et al. [125] subsequently reported the formation of carbosulfide sites on a Mo₂C surface during HDS, that promoted HDS but not hydrogenation reactions. CO-DRIFT spectroscopy was also used to study the sulfidation of a Ni-Mo₂C surface [159]. The similar position of the CO adsorption band on a H₂S/H₂ treated Mo-carbide catalyst compared to

⁴ A version of this chapter is in preparation to be submitted for publication. H. Wang, S. Liu., and K. J. Smith, “Understanding selectivity changes during hydrodesulfurization of dibenzothiophene on Mo₂C/carbon catalysts”.

a MoS₂/Al₂O₃ catalyst, suggested the partial sulfidation of Mo carbide under an H₂S environment.

In this chapter, the activity and stability of Mo₂C supported on activated petroleum coke (Mo₂C/APC) during the HDS of dibenzothiophene (DBT) is reported. In particular, the dynamic transition of the Mo₂C catalyst during the initial stages of HDS is examined. Although previous studies have reported that sulfidation of Mo₂C occurs during HDS, none have examined the dynamic transition at conditions that allow one to capture the changes in activity, and selectivity with time-on-steam (TOS). Experiments with relatively low sulfur concentration in the feed were done to capture the transition process. Since the dynamic of the sulfidation of the Mo₂C catalyst during HDS will depend on the Mo₂C particle size, the Mo₂C particle size was varied by varying the Mo₂C catalyst loading. The effect of S on the Mo₂C catalyst surface has been determined experimentally using several characterization methods (BET, XRD, XPS, HRTEM) applied to the catalysts before and after reaction. The data allow one to provide a more accurate description of the formation of MoS₂ covering the Mo₂C. Furthermore, density functional theory (DFT) calculations have been used to determine the impact of S on the binding energy of the reactant to the Mo₂C catalyst surface. These data have been used to better understand the correlation between Mo₂C catalyst structure and catalyst activity/stability as the Mo₂C is exposed to S.

5.2 Experimental

5.2.1 Preparation of Catalysts

Both APC and the catalyst precursors were prepared as described in Chapter 4. Subsequently catalysts with Mo loadings of 2%, 5% and 10 wt% were synthesized by CHR to a final reduction

temperature of 700 °C (See Appendix A.2 and A.3 for details). The resulting catalysts with different Mo loadings are designated as xxMo₂C/APC, where xx represents the nominal Mo loading (wt%). The synthesized catalysts were passivated in a flow of 1 vol% O₂/N₂ at room temperature for 2 h. The Mo loading of the prepared catalysts was confirmed by ICP-OES and all calculations were based on the measured Mo loading. In addition, a reference MoS₂ catalyst, also supported on APC (MoS₂/APC), was synthesized with a nominal Mo loading of 5 wt% to compare with the used Mo₂C/APC catalyst. The MoS₂/APC was prepared by wetness impregnation of AHM, and dried at 110 °C overnight. An in-situ presulfiding was conducted at 370 °C for 3 h under H₂ flow of 50 mL (STP)/min and 6.24 wt% CS₂ in decalin at a liquid flow rate of 0.83 mL/min and 3 MPa (with further details provided in Appendix C.3). Afterwards, a solvent wash was applied to remove excess H₂S adsorbed on the catalyst.

5.2.2 Catalyst Characterization

The specific surface area and pore volume (V_{micro} , V_{meso} , and V_{Total}) of the catalysts were measured using a Micromeritics ASAP 2020 analyzer (See details in Chapter 2 and Appendix B.1). The 2D-NLDFT methodology was applied in the P/P₀ range of 0.01~0.30 to obtain the specific surface area. The pore volume was reported using the same model with the definition of V_{meso} between 2 ~ 50 nm and $V_{\text{micro}} \leq 2$ nm and the total pore volume (V_{Total}) calculated as the sum of V_{meso} and V_{micro} .

The catalyst properties of both fresh and used catalysts were measured by X-ray diffraction (XRD) and XPS (X-ray photoelectron spectroscopy) (See details in Chapter 2, Appendix B.2 and B.3). The number of exposed Mo atoms was estimated from the CO uptake amount by assuming

one chemisorbed CO molecule titrates one active site (See details in Appendix B.4). The elemental quantification of Mo was done by inductively coupled plasma optical emission spectroscopy (ICP-OES) as described in Chapter 2.

The particle morphology was characterized by HRTEM/STEM/EDX (FEI Tecnai Osiris) under 200 kV with a resolution limit of 0.14 nm. The samples were ground, dispersed in ethanol and sonicated for 2 ~ 3 min to obtain a suspension. A drop of the suspension was placed on a 300 mesh lacey carbon film with Cu grid for analysis. The particle size was calculated by analyzing > 100 particles/clusters and then fitting the measured size to a lognormal distribution to determine the average particle size. High angle annular dark field scanning (HAADF) and energy-dispersive x-ray (EDX) elemental mapping were used to reveal the morphology and elemental composition of the used Mo₂C.

5.2.3 Catalytic Performance Measurement in HDS

The HDS of dibenzothiophene (DBT) was carried out in a packed bed reactor (length 500 mm, hot zone 300 mm and internal diameter of 8.64 mm) to assess the catalytic activities of the as-prepared Mo₂C/APC catalysts with different Mo loadings. Both the mass transfer and heat transfer effect were eliminated (see details of this calculation in Appendix G.1 ~ G.4). The experiments were operated at 350 °C and constant pressure of 4.1 MPa. The liquid feed, consisting of ca. 0.2 wt% DBT (340 ppmw S) in decalin, was fed to the reactor by means of a high-pressure piston pump (Gilson model 307). The H₂ flow was controlled by a mass flow controller (Brooks 5850TR). All the experiments were operated with a H₂/feed volumetric ratio of 600 and a liquid-hourly space velocity (LHSV) of 4 h⁻¹. An Aspen calculation demonstrated

that the reaction occurred in the gas phase at the chosen reaction conditions (see Appendix C.8). Following reactor heat up and stabilization period of 45 mins (the system dynamic response was measured as 41 mins; Appendix C.9 for calculation), liquid product was collected periodically from a condenser held at room temperature and placed after the reactor exit. Finally, all liquid samples were analyzed by gas chromatography - mass spectroscopy (Shimadzu GC/MS) using a capillary column (RTX5 30 m x 0.25 mm) and an external calibration method. Before performing the activity test, the passivated catalyst (containing 0.019 g_{Mo}, 2.5 mL) was activated in-situ under H₂ flow at 400 °C for 2 h to remove the passivation layer from the catalyst surface. Overall, the activity data reported herein were measured with a carbon balance ≥ 93% and several experiments were repeated to quantify the error in the activity data (Appendix F.3).

The reactant conversion and relevant product selectivities are calculated as follows:

$$\text{DBT conversion (\%)} = 100 \times \frac{\sum m_i}{m_{DBT}^0} \quad (\text{Eq. 5-1})$$

$$\text{HDS conversion (\%)} = 100 \times \frac{\sum m_i - \sum m_{Si}}{m_{DBT}^0} \quad (\text{Eq. 5-2})$$

$$\text{Selectivity of product } i \text{ (\%)} = 100 \times \frac{m_i}{\sum m_i} \quad (\text{Eq. 5-3})$$

where m_i is the molar fraction of product i ; $\sum m_i$ is the sum of molar fraction of all products; m_{DBT}^0 is the molar fraction of DBT in the liquid feed; m_{Si} is the molar fraction of product i that contains S.

5.2.4 Computational Model and Methods

Since there is no uniform model established for β -Mo₂C, the eclipsed configuration has often been applied in the building of bulk β -Mo₂C [162, 163]. In this part of the study, the eclipsed

configuration used in Wang et al.'s work [164] to generate bulk hexagonal Mo₂C was used. The calculated lattice parameters of the optimized bulk are a=5.994 Å, b=5.994 Å, and c=4.727 Å, consistent with the Kuo et al.'s XRD results for β-Mo₂C [165]. Since the surface termination (101) plane is the most stable, it has been modeled by periodic slabs with p(2×2) unit cells and used as the adsorption surface for DBT. The thickness of the four-layer slab is 5.0 Å with the top two layers relaxed and the bottom two layers fixed. A conjugated-gradient algorithm is used for ion relaxation. The vacuum layer between slabs is 15 Å to avoid interaction between the periodic slabs.

All density functional theory (DFT) related calculations were done using the plane-wave based periodic method in the Vienna ab initio simulation package (VASP) [147, 149]. The projector-augmented wave (PAW) method was used to describe the core-valance interaction while the generalized gradient approximation with Perdew-Burke-Ernzerhof (GGA-PBE) was used for the electron exchange correlation energy. All the calculations were done with cut-off energy of 400 eV with a total convergence of above 10⁻⁴. A 5 × 5 × 5 Monkhorst-Pack k-point grid for sampling the Brillouin zone was applied to bulk optimization. A 3 × 3 × 1 Monkhorst-Pack k-point grid set was used for supercell optimization. In these calculations, Van der Waals' force is considered with dDsC dispersion correction method to correct the conventional DFT calculations.

The adsorbed H₂ and DBT on the topmost layer were relaxed to their optimized positions.

The DBT adsorption energy E_{ads} was calculated by the following equation:

$$E_{\text{ads}} = E_{(\text{X/slab})} - E_{\text{X}} - E_{(\text{slab})} \quad (\text{Eq. 5-4})$$

Where $E_{(X/\text{slab})}$ is the energy of the adsorbed system with both slab and adsorbed X, E_X is the energy of specie X, and $E_{(\text{slab})}$ is the energy of the slab.

E_{IS} , E_{TS} , and E_{FS} are used to represent the energies of the initial state, transition state and final state, respectively, in the study of the dissociation adsorption energy of H_2 . The energy barrier (E_a) and reaction energy (E_r) were calculated by the equations as follows:

$$E_a = E_{TS} - E_{IS} \quad (\text{Eq. 5-5})$$

$$E_r = E_{FS} - E_{IS} \quad (\text{Eq. 5-6})$$

The Gibbs free adsorption energy ΔG_{Ads} is calculated by the following equation [166]:

$$\Delta G_{Ads}(T, P) = E_{ads} - 3kT + \Delta ZPE - kT \ln \left(\frac{1}{z_{DBT}^{rot}(T) * z_{DBT}^{trans}(T, P)} \right) - kT \ln \left(\frac{P}{P_0} \right) \quad (\text{Eq. 5-7})$$

Where $z_{DBT}^{trans}(T, P)$ represents the translational partition function of DBT; $z_{DBT}^{rot}(T)$ represents the rotational partition function of DBT; T is temperature in Kelvin; P is the partial pressure of DBT in the system, Pa; P_0 is the standard state pressure, Pa; ΔZPE is the zero point energy difference between adsorbed system and the adsorbate; k is the Boltzmann constant, 1.38×10^{-23} J/K.

5.3 Results

5.3.1 Fresh Catalyst Characterization

5.3.1.1 XRD and Physical Properties Analysis

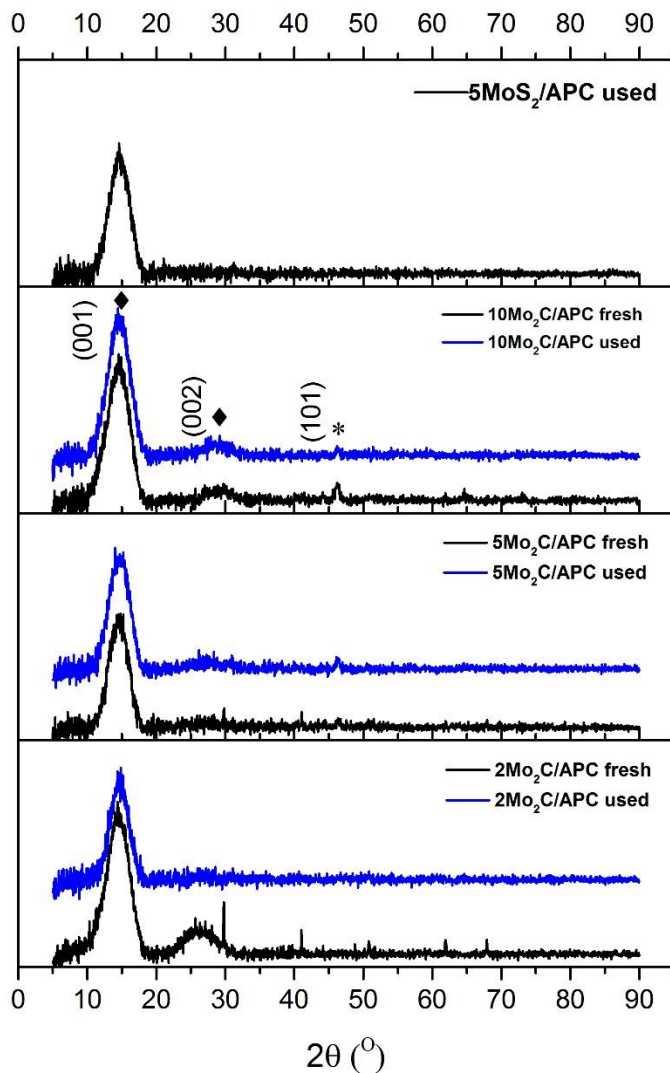


Figure 5.1: XRD diffraction patterns of fresh and used $\text{Mo}_2\text{C}/\text{APC}$ catalysts: (◆) carbon support; (*) Mo_2C .

Figure 5.1 shows the XRD patterns of the $\text{Mo}_2\text{C}/\text{APC}$ catalysts with different Mo loadings. No peaks were detected for the freshly-synthesized $2\text{Mo}_2\text{C}/\text{APC}$, probably due to the low metal

loading and small particle size. However, for the 5Mo₂C/APC and 10Mo₂C/APC catalysts, there is a small peak located at 2θ=46.07 °, corresponding to the (101) plan of β-Mo₂C (PDF card #: 00-035-0787) and indicative of Mo₂C formation. There are also two distinct broad diffraction peaks at ~14.8 ° and ~30.2 °, corresponding to the (001) and (002) diffraction planes of the carbon support, respectively (PDF card #: 00-041-1487).

Table 5.1: Physical properties of catalyst precursors, fresh, and used Mo₂C/APC catalysts with different Mo loadings.

Samples	Pore volume (cm ³ /g)		Surface area (m ² /g)	V _{total} (cm ³ /g)	Mesopore (%)	Burn-off%	Final yield (%)
	V _{Micro}	V _{Meso}					
<i>Catalyst Precursors</i>							
APC support	0.93 ^a	0.09 ^a	2028 ^b	1.02 ^c	9.05	34.50 ^d	65.50 ^e
2AHM/APC	0.90	0.05	1994	0.95	5.49	—	—
5AHM/APC	0.84	0.08	1832	0.93	9.05	—	—
10AHM/APC	0.69	0.07	1520	0.76	9.74	—	—
<i>Fresh Catalysts</i>							
2Mo ₂ C/APC	0.84	0.34	1829	1.17	28.67	22.87	46.26 ^f
5Mo ₂ C/APC	0.80	0.32	1722	1.12	28.91	32.37	37.66
10Mo ₂ C/APC	0.74	0.42	1651	1.16	36.21	53.67	30.35
<i>Used Catalysts</i>							
2Mo ₂ C/APC	0.86	0.31	1818	1.17	26.27	—	—
5Mo ₂ C/APC	0.64	0.29	1362	0.93	30.75	—	—
10Mo ₂ C/APC	0.60	0.19	1269	0.79	23.88	—	—
5MoS ₂ /APC	0.73	0.11	1566	0.79	7.82	—	—

a. The pore volume was reported based on NLDFT method provided by Micromeritics, where mesopore volume is between 2-50 nm and micropore is ≤ 2 nm.

b. The specific surface area was calculated from the measured N₂ adsorption isotherm using 2D-NLDFT-HS applied in the P/P₀ range of 0.01~0.30.

c. The total pore volume is the sum of V_{meso} and V_{micro}.

d. The carbon burn-off (%) during the CHR was calculated as: Burn-off (%) = 100 × [1 - $\frac{m_{CHR}}{m_o}$].

e. Final yield of activated petcoke (APC) was calculated by 100 minus burn-off.

f. The final yield of the catalyst was calculated based on the utilization of raw petcoke:

$$\text{Final yield\%} = \frac{(100 - \text{Burn off}) \times 65.50}{100}$$

Table 5.1 shows that the total pore volume (V_{Total}) and surface area of the catalyst precursors decreased with increased Mo loading. The micropore volume (V_{micro}) of the precursors decreased with Mo loading, indicating that some of the AHM blocked the micropores following impregnation and drying of the APC support. Following CHR, the catalysts all exhibited a significant increase in mesopore volume [167] with the 10Mo₂C/APC having the highest mesopore volume. Note, however, that a higher carbon burn-off was obtained during the synthesis with increased Mo loading so that the 10Mo₂C/APC had the lowest mass yield from the synthesis. The fresh catalysts all have similar surface areas ($1734 \pm 73 \text{ m}^2/\text{g}$) and total pore volumes ($1.15 \pm 0.02 \text{ cm}^3/\text{g}$).

5.3.1.2 XPS Analysis

The compositions and surface electronic state of the fresh Mo₂C/APC catalysts were further investigated by XPS. For the fresh catalysts, Mo, O, and C were detected and a detailed Mo 3d deconvolution of the spectra is reported in Table 5.2 and Figure 5.2. The Mo 3d spectra were deconvoluted into five different peaks attributed to Mo²⁺, Mo³⁺, Mo⁴⁺, Mo⁵⁺ and Mo⁶⁺ [128], each with Mo 3d_{5/2} and Mo3d_{3/2} spin-orbital splitting of 3.1 eV and an area ratio of 3:2. The peaks at 228.3 eV and 231.4 eV can be assigned to Mo₂C. The Mo³⁺, Mo⁴⁺, and Mo⁵⁺ species are ascribed to MoO_xC_y species, while the peaks at higher B.E. correspond to Mo⁶⁺ attributed to Mo(VI) oxide species [168, 169]. The ratio of Mo carbide plus oxycarbide species to oxide species on the synthesized fresh catalyst was ~85:15, indicative of a significant formation of Mo₂C related species at 700 °C. Moreover, there was no obvious difference in the Mo species composition as the Mo loading increased, which indicates that the CH₄ produced at 700 °C during CHR is sufficient to convert all Mo precursors to the carbide for Mo nominal loadings of

≤ 10 wt%. Furthermore, a good correlation between Mo loading and the XPS intensity ratio ($I_{\text{Mo}}/I_{\text{C}}$) for the fresh $\text{Mo}_2\text{C}/\text{APC}$ catalysts, shown in Appendix E.4, Figure E.17, indicates monodispersion of Mo species on APC [170] under the present CHR temperature of $700\text{ }^\circ\text{C}$ when the nominal Mo (wt.%) content was $\leq 10\%$.

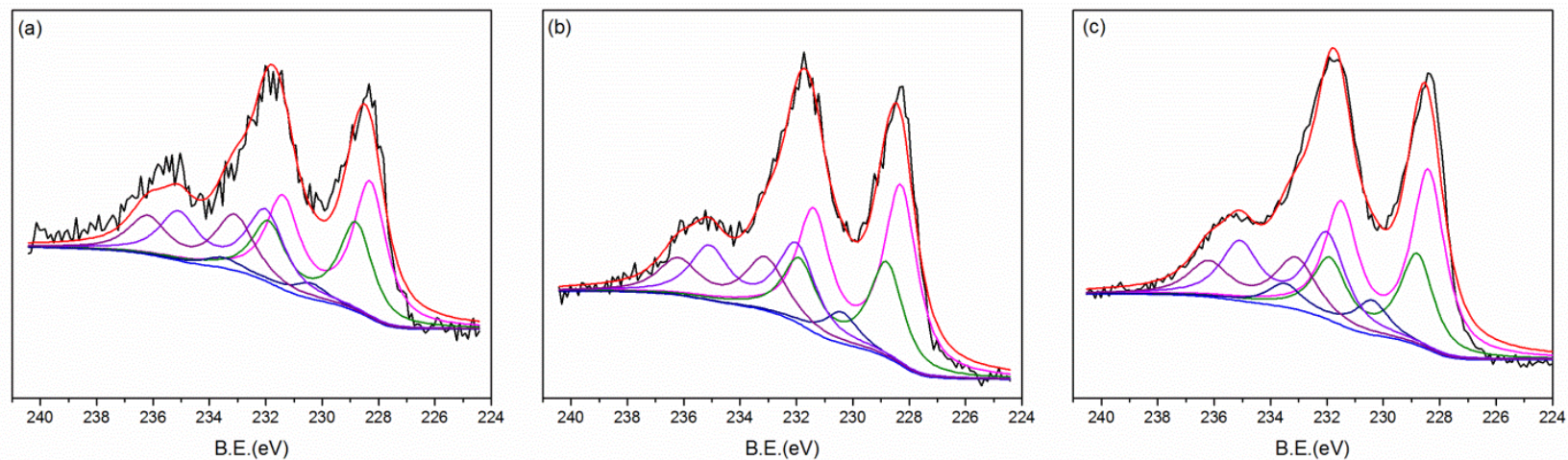


Figure 5.2: The deconvolution of Mo 3d of fresh Mo₂C/APC catalysts: (a) 2Mo₂C/APC; (b) 5Mo₂C/APC; and (c) 10Mo₂C/APC.

Table 5.2: XPS analysis of fresh Mo₂C/APC catalysts with different Mo loadings.

Samples	Mo 3d, At%	O 1s, At%	C 1s, At%	Mo loading by ICP, wt%	O/Mo atomic ratio	I _{Mo} /I _C	Mo ²⁺ (B.E.=228.3 eV)	Mo ³⁺ (B.E.=228.8 eV)	Mo ⁴⁺ (B.E.=230.4 eV)	Mo ⁵⁺ (B.E.=232.0 eV)	Mo ⁶⁺ (B.E.=233.1 eV)
2Mo ₂ C/APC	0.55	2.91	96.54	2.47 ^a	5.29	0.08 ^b	35.39 ^c	23.13 ^c	3.98 ^c	21.03 ^c	16.48 ^c
5Mo ₂ C/APC	1.03	2.86	96.11	5.90	2.78	0.19	40.08	21.27	4.30	20.04	14.32
10Mo ₂ C/APC	2.90	5.96	91.14	13.79	2.06	0.55	38.55	19.60	7.36	21.08	13.40

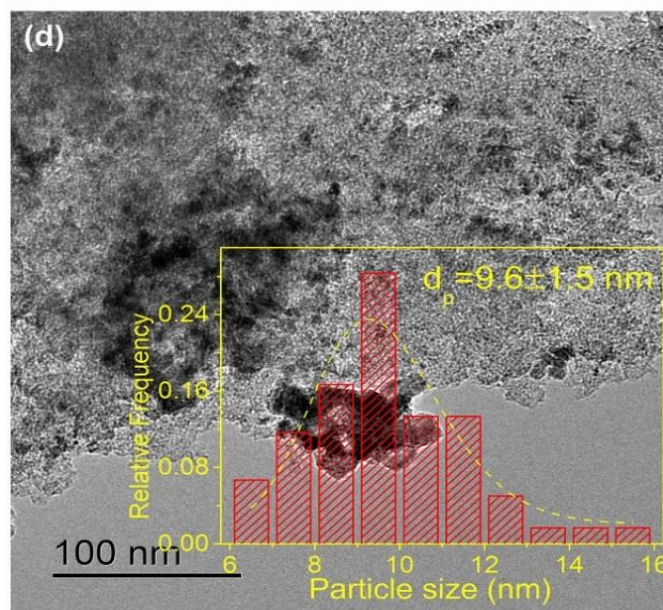
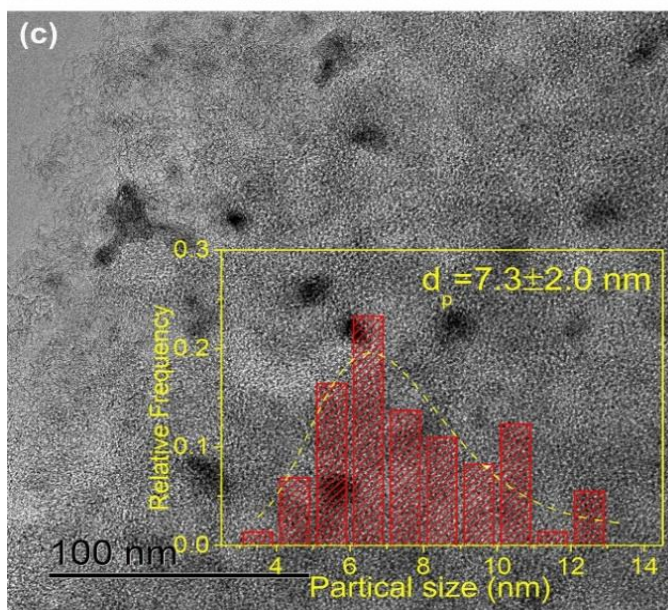
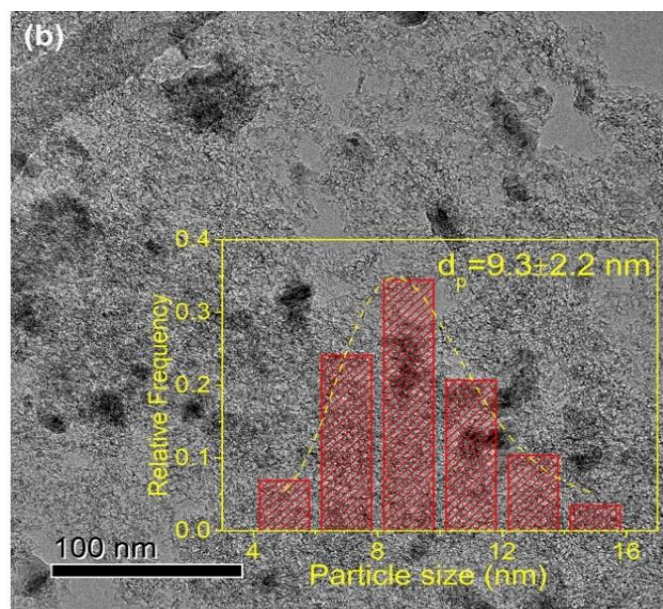
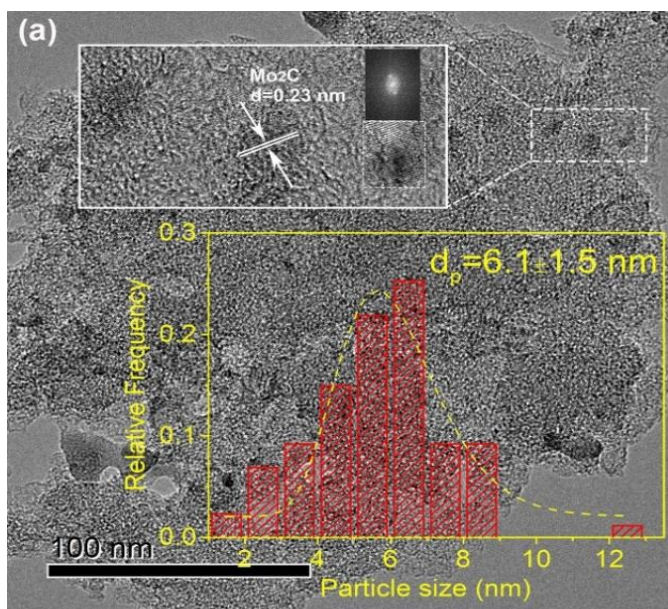
a. This value was measured by ICP-MS.

b. The relative intensity of Mo to carbon obtained from XPS data.

c. The deconvoluted peaks of Mo of different valences.

5.3.1.3 TEM/STEM-EDX Analysis and CO Uptake

TEM micrographs of both fresh and used catalysts with different metal loadings are presented in Figure 5.3. The particle size distribution of Mo species was taken from multiple TEM images, where the particle had a lattice fringe spacing of 0.23 nm. The average particle size increased from 6.1 nm to 10.3 nm as Mo content increased, as shown by the lognormal distribution of Figure 5.3 (a, c, and e). The analysis also showed that the particles were well-distributed under present preparation conditions with Mo loading ≤ 10 wt%. In addition, the standard deviation of the particle size increased with increased Mo loading, indicating that at higher loading there was less control of the particle size.



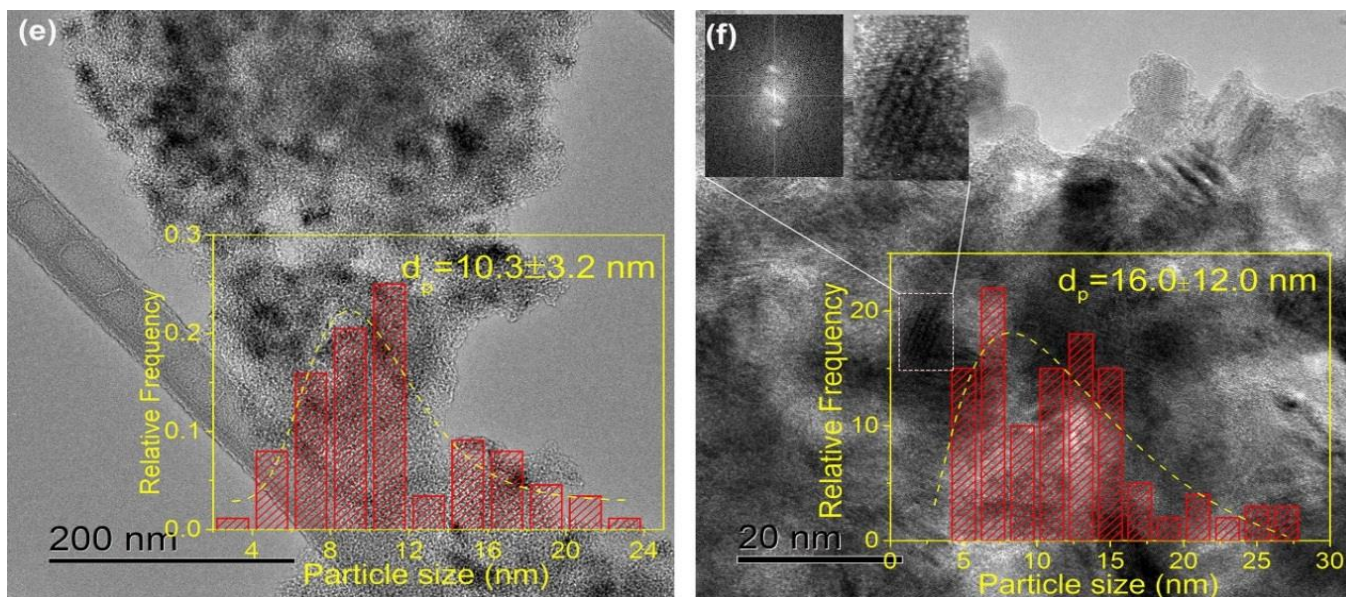


Figure 5.3: TEM images and cluster size distribution of Mo₂C/APC with different metal Mo loadings. (a) 2Mo₂C/APC fresh; (b) 2Mo₂C/APC used; (c) 5Mo₂C/APC fresh; (d) 5Mo₂C/APC used; (e) 10Mo₂C/APC fresh; and (f) 10Mo₂C/APC used.

The CO uptake data of the fresh catalyst (Table 5.3) also showed increased CO uptake as the Mo loading of the Mo₂C/APC catalysts decreased, consistent with the decreased particle size measured by TEM.

Table 5.3: The particle size and CO uptake of fresh and used Mo₂C/APC catalysts.

Samples	Fresh catalyst			Used catalysts	
	Identified phase ^a	Particle size (nm) ^b	CO uptake, $\mu\text{mol/g}_{\text{metal}}$ ^c	Particle size (nm) ^b	CO uptake, $\mu\text{mol/g}_{\text{metal}}$ ^c
2Mo ₂ C/APC-700	—	6.1±1.5	137	9.3±2.2	1
5Mo ₂ C/APC-700	β -Mo ₂ C	7.3±2.0	126	9.6±1.5	5
10Mo ₂ C/APC-700	β -Mo ₂ C	10.3±3.2	116	16.0±12.0	4

a. From XRD analysis;

b. The average particle size of Mo₂C is reported by counting ≥ 100 particles and applying a lognormal distribution to the particle count data to obtain mean and standard deviation values.

c. This data was obtained based on reduced passivated catalysts.

5.3.2 Catalyst Activity and Stability

Hydrodesulphurization of dibenzothiophene (350 °C, 4.1 MPa, H₂: feed = 600, LHSV= 4 h⁻¹) was used to determine the catalytic activity of the carbide catalysts. Before performing the tests, the passivated catalysts were reduced under H₂ flow at 400 °C for 2 h to remove the passivation layer. Subsequently DBT conversion data were collected in 30 to 40 min intervals until steady state was achieved. All the experiments were conducted for the same time on stream (TOS) of 600 min.

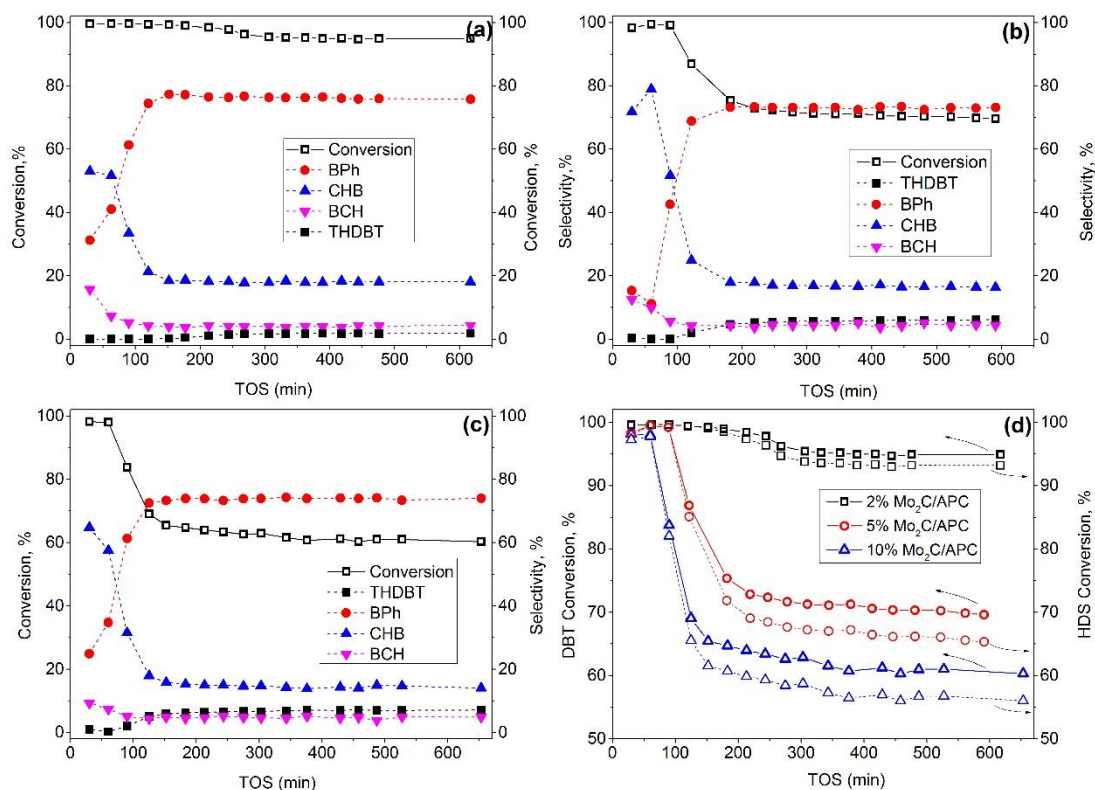


Figure 5.4: DBT conversion and selectivity of Mo₂C/APC catalysts with different Mo loadings with TOS. (All the experiments were done with the same amount of Mo loading in the reactor): (a) 2Mo₂C/APC; (b) 5Mo₂C/APC; (c) 10Mo₂C/APC; and (d) DBT conversion and HDS conversion for Mo₂C/APC catalysts with different Mo loadings as a function of TOS.

To assess the effect of Mo₂C particle size, the catalysts were tested with the same amount of Mo (0.019 g Mo) in the reactor. The conversion and selectivity data are presented in Figure 5.4, showing the changes in conversion and selectivity with TOS and Mo catalyst loading. All of the Mo₂C catalysts deactivated in the presence of S, as shown in Figure 5.4 (a-c). Note that the DBT conversion decreased from 98% to 60% in 600 min on larger Mo₂C particles (10Mo₂C/APC); whereas, on smaller Mo₂C particles (2Mo₂C/APC) the loss in conversion is much less severe (from 100 to 95 % conversion). The relative decay constants (k_d) associated with the loss in

conversion are reported in Table 5.4 (see details in Appendix D.3), and show increased deactivation rate with increased Mo₂C particle size. The DBT conversion and product selectivities reached a steady state after ~150 min TOS for all three catalysts. The averaged steady state DBT conversion and product selectivity are reported in Table 5.4, based on the last five data points collected during the experiment. The difference between the DBT conversion and HDS conversion reported in Figure 5.4(d) and Table 5.4, show that there was no significant loss in HDS conversion relative to DBT conversion.

The primary products of DBT conversion, as determined by GCMS, were biphenyl (BPh), cyclohexylbenzene (CHB) and bicyclohexane (BCH), with less significant quantities of hydrocarbons and minor amounts of S-containing product—tetrahydrodibenzothiophene (THDBT). The change in selectivity with TOS is shown in Figure 5.4 (a-c). All Mo₂C catalysts with different Mo loadings and hence particle sizes, showed very high selectivity towards CHB and BCH, at the beginning of the reaction (60% and 20%, respectively); whereas, both decreased with TOS until they reached a similar level (CHB ≈ 20%; BCH < 10%) and BPh became the primary product with selectivity > 70%. Importantly, this transformation occurred at a similar time (~150 min) for all Mo₂C catalysts, independent of the Mo₂C particle size. Note that over the 5MoS₂/APC catalyst, the DBT conversion and product selectivity did not undergo any measurable change with TOS and selectivity to BPh was 73% (Table 5.4).

Table 5.4: Conversion and product selectivity for the hydrodesulfurization of dibenzothiophene over Mo₂C/APC and MoS₂/APC catalysts at 350 °C and 4.1 MPa after stabilization and TOS > 150 mins.

Catalyst	Loading (g)	Conversion of DBT (%) ^a	HDS conversion of DBT (%) ^b	Selectivity (%) ^a				k _d (h ⁻¹) ^c	R ²
				THDBT	BPh	CHB	BCH		
<i>Mo₂C of different particle sizes</i>									
2Mo ₂ C/APC	0.77	94.89	93.19 ^b	1.79 ^a	76.02 ^a	18.11 ^a	4.08 ^a	2.60E-3 ± 1.28E-4	0.98
5Mo ₂ C/APC	0.32	70.08	65.86	6.02	73.01	16.48	4.49	9.65E-3 ± 1.71E-3	0.90
10Mo ₂ C/APC	0.14	60.77	56.49	7.05	73.92	14.43	4.61	2.53E-2 ± 5.78E-3	0.93
5MoS ₂ /APC	0.77	100.00	100.00	0.00	72.97	23.35	3.68	—	—

a. The conversion and selectivity were obtained as the average of the last 5 data points collected after 400 min TOS period.

b. The HDS conversion of DBT reported the HDS conversion to products free of S.

c. The decay constant was calculated based on exponential decay equation: $-\frac{da}{dt} = k_d a$.

5.3.3 Used Catalyst Characterization

5.3.3.1 XRD and Physical Properties Analysis

The XRD analysis of the used catalysts is reported in Figure 5.1. The used catalysts showed no visible phase change from Mo_2C , suggesting that bulk sulfidation did not occur under the present reaction conditions. Similar phenomenon were also observed by Aegerter et al. [124]. Note that there are no peaks associated with MoS_2 for the used $5\text{MoS}_2/\text{APC}$ catalyst, probably due to a high MoS_2 dispersion on this catalyst.

Table 5.1 shows that there was no noticeable change in surface area and pore volume for the used $2\text{Mo}_2\text{C}/\text{APC}$ catalyst; whereas, a small decrease occurred for the used 5 and $10\text{Mo}_2\text{C}/\text{APC}$ catalysts, when compared to the fresh catalyst. This decrease is probably due to the increased particle size blocking micropores.

5.3.3.2 XPS Analysis

The surface composition of the used catalysts included the presence of S as shown by the survey scan in Figure 5.5 (a) and the component concentrations reported in Table 5.5. The narrow scan of the S 2p region suggests the existence of S_1^{2-} , S_2^{2-} and SO_4^{2-} species [171, 172]. A detailed deconvolution of the S 2p signal is shown in Appendix E.4, Figure E.18. The peaks at 162.0 eV and 163.2 eV are assigned to $\text{S}^{2-} 2p_{3/2}$ and $\text{S}^{2-} 2p_{1/2}$, respectively, with a spin-orbit splitting of 1.2 eV and indicative of the presence of MoS_2 species. Moreover, the S 2p peaks at 163.6 eV and 164.7 eV represent the formation of S_2^{2-} of MoS_3 species. The presence of SO_4^{2-} species is also identified on the used Mo_2C catalysts. To identify the difference between the sulfided Mo_2C

surface and the MoS₂ catalyst, the 5%MoS₂/APC catalyst was analyzed as reported in Figure 5.5 (b). The same deconvolution method was applied and the same S species present as MoS₂, MoS₃, and SO₄²⁻ were identified, indicating that sulfidation of Mo does occur on the Mo₂C catalyst surface during the HDS reaction. Similar observations have been reported in previous studies [31, 124, 158]. The relative composition of the different S species on the used catalysts is reported in Table 5.5. The ratio of MoS₂ (S²⁻) species to MoS₃ (S₂²⁻) species is about 6 for the MoS₂ catalyst; whereas, the ratio is about 1 (S²⁻: S₂²⁻≈1) for the used Mo₂C catalysts. Furthermore, it is interesting to note that the S/Mo atom ratio (Table 5.5 column 8, 9) decreased with increased Mo loading.

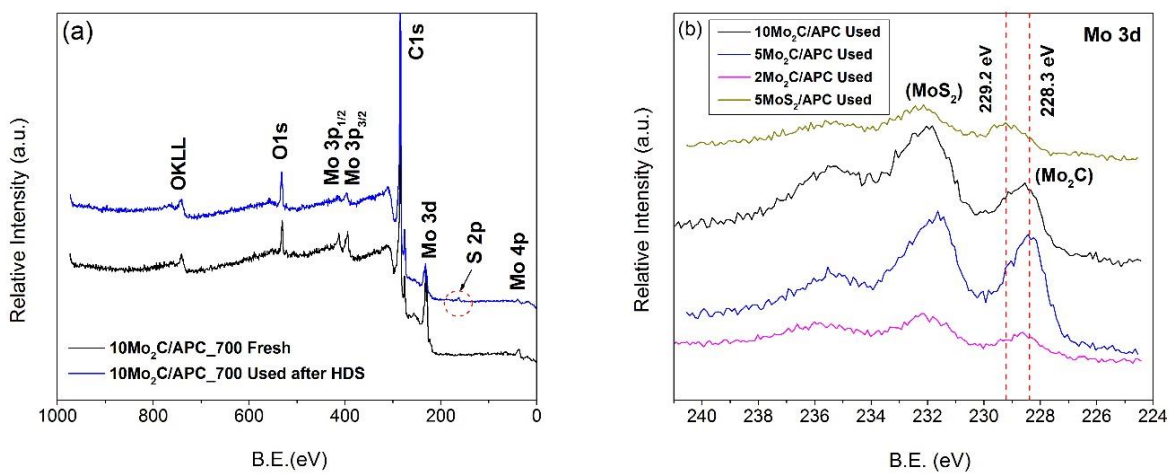


Figure 5.5: XPS spectra of Mo₂C catalysts: (a) Survey scan of fresh and used 10Mo₂C/APC catalyst; (b) Narrow scan of Mo 3d spectra for used Mo₂C catalysts with different metal loadings and used 5MoS₂/APC.

Table 5.5: XPS analysis of used Mo₂C/APC catalysts with different Mo loadings.

Samples	Mo 3d, At%	O 1s, At%	C 1s, At%	S 2p, At%	S, wt%	S, wt%	S/Mo atomic ratio, % ^c	S/Mo atomic ratio, % ^d	S ₁ ²⁻ 2p (B.E.=162.0 eV)	S ₂ ²⁻ 2p (B.E.=163.6 eV)	SO ₄ ²⁻ (B.E.=169.0 eV)
2Mo ₂ C/APC	0.50 ^a	3.99 ^a	95.04 ^a	0.47 ^a	1.19 ^a	0.22 ^b	0.94 ^c	0.27 ^d	21.66	35.17	43.17
5Mo ₂ C/APC	0.89	4.30	94.29	0.52	1.28	0.39	0.58	0.20	38.54	26.00	35.46
10Mo ₂ C/APC	2.78	5.53	90.95	0.74	1.61	0.65	0.27	0.14	37.20	26.97	35.83
5MoS ₂ /APC	0.62	4.16	94.35	0.87	2.16	0.31	1.40	0.19	76.84	12.94	10.23

a. Surface elemental (Mo, O, C, S) contents were measured by XPS.

b. Bulk phase S content (wt%) was obtained by CHNS analyzer.

c. The atomic ratio of S/Mo from XPS measurement.

d. The atomic ratio of S/Mo from CHNS analyzer.

5.3.3.3 TEM/STEM-EDX Analysis

As shown in Figure 5.3(b, d, and f), the bulk phase of Mo₂C was still present on the used catalysts after the HDS reaction. However, the presence of MoS₂ layers on top of the Mo₂C particles, was confirmed by the lattice fringe spacing of 0.62 nm. This result is consistent with the XPS data, which demonstrated the formation of MoS₂ on the used catalyst.

As part of the transition of Mo carbide species during the HDS reaction, the particle size distribution also changed. All the used catalysts showed an increase in particle size after reaction. For the 2Mo₂C/APC and 5Mo₂C/APC catalysts, the particle size increased to ~ 9.5 nm; whereas, it increased to 16.0 nm for the 10Mo₂C/APC catalyst. The HADDF-STEM image and EDX elemental mapping of the used 2Mo₂C/APC catalyst are presented in Figure 5.6, Figure E.19 and Figure E.20. This analysis shows that S is closely associated with the Mo, with the Mo and S elemental composition map of the selected area almost identical.

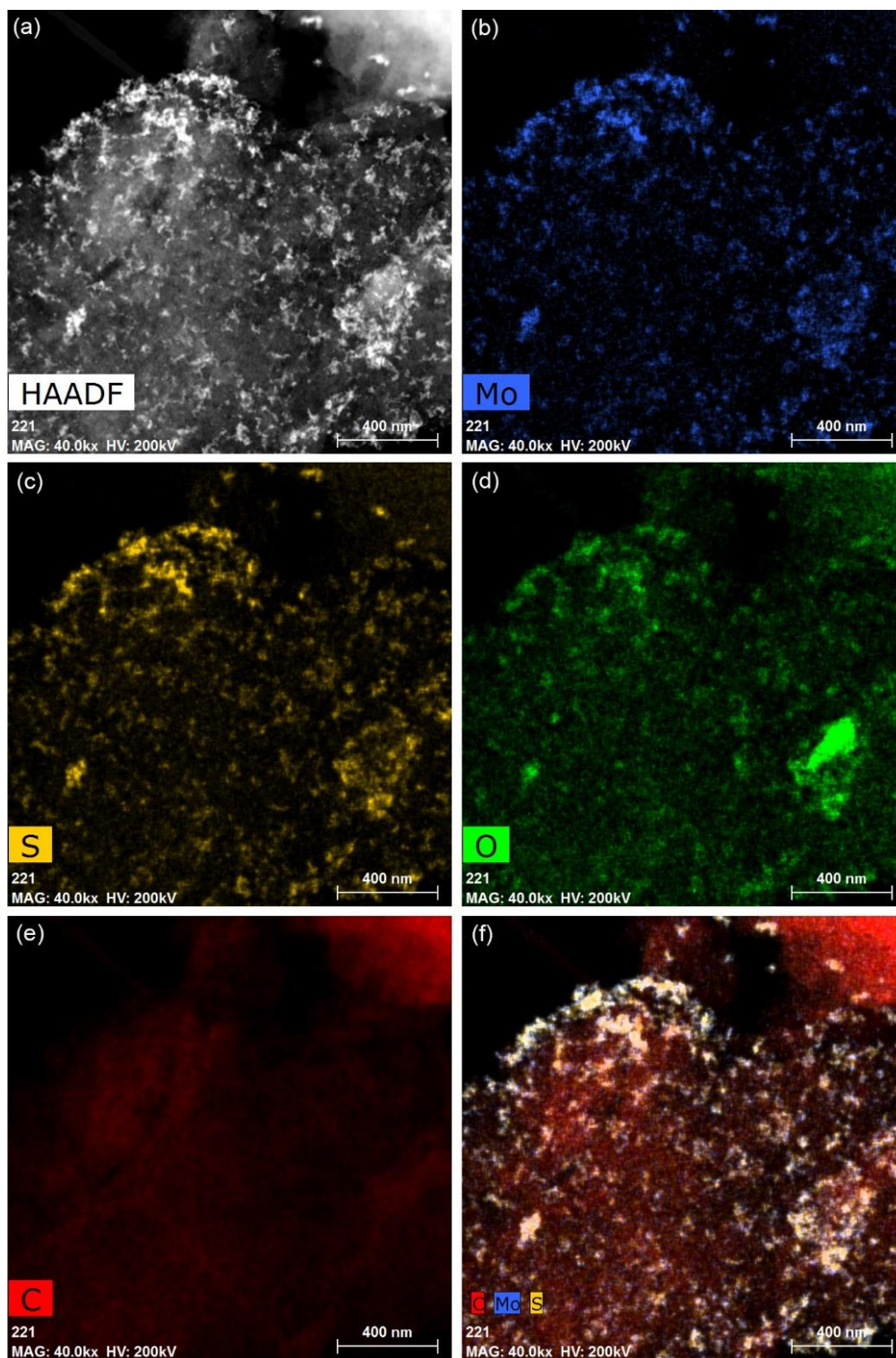


Figure 5.6: High angle annular dark field TEM scanning image (HAADF-STEM) of used $2\text{Mo}_2\text{C}/\text{APC}$ catalyst (a); (b-e) Energy dispersive X-ray (EDX) elemental mappings of Mo, S, O and C; and (f) Overlay of C, Mo, and S distributions.

The line scan image (Figure 5.7) of the same particles shows the relationship more clearly. As the Mo concentration increased, the S concentration increased. Moreover, the S content is much higher in the presence of Mo than in its absence, indicating that most S remained on the surface of Mo after reaction.

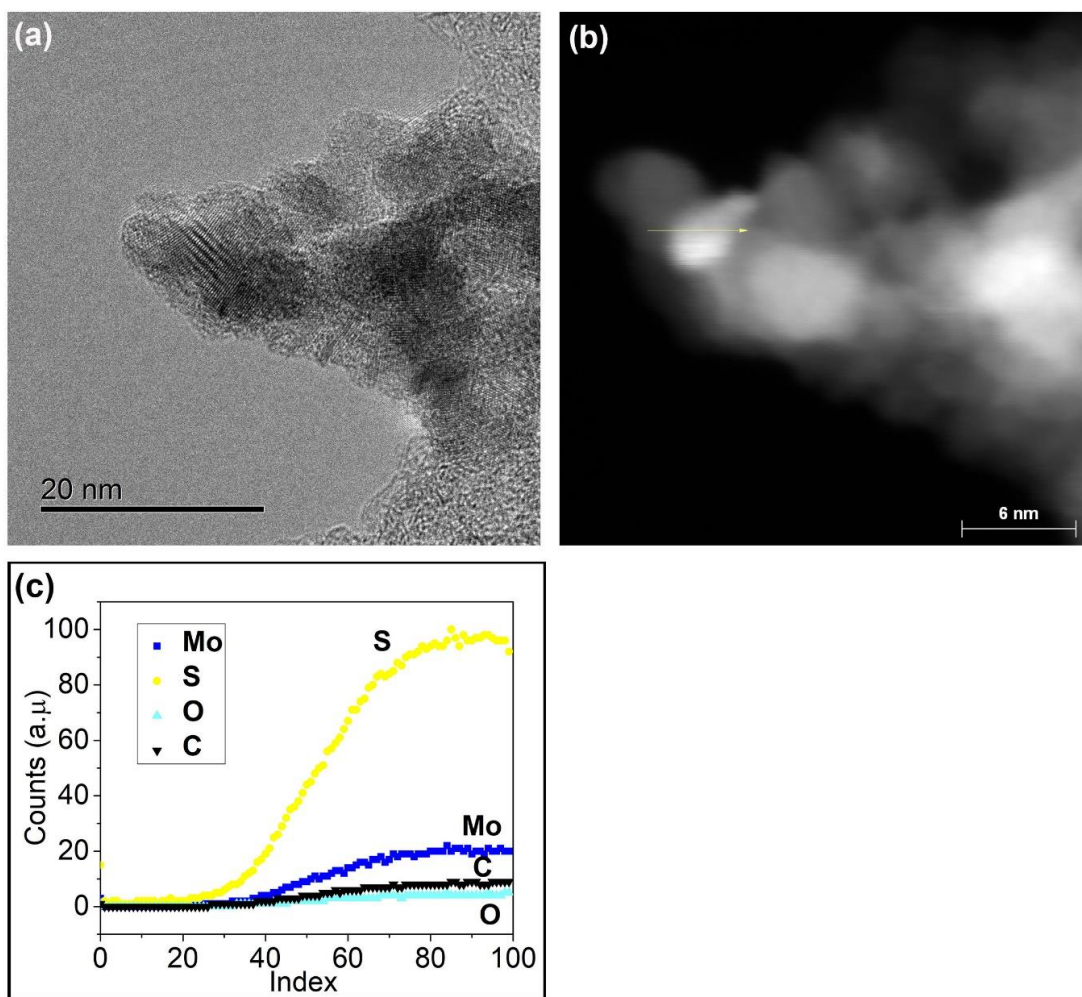


Figure 5.7: (a) TEM image of used 10Mo₂C/APC catalyst; (b) High angle annular dark field TEM scanning image (HAADF-STEM); and (c) Line scanning on selected particle.

5.4 Discussion and DFT Analysis

The Mo₂C/APC catalysts with 2, 5, and 10% Mo, prepared by CHR, showed similar surface compositions with ~85% of the Mo present as Mo carbide or oxycarbide species. The average particle size of the Mo species increased from 6.1 to 10.3 nm as the Mo loading increased from 2 to 10 wt%. Hence the catalysts are of similar composition but varying size, allowing one to examine the transition of Mo₂C during HDS, accounting for particle size effects.

Although the Mo₂C/APC catalysts of the present study showed different levels of DBT conversion, they all declined in activity within the first 600 min of the reaction, with the product selectivity also changing significantly. The data provide evidence that the transition of the Mo₂C caused by S is one possible reason for the change in activity and selectivity during the HDS reaction. To exclude the possibility of carbon deposition or other mechanism that may block pores leading to a loss in activity, the textural properties of the used catalysts were measured and compared to the fresh catalysts. Both the specific surface area and pore volume (Table 5.1) do not change significantly before and after reaction, indicative of no pore blockage, even though the size of the Mo₂C particles was observed to increase after reaction (Table 5.3).

The transition of Mo₂C during the HDS reaction with MoS₂ phase formation was also observed by Aegerter et al. [124] In the present study, both XPS and TEM analyses provide clear evidence of the transformation of Mo₂C to MoS₂ because of S species on the catalyst surface. However, the bulk phase of Mo₂C did not change, as confirmed by XRD. Since the catalyst activity and selectivity stabilized after approximately 150 min TOS, we conclude that the outer surface of the

Mo₂C particles are transformed to MoS₂ which then act as primary active sites for HDS reactions.

Characterization of the fresh and used catalysts has provided clear evidence of Mo₂C particle size varying with Mo loading of the Mo₂C/APC catalysts, while maintaining constant Mo carbide content. As expected, S incorporation increased the particle size of the Mo species following HDS, since the Mo molar density of MoS₂ (0.0316 mol/cm³) is lower than that of Mo₂C (0.0873 mol/cm³) [173]. For the 2Mo₂C/APC catalyst, the particle size increased ~50%; whereas, for the 5Mo₂C/APC catalyst a ~30% increase in size was observed. This result is consistent with the S/Mo ratio from XPS (Table 5.5, column 8), which demonstrates that smaller Mo₂C particles (with higher surface area) incorporated more S during HDS than larger Mo₂C particles. The degree of particle size growth for the 10Mo₂C/APC catalyst was ~56% and this relatively high value may be a consequence of agglomeration of adjacent particles.

Agglomeration of particles would further decrease the S content of the used 10Mo₂C/APC catalyst since the agglomerated particles would reduce the number of surface Mo₂C sites exposed to S. Also, there are more edge sites on smaller particles, which will enhance S adsorption and incorporation on the catalyst surface [174]. The line scan and EDX mapping (Figure 5.7) show the close correlation between Mo and S concentration. However, from the TEM image the MoS₂ layers appear as patches on top of Mo₂C particles, rather than fully developed overlayers of MoS₂ that cover the Mo₂C, as proposed by Aegerter et al. [124]. Also, the MoS₂-Mo₂C morphology is quite different from the core-shell (Mo₂C-MoS₂) structure on Ni-Mo₂C catalyst, reported previously in Chapter 3 [160].

From Figure 5.4, we observe that the activity change can be divided into two stages: (i) an initial deactivation period of about 150 mins; and (ii) a stabilized period where conversion and selectivity remain constant with TOS. This study reveals that the active sites of the Mo₂C catalysts in stage (ii) must be similar to those present on MoS₂ catalysts, since the catalyst selectivities were identical. As reported in the literature [103, 175], MoS₂ catalysts usually have a low CO uptake, which is consistent with the used Mo₂C catalyst CO uptake reported in Table 5.3.

Since the deactivation stage is relatively short and not easy to associate with catalyst characterization measurements, the effect of sulfur residue and C-S replacement on the catalyst surface was simulated through DFT calculation. Firstly, the adsorption energy of DBT on clean Mo₂C (101) surface has been calculated. Figure E.21 (Appendix E.4) shows one terminal Mo site (labeled as Mo-t1) and two terminal C sites (C-t1 and C-t2, respectively) used in the analysis. Table E.4 (Appendix E.4) summarizes the adsorption of DBT on the clean Mo₂C (101) surface, the most stable surface of Mo₂C. Two modes of adsorption have been examined; vertical adsorption (V) and horizontal adsorption (H) each with two different orientations relative to the surface. These modes are identified DBT-V1, DBT-V2, DBT-H1, and DBT-H2 respectively. To better compare the DBT binding energies, we assume Mo-S bonding between Mo-t1 and the S from DBT in all cases. The calculation results show that DBT-H1 and DBT-H2 have stronger adsorption energies, with values of -1.53 eV and -1.58 eV, respectively, than that of DBT-V1 and DBT-V2, with values of -0.94 eV and -1.01 eV, respectively. Hence horizontal adsorption of DBT on the clean Mo₂C (101) surface is most favourable. This result is consistent with the experimental selectivity data at the beginning of the reaction that show no BPh formation, a

product of the DDS of DBT (Figure 5.8). Secondly, at the beginning of the reaction, the high activity of Mo₂C results in rapid conversion of DBT and further reaction of primary products. At the beginning of the reaction period, the Mo₂C's (101) surface is free of S and horizontal adsorption of DBT is favoured over vertical adsorption, according to the DFT analysis. Horizontal adsorption of DBT means that ring hydrogenation will occur prior to S removal from DBT, i.e., the DBT conversion through the HYD route will be preferred. Vertical adsorption of DBT will yield direct breakage of the C-S bond and DBT conversion by the DDS route [176]. The DFT analysis shows that the horizontal adsorption energy for DBT is as high as -1.58 eV, higher than -1.3 eV for DBT adsorption on MoS₂ surface [176].

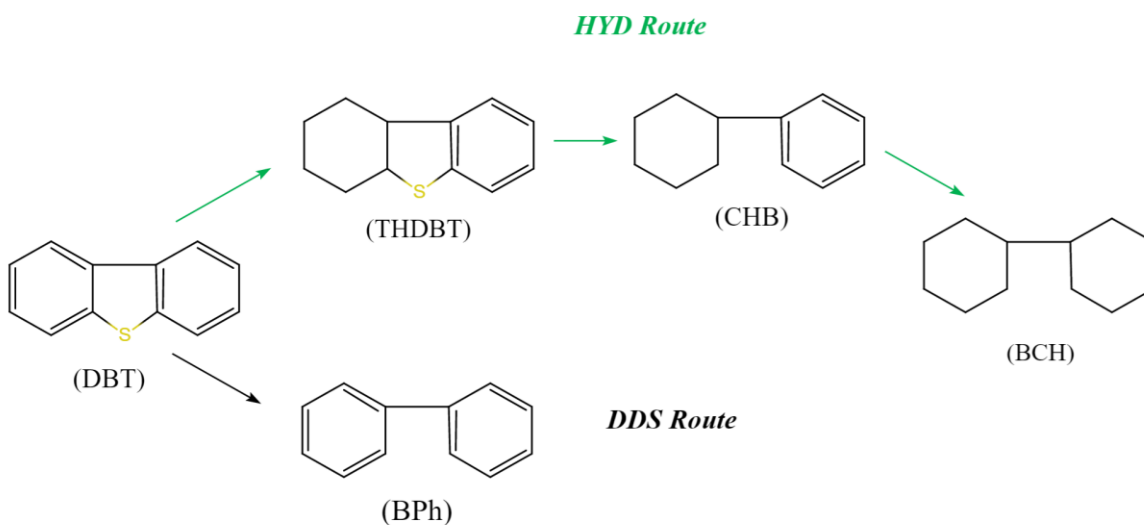


Figure 5.8: Simplified reaction pathway of dibenzothiophene HDS via HYD and DDS routes over all Mo₂C/APC catalysts with different Mo loadings.

Shortly after the beginning of the reaction, either S adsorption on the Mo₂C surface or S incorporation occur and result in a change in product selectivity as shown by the experimental

data of Figure 5.4. This change was completed within about 150 mins; whereas, the analysis of the used catalyst was done after a TOS of about 600 mins. Hence DFT was used to assess the impact of S deposition on the Mo_2C catalyst that would occur during the very initial stages of the DBT reaction. Since transition of the Mo_2C structure to MoS_2 is unlikely to occur at the beginning of the reaction, it is reasonable to assume that the selectivity change initially is caused by adsorption of sulfur from DBT on the Mo_2C surface. Table E.5 presents the adsorption of DBT on the same Mo site (Mo-t1) of the Mo_2C (101) surface but with a pre-adsorbed S atom located on-top the C-t1 site. Note that because of steric hindrance effects, only DBT-V1 and DBT-H1 adsorption orientations were evaluated. The results show that the adsorption energy of horizontal position is significantly lower than that of the clean Mo_2C surface, which may explain the loss in activity observed during the HDS reaction; whereas, the energy of the vertical adsorption is slightly higher than that of the clean Mo_2C surface. This indicates that the direct desulphurization route (DDS) is more favoured on the S- Mo_2C (101) adsorbed surface, as observed experimentally and reported in Figure 5.4.

After 600 min TOS and stabilized selectivity and conversion, MoS_2 formation is confirmed by multiple characterization methods. Since the catalyst characterization confirmed that S can change the Mo_2C structure and form MoS_2 species, S replacement of the carbon of Mo_2C must occur. Hence, DFT calculations to assess DBT adsorption on the Mo_2C (101) surface with different degrees of S replacement have been completed. Figure E.22 presents the C atoms replaced by S on the Mo_2C (101) surface with different degrees of S replacement. Three different replacements of S were assessed, as shown in Table 5.6 and Figure E.22 (Appendix E.4), where X indicates the number of S atoms' replaced on the surface. The calculations indicate that the S

replacement decreases the DBT adsorption strength on the Mo₂C (101) surface. In the case where C is replaced by S at the C-t1 position, even though the activity is reduced, horizontal adsorption still dominates (Table 5.6, 1S and 2S replacement). However, at the C-t2 position, with one more carbon being replaced, the S atom is raised from the surface making the horizontal adsorption impossible; whereas, it enhances the vertical adsorption of DBT (Appendix E.4-Table E.4 and Table 5.6, 3 S replacement). Hence, the DDS selectivity is favoured as the S incorporation increases above a certain concentration.

Table 5.6: The calculated Gibbs free adsorption energy of DBT on S replaced Mo₂C (101) surface with different adsorption angles.

Adsorption orientation	Gibbs free Adsorption energy with X (0~3) S replacement (eV)			
	0S ^a	1S	2S	3S
DBT-H1 ^b	-1.53	-1.41	-1.34	-0.89
DBT-H2	-1.58	-1.55	-1.32	-0.30
DBT-V1	-0.94	-1.07	-1.27	-0.53
DBT-V2	-1.01	-0.86	-0.67	-1.10

a. 0S represents clean (101) Mo₂C surface; 1S means one C-t1 was replaced by one S atom; 2S means two C-t1 were replaced by two S atoms; 3S means two C-t1 and one C-t2 were replaced by three S atoms.

b. Adsorption of DBT in a horizontal 1 (DBT-H1); Adsorption of DBT in a vertical 1 (DBT-V1).

Dissociative adsorption of H₂ on the Mo₂C (101) surface was also assessed on the Mo-t1. Figure E.23 shows the molecular adsorption of H₂ on Mo-t1 site, followed by dissociative adsorption on a nearby bridge site of the clean Mo₂C (101) surface, with S adsorbed on the C-t1 site, and with C-t1 site replaced by a S atom. The potential energy trends of dissociative adsorption of H₂ on

these three surfaces is also reported. The calculated energy barrier (E_a) for H_2 dissociative adsorption on clean Mo_2C (101) surface is about 0.28 eV (calculated by $-0.12 - (-0.40) = 0.28$), much lower than the barrier energy on conventional hydrotreating catalysts, MoS_2 ($10\bar{1}0$) Mo-edge site reported as 0.91 eV [177]. In addition to relatively low energy barrier for H_2 dissociative adsorption, the overall dissociative process (E_r) is exothermic at -0.53 eV (Calculated by $-0.93 - (-0.40) = -0.53$), higher than most cases on pure metal surfaces such as Co (0001) with -1.07 eV [178]; whereas, it is better than NiMoS, which is slightly endothermic (0.17 eV), or CoMoS, which is -0.15 eV. Figure E.23 shows that during the HDS reaction the energy barrier for dissociative adsorption of H_2 becomes higher with either S atom adsorbed on top of C or S replacing C. Either way the reaction becomes less likely, especially in the S adsorbed case where the dissociative adsorption state is unstable (> 0 eV). As a result, the hydrogenation ability of Mo_2C decreases during the HDS reaction possibly acting as one of the factors that cause the observed activity drop.

5.5 Conclusions

Different Mo loading Mo_2C/APC catalysts prepared at the same reduction temperature have different Mo_2C particle sizes, yet similar concentrations of Mo surface species. Reduction temperature is the crucial factor that determines the degree of Mo_2C formation from the precursor; whereas, the particle size primarily depends on the catalyst Mo loading. At the beginning of the HDS of DBT, the catalyst activity is very high and the HYD selectivity changes due to the adsorption of S species on Mo_2C surface. This change continues to develop as the adsorption and replacement of C by S continues. Finally, both selectivity and activity reach a stable state, while selectivity tends towards DDS products. Faster deactivation occurs on larger

particles. The $\text{Mo}_2\text{C} \rightarrow \text{MoS}_2$ transition is simulated with DFT calculation, and the change in DBT adsorption geometry follows the observed changes in product selectivities. After reaching a stable state, the Mo_2C surfaces are mostly covered by MoS_2 species according to XPS and TEM results.

Chapter 6: The Effect of Other Heteroatoms (N and O) on Mo₂C/APC

Catalysts

6.1 Introduction

Following Chapter 5, this chapter was conducted as an exploratory study of the effect of other heteroatoms (N and O) on the performance of Mo₂C/APC catalysts during hydrodenitrogenation (HDN) and hydrodeoxygenation (HDO) reactions, respectively. For the HDN study, carbazole (CBZ) was chosen as a model reactant because it has a similar structure to DBT, providing an opportunity to directly compare the impact of the N versus S on the reaction and the catalyst stability. Similarly, for the HDO reaction, dibenzofuran (DBF) was chosen as reactant, consistent with the reactants used for HDS and HDN.

6.2 Experimental

The experimental methods follow those described in Chapter 5. The reaction was conducted at 350 °C and with a constant pressure of 4.1 MPa in a packed bed reactor. The synthesis of Mo₂C/APC catalysts used in this chapter was the same as that described in Chapter 5. In addition, catalyst characterization methods followed those described in Chapter 5. The model compounds used in this chapter were carbazole (CBZ) and dibenzofuran (DBF), representing the N and O containing reactants typical of HDN and HDO processes, respectively.

6.3 Results and Discussion

6.3.1 Catalyst Activities in HDN of Carbazole

The Mo₂C/APC catalysts described in Chapter 5 with various particle sizes were tested for the HDN of carbazole with a carbazole concentration of ~ 0.2 wt.%, equivalent to 150 ppm N in the feed oil. As reported in the literature [51, 179], carbazole is a refractory N-containing compound.

Several products and intermediates were detected from the GC-MS product analysis as shown in Figure 6.1 and Table 6.1. For simplicity, the products are grouped into five categories, based on the reaction that generated the product. The product generated from direct denitrogenation (DDN) route is cyclohexylbenzene (CHB), which is produced following the hydrogenation of one aromatic ring of CBZ. The hydrogenation (HYD) route proceeds by hydrogenation of two rings, where cyclohexyl-cyclohexene (CHCHE) and bicyclohexyl (BCH) are the main products. The subsequent reaction is the isomerization of BCH to cyclopentylmethyl-cyclohexane (CPCHX) and hexylcyclohexane (HCH) along with the cracking reaction.

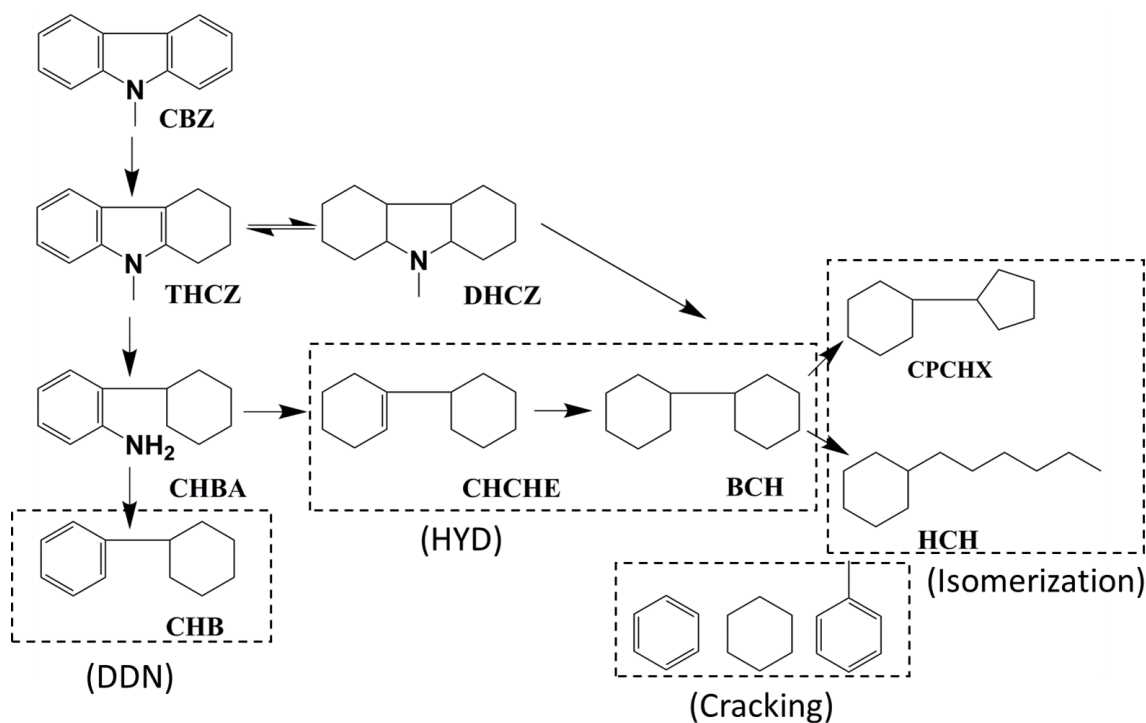


Figure 6.1: Reaction network of hydrodenitrogenation of carbazole over $\text{Mo}_2\text{C}/\text{APC}$ catalyst.

Table 6.1: Identified products from HDN of carbazole with $\text{Mo}_2\text{C}/\text{APC}$ catalysts at 350 °C and 4.1 MPa.

Symbol	Product name	Reaction route
CHB	Cyclohexylbenzene	Route of DDN
THCZ	Tetrahydrocarbazole	N-containing product
CHBA	2-Cyclohexyl-benzenamine	N-containing product
DHCZ	Dodecahydro-1H-carbazole	N-containing product
CHCHE	Cyclohexyl-cyclohexene	HYD
BCH	Bicyclohexyl	HYD
CPCHX	Cyclopentylmethyl-cyclohexane	Isomerization
HCH	Hexylcyclohexane	Isomerization
	Benzene, Cyclohexane, Toluene	Cracking products

Similar to the results reported by Szymanska et al. [51], there was no BPh detected in this study. Almost all the obtained products were generated from the hydrogenation of the aromatic rings followed by ring opening and cracking reactions to produce the relevant isomerization and cracked products. There were also some products detected that retained the N-atom, indicating incomplete denitrogenation.

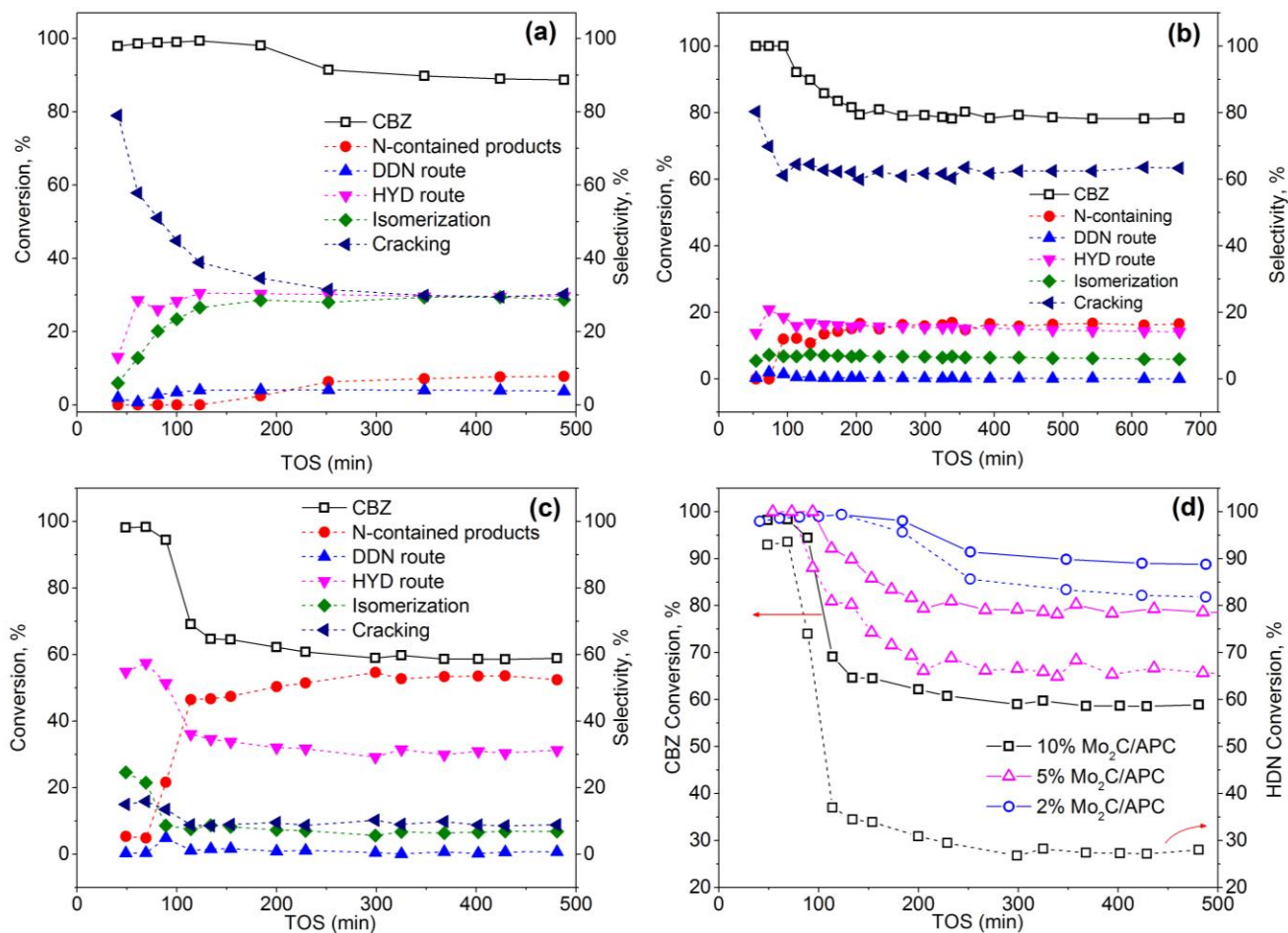


Figure 6.2: CBZ conversion and selectivity of Mo₂C/APC catalysts with different Mo loadings with time on stream. (Mo loading held constant at 0.019 g in the reactor): (a) 2Mo₂C/APC; (b) 5Mo₂C/APC; (c) 10Mo₂C/APC; and (d) CBZ conversion and HDN conversion for Mo₂C/APC catalysts with different Mo loadings as a function of TOS.

Figure 6.2 reports the carbazole conversion and product selectivity of the Mo₂C/APC catalysts with various Mo loadings and corresponding particle sizes, measured at 350 °C and 4.1 MPa in the packed bed reactor. The data clearly show that the conversion of CBZ was relatively high in the initial stages of the reaction for all catalysts. However, the conversion decreased with time on stream (TOS). This observation is similar to what was observed during the HDS of DBT and reported in Chapter 5. The CBZ conversion decreased from 98% to 90% on the 2%Mo₂C/APC catalyst; whereas, it decreased from 95% to 60% for the 10%Mo₂C/APC catalyst, suggesting that the smaller the particle size, the higher the stabilized CBZ conversion.

Figure 6.2 (d) clearly shows a difference between the CBZ conversion and HDN conversion at steady-state; where, this difference between the two represents the N-containing reaction products generated during the HDN reaction. For example, the difference is about 8% ($\frac{90-83}{90}$ %) for the 2%Mo₂C/APC catalyst; whereas, it increased to 54% ($\frac{59-27}{59}$ %) for the 10%Mo₂C/APC catalyst. The higher HDS activity compared to the HDN activity of the Mo₂C/APC catalysts, reflects the difficulty of removing N completely compared to S because of the higher bond energy of C-N versus C-S [180]. In addition, unlike the HDS reaction, HDN usually proceeds through a hydrogenation route prior to C-N bond cleavage. The presence of N may decrease the hydrogenation ability of Mo₂C, suggesting a detrimental effect of N on the Mo₂C surface. Furthermore, it is noted that the required time to reach a steady-state is independent with Mo₂C catalyst particle size, which is similar to the HDS reaction.

Table 6.2: Conversion and product selectivity for HDN of CBZ over Mo₂C/APC catalysts at 350 °C and 4.1 MPa.

Catalyst	Conversion of CBZ (%) ^a	HDN conversion of CBZ (%) ^b	Selectivity (%) ^a				
			N-contained products	DDN route	HYD products	Isomerization	Cracking
2Mo ₂ C/APC	89.75	83.26 ^b	7.23 ^a	3.92 ^a	29.74 ^a	28.86 ^a	30.25 ^a
5Mo ₂ C/APC	78.49	65.64	16.38	0.12	14.62	6.19	62.69
10Mo ₂ C/APC	58.67	27.45	53.21	0.55	30.62	6.65	8.97

a. The conversion and selectivity were obtained by the average number at steady-state.

b. The HDN conversion of CBZ represented the percentage of N removed products from the initial reactant.

Figure 6.2 (a-c) also shows the selectivity change of Mo₂C/APC catalysts with time on stream. Taking 2Mo₂C/APC catalyst as an example, the data clearly show a decrease in cracking products with TOS compared to the beginning of the reaction. The increase in N-containing products stabilized after ~250 min, indicating the complete transformation of the 2Mo₂C/APC catalyst. On the 10Mo₂C/APC catalyst, cracking, isomerization and HYD products all decreased and there was an obvious increase in N-containing products at the very beginning of the reaction (~100 min).

Table 6.3: The calculated decay constants (k_d) of Mo₂C/APC catalysts with various metal loadings in HDN of carbazole at 350 °C and 4.1 MPa.

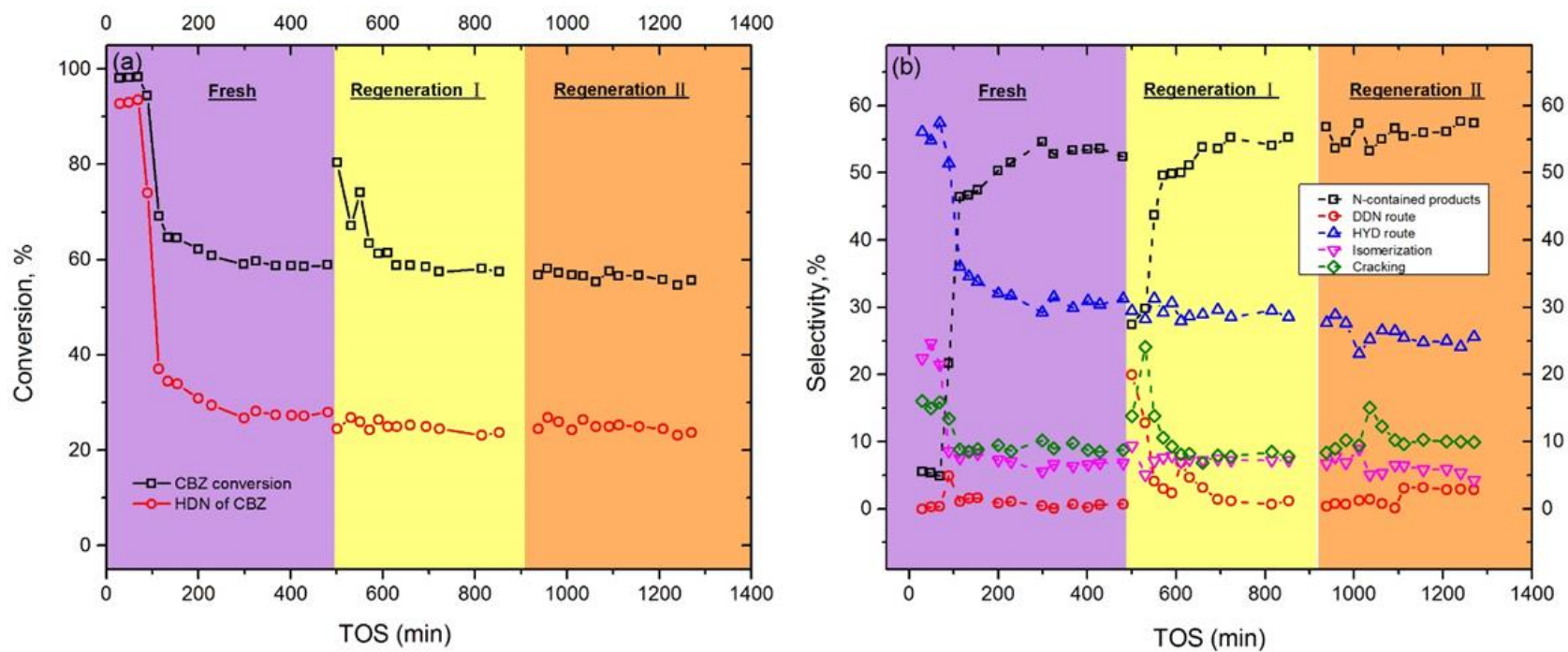
Catalyst	k _d (h ⁻¹) ^a	R ²
2Mo ₂ C/APC	3.70E-03±5.83E-04	0.97
5Mo ₂ C/APC	5.62E-03±3.14E-04	0.98
10Mo ₂ C/APC	2.26E-02±2.72E-03	0.90

a. The decay constant was calculated based on exponential decay equation: $-\frac{da}{dt} = k_d a$

Similar to the effect of S reported in Chapter 5, the relative decay constants (k_d) were calculated for the HDN reaction and these are reported in Table 6.3. The effect of N showed an increased deactivation rate with increased Mo₂C particle size, similar to the trend observed during HDS. Moreover, the N poison effect is much stronger than that of S for smaller particle size Mo₂C catalysts, including 2Mo₂C/APC; whereas, there is no significant difference in the HDN and HDS deactivation rates on 10Mo₂C/APC catalyst.

After observing the serious drop of catalyst activity in HDN of CBZ, a H₂ reduction process was applied on the used Mo₂C/APC catalyst as a way to regenerate the used catalyst. Considering the properties of the synthesized catalyst, the regeneration was conducted under pure H₂ flow of 100 mL (STP)/min at 400 °C for 2 h, consistent with the process conditions used to remove the catalyst passivation layer after synthesis. The corresponding experimental data are reported in Figure 6.3. It can be observed that after the 1st regeneration, the catalyst performance improved marginally at the beginning of the regeneration (Figure 6.3, phase I regeneration). However, the catalyst activity did not return to the activity of the fresh 10Mo₂C/APC catalyst. Furthermore, the CBZ conversion decreased to the same level as that of the stabilized fresh Mo₂C catalyst. After the phase II regeneration period shown in Figure 6.3, there was no further recovery of the catalyst performance, indicative of the irreversible effects of N on Mo₂C/APC catalyst surface modification. Also, the product selectivity at steady-state did not change significantly among the fresh catalyst and after the two regeneration periods, as shown in Figure 6.3 (b). As reported in Zheng et al. [6], the N atoms tend to occupy some subsurface sites of Mo₂C, thus the nitridation of carbide can be initiated during ammonia decomposition.

Figure 6.3: Catalyst regeneration (Phase I and II) of 10%Mo₂C/APC after HDN reaction of carbazole: (a) Conversion of CBZ; and (b) Selectivity of the products.



6.3.2 Catalyst Activities in HDO of Dibenzofuran

The O effect on the Mo₂C/APC catalyst has also been studied using dibenzofuran (DBF) as the model reactant. The same reaction conditions as those used for the HDS and HDN reactions were applied for the HDO. The HDO reaction usually occurs through two kinetically significant pathways: DDO and HYD as shown in Figure 6.4. The obtained products can be grouped into several categories as listed in Table 6.4.

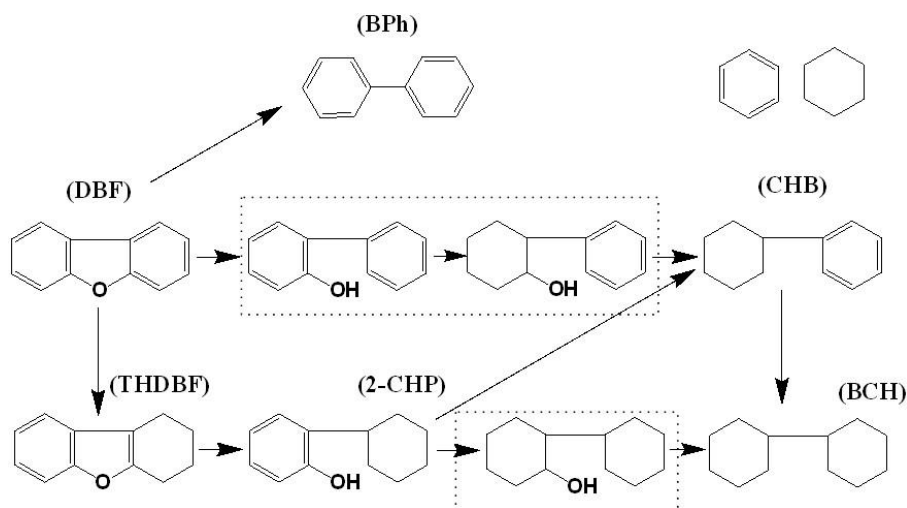


Figure 6.4: Reaction network of hydrodeoxygenation of dibenzofuran over Mo₂C/APC catalyst.

Table 6.4: Identified products from HDO of dibenzofuran with Mo₂C/APC catalysts at 350 °C and 4.1 MPa.

Symbol	Product name	Grouped route
BPh	Biphenyl	DDO
CHB	Cyclohexylbenzene	HYD
BCH	Bicyclohexyl	HYD
CH	Cyclohexane	HYD
2-CHP	Phenol, 2-cyclohexyl-	O-containing products
THDBF	Tetrahydrodibenzofuran	O-containing products
	Benzene, Cyclohexane	Cracking products

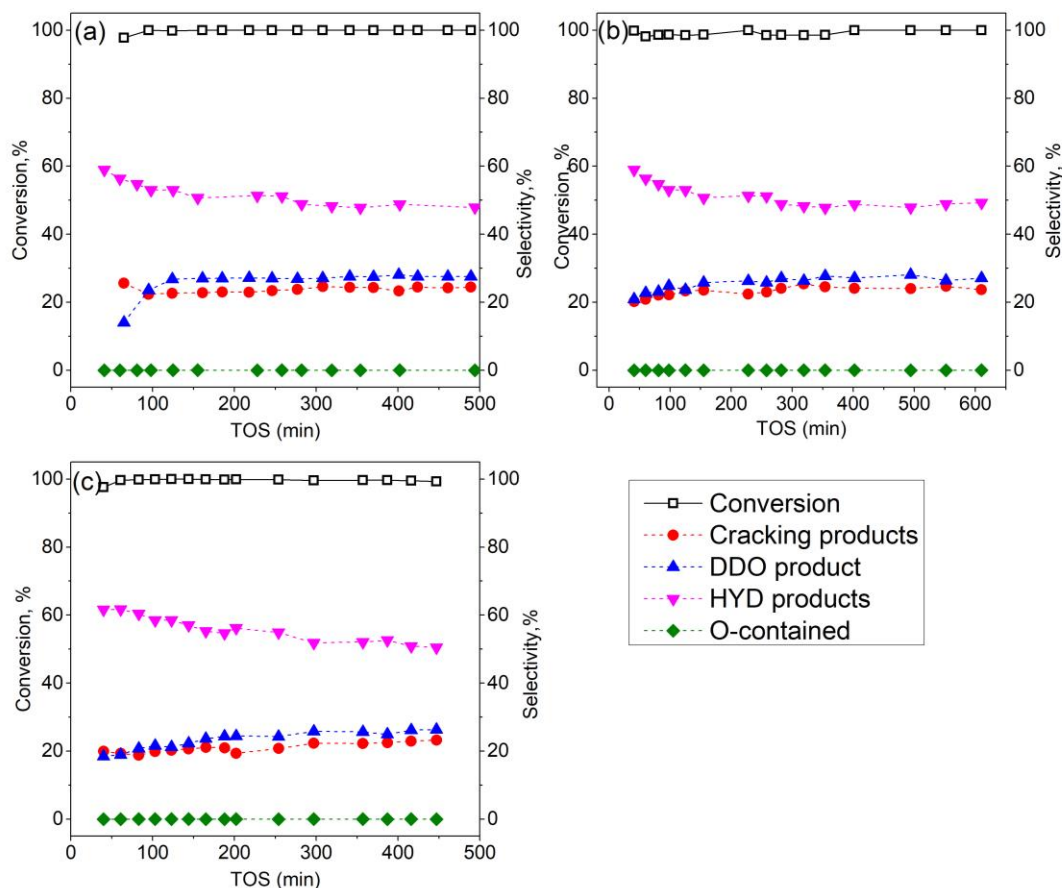


Figure 6.5: DBF conversion and selectivity of $\text{Mo}_2\text{C}/\text{APC}$ catalysts with different Mo loadings with time on stream. (Mo loading held constant at 0.019 g in the reactor): (a) $2\text{Mo}_2\text{C}/\text{APC}$; (b) $5\text{Mo}_2\text{C}/\text{APC}$; and (c) $10\text{Mo}_2\text{C}/\text{APC}$.

Figure 6.5 shows the performance of $\text{Mo}_2\text{C}/\text{APC}$ catalysts with various Mo loadings for the HDO of dibenzofuran (DBF; equiv. 170 ppm O). The data show that DBF is completely converted for all three catalysts at 350 °C, 4.1 MPa and LHSV = 4 h⁻¹. However, the selectivity shows a different trend. For the 2% $\text{Mo}_2\text{C}/\text{APC}$ catalyst (Figure 6.5 (a)), the HYD product-CHB decreased from ~55% to ~38%, while there was an obvious increase in BPh from ~15% to 27%.

Also note that the selectivity reached a relatively stable status after 150 min of HDO reaction. For the 10%Mo₂C/APC catalyst (Figure 6.5 (c)), the time taken to reach steady-state is longer at ≥ 400 min. Moreover, it is interesting to observe that all catalysts reach the similar selectivity, independent of the Mo₂C particle size. This result shows that larger particles are less prone to surface oxidation and hence have the ability to reduce oxidation. A similar phenomenon was also reported by Stellwagen et al. [168].

6.4 Conclusion

The effect of reactants containing N and O atoms on Mo₂C catalysts with different particle sizes have been studied during hydrotreating. N has a detrimental effect on Mo₂C performance and results in irreversible catalyst deactivation; whereas, the effect of O is reversible. Moreover, the impact of these three atoms on catalyst deactivation severity can be arranged in decreasing order as $N > S > O$.

Chapter 7: Conclusions and Recommendations

7.1 Conclusions

The main contribution from this study is the synthesis of a mesoporous carbon supported Mo_2C catalyst, derived from Canadian oil sands petroleum coke and the successful application of these catalysts in several hydrotreating reactions.

The first part of the study was conducted using a commercial activated charcoal (AC) to assess the viability of carbon supported Mo_2C catalyst synthesis. This study showed the successful preparation of $\text{Mo}_2\text{C-MoO}_x\text{C}_y/\text{AC}$ catalysts at relatively low temperature (600~800 °C). The corresponding catalysts prepared at different reduction temperatures were tested for the HDO of 4-methylphenol at 350 °C and 4.3 MPa H_2 . Catalyst screening identified the optimal $\text{Mo}_2\text{C}/\text{AC}$ catalyst with a CHR temperature of 650 °C based on catalytic activity. Also, both Mo_2C and MoO_xC_y function as active sites and the formation of these active sites is the result of O adsorption and/or exchange with the catalyst during HDO. The kinetics was closely related to the amount of $\text{Mo}_2\text{C}/\text{MoO}_x\text{C}_y$ active sites. Moreover, a high DDO selectivity was identified.

The application of $\text{Mo}_2\text{C}/\text{AC}$ catalysts was extended to HDS and the effect of Ni addition to the $\text{Mo}_2\text{C}/\text{AC}$ was determined. The addition of Ni reduced the CHR temperature required for Mo_2C generation by ~100 °C. A phase separation occurred when the Ni:Mo ratio was > 0.38, resulting in decreased catalyst activity. The highest HDS activity occurred for the catalysts with Ni:Mo ratios of 0.38 and 0.19, when prepared at the relatively low CHR temperature of 550 and 600 °C. Sulfidation of the Ni- $\text{Mo}_2\text{C}/\text{AC}$ catalysts occurred during reaction in 2.0 wt% dibenzothiophene (DBT) at 350 °C and 2.1 MPa H_2 . The uptake of S was enhanced with increased Ni content,

resulting in the formation of Mo₂C-MoS₂ core-shell structures. The stacking height of the MoS₂ shell increased with increased Ni content and promoted the direct desulfurization of DBT.

The synthesis of Mo₂C on activated petroleum coke (APC) was also investigated, with a focus on mesopore development. From the previous study using AC, it was known that CHR temperature is an important variable for Mo₂C synthesis. Therefore, a series of APC supported catalysts were prepared by varying the CHR temperature from 500 to 800 °C, to yield mesoporous Mo₂C/APC catalysts. The transition of Mo species (MoO_x → MoO_xC_y → Mo₂C) was identified as a function of CHR temperature. The generated Mo₂C species had a significant effect on CH₄ generation, which in turn modified the physical structure of APC. The maximum mesopore volume was achieved at a CHR temperature of 750 °C, with 37% of the total pore volume appearing as mesopores. A longer CHR hold time facilitates total pore/mesopore volume development. The 4-methylphenol HDO activity of the synthesized Mo₂C/APC catalysts was relatively high compared with Mo₂C/AC catalysts and the activity increased with increased mesoporosity.

The impact of S on Mo₂C/APC catalyst activity was also investigated for a series of catalysts with varying Mo₂C loadings and hence particle size. XPS results of the fresh catalysts showed an invariant Mo composition with different Mo catalyst loading, where a constant ~40% of Mo₂C species was achieved. Analysis of the used catalysts after the HDS of DBT showed that a patchy MoS₂ surface structure was formed on top of the Mo₂C. Initial catalyst deactivation was observed for all catalysts and the HDS activities decreased with increased particle size of the Mo₂C. DFT was used to demonstrate the significant effect of S adsorbed on Mo₂C (101) and S substituted on

the Mo₂C (101) surface, on the adsorption of DBT. The calculated results were consistent with the observed selectivity shift during DBT HDS from HYD to DDS products.

Finally, an exploratory study was conducted of the effect of the two heteroatoms N and O. The model reactants carbazole (CBZ) and dibenzofuran (DBF), having similar structure to DBT but for the presence of N or O in place of the S atom, were used to assess the impact of the heteroatom on the activity and stability of the Mo₂C/APC catalysts. N has a stronger deactivation effect than S, and the deactivation was irreversible even after H₂ regeneration. Most of the active sites for hydrogenation were poisoned by the presence of N. For HDO higher activity (almost 100% conversion) was observed and the selectivity changed with time on stream, with decreasing hydrogenation and increasing direct deoxygenation. Hence one concludes that the O can modify the catalyst surface but the modification is reversible and the formed species (MoO_xC_y) are active for HDO reaction.

7.2 Recommendations

7.2.1 Mo₂C Catalyst Properties

Since Mo₂C is air-sensitive, all the catalyst samples of the study were handled in two ways: (a) passivation; (b) fast transfer in a N₂ glove bag, to minimize the effects of air exposure. As reported in Chapter 2, there is a large difference between passivated Mo₂C catalysts and fresh catalysts, based on the measured CO uptake data. Thus, it is important to consider in-situ catalyst characterization techniques to monitor the catalyst surface change during reaction, without exposure to air, which will provide more insight into catalyst property-activity relationships. Examples include FT-IR analysis of probe molecule adsorption (CO, for example) using a

DRIFTS reaction cell that would allow reactions on samples to be followed by adsorption experiment without exposing the catalyst to the atmosphere. In addition, an XPS unit with a high pressure chamber and sample transfer station would allow surface analysis of fresh catalysts and catalysts after exposure to different reactants to be completed without air exposure of the catalyst sample. Furthermore, electron energy loss spectroscopy (EELS) is a good characterization method to determine the oxide state of a material. Thus, we can further apply EELS to clearly identify the Mo oxycarbide species present in the catalysts.

7.2.2 Promoter Effect in HDS Reaction

Ni addition was shown to significantly decrease the CHR temperature required for Mo₂C formation by 100 °C. In future work, other promoters should be explored, especially Co, since it is another commonly used promoter in conventional Co (Ni)MoS/Al₂O₃ hydrotreating catalysts. In preliminary work completed during the present study, Co was less effective than Ni for Mo₂C catalyst generated by CHR at 550 °C, but other synthesis conditions need to be explored to determine the best synthesis conditions.

Also, since the data reported in Chapter 3 were based on activated charcoal (AC), it is recommended that APC be used as a support of the Ni-Mo₂C catalyst, to determine the impact of the carbon supports. In addition, based on the data reported in Appendix H-Table H.2, Ni-Mo₂C catalyst has a significant effect on the APC mesopore development. A further study should be conducted to determine how the various metal/metal carbide active sites contribute to the pore development.

7.2.3 Deactivation of Mo₂C and Ni-Mo₂C in HDS

As reported in Chapters 3 and 5, both Mo₂C and Ni-Mo₂C catalysts supported on carbon deactivated in the presence of S. For the Mo₂C/APC catalyst, patches of MoS₂ were formed on top of the Mo₂C during HDS; whereas, for Ni-Mo₂C/AC, a core-shell structure was formed. Both structures have catalytic activity in HDS, although all are less effective than the fresh Mo₂C. One possible approach to limit the transformation of the Mo₂C is to encapsulate the Mo₂C into a frame/shell structure that would prevent direct S contact with the Mo₂C, thereby improving catalyst stability [181].

In Chapter 5, the transition of Mo₂C/APC catalyst in the presence of S was studied. In future work, the deactivation study should be expanded to Ni-Mo₂C/APC to compare the performance between these two APC supported catalysts. Considering the results in Chapter 3, it was shown that Ni-Mo₂C/AC deactivated faster than Mo₂C/AC in HDS of DBT. If it also occurs on Ni-Mo₂C/APC, some experiments need to be designed to capture the faster transition, such as reducing the reactant concentration and decreasing the reaction temperature.

7.2.4 Effect of N and O on Mo₂C Catalysts

In Chapter 6, the deactivation of Mo₂C catalysts in the presence of N during HDN was demonstrated. However, no relevant characterization data were obtained that could clarify the changes in catalyst morphology and/or the surface chemical and physical properties that could account for the deactivation. Several characterization methods have been proposed here which can be applied in future work: (1) CHNS analyzer can be used to measure the bulk concentration of N on the used Mo₂C/APC catalyst, which provides an idea of how much N is left on the catalyst.

(2) Pyridine can be used as the N reactant in FT-IR measurement since it is easier to be evaporated/removed. After pyridine treatment, a high vacuum can be applied to remove all the physically adsorbed N species. Followed by this, CO can be used as the probe molecule to measure the N-modified Mo₂C/APC surface. (3) NH₃-TPD is another potential method to measure the N on Mo₂C/APC catalyst. It will provide an idea as to how N interacts with Mo₂C species. (4) Electron energy-loss spectroscopy (EELS) will be a potential technique as well to study the N modification on Mo₂C catalyst [6]. (5) DFT calculation can be applied to the N adsorbed Mo₂C catalyst, similar to the S study as illustrated in Chapter 5, to explore the catalyst poisoning by N. For the O study, since we didn't see any deactivation at present conditions, the experimental conditions should be adjusted to capture this change. Besides, some small molecules should be considered, such as pyridine and furan to see if this deactivation is related to molecular structure.

Additionally, it is recommended that to apply Mo₂C/C catalyst into real bio-oil upgrading study due to the good performance and coke resistant ability.

7.2.5 Mesoporous Carbon Applications

From the study of Chapter 2 that demonstrated the successful preparation of a mesoporous carbon material and an application in HDO of 4-methylphenol reaction, further study to utilize the mesoporous carbon as an adsorbent or electrode material is worth investigating. Also, this can be extended to other catalyst (MoS₂/APC) synthesis based on the mesoporous structure. Due to the coke resistant ability of carbon supported catalyst, it is worth to utilize it in heavy oil upgrading. The used C based catalyst should be easily recycled and regenerated after several

cycles' utilization. The properties of the used catalyst can be compared with the coke-catalyst mixture formed in slurry-phase residue hydroconversion as reported in our group's previous work [182].

Bibliography

1. R.B. Levy and M. Boudart, Platinum-like behavior of tungsten carbide in surface catalysis. *science*, 1973. 181(4099): p. 547-549
2. S.T. Oyama, Preparation and catalytic properties of transition metal carbides and nitrides. *Catalysis Today*, 1992. 15(2): p. 179-200.
3. D.J. Sajkowski and S.T. Oyama, Catalytic hydrotreating by molybdenum carbide and nitride: unsupported Mo₂N and Mo₂C/Al₂O₃. *Applied Catalysis A: General*, 1996. 134(2): p. 339-349.
4. F.H. Ribeiro, M. Boudart, R.A. Dalla Betta, and E. Iglesia, Catalytic reactions of n-Alkanes on β -W₂C and WC: The effect of surface oxygen on reaction pathways. *Journal of Catalysis*, 1991. 130(2): p. 498-513
5. C. Bouchy, C. Pham-Huu, B. Heinrich, C. Chaumont, and M.J. Ledoux, Microstructure and Characterization of a Highly Selective Catalyst for the Isomerization of Alkanes: A Molybdenum Oxycarbide. *Journal of Catalysis*, 2000. 190(1): p. 92-103.
6. W. Zheng, T.P. Cotter, P. Kaghazchi, T. Jacob, B. Frank, K. Schlichte, W. Zhang, D.S. Su, F. Schüth, and R. Schlögl, Experimental and Theoretical Investigation of Molybdenum Carbide and Nitride as Catalysts for Ammonia Decomposition. *Journal of the American Chemical Society*, 2013. 135(9): p. 3458-3464.
7. K.D. Sabnis, M.C. Akatay, Y. Cui, F.G. Sollberger, E.A. Stach, J.T. Miller, W.N. Delgass, and F.H. Ribeiro, Probing the active sites for water–gas shift over Pt/molybdenum carbide using multi-walled carbon nanotubes. *Journal of Catalysis*, 2015. 330: p. 442-451
8. J.A. Schaidle, A.C. Lausche, and L.T. Thompson, Effects of sulfur on Mo₂C and Pt/Mo₂C catalysts: Water gas shift reaction. *Journal of Catalysis*, 2010. 272(2): p. 235-245.

9. W.F. Chen, C.H. Wang, K. Sasaki, N. Marinkovic, W. Xu, J.T. Muckerman, Y. Zhu, and R.R. Adzic, Highly active and durable nanostructured molybdenum carbide electrocatalysts for hydrogen production. *Energy & Environmental Science*, 2013. 6(3): p. 943-951.
10. J.S. Lee and M. Boudart, Hydrodesulfurization of thiophene over unsupported molybdenum carbide. *Applied Catalysis*, 1985. 19(1): p. 207-210.
11. A. Hynaux, C. Sayag, S. Suppan, J. Trawczynski, M. Lewandowski, A. Szymanska-Kolasa, and G. Djéga-Mariadassou, Kinetic study of the hydrodesulfurization of dibenzothiophene over molybdenum carbides supported on functionalized carbon black composite: Influence of indole. *Applied Catalysis B: Environmental*, 2007. 72(1-2): p. 62-70.
12. J.A. Schaidle, N.M. Schweitzer, O.T. Ajenifujah, and L.T. Thompson, On the preparation of molybdenum carbide-supported metal catalysts. *Journal of catalysis*, 2012. 289: p. 210-217
13. Y. Chen, S. Choi, and L.T. Thompson, Low temperature CO₂ hydrogenation to alcohols and hydrocarbons over Mo₂C supported metal catalysts. *Journal of Catalysis*, 2016. 343: p. 147-156
14. J. Lee, S. Oyama, and M. Boudart, Molybdenum carbide catalysts: I. Synthesis of unsupported powders. *Journal of Catalysis*, 1987. 106(1): p. 125-133.
15. T. Xiao, A.P.E. York, V.C. Williams, H. Al-Megren, A. Hanif, X. Zhou, and M.L.H. Green, Preparation of Molybdenum Carbides Using Butane and Their Catalytic Performance. *Chemistry of Materials*, 2000. 12(12): p. 3896-3905.
16. P.D. Costa, C. Potvin, J.-M. Manoli, B. Genin, and G. Djéga-Mariadassou, Deep hydrodesulphurization and hydrogenation of diesel fuels on alumina-supported and bulk molybdenum carbide catalysts. *Fuel*, 2004. 83(13): p. 1717-1726.

17. T. Xiao, A.P.E. York, H. Al-Megren, C.V. Williams, H. Wang, and M.L.H. Green, Preparation and characterisation of bimetallic cobalt and molybdenum carbides. *Journal of Catalysis*, 2001. 202(1): p. 100-109
18. Q. Zhu, Q. Chen, X. Yang, and D. Ke, A new method for the synthesis of molybdenum carbide. *Materials Letters*, 2007. 61(29): p. 5173-5174.
19. A.L. Jongerius, R.W. Gosselink, J. Dijkstra, J.H. Bitter, P.C.A. Bruijninx, and B.M. Weckhuysen, Carbon nanofiber supported transition-metal carbide catalysts for the hydrodeoxygenation of guaiacol. *ChemCatChem*, 2013. 5(10): p. 2964-2972.
20. D. Mordenti, D. Brodzki, and G. Djéga-Mariadassou, New synthesis of Mo₂C 14 nm in average size supported on a high specific surface area carbon material. *Journal of solid state chemistry*, 1998. 141(1): p. 114-120
21. C. Liang, P. Ying, and C. Li, Nanostructured β -Mo₂C prepared by carbothermal hydrogen reduction on ultrahigh surface area carbon material. *Chemistry of materials*, 2002. 14(7): p. 3148-3151.
22. M. Kaewpanha, G. Guan, Y. Ma, X. Hao, Z. Zhang, P. Reubroychareon, K. Kusakabe, and A. Abudula, Hydrogen production by steam reforming of biomass tar over biomass char supported molybdenum carbide catalyst. *International journal of hydrogen energy*, 2015. 40(25): p. 7974-7982
23. J. Han, J. Duan, P. Chen, H. Lou, X. Zheng, and H. Hong, Carbon-supported molybdenum carbide catalysts for the conversion of vegetable oils. *ChemSusChem*, 2012. 5(4): p. 727-733

24. B. Frank, K. Friedel, F. Girgsdies, X. Huang, R. Schlögl, and A. Trunschke, CNT - Supported MoxC Catalysts: Effect of Loading and Carburization Parameters. *ChemCatChem*, 2013. 5(8): p. 2296-2305
25. T. Mo, J. Xu, Y. Yang, and Y. Li, Effect of carburization protocols on molybdenum carbide synthesis and study on its performance in CO hydrogenation. *Catalysis Today*, 2016. 261(Supplement C): p. 101-115.
26. C. Liang, W. Ma, Z. Feng, and C. Li, Activated carbon supported bimetallic CoMo carbides synthesized by carbothermal hydrogen reduction. *Carbon*, 2003. 41(9): p. 1833-1839.
27. C. Liang, F. Tian, Z. Li, Z. Feng, Z. Wei, and C. Li, Preparation and adsorption properties for thiophene of nanostructured W₂C on ultrahigh-surface-area carbon materials. *Chemistry of materials*, 2003. 15(25): p. 4846-4853
28. N. Ji, T. Zhang, M. Zheng, A. Wang, H. Wang, X. Wang, and J.G. Chen, Direct Catalytic Conversion of Cellulose into Ethylene Glycol Using Nickel-Promoted Tungsten Carbide Catalysts. *Angewandte Chemie*, 2008. 120(44): p. 8638-8641
29. Z. Zhao, H. Yang, Y. Li, and X. Guo, Cobalt-modified molybdenum carbide as an efficient catalyst for chemoselective reduction of aromatic nitro compounds. *Green chemistry*, 2014. 16(3): p. 1274-1281.
30. L.A. Santillán-Vallejo, J.A. Melo-Banda, A.I.R. de la Torre, G. Sandoval-Robles, J.M. Domínguez, A. Montesinos-Castellanos, and J.A. de los Reyes-Heredía, Supported (NiMo, CoMo)-carbide, -nitride phases: Effect of atomic ratios and phosphorus concentration on the HDS of thiophene and dibenzothiophene. *Catalysis today*, 2005. 109(1): p. 33-41.

31. E. Puello-Polo and J.L. Brito, Effect of the type of precursor and the synthesis method on thiophene hydrodesulfurization activity of activated carbon supported Fe-Mo, Co-Mo and Ni-Mo carbides. *Journal of Molecular Catalysis A: Chemical*, 2008. 281(1): p. 85-92
32. J.G. Speight, *The desulfurization of heavy oils and residua* 1999: CRC Press.
33. X. Li, A. Wang, M. Egorova, and R. Prins, Kinetics of the HDS of 4,6-dimethyldibenzothiophene and its hydrogenated intermediates over sulfided Mo and NiMo on γ -Al₂O₃. *Journal of Catalysis*, 2007. 250(2): p. 283-293.
34. M. Houalla, D.H. Broderick, A.V. Sapre, N.K. Nag, V.H.J. de Beer, B.C. Gates, and H. Kwart, Hydrodesulfurization of methyl-substituted dibenzothiophenes catalyzed by sulfided CoMo/ γ -Al₂O₃. *Journal of Catalysis*, 1980. 61(2): p. 523-527.
35. F. Bataille, J.-L. Lemberon, P. Michaud, G. Pérot, M. Vrinat, M. Lemaire, E. Schulz, M. Breyse, and S. Kasztelan, Alkyldibenzothiophenes Hydrodesulfurization-Promoter Effect, Reactivity, and Reaction Mechanism. *Journal of Catalysis*, 2000. 191(2): p. 409-422.
36. M. Egorova and R. Prins, Hydrodesulfurization of dibenzothiophene and 4, 6-dimethyldibenzothiophene over sulfided NiMo/ γ -Al₂O₃, CoMo/ γ -Al₂O₃, and Mo/ γ -Al₂O₃ catalysts. *Journal of Catalysis*, 2004. 225(2): p. 417-427
37. D. Ferdous, A.K. Dalai, and J. Adjaye, Comparison of hydrodenitrogenation of model basic and nonbasic nitrogen species in a trickle bed reactor using commercial NiMo/Al₂O₃ Catalyst. *Energy & Fuels*, 2003. 17(1): p. 164-171
38. H. Topsøe, B.S. Clausen, and F.E. Massoth, *Hydrotreating catalysis* 1996: Springer.
39. S. Eijsbouts, On the flexibility of the active phase in hydrotreating catalysts. *Applied Catalysis A: General*, 1997. 158(1-2): p. 53-92.

40. K. Sakanishi, T. Nagamatsu, I. Mochida, and D.D. Whitehurst, Hydrodesulfurization kinetics and mechanism of 4, 6-dimethyldibenzothiophene over NiMo catalyst supported on carbon. *Journal of Molecular Catalysis A: Chemical*, 2000. 155(1): p. 101-109.
41. H. Farag, I. Mochida, and K. Sakanishi, Fundamental comparison studies on hydrodesulfurization of dibenzothiophenes over CoMo-based carbon and alumina catalysts. *Applied Catalysis A: General*, 2000. 194–195: p. 147-157.
42. H. Farag, D.D. Whitehurst, K. Sakanishi, and I. Mochida, Carbon versus alumina as a support for Co–Mo catalysts reactivity towards HDS of dibenzothiophenes and diesel fuel. *Catalysis Today*, 1999. 50(1): p. 9-17.
43. S. Eijsbouts, V.H.J. De Beer, and R. Prins, Hydrodenitrogenation of quinoline over carbon-supported transition metal sulfides. *Journal of Catalysis*, 1991. 127(2): p. 619-630.
44. M. Pang, C. Liu, W. Xia, M. Muhler, and C. Liang, Activated carbon supported molybdenum carbides as cheap and highly efficient catalyst in the selective hydrogenation of naphthalene to tetralin. *Green chemistry*, 2012. 14(5): p. 1272-1276.
45. I. Kojima and E. Miyazaki, Catalysis by transition metal carbides: V. Kinetic measurements of hydrogenation of CO over TaC, TiC, and Mo₂C catalysts. *Journal of Catalysis*, 1984. 89(1): p. 168-171.
46. H.K. Park and K.L. Kim, Hydrodesulfurization of dibenzothiophene over supported and unsupported molybdenum carbide catalysts. *Korean Journal of Chemical Engineering*, 1998. 15(6): p. 625-630.
47. P. Da Costa, C. Potvin, J.M. Manoli, J.L. Lemberton, G. Pérot, and G. Djéga-Mariadassou, New catalysts for deep hydrotreatment of diesel fuel: Kinetics of 4,6-

- dimethyldibenzothiophene hydrodesulfurization over alumina-supported molybdenum carbide. *Journal of Molecular Catalysis A: Chemical*, 2002. 184(1–2): p. 323-333.
48. A. Hynaux, C. Sayag, S. Suppan, J. Trawczynski, M. Lewandowski, A. Szymanska-Kolasa, and G. Djéga-Mariadassou, Kinetic study of the hydrodesulfurization of dibenzothiophene over molybdenum carbides supported on functionalized carbon black composite: Influence of indole. *Applied Catalysis B: Environmental*, 2007. 72(1–2): p. 62-70.
 49. P. Da Costa, J.-M. Manoli, C. Potvin, and G. Djéga-Mariadassou, Deep HDS on doped molybdenum carbides: From probe molecules to real feedstocks. *Catalysis today*, 2005. 107: p. 520-530
 50. J.-G. Choi, J.R. Brenner, and L.T. Thompson, Pyridine hydrodenitrogenation over molybdenum carbide catalysts. *Journal of Catalysis*, 1995. 154(1): p. 33-40
 51. A. Szymańska, M. Lewandowski, C. Sayag, and G. Djéga-Mariadassou, Kinetic study of the hydrodenitrogenation of carbazole over bulk molybdenum carbide. *Journal of Catalysis*, 2003. 218(1): p. 24-31.
 52. J. Fan, T.N. Kalnes, M. Alward, J. Klinger, A. Sadehvandi, and D.R. Shonnard, Life cycle assessment of electricity generation using fast pyrolysis bio-oil. *Renewable Energy*, 2011. 36(2): p. 632-641
 53. D. Mohan, C.U. Pittman, and P.H. Steele, Pyrolysis of wood/biomass for bio-oil: a critical review. *Energy & Fuels*, 2006. 20(3): p. 848-889
 54. Q. Lu, W.-Z. Li, and X.-F. Zhu, Overview of fuel properties of biomass fast pyrolysis oils. *Energy Conversion and Management*, 2009. 50(5): p. 1376-1383.

55. P.M. Mortensen, J.D. Grunwaldt, P.A. Jensen, K.G. Knudsen, and A.D. Jensen, A review of catalytic upgrading of bio-oil to engine fuels. *Applied Catalysis A: General*, 2011. 407(1): p. 1-19.
56. S. Xiu and A. Shahbazi, Bio-oil production and upgrading research: A review. *Renewable and Sustainable Energy Reviews*, 2012. 16(7): p. 4406-4414.
57. J.A.R. Van Veen, H.A. Colijn, P. Hendriks, and A.J. Van Welsenes, On the formation of type I and type II NiMoS phases in NiMo/Al₂O₃ hydrotreating catalysts and its catalytic implications. *Fuel Processing Technology*, 1993. 35(1): p. 137-157
58. Q. Bu, H. Lei, A.H. Zacher, L. Wang, S. Ren, J. Liang, Y. Wei, Y. Liu, J. Tang, Q. Zhang, and R. Ruan, A review of catalytic hydrodeoxygenation of lignin-derived phenols from biomass pyrolysis. *Bioresource Technology*, 2012. 124: p. 470-477.
59. A.L. Jongerius, R. Jastrzebski, P.C.A. Bruijninx, and B.M. Weckhuysen, CoMo sulfide-catalyzed hydrodeoxygenation of lignin model compounds: An extended reaction network for the conversion of monomeric and dimeric substrates. *Journal of Catalysis*, 2012. 285(1): p. 315-323.
60. E. Furimsky, *Carbons and Carbon-supported Catalysts in Hydroprocessing 2008*: Royal Society of Chemistry.
61. F. Luck, A review of support effects on the activity and selectivity of hydrotreating catalysts. *Bulletin des Sociétés Chimiques Belges*, 1991. 100(11 - 12): p. 781-800
62. G. De La Puente, A. Gil, J.J. Pis, and P. Grange, Effects of support surface chemistry in hydrodeoxygenation reactions over CoMo/activated carbon sulfided catalysts. *Langmuir*, 1999. 15(18): p. 5800-5806.

63. M. Ferrari, B. Delmon, and P. Grange, Influence of the active phase loading in carbon supported molybdenum–cobalt catalysts for hydrodeoxygenation reactions. *Microporous and mesoporous materials*, 2002. 56(3): p. 279-290
64. J. Wildschut, M. Iqbal, F.H. Mahfud, I.M. Cabrera, R.H. Venderbosch, and H.J. Heeres, Insights in the hydrotreatment of fast pyrolysis oil using a ruthenium on carbon catalyst. *Energy & Environmental Science*, 2010. 3(7): p. 962-970.
65. J.M. Solar, F.J. Derbyshire, V.H.J. de Beer, and L.R. Radovic, Effects of surface and structural properties of carbons on the behavior of carbon-supported molybdenum catalysts. *Journal of Catalysis*, 1991. 129(2): p. 330-342.
66. J.-S. Choi, G. Bugli, and G. Djéga-Mariadassou, Influence of the Degree of Carburization on the Density of Sites and Hydrogenating Activity of Molybdenum Carbides. *Journal of Catalysis*, 2000. 193(2): p. 238-247.
67. B. Dhandapani, T. St. Clair, and S.T. Oyama, Simultaneous hydrodesulfurization, hydrodeoxygenation, and hydrogenation with molybdenum carbide. *Applied Catalysis A: General*, 1998. 168(2): p. 219-228.
68. G.M. Dolce, P.E. Savage, and L.T. Thompson, Hydrotreatment activities of supported molybdenum nitrides and carbides. *Energy & fuels*, 1997. 11(3): p. 668-675.
69. W.-S. Lee, Z. Wang, R.J. Wu, and A. Bhan, Selective vapor-phase hydrodeoxygenation of anisole to benzene on molybdenum carbide catalysts. *Journal of Catalysis*, 2014. 319: p. 44-53.
70. H. Ren, W. Yu, M. Saliccioli, Y. Chen, Y. Huang, K. Xiong, D.G. Vlachos, and J.G. Chen, Selective hydrodeoxygenation of biomass-derived oxygenates to unsaturated hydrocarbons using molybdenum carbide catalysts. *ChemSusChem*, 2013. 6(5): p. 798-801.

71. F. Rodriguez-Reinoso, M. Molina-Sabio, and M.T. González, The use of steam and CO₂ as activating agents in the preparation of activated carbons. *Carbon*, 1995. 33(1): p. 15-23
72. J.M. Hill, A. Karimi, and M. Malekshahian, Characterization, gasification, activation, and potential uses for the millions of tonnes of petroleum coke produced in Canada each year. *The Canadian Journal of Chemical Engineering*, 2014. 92(9): p. 1618-1626
73. R. Dippanfilo and N.O. Egiebor, Structural Features of Activated Carbon Produced From Oil Sands Coke. *Developments in Chemical Engineering and Mineral Processing*, 1995. 3(1): p. 3-13.
74. A. Karimi, O. Thinon, J. Fournier, and J.M. Hill, Activated carbon prepared from Canadian oil sands coke by CO₂ activation: I. Trends in pore development and the effect of pre-oxidation. *The Canadian Journal of Chemical Engineering*, 2013. 91(9): p. 1491-1499
75. C.C. Small, Z. Hashisho, and A.C. Ulrich, Preparation and characterization of activated carbon from oil sands coke. *Fuel*, 2012. 92(1): p. 69-76.
76. M. Wu, Q. Zha, J. Qiu, X. Han, Y. Guo, Z. Li, A. Yuan, and X. Sun, Preparation of porous carbons from petroleum coke by different activation methods. *Fuel*, 2005. 84(14–15): p. 1992-1997.
77. S.H. Lee and C.S. Choi, Chemical activation of high sulfur petroleum cokes by alkali metal compounds. *Fuel Processing Technology*, 2000. 64(1-3): p. 141-153
78. H. Zhang, J. Chen, and S. Guo, Preparation of natural gas adsorbents from high-sulfur petroleum coke. *Fuel*, 2008. 87(3): p. 304-311.
79. R. Xiao, S. Xu, Q. Li, and Y. Su, The effects of hydrogen on KOH activation of petroleum coke. *Journal of Analytical and Applied Pyrolysis*, 2012. 96: p. 120-125

80. E. Raymundo-Pinero, P. Azais, T. Cacciaguerra, D. Cazorla-Amorós, A. Linares-Solano, and F. Béguin, KOH and NaOH activation mechanisms of multiwalled carbon nanotubes with different structural organisation. *Carbon*, 2005. 43(4): p. 786-795.
81. A. Tomita, K. Higashiyama, and Y. Tamai, Scanning electron microscopic study on the catalytic gasification of coal. *Fuel*, 1981. 60(2): p. 103-114
82. A. Oya, S. Yoshida, J. Alcaniz-Monge, and A. Linares-Solano, Formation of mesopores in phenolic resin-derived carbon fiber by catalytic activation using cobalt. *Carbon*, 1995. 33(8): p. 1085-1090.
83. Z.L. Liu, Licheng; Liu, Lang, Effect of CO₂ activation on the formation of mesopore of pitch-based carbon sphere containing iron. *Coal Conversion*, 1999. 22(2): p. 71-75.
84. D. Cazorla-Amorós, D. Ribes-Pérez, M. Roman-Martinez, and A. Linares-Solano, Selective porosity development by calcium-catalyzed carbon gasification. *Carbon*, 1996. 34(7): p. 869-878.
85. R. Leboda, J. Skubiszewska-Zięba, and W. Grzegorzczuk, Effect of calcium catalyst loading procedure on the porous structure of active carbon from plum stones modified in the steam gasification process. *Carbon*, 1998. 36(4): p. 417-425.
86. W. Shen, J. Zheng, Z. Qin, and J. Wang, Preparation of mesoporous carbon from commercial activated carbon with steam activation in the presence of cerium oxide. *Journal of Colloid and Interface Science*, 2003. 264(2): p. 467-473.
87. H. Yasuda, H. Tamai, M. Ikeuchi, and S. Kojima, Extremely large mesoporous carbon fibers synthesized by the addition of rare earth metal complexes and their unique adsorption behaviors. *Advanced Materials*, 1997. 9(1): p. 55-58

88. Y. Li, Z.-h. Huang, F.-y. Kang, and B.-h. Li, Preparation of activated carbon microspheres from phenolic resin with metal compounds by sub-and supercritical water activation. *New carbon materials*, 2010. 25(2): p. 109-113.
89. W. Shen, J. Zheng, Z. Qin, J. Wang, and Y. Liu, The effect of temperature on the mesopore development in commercial activated carbon by steam activation in the presence of yttrium and cerium oxides. *Colloids and Surfaces A: Physicochemical and Engineering Aspects*, 2003. 229(1): p. 55-61
90. R.T.K. Baker, R.D. Sherwood, and J.A. Dumesic, Catalytic hydrogenation of graphite by platinum, iridium, and platinum-iridium. *Journal of Catalysis*, 1980. 66(1): p. 56-64
91. C.W. Keep, S. Terry, and M. Wells, Studies of the nickel-catalyzed hydrogenation of graphite. *Journal of Catalysis*, 1980. 66(2): p. 451-462.
92. A. Tomita, N. Sato, and Y. Tamai, Hydrogenation of carbons catalyzed by nickel, platinum and rhodium. *Carbon*, 1974. 12(2): p. 143-149
93. P.J. Goethel and R.T. Yang, Mechanism of graphite hydrogenation catalyzed by nickel. *Journal of Catalysis*, 1987. 108(2): p. 356-363
94. P.J. Goethel and R.T. Yang, Mechanism of graphite hydrogenation catalyzed by ruthenium particles. *Journal of Catalysis*, 1988. 111(1): p. 220-226
95. P.J. Goethel and R.T. Yang, Platinum-catalyzed hydrogenation of graphite: Mechanism studied by the rates of monolayer channeling. *Journal of Catalysis*, 1986. 101(2): p. 342-351.
96. L. Stockman, *Petroleum coke: The coal hiding in the tar sands*, 2013, Oil Change International: Washington DC, USA.

97. E. Furimsky, Gasification of oil sand coke: Review. *Fuel Processing Technology*, 1998. 56(3): p. 263-290
98. J.G. Speight and B. Özüm, *Petroleum refining processes* 2001: CRC Press.
99. M. Malekshahian and J.M. Hill, Effect of pyrolysis and CO₂ gasification pressure on the surface area and pore size distribution of petroleum coke. *Energy & Fuels*, 2011. 25(11): p. 5250-5256
100. R. Alcántara, P. Lavela, G.F. Ortiz, J.L. Tirado, R. Menéndez, R. Santamaría, and J.M. Jiménez-Mateos, Electrochemical, textural and microstructural effects of mechanical grinding on graphitized petroleum coke for lithium and sodium batteries. *Carbon*, 2003. 41(15): p. 3003-3013.
101. J. Choi, Z.G. Barnard, S. Zhang, and J.M. Hill, Ni catalysts supported on activated carbon from petcoke and their activity for toluene hydrogenation. *The Canadian Journal of Chemical Engineering*, 2012. 90(3): p. 631-636.
102. R.K. Lattanzio, *Petroleum coke: Industry and environmental issues*, 2013.
103. V.M.L. Whiffen and K.J. Smith, Hydrodeoxygenation of 4-methylphenol over unsupported MoP, MoS₂, and MoO_x catalysts. *Energy & Fuels*, 2010. 24(9): p. 4728-4737
104. B.S. Gevert, J.E. Otterstedt, and F.E. Massoth, Kinetics of the HDO of methyl-substituted phenols. *Applied Catalysis*, 1987. 31(1): p. 119-131
105. H. Wang, J. Male, and Y. Wang, Recent advances in hydrotreating of pyrolysis bio-oil and its oxygen-containing model compounds. *ACS Catalysis*, 2013. 3(5): p. 1047-1070
106. P. Delporte, C. Pham-Huu, P. Vennegues, M.J. Ledoux, and J. Guille, Physical characterization of molybdenum oxycarbide catalyst; TEM, XRD and XPS. *Catalysis today*, 1995. 23(3): p. 251-267.

107. J.G. Choi and L.T. Thompson, XPS study of as-prepared and reduced molybdenum oxides. *Applied Surface Science*, 1996. 93(2): p. 143-149.
108. Y. Li, Y. Fan, J. He, B. Xu, H. Yang, J. Miao, and Y. Chen, Selective liquid hydrogenation of long chain linear alkadienes on molybdenum nitride and carbide modified by oxygen. *Chemical Engineering Journal*, 2004. 99(3): p. 213-218.
109. S. Izhar, H. Kanesugi, H. Tominaga, and M. Nagai, Cobalt molybdenum carbides: Surface properties and reactivity for methane decomposition. *Applied Catalysis A: General*, 2007. 317(1): p. 82-90
110. K. Oshikawa, M. Nagai, and S. Omi, Characterization of molybdenum carbides for methane reforming by TPR, XRD, and XPS. *The Journal of Physical Chemistry B*, 2001. 105(38): p. 9124-9131
111. P. Delporte, C. Pham-Huu, P. Vennegues, M.J. Ledoux, and J. Guille, Physical characterization of molybdenum oxycarbide catalyst; TEM, XRD and XPS. *Catalysis today*, 1995. 23(3): p. 251-267
112. V.M.L. Whiffen and K.J. Smith, A comparative study of 4-methylphenol hydrodeoxygenation over high surface area MoP and Ni₂P. *Topics in Catalysis*, 2012. 55(14-15): p. 981-990
113. Y.Q. Yang, C.T. Tye, and K.J. Smith, Influence of MoS₂ catalyst morphology on the hydrodeoxygenation of phenols. *Catalysis Communications*, 2008. 9(6): p. 1364-1368.
114. R. Wandas, J. Surygala, and E. Śliwka, Conversion of cresols and naphthalene in the hydroprocessing of three-component model mixtures simulating fast pyrolysis tars. *Fuel*, 1996. 75(6): p. 687-694.

115. C.R. Lee, J.S. Yoon, Y.-W. Suh, J.-W. Choi, J.-M. Ha, D.J. Suh, and Y.-K. Park, Catalytic roles of metals and supports on hydrodeoxygenation of lignin monomer guaiacol. *Catalysis Communications*, 2012. 17(0): p. 54-58.
116. H. Yoshida, S. Takeda, T. Uchiyama, H. Kohno, and Y. Homma, Atomic-scale in-situ observation of carbon nanotube growth from solid state iron carbide nanoparticles. *Nano letters*, 2008. 8(7): p. 2082-2086
117. A. Okita, Y. Suda, A. Ozeki, H. Sugawara, Y. Sakai, A. Oda, and J. Nakamura, Predicting the amount of carbon in carbon nanotubes grown by CH₄ rf plasmas. *Journal of applied physics*, 2006. 99(1): p. 1-7.
118. A.W. Orbaek, A.C. Owens, and A.R. Barron, Increasing the efficiency of single walled carbon nanotube amplification by Fe–Co catalysts through the optimization of CH₄/H₂ partial pressures. *Nano letters*, 2011. 11(7): p. 2871-2874
119. F. Massoth, P. Politzer, M. Concha, J. Murray, J. Jakowski, and J. Simons, Catalytic hydrodeoxygenation of methyl-substituted phenols: Correlations of kinetic parameters with molecular properties. *The Journal of Physical Chemistry B*, 2006. 110(29): p. 14283-14291.
120. N. Liu, S.A. Rykov, and J.G. Chen, A comparative surface science study of carbide and oxycarbide: the effect of oxygen modification on the surface reactivity of C/W(1 1 1). *Surface Science*, 2001. 487(1–3): p. 107-117.
121. M.M. Sullivan, J.T. Held, and A. Bhan, Structure and site evolution of molybdenum carbide catalysts upon exposure to oxygen. *Journal of Catalysis*, 2015. 326: p. 82-91.
122. S. Badoga, R.V. Sharma, A.K. Dalai, and J. Adjaye, Synthesis and characterization of mesoporous aluminas with different pore sizes: Application in NiMo supported catalyst for hydrotreating of heavy gas oil. *Applied Catalysis A: General*, 2015. 489: p. 86-97

123. Y. Sun, H. Wang, and R. Prins, Hydrodesulfurization with classic Co–MoS₂ and Ni–MoS₂/γ-Al₂O₃ and new Pt–Pd on mesoporous zeolite catalysts. *Catalysis Today*, 2010. 150(3): p. 213-217
124. P.A. Aegerter, W.W.C. Quigley, G.J. Simpson, D.D. Ziegler, J.W. Logan, K.R. McCrea, S. Glazier, and M.E. Bussell, Thiophene hydrodesulfurization over alumina-supported molybdenum carbide and nitride catalysts: adsorption sites, catalytic activities, and nature of the active surface. *Journal of Catalysis*, 1996. 164(1): p. 109-121.
125. B. Dhandapani, T.S. Clair, and S.T. Oyama, Simultaneous hydrodesulfurization, hydrodeoxygenation, and hydrogenation with molybdenum carbide. *Applied Catalysis A: General*, 1998. 168(2): p. 219-228
126. E. Puello-Polo, M. Ayala-G, and J.L. Brito, Sulfidability and thiophene hydrodesulfurization activity of supported NiMo carbides. *Catalysis Communications*, 2014. 53: p. 9-14
127. G. Jin, J. Zhu, X. Fan, G. Sun, and J. Gao, Effect of Ni Promoter on Dibenzothiophene Hydrodesulfurization Performance of Molybdenum Carbide Catalyst. *Chinese Journal of Catalysis*, 2006. 27(10): p. 899-903.
128. H. Wang, S. Liu, and K.J. Smith, Synthesis and Hydrodeoxygenation Activity of Carbon Supported Molybdenum Carbide and Oxycarbide Catalysts. *Energy & Fuels*, 2016. 30(7): p. 6039-6049
129. X. Liu, A. Wang, X. Wang, C.-Y. Mou, and T. Zhang, Au–Cu Alloy nanoparticles confined in SBA-15 as a highly efficient catalyst for CO oxidation. *Chemical Communications*, 2008(27): p. 3187-3189.

130. C. Wan and B.M. Leonard, Iron-doped molybdenum carbide catalyst with high activity and stability for the hydrogen evolution reaction. *Chemistry of Materials*, 2015. 27(12): p. 4281-4288
131. V. Sundaramurthy, A.K. Dalai, and J. Adjaye, HDN and HDS of different gas oils derived from Athabasca bitumen over phosphorus-doped NiMo/ γ -Al₂O₃ carbides. *Applied Catalysis B: Environmental*, 2006. 68(1–2): p. 38-48.
132. G.H. Singhal, R.L. Espino, J.E. Sobel, and G.A. Huff, Hydrodesulfurization of sulfur heterocyclic compounds: kinetics of dibenzothiophene. *Journal of Catalysis*, 1981. 67(2): p. 457-468
133. A.A. Smirnov, S.A. Khromova, D.Y. Ermakov, O.A. Bulavchenko, A.A. Saraev, P.V. Aleksandrov, V.V. Kaichev, and V.A. Yakovlev, The composition of Ni-Mo phases obtained by NiMoO_x-SiO₂ reduction and their catalytic properties in anisole hydrogenation. *Applied Catalysis A: General*, 2016. 514: p. 224-234
134. E. Schachtl, E. Kondratieva, O.Y. Gutiérrez, and J.A. Lercher, Pathways for H₂ Activation on (Ni)-MoS₂ Catalysts. *The journal of physical chemistry letters*, 2015. 6(15): p. 2929-2932.
135. P.A. Nikulshin, D.I. Ishutenko, A.A. Mozhaev, K.I. Maslakov, and A.A. Pimerzin, Effects of composition and morphology of active phase of CoMo/Al₂O₃ catalysts prepared using Co₂Mo₁₀-heteropolyacid and chelating agents on their catalytic properties in HDS and HYD reactions. *Journal of Catalysis*, 2014. 312: p. 152-169.
136. L. Zhang, J. Feng, Q. Chu, W. Li, K. Xu, and T.S. Wiltowski, Effect of potassium on the catalytic performance of Ni₂Mo₃N catalyst during hydrogenation of thiophene-containing benzene. *Catalysis Communications*, 2015. 66: p. 50-54.

137. J. Laine, M. Labady, F. Severino, and S. Yunes, Sink effect in activated carbon-supported hydrodesulfurization catalysts. *Journal of Catalysis*, 1997. 166(2): p. 384-387
138. Z. Yao, J. Jiang, Y. Zhao, F. Luan, J. Zhu, Y. Shi, H. Gao, and H. Wang, Insights into the deactivation mechanism of metal carbide catalysts for dry reforming of methane via comparison of nickel-modified molybdenum and tungsten carbides. *RSC Advances*, 2016. 6(24): p. 19944-19951.
139. M. Daage and R.R. Chianelli, Structure-function relations in molybdenum sulfide catalysts: the "rim-edge" model. *Journal of Catalysis*, 1994. 149(2): p. 414-427
140. T. Kawano, M. Kubota, M.S. Onyango, F. Watanabe, and H. Matsuda, Preparation of activated carbon from petroleum coke by KOH chemical activation for adsorption heat pump. *Applied Thermal Engineering*, 2008. 28(8-9): p. 865-871.
141. L.D. Virla, V. Montes, J. Wu, S.F. Ketep, and J.M. Hill, Synthesis of porous carbon from petroleum coke using steam, potassium and sodium: Combining treatments to create mesoporosity. *Microporous and Mesoporous Materials*, 2016. 234: p. 239-247.
142. V. Montes and J.M. Hill, Pore enlargement of carbonaceous materials by metal oxide catalysts in the presence of steam: Influence of metal oxide size and porosity of starting material. *Microporous and Mesoporous Materials* 2017. 256: p. 91-101.
143. X. Li, D. Ma, L. Chen, and X. Bao, Fabrication of molybdenum carbide catalysts over multi-walled carbon nanotubes by carbothermal hydrogen reduction. *Catalysis letters*, 2007. 116(1-2): p. 63-69.
144. O. Ostrovski and G. Zhang, Reduction and carburization of metal oxides by methane - containing gas. *AIChE journal*, 2006. 52(1): p. 300-310

145. I. Wolf and H.J. Grabke, A study on the solubility and distribution of carbon in oxides. Solid state communications, 1985. 54(1): p. 5-10
146. R.G. Kaldenhoven and J.M. Hill, Determining the pore structure of activated carbon by nitrogen gas adsorption, in Catalysis 2018. p. 41-63.
147. G. Kresse and J. Furthmüller, Efficiency of ab-initio total energy calculations for metals and semiconductors using a plane-wave basis set. Computational Materials Science, 1996. 6(1): p. 15-50.
148. P.E. Blöchl, Projector augmented-wave method. Physical review B, 1994. 50(24): p. 17953.
149. G. Kresse and J. Furthmüller, Efficient iterative schemes for ab initio total-energy calculations using a plane-wave basis set. Physical Review B, 1996. 54(16): p. 11169-11186.
150. J.P. Perdew, K. Burke, and M. Ernzerhof, Generalized gradient approximation made simple. Physical review letters, 1996. 77(18): p. 3865.
151. B. Liu, Z. Zhao, G. Henkelman, and W. Song, Computational design of a CeO₂-supported Pd-based bimetallic nanorod for CO oxidation. The Journal of Physical Chemistry C, 2016. 120(10): p. 5557-5564
152. Z.M. Hanafi, M.A. Khilla, and M.H. Askar, The thermal decomposition of ammonium heptamolybdate. Thermochemica Acta, 1981. 45(3): p. 221-232.
153. C. Thomazeau, V. Martin, and P. Afanasiev, Effect of support on the thermal decomposition of (NH₄)₆Mo₇O₂₄·4H₂O in the inert gas atmosphere. Applied Catalysis A: General, 2000. 199(1): p. 61-72

154. J. Dang, G.-H. Zhang, and K.-C. Chou, Phase transitions and morphology evolutions during hydrogen reduction of MoO_3 to MoO_2 . *High Temperature Materials and Processes*, 2014. 33(4): p. 305-312
155. E. Lalik, W.I.F. David, P. Barnes, and J.F.C. Turner, Mechanisms of reduction of MoO_3 to MoO_2 reconciled ? *The Journal of Physical Chemistry B*, 2001. 105(38): p. 9153-9156
156. M. Chen, C.M. Friend, and E. Kaxiras, The chemical nature of surface point defects on MoO_3 (010): adsorption of hydrogen and methyl. *Journal of the American Chemical Society*, 2001. 123(10): p. 2224-2230
157. J.A. Rodriguez, J.C. Hanson, A.I. Frenkel, J.Y. Kim, and M. Pérez, Experimental and theoretical studies on the reaction of H_2 with NiO : role of O vacancies and mechanism for oxide reduction. *Journal of the American Chemical Society*, 2002. 124(2): p. 346-354.
158. E. Furimsky, Metal carbides and nitrides as potential catalysts for hydroprocessing. *Applied Catalysis A: General*, 2003. 240(1): p. 1-28
159. V. Sundaramurthy, A.K. Dalai, and J. Adjaye, Effect of phosphorus addition on the hydrotreating activity of $\text{NiMo}/\text{Al}_2\text{O}_3$ carbide catalyst. *Catalysis today*, 2007. 125(3): p. 239-247
160. H. Wang, S. Liu, R. Govindarajan, and K.J. Smith, Preparation of $\text{Ni-Mo}_2\text{C}/\text{carbon}$ catalysts and their stability in the HDS of dibenzothiophene. *Applied Catalysis A: General*, 2017. 539(5): p. 114-127.
161. T.-C. Xiao, H.-T. Wang, A.P. York, and M.L. Green, Effect of sulfur on the performance of molybdenum carbide catalysts for the partial oxidation of methane to synthesis gas. *Catalysis letters*, 2002. 83(3-4): p. 241-246.

162. X.-R. Shi, S.-G. Wang, H. Wang, C.-M. Deng, Z. Qin, and J. Wang, Structure and stability of β - Mo_2C bulk and surfaces: A density functional theory study. *Surface Science*, 2009. 603(6): p. 852-859
163. J.W. Han, L. Li, and D.S. Sholl, Density functional theory study of H and CO adsorption on alkali-promoted Mo_2C surfaces. *The Journal of Physical Chemistry C*, 2011. 115(14): p. 6870-6876
164. T. Wang, Y.-W. Li, J. Wang, M. Beller, and H. Jiao, Dissociative hydrogen adsorption on the hexagonal Mo_2C phase at high coverage. *The Journal of Physical Chemistry C*, 2014. 118(15): p. 8079-8089
165. K. KuO and G. HÄGg, A New Molybdenum Carbide. *Nature*, 1952. 170: p. 245.
166. D. Loffreda, F. Delbecq, and P. Sautet, Adsorption thermodynamics of acrolein on Pt (1 1 1) in realistic temperature and pressure from first-principle calculations. *Chemical physics letters*, 2005. 405(4-6): p. 434-439.
167. H. Wang, S. Liu, B. Liu, V. Montes, J.M. Hill, and K.J. Smith, Carbon and Mo transformations during the synthesis of mesoporous Mo_2C /carbon catalysts by carbothermal hydrogen reduction. *Journal of Solid State Chemistry*, 2018. 258: p. 818-824.
168. D.R. Stellwagen and J.H. Bitter, Structure–performance relations of molybdenum-and tungsten carbide catalysts for deoxygenation. *Green Chemistry*, 2015. 17(1): p. 582-593.
169. Y. Qin, L. He, J. Duan, P. Chen, H. Lou, X. Zheng, and H. Hong, Carbon-supported molybdenum-based catalysts for the hydrodeoxygenation of maize oil. *ChemCatChem*, 2014. 6(9): p. 2698-2705.
170. J.C. Rivière and S. Myhra, *Handbook of surface and interface analysis: methods for problem-solving* 2009: CRC press.

171. C. Tang, W. Wang, A. Sun, C. Qi, D. Zhang, Z. Wu, and D. Wang, Sulfur-Decorated Molybdenum Carbide Catalysts for Enhanced Hydrogen Evolution. *ACS Catalysis*, 2015. 5(11): p. 6956-6963.
172. Y. Li, H. Wang, L. Xie, Y. Liang, G. Hong, and H. Dai, MoS₂ Nanoparticles Grown on Graphene: An Advanced Catalyst for the Hydrogen Evolution Reaction. *Journal of the American Chemical Society*, 2011. 133(19): p. 7296-7299.
173. NIST Chemistry WebBook, NIST Standard Reference Database Number 69, ed. P.J. Linstrom and W.G. Mallard 2005: National Institute of Standards and Technology.
174. P. Liu, J.A. Rodriguez, and J.T. Muckerman, Sulfur adsorption and sulfidation of transition metal carbides as hydrotreating catalysts. *Journal of Molecular Catalysis A: Chemical*, 2005. 239(1-2): p. 116-124.
175. D. Wang, Z. Wang, C. Wang, P. Zhou, Z. Wu, and Z. Liu, Distorted MoS₂ nanostructures: An efficient catalyst for the electrochemical hydrogen evolution reaction. *Electrochemistry Communications*, 2013. 34: p. 219-222.
176. S. Cristol, J.-F. Paul, E. Payen, D. Bougeard, F. Hutschka, and S. Clémendot, DBT derivatives adsorption over molybdenum sulfide catalysts: a theoretical study. *Journal of Catalysis*, 2004. 224(1): p. 138-147
177. M. Sun, A.E. Nelson, and J. Adjaye, Ab initio DFT study of hydrogen dissociation on MoS₂, NiMoS, and CoMoS: mechanism, kinetics, and vibrational frequencies. *Journal of Catalysis*, 2005. 233(2): p. 411-421
178. B. Jiang, X. Hu, S. Lin, D. Xie, and H. Guo, Six-dimensional quantum dynamics of dissociative chemisorption of H₂ on Co(0001) on an accurate global potential energy surface. *Phys Chem Chem Phys*, 2015. 17(36): p. 23346-23355.

179. A. Szymańska-Kolasa, M. Lewandowski, C. Sayag, D. Brodzki, and G. Djéga-Mariadassou, Comparison between tungsten carbide and molybdenum carbide for the hydrodenitrogenation of carbazole. *Catalysis today*, 2007. 119(1): p. 35-38.
180. I.I. Abu and K.J. Smith, HDN and HDS of model compounds and light gas oil derived from Athabasca bitumen using supported metal phosphide catalysts. *Applied Catalysis A: General*, 2007. 328(1): p. 58-67.
181. T. Iida, M. Shetty, K. Murugappan, Z. Wang, K. Ohara, T. Wakihara, and Y. Román-Leshkov, Encapsulation of Molybdenum Carbide Nanoclusters inside Zeolite Micropores Enables Synergistic Bifunctional Catalysis for Anisole Hydrodeoxygenation. *ACS Catalysis*, 2017. 7(12): p. 8147-8151.
182. H. Rezaei and K.J. Smith, Catalyst deactivation in slurry-phase residue hydroconversion. *Energy & Fuels*, 2013. 27(10): p. 6087-6097.
183. A. Calafat, J. Laine, A. López-Agudo, and J.M. Palacios, Effect of Surface Oxidation of the Support on the Thiophene Hydrodesulfurization Activity of Mo, Ni, and NiMo Catalysts Supported on Activated Carbon. *Journal of Catalysis*, 1996. 162(1): p. 20-30.
184. J. Matos, J.L. Brito, and J. Laine, Activated carbon supported Ni-Mo: effects of pretreatment and composition on catalyst reducibility and on ethylene conversion. *Applied Catalysis A: General*, 1997. 152(1): p. 27-42
185. S.P.A. Louwers and R. Prins, Ni EXAFS studies of the Ni-Mo-S structure in carbon-supported and alumina-supported Ni-Mo catalysts. *Journal of Catalysis*, 1992. 133(1): p. 94-111.

186. K.S.W. Sing, Reporting physisorption data for gas/solid systems with special reference to the determination of surface area and porosity (Recommendations 1984). Pure and applied chemistry, 1985. 57(4): p. 603-619
187. J.M.D. Tascón, Novel carbon adsorbents 2012: Elsevier.
188. N.A. Seaton, J.P.R.B. Walton, and N. Quirke, A new analysis method for the determination of the pore size distribution of porous carbons from nitrogen adsorption measurements. Carbon, 1989. 27(6): p. 853-861.
189. C. Lastoskie, K.E. Gubbins, and N. Quirke, Pore size distribution analysis of microporous carbons: a density functional theory approach. The journal of physical chemistry, 1993. 97(18): p. 4786-4796.
190. J. Jagiello and J.P. Olivier, 2D-NLDFT adsorption models for carbon slit-shaped pores with surface energetical heterogeneity and geometrical corrugation. Carbon, 2013. 55: p. 70-80.
191. J. Jagiello and J.P. Olivier, Carbon slit pore model incorporating surface energetical heterogeneity and geometrical corrugation. Adsorption, 2013. 19(2-4): p. 777-783.
192. A. Hayter, Probability and statistics for engineers and scientists 2012: Nelson Education.
193. H.S. Fogler, Elements of chemical reaction engineering 1999.
194. R.B. Bird, W.E. Stewart, and E.N. Lightfoot, Transport Phenomena, 2nd Edition 2002: New York: Wiley.
195. M.C. Tsai, Y.W. Chen, B.C. Kang, J.C. Wu, and L.J. Leu, Hydrodesulfurization and hydrodemetalation reactions of residue oils over cobalt-molybdenum/aluminum borate catalysts in a trickle bed reactor. Industrial & engineering chemistry research, 1991. 30(8): p. 1801-1810

196. V. Whiffen, A study of metal phosphides for the hydrodeoxygenation of phenols and pyrolysis oil, 2013, University of British Columbia.

Appendices

Appendix A Catalyst Preparation

A.1 Raw Petroleum Coke (PC) and Activated Petcoke (APC)

The petroleum coke used in this study was provided by Suncor Energy Inc. (Calgary, AB, Canada) generated in a delayed coking process. Several characterization methods have been used to determine the properties of raw petcoke, as listed below.

- Elemental analysis

Table A.1: CHNS/O wt% analysis of raw petroleum coke and activated petroleum coke.

Sample	C	H	N	S	O	O/C (at.)
Raw petcoke	83.27±0.01	3.60±0.01	2.02±0.05	6.58±0.00	4.53±0.06	0.04
APC_800 ^a	89.87±0.00	0.00±0.00	0.67±0.02	0.00±0.00	9.46±0.03	0.08

Note: ^a It was prepared by activating raw petcoke with KOH in a mass ratio of 1:3 at 800 °C for 2h.

- XRD

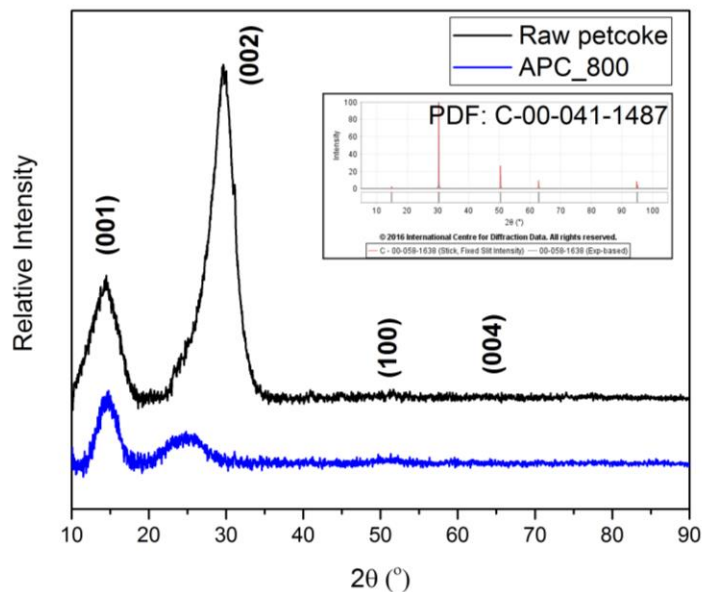


Figure A.1: XRD scan of raw petroleum coke and activated petroleum coke.

- SEM-EDX

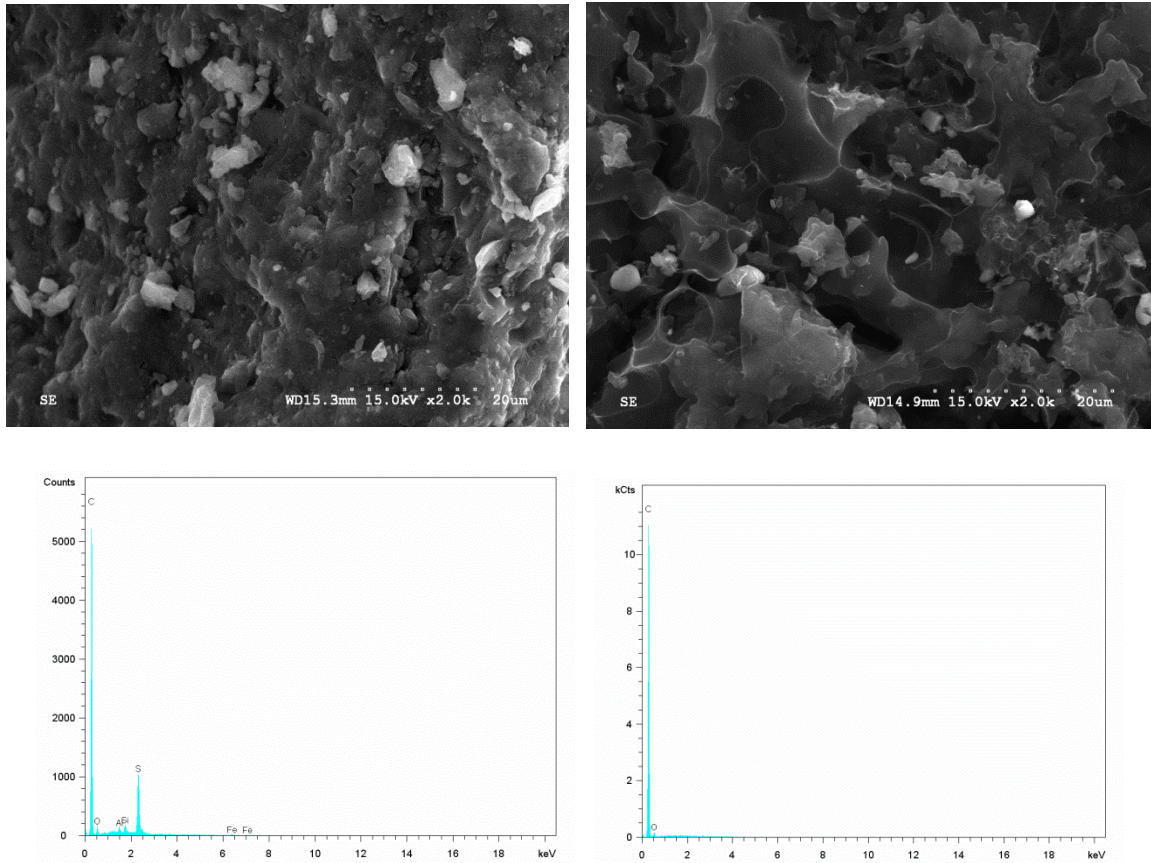


Figure A.2: SEM graphs of raw petroleum coke (Left) and activated petroleum coke (Right).

Table A.2: EDX analysis of raw petroleum coke (PC) and activated petroleum coke (APC).

Sample	Elements (wt%)				
	C	O	S	Al	Si
<i>PC-Raw Petroleum Coke</i>					
Ave.	89.96	5.91	3.58	0.20	0.28
Std. Dev.	0.57	0.43	0.66	0.03	0.07
<i>APC-Activated Petroleum Coke at 800 °C (APC_800)</i>					
Ave.	93.04	6.78	0.00	0.18	0.00
Std. Dev.	0.61	0.47	0.00	0.05	0.00

- Raman Spectroscopy

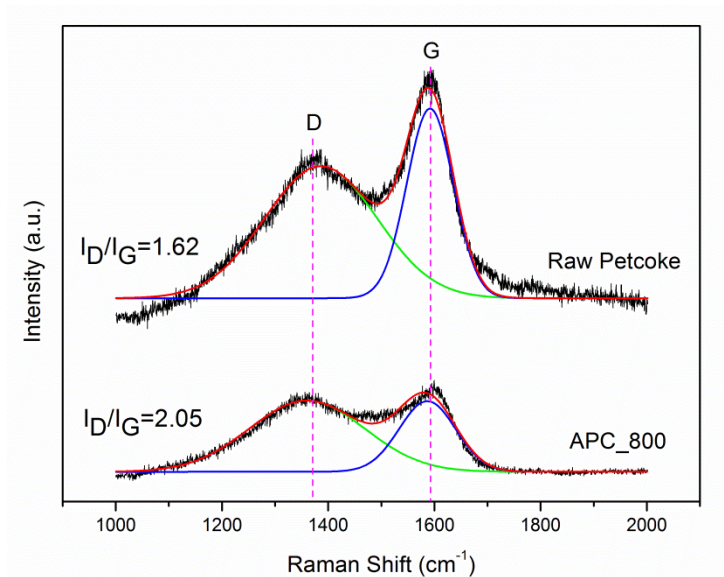


Figure A.3: Raman spectroscopy of raw petroleum coke (PC) and activated petroleum coke (APC_800).

The peaks at 1360 and 1590 cm⁻¹ are characteristic peaks of carbon materials, represented as the D band and G band, respectively. The ratio of the relative intensity of I_D/I_G can clearly present the degree of disorder. Figure A.3 shows that I_D/I_G = 1.62 for raw petroleum coke which is lower than that of APC_800 sample. It suggests that the disorder of the carbon material was increased during activation due to the formation of pores during activation. This is consistent with the XRD results.

A.2 Mo₂C/C based Catalyst Precursors and Catalysts Preparation

(I) Preparation of Mo₂C/C catalyst precursors: sample calculations for the required chemicals for preparing 10 wt% Mo on Carbon (carbon refers to AC or APC; the catalyst is designated as 10 wt.% Mo/C) are as follows:

1. Required amount of 10 wt.% Mo/C catalyst = 10.0 g

2. Amount of Mo in 10 wt.%Mo/C catalyst

$$= \frac{10 \text{ g Mo}}{100 \text{ g Mo/Carbon}} \times 10 \frac{\text{g Mo}}{\text{Carbon}} = 1.0 \text{ g} \quad (\text{Eq. A-1})$$

3. Required amount of ammonium heptamolybdate (AHM)

$$= \frac{1235.86 \frac{\text{g}}{\text{mol}} \text{AHM}/7}{95.94 \text{ g Mo}} \times 1.0 \text{ g Mo} = 1.84 \text{ g} \quad (\text{Eq. A-2})$$

4. Required amount of Carbon

$$= 10.0 \text{ g (10wt. \%Mo/C)} - 1.0 \text{ g Mo} = 9 \text{ g} \quad (\text{Eq.A-3})$$

5. Required amount of acetone to DI water solution with a mass ratio of 1:9

$$= 5.0 \frac{\text{g}}{\text{g Carbon}} * 9 \text{ g Carbon} = 45.0 \text{ g} \quad (\text{Eq.A-4})$$

(II) Preparation of Ni-Mo₂C/C catalyst precursors

The calculation of required chemicals for 1 wt% Ni and 10 wt% of Mo on Carbon (designated as 1 wt.%Ni-10 wt%Mo/C) are as follows:

1. Required amount of 1wt.%Ni-10 wt.%Mo/C catalyst = 10.0 g

2. Amount of Mo is 1.0 g as calculated by Eq. A-1.

3. Amount of Ni is calculated by

$$= \frac{1 \text{ g Ni}}{100 \frac{\text{g metal}}{\text{Carbon}}} \times 10 \frac{\text{g metal}}{\text{Carbon}} = 0.1 \text{ g} \quad (\text{Eq. A-5})$$

4. Required amount of Carbon

$$= 10.0 \frac{\text{g Metal}}{\text{Carbon}} - 1.0 \text{ g Mo} - 0.1 \text{ g Ni} = 8.9 \text{ g} \quad (\text{Eq. A-6})$$

5. A successive impregnation method is used for bimetallic catalyst preparation [183-185].

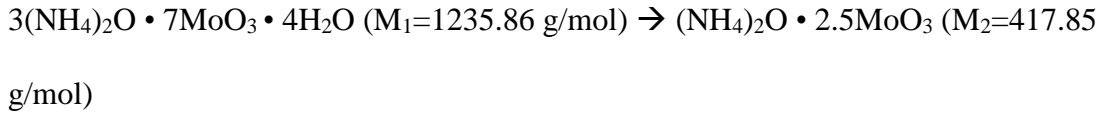
The catalyst is prepared by first impregnated with Mo and then by Ni.

6. Required amount of AHM in the 1st step of impregnation

$$= \frac{1235.86 \frac{\text{g}}{\text{mol}} \text{AHM}/7}{95.94 \text{ g Mo}} \times 1.0 \text{ g Mo} = 1.84 \text{ g} \quad (\text{Eq. A-7})$$

Note: The obtained precursor is designated as 10AHM/C.

- Apply a drying process for 10AHM/C precursor before 2nd step impregnation. According to Hanafi et al.'s study [152], it knows that AHM could decompose in air by losing H₂O and NH₃ at 110 °C as shown by the following formula:



- Calculate the weight of obtained and dried 10AHM/C precursor

$$= \frac{\frac{1.84 \text{ g} \cdot 7.0}{\text{M}_1}}{2.5} \times \text{M}_2 + 8.9 \text{ g} = 1.74 \text{ g} + 8.9 \text{ g} = 10.64 \text{ g} \quad (\text{Eq. A-8})$$

Note: this calculated mass is designated as m₂.

- Take m₁ (g) of step 8 prepared precursor and apply for the 2nd step impregnation
- Calculate the weight of carbon contained in m₁ (g) 10AHM/C precursor

$$= \frac{m_1}{m_2} \times 8.9 \text{ g} \quad (\text{Eq. A-9})$$

Note: this calculated mass is recorded as m₃.

- Required amount of Ni, recorded as m₄

$$= \frac{m_3 \text{ (g)}}{8.9 \text{ g}} * 0.1 \text{ g} \quad (\text{Eq. A-10})$$

- Required amount of Ni(NO₃)₂·6H₂O

$$= \frac{m_4 \text{ (g)}}{58.69 \text{ g/mol}} * 290.79 \text{ g/mol} \quad (\text{Eq. A-11})$$

(III) Carbothermal hydrogen reduction (CHR)

- Place 0.9 g catalyst precursor in the U-tube reactor, as shown in Figure A.4.

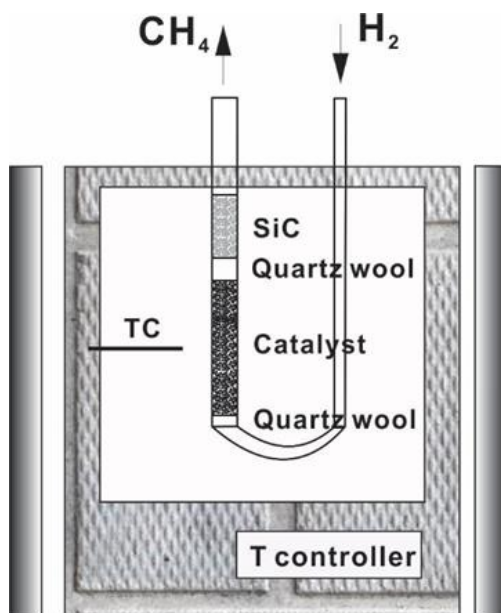


Figure A.4: Schematic illustration of the preparation of Mo₂C/C catalysts in quartz U-tube.

2. Apply a continuous H₂ flow of 100 mL (STP)/min through the catalyst bed from bottom to top.
3. Set up a temperature program from room temperature to the target temperature by 1 °C/min, holding at the final temperature for 90 min.

Note: the temperature program may vary based on different requirements.

4. After CHR, the catalyst was quickly quenched to room temperature in N₂ flow.
5. Immerse the tube into water bath for a further cooling down when temperature < 50 °C.
6. Apply a passivation process by 1% O₂/N₂ at 15 mL (STP)/min for 2 h.

A.3 Methodology of Petroleum Coke Activation

In general, the activation of petroleum coke can be grouped into three parts:

I) Preparation of petcoke powder

- 1) Add raw petcoke into the mortar
- 2) Crush the petcoke slowly using the pestle until all pieces become smaller
- 3) Use the sieve tray to sieve the petcoke into the desired particle diameter of 90-180 μm
- 4) Repeat the process by returning the larger diameter petcoke to the mortar for further grinding to produce finer particles

II) Activation

- 5) Apply drying process to remove the contained moisture from raw petcoke
- 6) Weigh x^* amount of prepared petcoke powder
- 7) Weigh y^* amount of KOH pellets, the mass ratio of y^* to x^* was set at ~ 3.0 (An exact value z^* can be obtained based on y^* to x^* ratio)
- 8) Add the KOH pellets in the mortar and crush it until it turns into a fine powder
- 9) Add the petcoke powder into the mortar and mix the two powders together
- 10) Place a clean ceramic boat on the scale, tare the balance and then add the mixture from step 9) into the boat
- 11) Record the number from step 10) as quickly as possible to avoid the moisture adsorption from the air
- 12) Calculated the real amount of petcoke (recorded as m_1) from the ratio z^* and the actual mixture mass in ceramic boat
- 13) Place the ceramic boat to the center of the tubular furnace and then place thermos blocks on both ends of the tube (See illustration: Figure A.1)
- 14) Secure the ends of the ceramic tube by using the metal connections
- 15) Open the N_2 valve and purge the tube for several minutes prior heating up

- 16) Set the temperature, activation time and ramping rate on the controller and then start the program
- 17) After activation, a natural cooling down is proceed under N₂ before taking the sample out

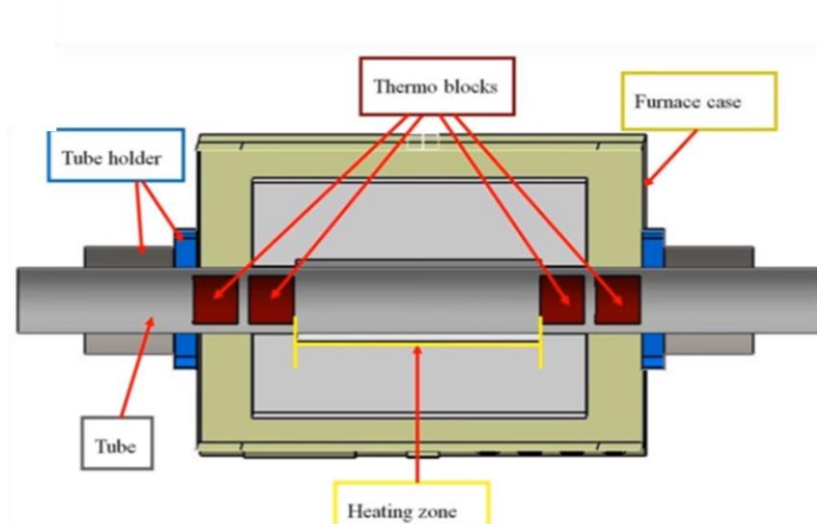


Figure A.5: Schematic illustration of the tubular furnace for petroleum coke activation.

III) Washing activated petroleum coke

- 18) Remove the activated petcoke sample into the filter funnel with DI water
- 19) Use DI and 1 M HCl solution to wash the samples in turn for at least 3 times until the pH=7
- 20) Dry the sample in the oven at 110 °C overnight
- 21) Weigh the obtained activated petcoke on scale (recorded as m_2) and then a burn-off rate (%) can be calculated by the following equation:

$$\text{Burnoff rate \%} = \frac{m_1 - m_2}{m_1}$$

Appendix B Catalyst Characterization

B.1 Physical Properties Test

Two models have been listed here for the study of pore structure:

- (1) Brunauer, Emmett and Teller (BET) method

The BET theory applies to multilayer adsorption systems. The isotherm measurement is used to quantify the specific surface area of the testing materials at a constant temperature. The standard BET test is often operated in N₂ at boiling point temperature of -196 °C and the relative equation can be expressed as follows:

$$\frac{P/P_o}{V(1-P/P_o)} = \frac{c-1}{V_m c} \left(\frac{P}{P_o} \right) + \frac{1}{V_m c} \quad (\text{Eq. B-1})$$

where C is the BET constant, representing the attraction between the adsorbate and adsorbent, V_m is the monolayer coverage, V is the adsorbed gas quantity, P is the equilibrium pressure of the adsorbate, and P_o is the saturation pressure of the adsorbate.

A plot of $x=P/P_o$ vs. $y=\frac{P/P_o}{V(1-P/P_o)}$ can generate a linear curve with a slope of $\frac{C-1}{V_m C}$ and an intercept of $\frac{1}{V_m C}$. Thus, V_m and C can be obtained.

Furthermore, the BET surface area can be calculated by $S_{BET} = 4.35V_m$ for N₂ isotherms. The valid linear range of this measurement is between $P/P_o = 0.05 \sim 0.35$. In the meanwhile, the shape of the isotherm can be used to determine the adsorption process and generally it is classified into six types as shown in Figure B1.

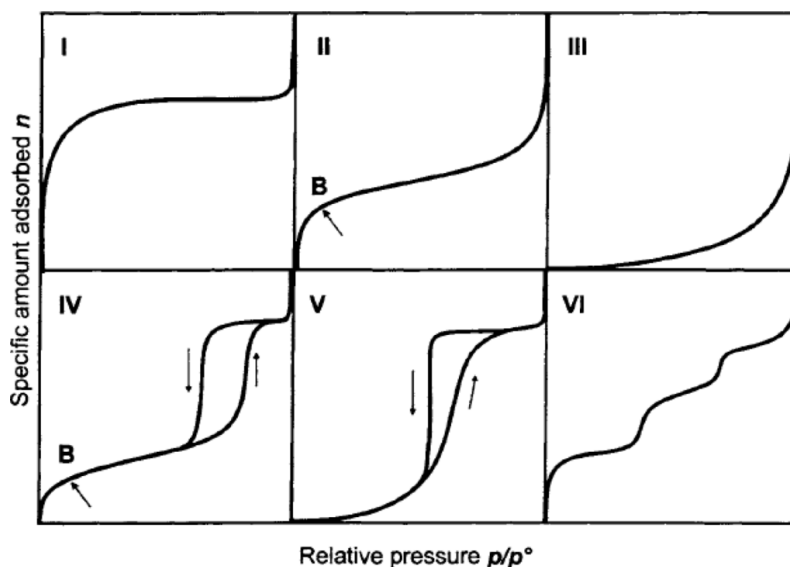


Figure B.1: Gas physisorption isotherms. (Reprinted with permission from [186])

(II) Non-local density functional theory (NLDFT)

The surface area determined from BET equation is often being overestimated, especially for microporous materials, based on Bottani and Tascon's study [187]. Thus, it was considered worthwhile to assess several NLDFT models in this study.

The Density Functional Theory model was firstly developed by Seaton et al. [188] combining micropore filling and capillary condensation. After that, it has been improved by Lastoskie et al. [189] through a non-local mean field theory (NLDFT), mainly for slit-like porous activated carbons. Furthermore, it has been modified into a 2-D Non-Local Density Functional Theory with finite pores (2D-NLDFT) and 2-D Non-Local Density Functional Theory with heterogeneous surfaces (2D-NLDFT-HS). The DFT models can be applied to accurately determine the surface area and pore size distribution of microporous carbon materials.

Example for data processing:

Sample: activated petroleum coke at 800 °C (APC_800)

Method: Carbon-N₂, 2D NLDFT-HS [190, 191]

Table B.1: Isotherm data both from experimentally measured and 2D-NLDFT-HS model fitted.

P/P ₀	Experimental adsorbed amount (cm ³ /g)	Fitted adsorbed amount (cm ³ /g)	Difference between experimental and fitted data (cm ³ /g)
0.009902	461.39811	457.55926	3.838851879
0.019757	496.70208	492.94613	3.755953429
0.030420	523.66742	530.92839	-7.260961022
0.046162	554.46160	559.68722	-5.225615080
0.058677	574.21795	580.89948	-6.681529288
0.081822	603.23738	598.90861	4.328762393
0.101198	621.79555	620.02272	1.772833683
0.122760	638.01360	633.90901	4.104588236
0.144364	650.54058	646.90584	3.634732701
0.166597	660.56502	657.41622	3.148807393
0.189013	668.38688	667.76454	0.622341025
0.209578	674.04333	674.69169	-0.648361622
0.253308	682.81875	684.75733	-1.938574522
0.306232	689.78627	692.94519	-3.158917368
<i>Ave. std. dev. of the fit</i>			4.0525

Note: The specific surface area was calculated from the measured N₂ adsorption isotherm using 2D-NLDFT-HS applied in the P/P₀ range of 0.01~0.30.

The calculated surface area is 2028 m²/g, which is smaller than the BET method calculated (2097 m²/g; calculated in the range of P/Po = 0.05 ~ 0.30).

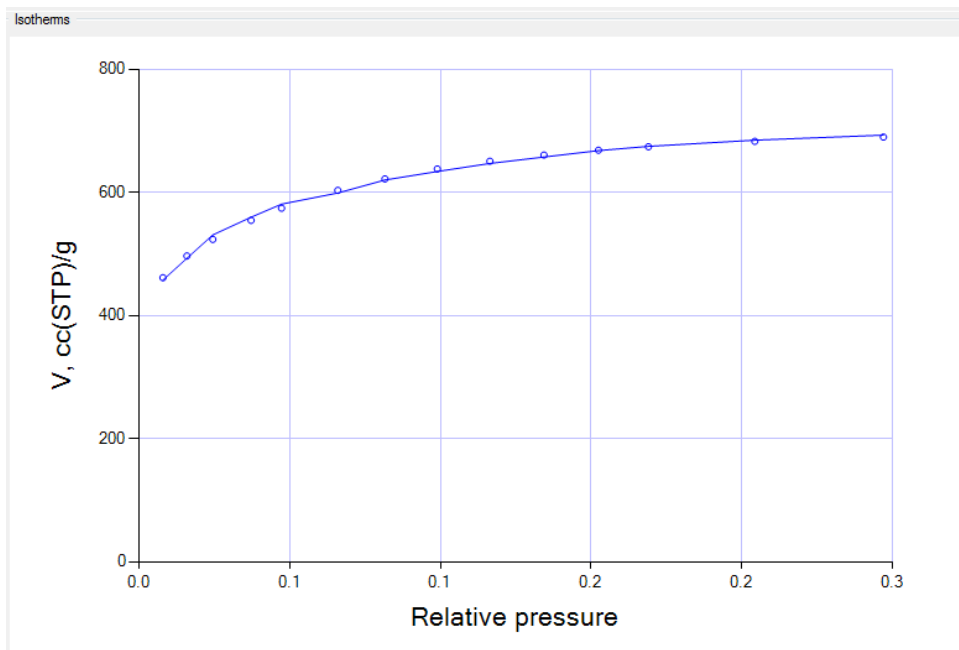


Figure B.2: Fitted isotherm by 2D-NLDFT-HS model. ("o" represents measured experimental data)

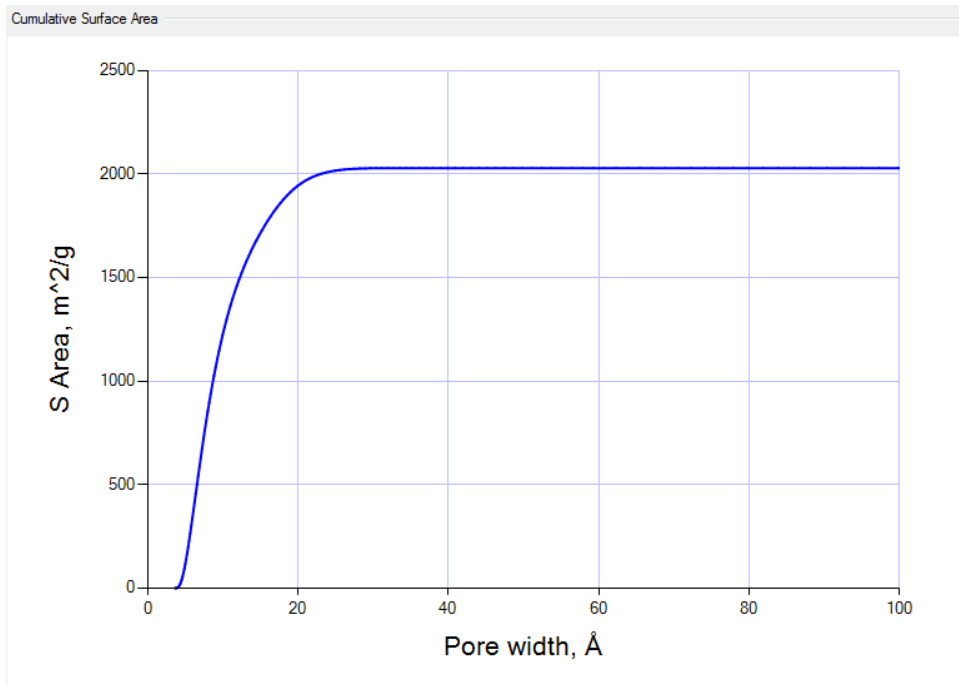


Figure B.3: Cumulative surface area by 2D-NLDFT-HS model.

B.2 XRD

Power X-ray diffraction (XRD) is used to determine the bulk properties of the samples. From this measurement, several pieces of information can be obtained: (I) Identify the bulk phases present in the catalyst by Bragg's law (usually the required conc. of measured components is ≥ 5 wt%; as shown in Eq. (B-2)); (II) Estimate the crystallite or grain size of the particles by Scherrer equation (Eq. (B-3)); (III) Determine the lattice parameters of the crystals.

$$\text{Bragg's law: } d = \frac{n\lambda}{2\sin\theta} \quad (\text{Eq. B-2})$$

where n is the integer, λ is the wavelength of the incident X-ray beam, θ is the angles of incidence, and d is the distance between atomic layers in a crystal.

$$\text{Scherrer equation: } D = \frac{k\lambda}{B\cos\theta} \quad (\text{Eq. B-3})$$

where k is the dimensionless shape factor (it varies with the actual shape of the crystallite, typically 0.9 or 1), λ is the X-ray wavelength, B is the line broadening at half the maximum intensity (FWHM) in radians (This number can be obtained after subtracting the instrumental line broadening), θ is the angle of incidence, and D is the mean crystallize size.

For example, the β - Mo_2C we obtained in this research has a hexagonal crystal structure, where $a=b \neq c$, $\alpha=\gamma=90^\circ$, $\beta=120^\circ$. The relative correlation is shown in Eq. B-4.

$$\frac{1}{d_{hkl}^2} = \frac{4}{3} \frac{(h^2+hk+k^2)}{a^2} + \frac{1}{c^2} \quad (\text{Eq. B-4})$$

where (h, k, l) is the Miller index, d is the interplanar lattice spacing of the (h, k, l) plane, a , b , and c are lattice parameters.

An example of particle size calculation by Scherrer equation:

Sample: 10Mo₂C/AC_750

Fitting method: Gaussian fit by the equation (Eq. B-5) below.

$$y = y_0 + \frac{Ae^{-\frac{4\ln(2)(x-x_c)^2}{w^2}}}{w\sqrt{\frac{\pi}{4\ln(2)}}}$$

(Eq. B-5)

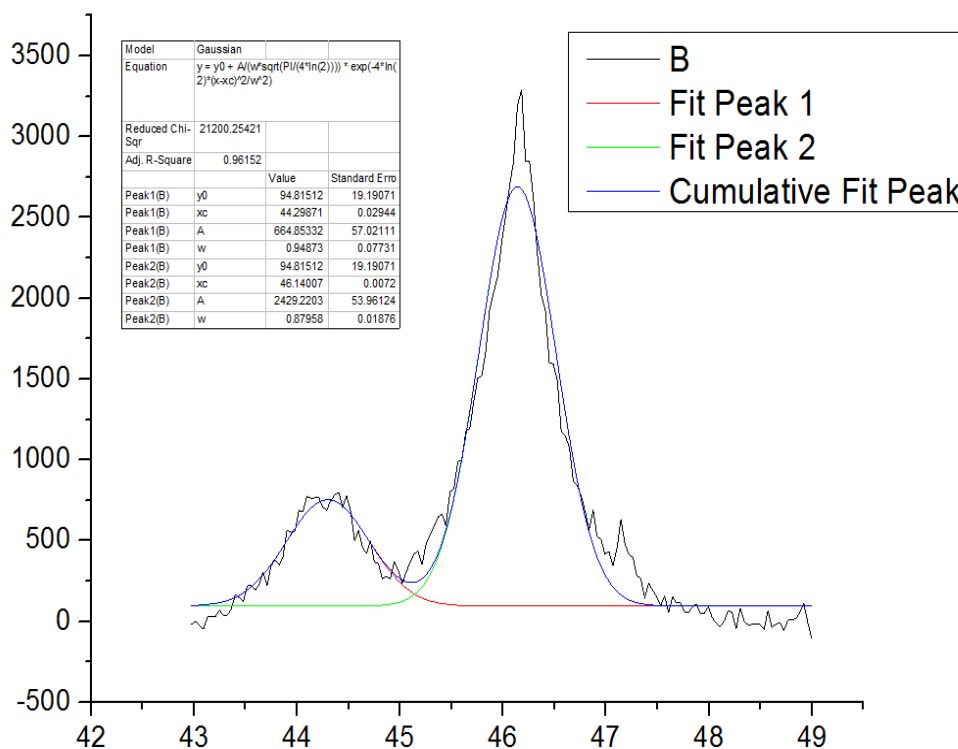


Figure B.4: XRD profile of 10Mo₂C/APC_750 catalyst and Gaussian curve fitting for (002) (Left peak) and (101) (Right peak) planes.

The calculated result for (101) plane is as follows:

10Mo ₂ C/AC_750 (101) plane		
Parameter	Value	Error (±)
y _o (PSD)	94.82	19.19
x _c (2θ)	46.14	0.077
w (2θ)	0.88	0.019
FWHM (2θ)	1.04	0.022
D (nm)	19.33	0.41

Note: $\lambda=0.17902$ nm (for Co source); $k=0.9$; $1^\circ = 0.0175$ radian.

B.3 XPS

X-ray photoelectron spectroscopy (XPS) works by irradiating the sample surface with a soft X-ray. If the binding energy (E_b) of the sample atoms is lower than the X-ray ($h\nu$), it will be excited and emitted from the parent atom as photoelectron (E_k). It is a surface technique since only the photoelectrons from the outer surface (1 ~ 10 nm) has the capability to escape. XPS is usually used to measure the elemental composition of the surface and the electronic state of each element in the surface. The calculation formula of binding energy (E_b) and atomic concentration of an element (C_i) are given by the following equations:

$$E_b = h\nu - E_k - \phi \quad (\text{Eq. B-6})$$

$$C_i = \frac{I_i/S_i}{\sum_i I_i/S_i} \quad (\text{Eq. B-7})$$

Where h is the X-ray photo energy (for monochromatic Mg $K\alpha$, $h = 1253.6$ eV); E_k is the kinetic energy of the photoelectron, and ϕ is the work function from the instrument; I_i is the peak intensity of element i , and S_i is the sensitivity factor for the peak i .

In the present study, there is no charging effect due to the good conductivity of the carbon support. The C 1s peak located at 284.5 eV is used as the internal reference peak for all elements analysis. Both elements quantification, survey scan, and narrow scan were conducted (See Figure B.5 and B.6). All the experimental data were processed by Vision Processing and XPSPEAKER 41 softwares.

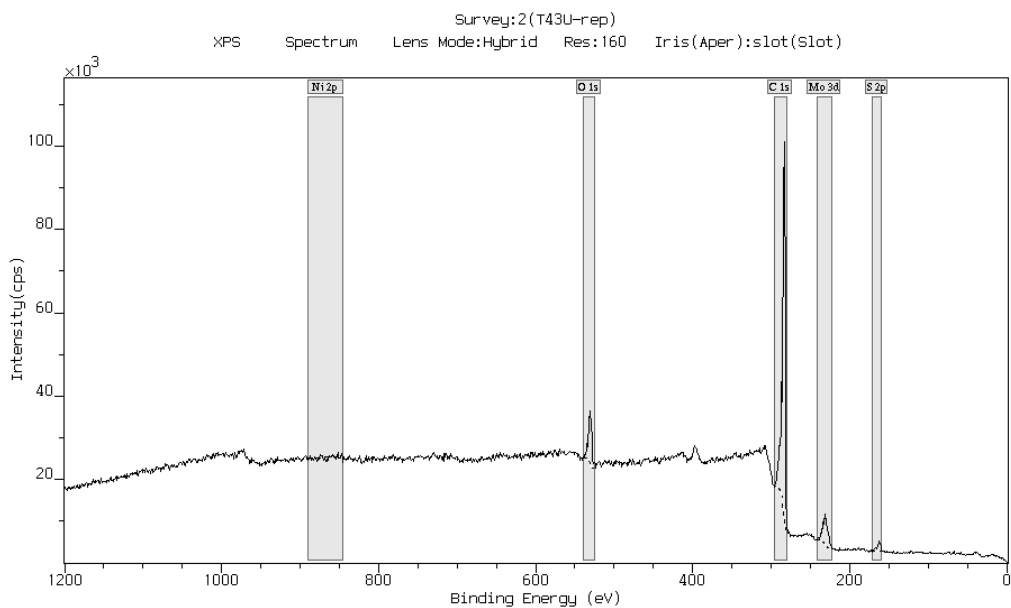


Figure B.5: XPS survey scan of used 1%Ni-10%Mo₂C/APC catalyst.

Quantification Report

Print

Quantification Report
/c:/data/HaiyanWang/3rd_training/T43U-rep.dset Tue Dec 5 15:54:37 2017

State #0 : Etch Time 0.00 seconds

Peak	Type	Position BE (eV)	FWHM (eV)	Raw Area (cps eV)	RSF	Atomic Mass	Atomic Conc %	Mass Conc %
Mo 3d	Reg	232.000	7.328	51257.9	3.321	95.922	1.13	8.06
O 1s	Reg	531.000	4.709	68176.8	0.780	15.999	5.83	6.95
C 1s	Reg	284.000	2.911	351909.8	0.278	12.011	91.84	82.13
Ni 2p	Reg	853.000	0.997	0.0	4.044	58.702	0.00	0.00
S 2p	Reg	163.000	3.570	11244.9	0.668	32.065	1.20	2.86

Figure B.6: Quantification results of used 1%Ni-10%Mo₂C/APC catalyst. (Note: the integration of each element was based on Figure B.2)

B.4 CO Chemisorption

The CO uptake of the catalysts was carried on using a Micromeritics AutoChem II 2920 unit using pulsed chemisorption at 35 °C. Two types of catalysts were tested here: one is in-situ synthesized Mo₂C catalyst with no passivation process; another one is passivated Mo₂C catalyst with a TPR prior the CO uptake test. The calculation process is as follows.

(1) In-situ synthesized Mo₂C/C catalysts

- Preparation of the in-situ synthesized catalyst:
 - a. Synthesis the catalyst by 50 mL(STP)/min of 9.5 mol% H₂/Ar while heating to the final temperature at 1°C/min, and maintaining the final temperature for 90 min;
 - b. The obtained Mo₂C/C was then flushed in He at 400 °C for 4 h and then cooled to room temperature.
 - c. Next 0.5 mL pulses of CO were injected into a flow of He (50 mL(STP)/min) and the CO uptake was measured using a TCD. CO pulses were repeatedly injected until no further CO uptake was observed after consecutive injections.
- Obtain the result from Micromeritics instrument

Example: 10% Mo₂C/AC-600 fresh catalyst synthesized in-situ

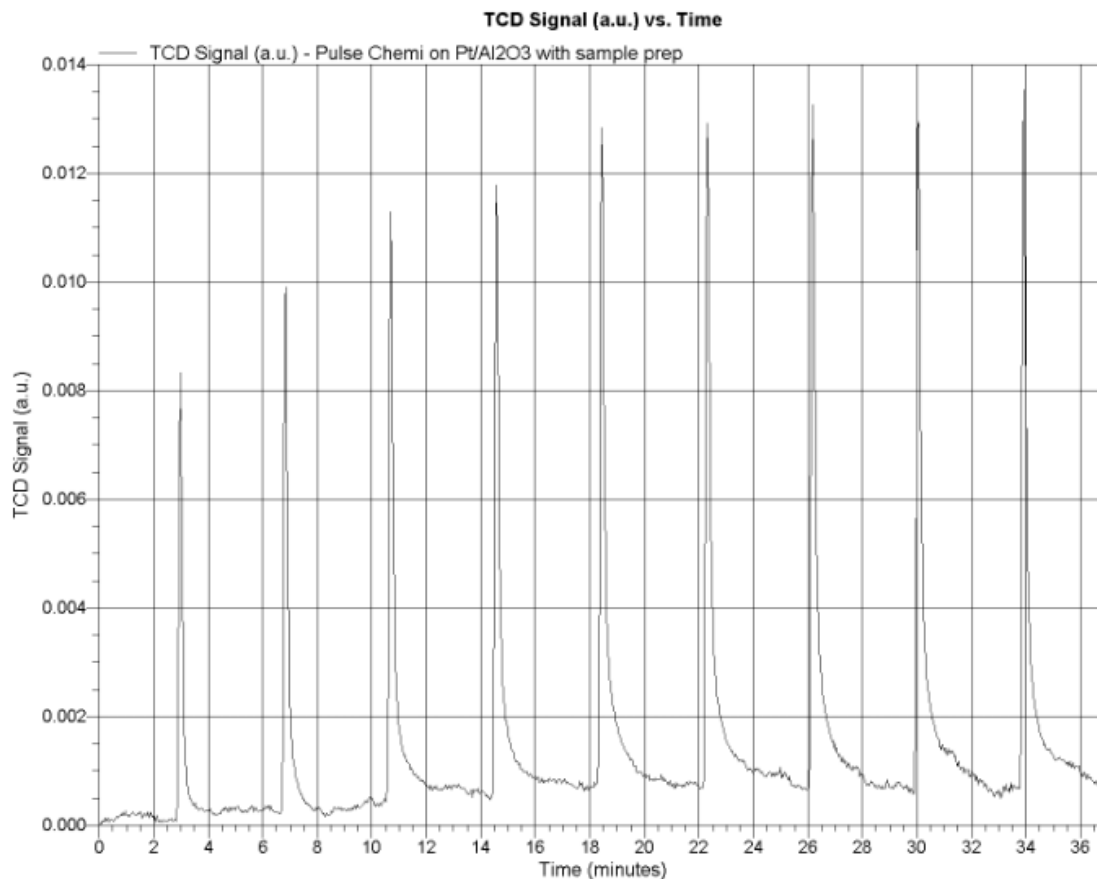


Figure B.7: TCD signal vs. time for in-situ synthesized 10% Mo₂C/AC-600 catalyst at 32 °C.

Table B.2: Peak table of adsorbed CO on in-situ synthesized 10% Mo₂C/AC-600 catalyst.

Peak number	Temperature (°C)	Quantity Adsorbed (μmol/g _{cat})	Cumulative Quantity (μmol/g _{cat})
1	32.5	6.78554	6.78554
2	32.2	4.64694	11.43248
3	32.5	2.96738	14.39986
4	32.4	1.97577	16.37563
5	32.2	0.34299	16.71862
6	32.3	0.00000	16.71862
7	32.4	0.00000	16.71862

So, the CO uptake is 16.7 μmol/g_{cat}.

- Calculate the CO uptake based on per gram of Mo
 - 10 wt%Mo/AC precursor was used for 10% Mo₂C/AC-600 catalyst synthesis, thus there is $0.1 \frac{g_{Mo}}{g_{precursor}}$;
 - The calculated Mo amount in catalyst can be calculated by $\frac{0.1 \frac{g_{Mo}}{g_{precursor}}}{(1-Burnoff\%)}$; in this case, the burn-off rate is 11%, thus the result is $\frac{0.1 \frac{g_{Mo}}{g_{precursor}}}{(1-0.11)} = 0.1124 \frac{g_{Mo}}{g_{cat}}$;
 - Combined with the measured CO uptake, the adsorbed CO based on per gram of Mo is

$$\frac{16.7 \frac{\mu mol}{g_{cat}}}{0.1124 \frac{g_{Mo}}{g_{cat}}} = 148 \frac{\mu mol}{g_{Mo}}$$

(2) Passivated Mo₂C/C catalyst

Prior to the measurement, the sample was pretreated to remove the passivation layer by passing 50 mL(STP)/min of 9.5 mol% H₂/Ar while heating to 400 °C at 10 °C/min, and maintaining the final temperature for 2 h. The flow was then switched to He (50 mL(STP)/min) at 400 °C for 4 h in order to remove the adsorbed species. After cooling in a He flow, 0.5 mL pulses of CO were injected into a flow of He (50 mL(STP)/min) and the CO uptake was measured using a TCD as before. Here, passivated 10% Mo₂C/AC-600 catalyst is put here as an example.

Table B.3: Peak table of adsorbed CO on reduced passivated 10% Mo₂C/AC-600 catalyst.

Peak number	Temperature (°C)	Quantity Adsorbed (μmol/g _{cat})	Cumulative Quantity (μmol/g _{cat})
1*	33.7	2.95816	9.61747
2	33.5	0.01899	9.63646
3	33.4	0.00000	9.63646
4	33.3	0.37331	10.00977
5	33.4	0.00000	10.00977
6	33.1	0.44632	10.45609
7	33.2	0.00000	10.45609
8	33.1	0.18901	10.64510
9	33.2	0.00000	10.64510

* 1st dose was completely adsorbed with a quantity of 6.65931 μmol/g.

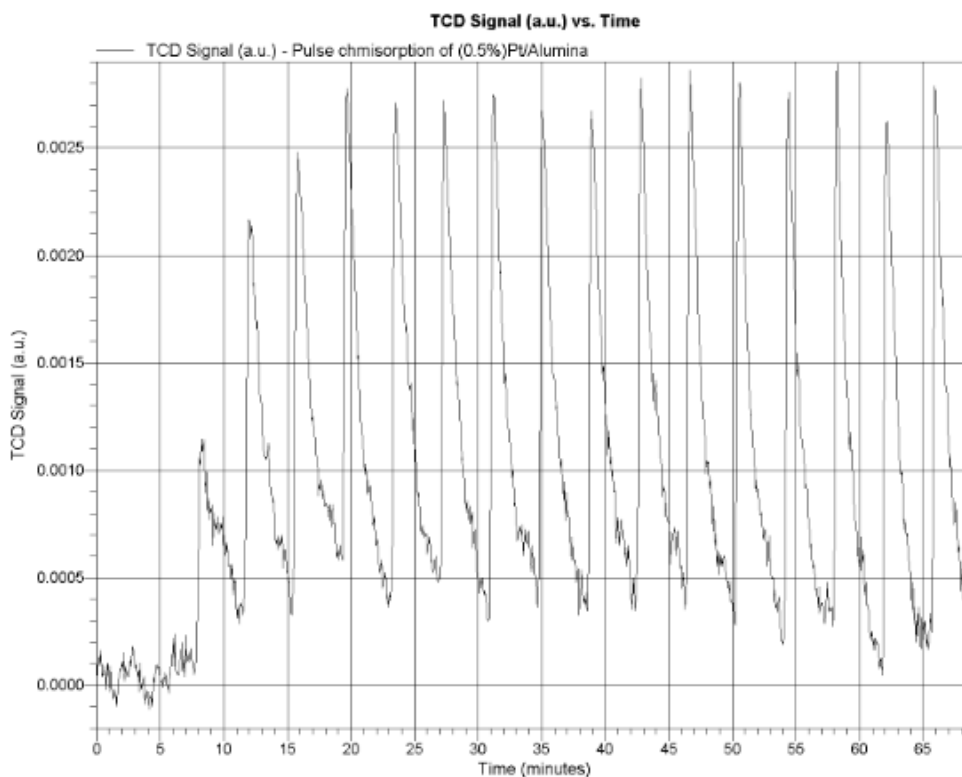


Figure B.8: TCD signal vs. time for reduced passivated 10% Mo₂C/AC-600 catalyst at 33 °C.

B.5 GC-FID/TCD

The GC used in the present study was a Shimadzu GC-14B equipped with C-R8A Chromatopac integrator. There are two columns and two detector equipped in this equipment. One is flame ionization detector (FID) with Agilent HP-PLOT U capillary column (19095P-UO4, ID: 0.530 mm, Length: 30 m, film: 20 μ m); another one is thermal conductivity detector (TCD) with a packed column (5682PC, OD: 3.175 mm, Length: 0.154 m, 316 stainless steel).

In Chapter 4's study, the outlet of the U-tube is connected with the GC-FID/TCD inlet, thus an in-situ analysis can be applied. The parameters set for the analysis are as follows: For FID, three gases were used, which are H₂, Air, and He, functionalized as combustion, oxidant, and carrier/make-up gas, representatively. The gas pressure has been set as: Carrier P = 40 kPa, Carrier M = 40 kPa, H₂ = 60 kPa, and Air = 25 kPa. The temperature program used in this study is shown in Table B.2.

Table B.4: Temperature program used for GC-FID/TCD analysis.

	Program rate ($^{\circ}$ C/min)	Temperature ($^{\circ}$ C)	Time (min)
Initial	×	35	3
1 st step	5	120	2
2 nd step	10	170	2

For TCD, only He gas is needed, where the pressure of Carrier P = 160 kPa and Carrier M = 100 kPa. The detector temperature is set at 200 $^{\circ}$ C.

A gas calibration was conducted prior to the in-situ analysis. The procedure is as follows:

1. Identify the mixture gas composition:

Table B.5: The mole composition of the mixture gas.

Calibration Gas	Mol%
Butane	4
Carbon Dioxide	8
Ethane	8
Ethylene	2
Hydrogen	25
Isobutane	2
Methane	10
Nitrogen	10
Propane	6
Carbon Monoxide	25

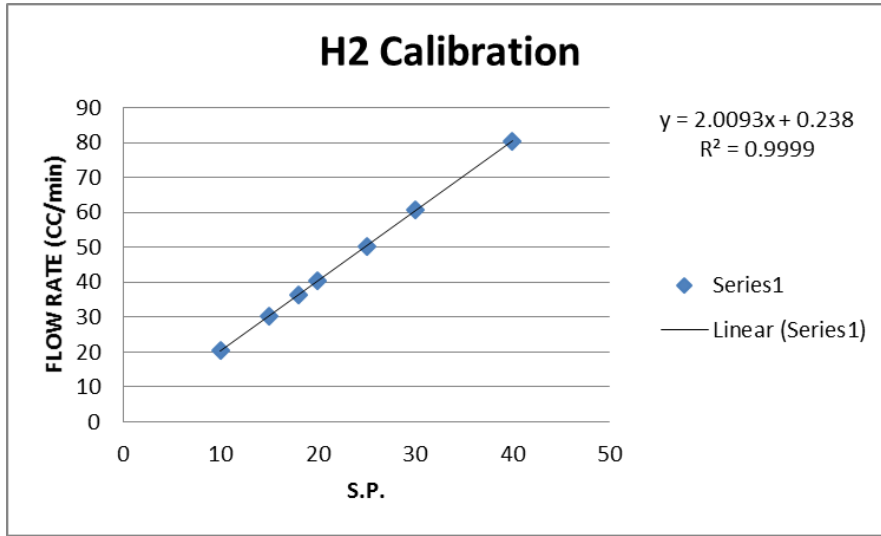
2. Chose H₂ as the diluting gas.
3. Apply gas calibration both for H₂ and mixture gas, respectively (See H₂ calibration as an example: Table B.6).

Table B.6: Gas calibration result for carrier gas H₂.

H2 calibration-- initial P:130 psi										
S.P.	Time (s)						Ave. Time (s)	Ave. time (min)	cc/min	
10	14.84	14.65	14.68	14.88	14.85	14.66	14.76	0.2460	20.3252	
15	9.88	9.84	9.93	9.94	9.69	9.84	9.85	0.1642	30.44655	
18	8.18	8.38	8.06	8.31	8.31	8.31	8.26	0.1376	36.32694	
20	7.44	7.37	7.47	7.22	7.53	7.43	7.41	0.1235	40.48583	
25	5.91	6.09	6.09	5.97	5.85	5.94	5.98	0.0996	50.20921	
30	5.09	4.85	4.97	4.84	4.94	4.91	4.93	0.0822	60.81081	
40	3.65	3.78	3.75	3.72			3.73	0.0621	80.53691	

Where x represents the Set point (S.P.) of MFC and y represents the actual flow rate. The linear correlation can be obtained as shown in Figure B.9.

Figure B.9: Linear correlation of set point vs. H₂ flow rate.



4. The calibration was run by adjusting the flow rate of diluting gas H₂. (See Table B.7)

Table B.7: Calculation of mol. concentration of each gas in gas mixture.

	MFC for Mixture gas	Point 1 MFC for diluting H ₂	Unit	Point 2 MFC for diluting H ₂	Unit	Point 3 MFC for diluting H ₂	Unit
Setpoint	14	0	—	10		20	
Actual Flow	20.2983	0	Sccm	20.331	Sccm	40.424	Sccm
Calibration Gas	Mol%	Diluted Gas	Mol%	Diluted Gas	Mol%	Diluted Gas	Mol%
Butane	4	Butane	4	Butane	1.998390324	Butane	1.337123264
Carbon Dioxide	8	Carbon Dioxide	8	Carbon Dioxide	3.996780648	Carbon Dioxide	2.674246529
Ethane	8	Ethane	8	Ethane	3.996780648	Ethane	2.674246529
Ethylene	2	Ethylene	2	Ethylene	0.999195162	Ethylene	0.668561632
Hydrogen	25	Hydrogen	25	Hydrogen	12.48993953	Hydrogen	8.357020403
Isobutane	2	Isobutane	2	Isobutane	0.999195162	Isobutane	0.668561632
Methane	10	Methane	10	Methane	4.995975811	Methane	3.342808161
Nitrogen	10	Nitrogen	10	Nitrogen	4.995975811	Nitrogen	3.342808161
Propane	6	Propane	6	Propane	2.997585486	Propane	2.005684897
Carbon Monoxide	25	Carbon Monox	25	Carbon Monoxide	12.48993953	Carbon Monoxide	8.357020403
		Hydrogen	0	Hydrogen	50.04024189	Hydrogen	66.57191839
			100		100		100

Note: CH₄ has been highlighted since it is the main generated gas during CHR; only three points were listed here as an example.

5. Build up a correlation between peak area and mole concentration.

Table B.8: Linear correlation between CH₄ mole concentration and measured peak area of CH₄.

H2 flow rate (cc/min)	Measured peak area	Measured peak area/10 ⁵	Mole(%)
0	2253701	22.53701	10
10	1021335	10.21335	4.995976
40	651707	6.51707	3.342808161
60	491258	4.91258	2.505460943
80	398489	3.98489	2.01155901
100	322833	3.22833	1.674746413

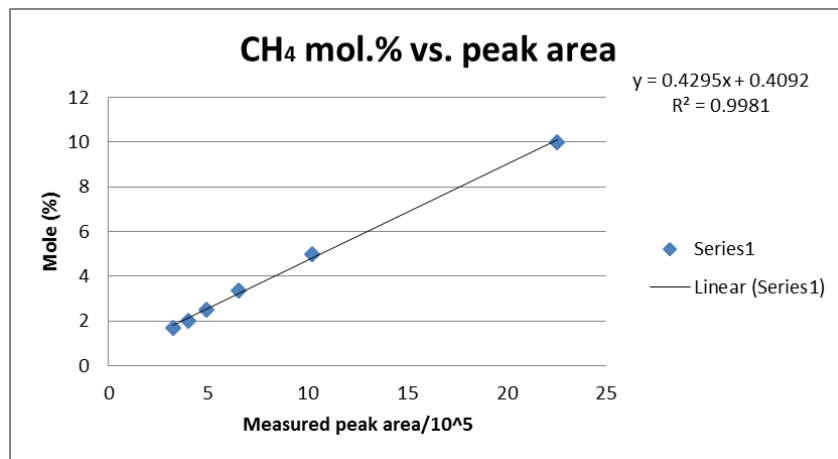


Figure B.10: Linear correlation of measured peak area of CH₄ from GC-FID vs. CH₄ mole concentration.

Appendix C Sample Calculation

C.1 Feed and Products Calculation

(1) Feed Calculation for HDO of 4-methylphenol

4-Methylphenol was chosen as the reactant to mimic the phenol content of a biomass-derived fast pyrolysis oil. This model component was used both in the study of Chapter 2 and Chapter 4.

The compositions of the feed are listed in Table C.1:

Table C.1: Feed compositions for HDO of 4-methylphenol.

Chemicals	Mass (g)
4-methylphenol (4-MP)	2.76
Decalin	87.5 (~ 100 mL)
<i>Calculated wt.% of 4-MP</i>	<i>3.1</i>

Note: after dissolving 4-MP in decalin, a sonication was applied to facilitate the dissolving process and remove the dissolved O₂ from the solvent.

(2) Feed Calculation for HDS of Dibenzothiophene

Dibenzothiophene (DBT) is one of the refractory S components contained in the heavy oil. It was chosen as the model component for synthesized catalysts testing both in Chapter 3 and Chapter 5. The concentration of DBT is 10x's lower in the study of Chapter 5 than in Chapter 3, since the aim of Chapter 5 is to study the S effect on Mo₂C based catalyst and a low concentration could help for capturing this phenomenon. The concentration of the prepared feed are present in Table C.2.

Table C.2: Feed compositions for HDS of dibenzothiophene.

Chemicals	Mass (g) ^a	Mass (g) ^b
Dibenzothiophene (DBT)	1.79	0.179
Decalin	87.5 (~ 100 mL)	87.5 (~100 mL)
<i>Calculated wt.% of DBT</i>	<i>2.0</i>	<i>0.2</i>

a. This feed was used in Chapter 3's study.

b. This feed was used in Chapter 5's study.

(3) Products Calculation by GC-MS Measurement

Two types of calibration methods were used in the present study for the calculation of reaction conversion and product selectivity. In Chapter 3, an internal calibration method was applied by using diphenylmethane (DPM) as the internal standard. Both the reactant DBT and two main products biphenyl (BPh) and cyclohexylbenzene (CHB) were prepared into different concentrations for the accuracy of the experiment with the addition of DPM. Also, the obtained samples as drawn from the reactor were prepared by the same methodology as the standards.

Here, a calibration table was built for all standards, as shown in Table C.3 (a calibration for DBT with two different concentration ranges).

Table C.3: GC-MS calibration table for DBT concentration with the addition of DPE as internal standard (IS).

No.	aim wt%	DBT(g)	Decalin(g)	real wt% of DBT	—	Area of DPE	Area of DBT	Area Ratio of DBT:DPE	DPE(mg)	sample (mg)	Real wt% of DBT	DBT (mg) ^a	wt% of DBT in prepared sample with IS ^b	wt% of DPE ^c	wt% ratio of DBT to DPE
1	1	0.0958	8.9273	1.061719365	—	3647782	9488086	2.601056203	0.612	191.21	1.06172	2.030134832	1.058332029	0.319042456	3.3172138
	Aim wt%	1 wt% DBT solvent(g)	Diluted to xx g	real DBT (g)	Real wt% of DBT	Area of DPE	Area of DBT	Area Ratio of DBT:DPE	DPE(mg)	sample (mg)	Real wt% of DBT	DBT (mg)	wt% of DBT in prepared sample with IS	wt% of DPE	wt% ratio of DBT to DPE
2	0.1	1.0957	10.1299	0.011633259	0.114840813	4022566	1116961	0.277673754	0.612	185.78	0.11484	0.213350113	0.114463742	0.328342034	0.3486113
3	0.3	1.0639	3.3738	0.011295633	0.334804455	5168344	3230321	0.625020509	0.606	184.51	0.3348	0.617751048	0.333708437	0.327360534	1.0193912
4	0.5	1.0248	2.1398	0.0108805	0.50848212	4736680	4738576	1.00040028	0.602	187.09	0.50848	0.951324284	0.506851232	0.320736522	1.5802729
5	0.7	0.9989	1.4204	0.010605515	0.746656934	3785651	6895621	1.821515243	0.611	185.59	0.74666	1.385735536	0.74420688	0.328136496	2.2679796
ed on 0.1148408 wt% DBT sample (Sample #: 2)															
No.	Aim wt%	1 wt% DBT solvent(g)	Diluted to xx g	real DBT (g)	Real wt% of DBT	Area of DPE	Area of DBT	Area Ratio of DBT:DPE	DPE(mg)	sample (mg)	Real wt% of DBT	DBT (mg)	wt% of DBT in prepared sample with IS	wt% of DPE	wt ratio of DBT to DPE
6	0.01	1.0892	10.0412	0.001250846	0.012457137	5639137	91056	0.016147152	0.598	186.76	0.01246	0.023264699	0.012417376	0.319178462	0.0389042
7	0.03	1.1641	3.3819	0.001336862	0.039529902	6231039	367535	0.058984545	0.614	182.61	0.03953	0.072187135	0.039397437	0.335101622	0.1175686
8	0.0076	1.0715	13.0998	0.001230519	0.00939342	4314765	74821	0.017340689	0.624	190.8	0.00939	0.017922175	0.009362798	0.325986449	0.0287214

- DBT (mg) was calculated by $\frac{\text{sample (mg)} \times \text{Real wt\%}}{100}$;
- wt% of DBT was calculated by $\frac{\text{DBT (mg)}}{\text{DPE (mg)} + \text{sample (mg)}}$;
- wt% of DPE was calculated by $\frac{\text{DPE (mg)}}{\text{DPE (mg)} + \text{sample (mg)}}$.

For sample No.1~No.5, the obtained calibration curve is shown in Figure C.1:

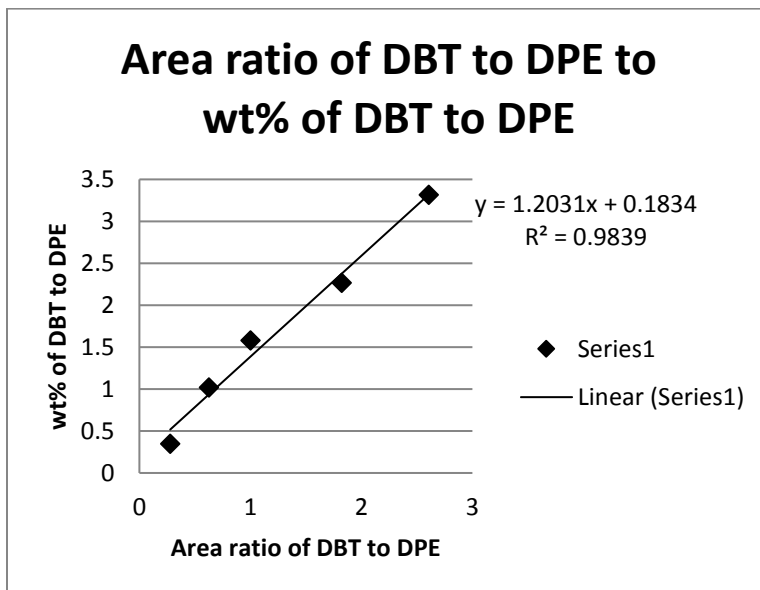


Figure C.1: A linear correlation between area ratio of DBT to DPE and wt% of DBT to DPE in high concentration range.

For sample No.5~No.8, the obtained calibration curve is shown in Figure C.2:

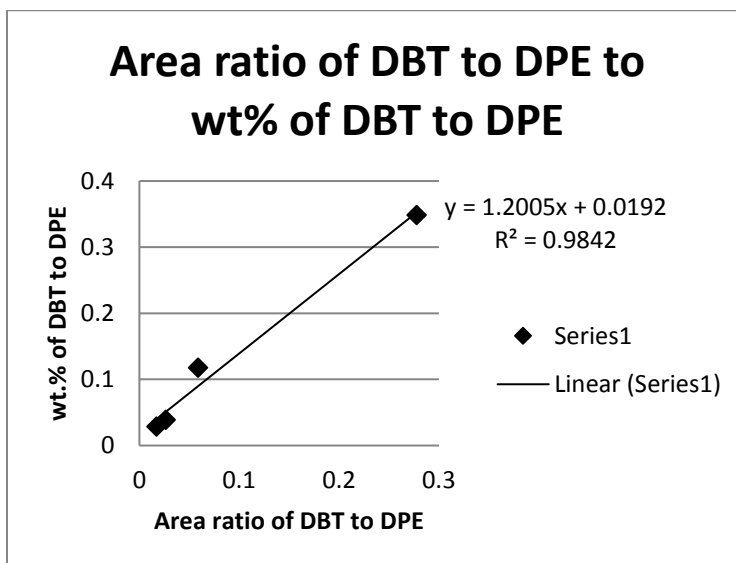


Figure C.2: A linear correlation between area ratio of DBT to DPE and wt% of DBT to DPE in low concentration range.

C.2 Calculation Procedure of MoO_xC_y Formula

Table C.4: The calculation procedure for Mo₂C and MoO_xC_y contents in 10%Mo/AC catalysts.

Catalyst	Burn-off	Mo	Mo ²⁺ by XPS	Mo ₂ C	MoO _x C _y	O content		x	y
		loading μmol/g cat	mol%	μmol/gcat	μmol/gcat	wt%	μmol/gcat		
10%Mo/AC-600	11.96	1095.2	9.94	108.9	986.3	2.59	1618.8	1.64	0.33
10%Mo/AC-650	21.34	1225.4	23.69	277.7	947.7	1.76	1099.3	1.16	0.61
10%Mo/AC-700	43.01	1619.0	50.47	853.9	752.1	1.00	624.2	0.83	0.90

Calculation process:

For 10 g of 10%Mo/AC precursor, it contains 1 g of Mo (eqv. 1.81 g AHM) and 9 g of AC.

The total amount of catalyst precursor: 1.81g + 9.0 g = 10.81 g

The mass loss of 10%Mo/AC-650 catalyst: 10.81 g x 21.34 % = 2.31 g

The remaining mass of 10%Mo/AC-650 catalyst: 10.81 g - 2.31 g = 8.50 g

The Mo amount as per gram of synthesized catalyst: $\frac{1 \text{ gMo}}{8.50 \text{ gcat.}} = 0.1176 \frac{\text{gMo}}{\text{gcat.}} = 1225.4 \frac{\mu\text{molMo}}{\text{gcat.}}$

The Mo composition (%) of different valences as measured by XPS are as follows:

Mo²⁺: 23.69; Mo³⁺: 18.01; Mo⁴⁺: 3.79; Mo⁵⁺: 31.96; Mo⁶⁺: 22.55

The Mo amount from Mo₂C: $1225.4 \frac{\mu\text{molMo}}{\text{gCat.}} \times 23.69\% = 277.68 \frac{\mu\text{molMo}}{\text{gCat.}}$

The Mo amount from MoO_xC_y: $1225.4 \frac{\mu\text{molMo}}{\text{gCat.}} - 277.68 \frac{\mu\text{molMo}}{\text{gCat.}} = 947.72 \frac{\mu\text{molMo}}{\text{gCat.}}$

The O content for 10%Mo/AC-650 is 5.68 wt% from O analyzer; the O content from SiO₂ is $\frac{3.12\%}{(1-21.4\%)} = 3.92\%$; the O content from

MoO_xC_y: $5.68\% - 3.92\% = 1.76\% = \frac{1.76 \text{ wt}\%}{16 \text{ g/mol}} = 1099.34 \frac{\mu\text{molO}}{\text{gCat.}}$

So, $x = \frac{1099.24}{947.72} = 1.16$.

The formula of MoO_xC_y becomes MoO_{1.16}C_y, where y can be calculated as below:

$$y = \frac{\frac{18.01\% \times 3 + 3.79\% \times 4 + 31.96\% \times 5 + 22.55\% \times 6}{100\% - 23.69\%} - 1.16 \times 2}{4} = 0.61$$

The formula of MoO_xC_y of 10%Mo/AC-650 is MoO_{1.16}C_{0.61}.

C.3 Calculation of Presulfiding Parameters for MoS₂/AC Catalyst Preparation

(I) The presulfiding was carried out in a batch reactor as reported in Chapter 3 and the details are as follows:

- Calculate the amount of Mo in 10%Mo/AC precursor;

For example: in each batch of presulfiding, 5 g of 10%Mo/AC precursor was used.

The relative amount of Mo in 10%Mo/AC precursor is 0.5 g, which is equivalently to 5.2×10^{-3} mol.

- Calculate the required amount CS₂ to sulfide Mo;

In order to provide enough S to sulfide Mo, the added CS₂ amount is 1.5x's higher than Mo in present study.

$$\text{CS}_2(\text{mL}) = \frac{1.5 \cdot \text{Mo}(\text{mol}) \cdot \left(\frac{76.14 \text{ g}}{\text{mol}}\right)}{\left(\frac{1.266 \text{ g}}{\text{mL}}\right)} \quad (\text{Eq. C-1})$$

So, for 5 g of precursor, the required CS₂ is 0.469 mL.

- Calculate the required amount of H₂ pressure for 10 vol% H₂S/H₂;

Since $\text{CS}_2 + 2\text{H}_2 \rightarrow 2\text{H}_2\text{S}$, the required amount of H₂ to convert CS₂ into H₂S is 2x's of CS₂ mole amount. The total required H₂ amount is roughly calculated as follows:

$$\text{H}_2(\text{mL}) = 1.5 \cdot \text{Mo}(\text{mol}) \cdot 2 \cdot \left(\frac{22.4 \text{ L}}{\text{mol}}\right) \left(\frac{1000 \text{ mL}}{\text{L}}\right) \cdot 10 \quad (\text{Eq. C-2})$$

So, for 5 g of precursor, the total required H₂ is 3494.4 mL.

- Calculate the required initial pressure of H₂.

100 mL decalin was used as solvent during presulfiding. The left volume in 300 mL autoclave is 200 mL. The required initial pressure of H₂ was estimated by the ideal gas law ($PV=nRT$) of $P_1V_1=P_2V_2$, where $P_1=1 \text{ atm}$, $V_1=3494.4 \text{ mL}$, $V_2=200 \text{ mL}$.

$$P_2 = \frac{P_1 V_1}{V_2} = \frac{(1 \text{ atm})(3494.4 \text{ mL})}{(200 \text{ mL})} = 17.47 \text{ atm} = 253.34 \text{ psi} \quad (\text{Eq. C-3})$$

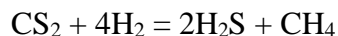
(II) In Chapter 5, the presulfiding was carried out in a continuous flow fixed bed reactor to prepare MoS₂/APC in-situ.

Presulfiding conditions:

3.0 MPa and 370 °C for 3 hrs from under 50 cc (STP)/min H₂ with 0.0833 cc (STP)/min CS₂ in decalin to prepare 5.75 vol% H₂S/H₂.

Calculation process:

$$\text{H}_2 \text{ flow rate} = 50 \left[\frac{\text{mL}}{\text{min}} \right] = 3 \left[\frac{\text{L}}{\text{h}} \right] = \frac{3 \left[\frac{\text{L}}{\text{h}} \right]}{22.4 \left[\frac{\text{L}}{\text{mol}} \right]} = 0.1339 \left[\frac{\text{mol}}{\text{h}} \right]$$



$$\text{Mass flow rate of CS}_2 = 0.1339 \left[\frac{\text{mol}}{\text{h}} \right] \times 5.75 \% \div 2 = 3.84 \times 10^{-3} \left[\frac{\text{mol}}{\text{h}} \right] = 0.2923 \left[\frac{\text{g}}{\text{h}} \right]$$

$$\text{Volumetric flow rate of mixture (CS}_2 \text{ and decalin)} = 0.0833 \left[\frac{\text{cc}}{\text{min}} \right] = 5.0 \left[\frac{\text{mL}}{\text{h}} \right]$$

Set mass concentration of CS₂ in decalin as x,

$$\text{The density of the mixture (CS}_2 \text{ and decalin)} \rho_{\text{mix}} = \rho_{\text{CS}_2} * x + \rho_{\text{Decalin}} * (1-x) = 1.266 x + 0.896 * (1-x) \left[\frac{\text{g}}{\text{cm}^3} \right]$$

$$\text{The mass flow rate of the mixture (CS}_2 \text{ + Decalin)} = 5.0 \left[\frac{\text{mL}}{\text{h}} \right] \times \rho_{\text{mix}} = 5 * (1.266 x + 0.896 (1-x))$$

$$\text{The mass flow rate of mixture} * x = \text{CS}_2 \text{ mass flow rate} \rightarrow x = 6.24\%$$

So, the calculated concentration of CS₂ in decalin is 6.24 wt%.

C.4 Stacking Degree (N) Calculation for MoS₂ from TEM Images

As reported in Chapter 3, the used Ni-Mo₂C/AC catalyst could form some MoS₂ layers. The number of slabs per stack was recorded by an average stacking degree (N), calculated by $N = \frac{\sum_{i=1..t} n_i N_i}{\sum_{i=1..t} n_i}$, where n_i is the number of stacks with N_i layers.

For example:

For Ni_{0.19}MoC-600 catalyst (In Chapter 3), there are 39 particles being calculated, with 7 of one layer, 28 of two layers and 4 of three layers. So, the calculation is $N = \frac{28 \times 2 + 1 \times 7 + 3 \times 4}{28 + 7 + 4} = 1.9230$.

The same methodology was applied on other catalysts and the results are summarized in Table C.5.

Table C.5: MoS₂ stacking degree (N) of different used Ni-Mo₂C/AC catalysts as reported in Chapter 3.

Used catalyst	N
Ni _{0.09} Mo ₂ C/AC-600	0.4324
Ni _{0.19} Mo ₂ C/AC-600	1.9230
Ni _{0.38} Mo ₂ C/AC-600	2.7800
Ni _{0.44} Mo ₂ C/AC-600	4.2000
Ni _{0.76} Mo ₂ C/AC-600	4.8182

C.5 Experimental Details for Chapter 4

A detailed experimental recording of activated petroleum coke (APC) supported Mo₂C catalysts prepared at three different CHR temperatures with 90 min holding time as reported in Chapter 2 are listed in Table C.6:

Table C.6: Experimental lists of HDO of 4-MP in Chapter 2.

Catalyst	Burn-off %	g _{Mo} /g _{cata} a	Added cata. amount (g)	Calc Mo amount in added cata.(g) ^b	Mo wt% measured by ICP	Real Mo amount in added cata. (g) ^c	Feed		g _{Mo} /g _{4-MP} ^d	g _{Mo} /mol _{4-MP} ^e	g _{Mo} /mL _{4-MP} ^f
							4-MP (g)	Decalin(g)			
Mo600_APC-90	20.10	0.1252	0.5776	0.0723	10.23	0.0591	2.7839	87.3272	0.0212	2.2951	0.000591
Mo650_APC-90	35.42	0.1548	0.4583	0.0710	12.59	0.0577	2.7720	87.0618	0.0208	2.2508	0.000577
Mo700_APC-90	53.67	0.2158	0.3323	0.0717	17.76	0.0590	2.7741	86.5691	0.0213	2.3004	0.000590

a. It was calculated by $\frac{0.1}{(1 - \frac{\text{burn off}\%}{100})}$;

b. The calculated Mo amount in added catalyst was calculated by $\frac{g_{Mo}}{g_{cata.}} \times \text{added cata. amount}$;

c. The real added Mo amount in added catalyst was calculated by $\frac{\text{Mo wt\% measured by ICP}}{100} \times \text{added cata. amount}$;

d. It was calculated by $\frac{\text{Real Mo amount in added catalyst (g)}}{\text{mass of 4-MP in Feed (g)}}$;

e. It was calculated by $\frac{g_{Mo}}{g_{cata.}} \times 108.13 \left(\frac{g}{mol}\right)$;

f. It was calculated by $\frac{\text{Real Mo amount in added catalyst (g)}}{100 \text{ (mL)}}$.

C.6 Rate Constants Calculation Reported in Chapter 4

All the experiment were run in a batch reactor at 350 °C and 4.3 MPa for 5 h. In order to exclude the reactor heat up period from the experiment, a liquid was drawn from the side line of the reactor and recorded as the first point (t=0 min). Also, other three samples were drawn at t = 60, 180, and 300 min, respectively. An identification and quantitative analysis were achieved using a Shimadzu GC/MS analyzer. The rate constants were calculated by assuming pseudo 1st order reaction. The used matlab code is shown in Appendix D.1.

Table C.7: Activity, selectivity, and kinetic rate constants for HDO of 4-methylphenol reported in Chapter 2.

Catalyst	$S_{DDO/HYD}$ ^b	k_{DDO} (mL/g _{Mo} .min) ^c	k_{HYD} (mL/g _{Mo} .min) ^c	k (mL/g _{Mo} .min) ^d
Mo600_APC-90	4.89	4.66±0.53	0.95±0.42	5.62±0.95
Mo650_APC-90	6.88	5.40±0.38	0.79±0.29	6.19±0.67
Mo700_APC-90	8.23	6.69±0.53	0.61±0.40	7.30±0.93

- Reaction conversion (γ) was obtained by running experiment for 5 h.
- Selectivity of DDO to HYD was calculated by $S_{DDO/HYD} = \frac{k_{DDO}}{k_{HYD}}$.
- Both DDO (k_{DDO}) and HYD (k_{HYD}) rate constants were calculated by assuming pseudo 1st order reaction.
- It was calculated by $K = k_{DDO} + k_{HYD}$.

C.7 Calculation of Activation Energy of Carbon Hydrogenation in Chapter 4

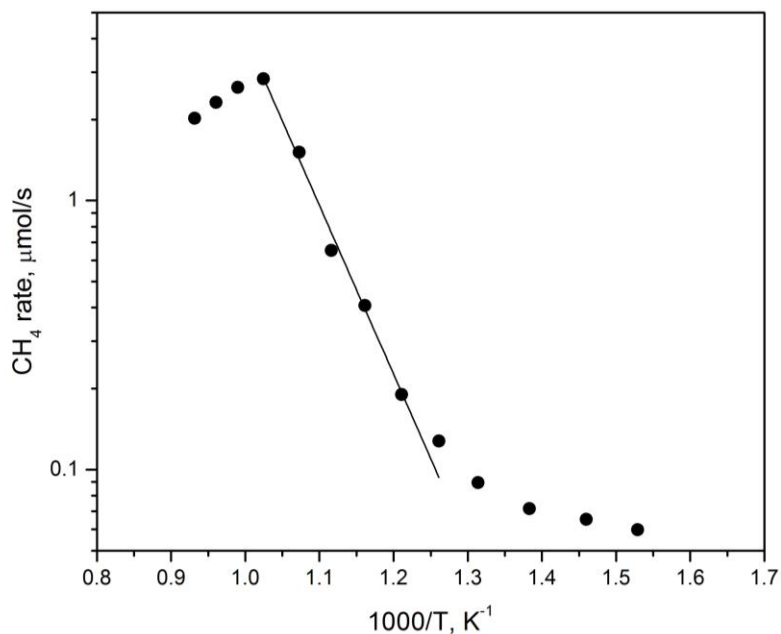
Table C.8: Experimental data of in-situ exit gas analysis of Mo800_APC catalyst by carbothermal hydrogenation reduction.

Temp.(°C)	Time	Time interval (min)	CH ₄ area (RT = 1.45 min)	CH ₄ mole%	1000/T (1/K)	CH ₄ rate (μmol/s) ^a
62	3/8/2017 13:03	37	0	0	2.98507	0
110	3/8/2017 13:50	84	0	0	2.61097	0
174	3/8/2017 14:54	148	0	0	2.23714	0
251	3/8/2017 16:11	225	130	0.00416	1.9084	0.00309
297	3/8/2017 16:57	271	161	0.005152	1.75439	0.00383
341	3/8/2017 17:42	316	390	0.01248	1.62866	0.00928
381	3/8/2017 18:21	355	2514	0.0804238	1.52905	0.0598
412	3/8/2017 18:52	386	2950	0.0877813	1.45985	0.06527
450	3/8/2017 19:30	424	3460	0.0963875	1.38313	0.07167
488	3/8/2017 20:08	462	4883	0.1204006	1.31406	0.08953
520	3/8/2017 20:47	501	7937	0.1719369	1.26103	0.12785
553	3/8/2017 21:13	527	12919	0.2560081	1.21065	0.19036
588	3/8/2017 21:50	564	32346	0.5481261	1.16144	0.40758
623	3/8/2017 22:23	597	108809	0.8765347	1.11607	0.65178
659	3/8/2017 22:59	633	378360	2.0342562	1.07296	1.51264
703	3/8/2017 23:44	678	793443	3.8170377	1.02459	2.83828
737	3/9/2017 0:17	711	729335	3.5416938	0.9901	2.63354
768	3/9/2017 0:48	742	631151	3.1199935	0.96061	2.31997
800	3/9/2017 1:21	775	537979	2.7198198	0.93197	2.02241

a.
$$\text{CH}_4 \text{ rate} = \frac{\frac{\text{CH}_4 \text{ mol\%} \times 100 \text{ mL/min}}{100} \times 10^6 \frac{\mu\text{mol}}{\text{mol}}}{22414 \frac{\text{mol}}{\text{mL}} \times 60 \frac{\text{s}}{\text{min}}} \times 10^6 \frac{\mu\text{mol}}{\text{mol}}$$

A linear regression can be obtained in the range of $T = 550 \sim 700 \text{ }^\circ\text{C}$ with a $R^2 = 0.9950$.

Figure C.3: Arrhenius plot of temperature dependence in the range of 550-700 °C for CH₄ formation.



The calculated results are shown in Figure C.4:

Figure C.4: Calculated activation energy (Ea) for carbon hydrogenation.

Update Table			
	A	B	
1	Model	Exp2PMod1	
2	Equation	$y = a \cdot \exp(b \cdot x)$	
3	Reduced Chi-Sqr	0.00558	
4	Adj. R-Square	0.99495	
5			Value
6	E	a	7.73236E6
7	E	b	-14.45548
			Standard Error
			5.65784E6
			0.70249

Then, $E_a = b \cdot (-8.314) = 120.1 \text{ kJ/mol}$; the pre-exponential factor $k_0 = a = 7.7$.

C.8 Reaction Phase Determination from ASPEN Plus Calculation

A phase determination was simulated by ASPEN plus in a flash to see if the reaction was running in one phase or two phases in Chapter 5 and Chapter 6.

As an example, HDS of 0.2 wt% DBT in a fixed bed reactor was put here:

Simulation conditions: 350 °C (662 F), 4.1 MPa (600 psi), and $H_2/\text{Feedmix} = 600$

Reactant: 0.2 wt% DBT in decalin (equiv. to 0.1541 mol%)

Thermodynamics method: Wilson

Steams:

Table C.9: Mole flow rates of different components in HDS of dibenzothiophene in fixed bed reactor.

Component	Name	Flow rate (mol/h)
H ₂	H ₂	414.0
DBT	Feedmix	0.1541
Decalin		99.8459

The calculation details for mole flow rates are as follows:

$$\text{Density of Feedmix: } \rho_{mix} = \frac{0.896 \times 1.252}{0.896 \times 0.2\% + 1.252 \times 99.8\%} = 0.8965 \text{ g/cm}^3$$

Mole weight of the Feedmix:

$$M_{mix} = 138.25 \frac{\text{g}}{\text{mol}} \times 99.8459\% + 184.26 \frac{\text{g}}{\text{mol}} \times 0.1541\% = 138.32 \frac{\text{g}}{\text{mol}}$$

Assume there is 1 L of feedmix,

$$\text{Mole of Feedmix: } n_{mix} = \frac{\rho_{mix} \times V_{mix}}{M_{mix}} = \frac{0.8965 \frac{\text{g}}{\text{cm}^3} \times 1.0 \text{ L} \times 1000 \frac{\text{cm}^3}{\text{L}}}{138.32 \frac{\text{g}}{\text{mol}}} = 6.48 \text{ mol}$$

Since $H_2/\text{Feedmix}$ (v/v) = 600, 1 L of feedmix needs 600 L H₂,

Mole of H₂:

$$n_{H_2} = \frac{600 \text{ L}}{22.4 \frac{\text{L}}{\text{mol}}} = 26.79 \text{ mol}$$

The mole ratio between Feedmix and H₂ is:

$$\frac{6.48 \text{ mol}}{26.79 \text{ mol}} = \frac{1}{4.14}$$

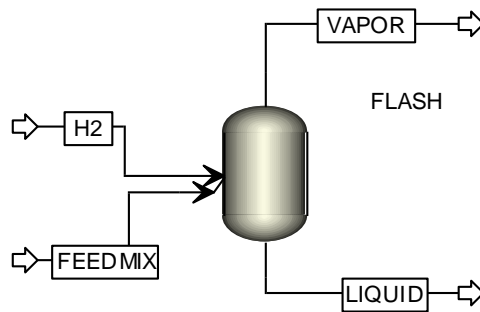


Figure C.5: Aspen flowsheet for H₂ and feedmix in a flash reactor.

Table C.10: Calculated heat and material balance table.

Heat and Material Balance Table					
Stream ID		FEEDMIX	H2	LIQUID	VAPOR
Temperature	F	662.0	662.0		662.0
Pressure	psia	600.00	600.00	600.00	600.00
VaporFrac		0.000	1.000		1.000
Mole Flow	lbmol/hr	0.220	0.913	0.000	1.133
Mass Flow	lb/hr	30.495	1.840	0.000	32.335
Volume Flow	cuft/hr	0.832	18.311	0.000	22.734
Enthalpy	MMBtu/hr	-0.010	0.004		-0.004
Mole Flow	lbmol/hr				
H2			0.913		0.913
C10H1-01		0.220			0.220
C12H8-01		<0.001			<0.001

The simulation shows that every component will go into vapor phase. So, it demonstrates that this reaction happened in one phase. The same simulation has been applied in HDN of carbazole (CBZ) and HDO of dibenzofuran (DBF). All the results show the gas phase reaction.

C.9 System Dynamic Response in Fixed-bed Reactor

The system dynamic response time was measured to make sure all data reported in Chapter 5 and Chapter 6 are effective to show the transition/deactivation of Mo₂C/APC catalyst. 2% DBT in decalin was used as feed to pump into the reactor with a LHSV of 4 h⁻¹. The feed was injected into the reactor once the furnace started heating. SiC was used here to represent the catalyst bed. The reactor temperature can reach to 350 °C after 31 min. Then, the 1st sample was drawn from the reactor. The experiment was keep running by drawing samples from the condenser every 20 min. The total C mol.% was calculated and shown in Figure C.6.

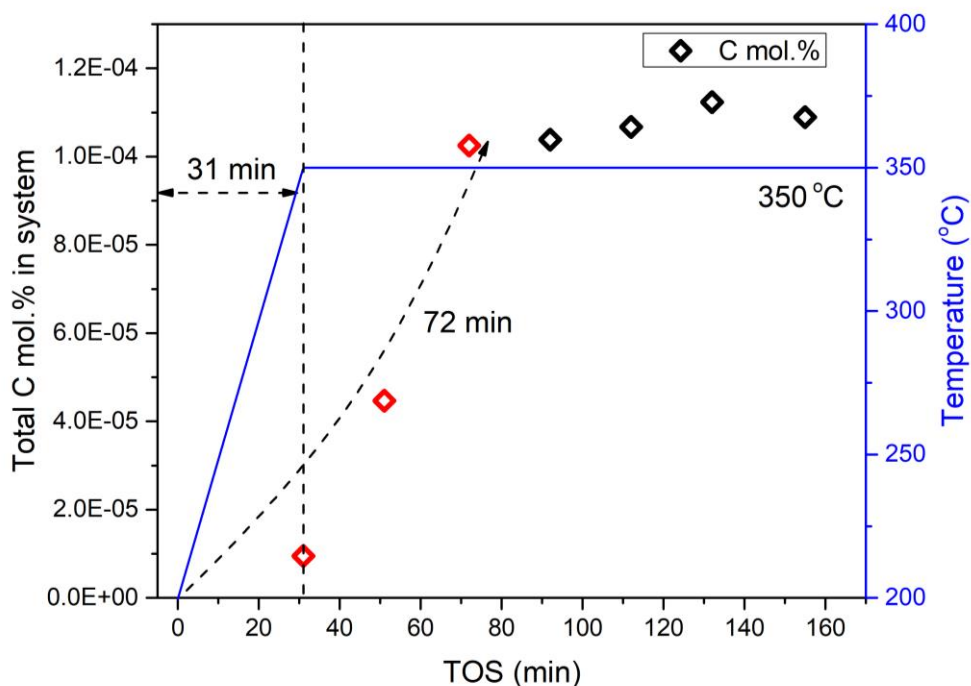


Figure C.6: Total C mol.% in fixed-bed system at 350 °C and LHSV=4 h⁻¹.

It shows that the system took 72 min to reach a C mol.% balance. Excluded the 31 min from heating up phase, it only takes 41 min to get mass balance. This measured experimental data is

accordance with the calculated response time (usually it is 3x's residence time; 45 min). So, all the experimental data reported in Chapter 5 and Chapter 6 is after 41 min.

Appendix D Kinetic Model Code

D.1 Matlab Code for HDO of 4-methylphenol in Batch Reactor

This code has been used for many years by this research group. In the present study, it is used to calculate the rate constants of HDO of 4-methylphenol presented in Chapter 2 and Chapter 4. All the products have been grouped into HYD and DDO.

For example, the product distribution of 10%Mo/AC-650 catalyst in HDO of 4-methylphenol at 350 °C is reported in Table D.1. These data shown here were used for the modeling as below.

Since modelmulti code, Jacobian matrix and least square code won't change for HDO of 4-methylphenol and HDS of dibenzothiophene, they are present one time in this thesis in Appendix D.2.

Table D.1: Products distribution of HDO of 4-methylphenol at 350 °C with 10%Mo/AC-650 catalyst.

Time (min)	4- methylphenol	DDO product	HYD products			Sum of HYD products
		(mol/L)	(mol/L)	1- Methylcycloh exene	4- Methylcyclohe xene	
60	0.226123	0.024646849	0.001851564	0.001820452	0.002706077	0.006378
180	0.185071	0.057222816	0.005373534	0.004825215	0.005081097	0.01528
300	0.143882	0.087081926	0.009559886	0.008039904	0.008519898	0.02612
420	0.114825	0.109486825	0.013872935	0.006260651	0.01324843	0.033382

(1) Main body

```
clear all
```

```
global nvar nx x0 y0
```

```
global verbose
```

```

global n1 n2 n3 n4 H2
verbose(1:2)=1;

% x is the indep variable vector e.r. time measurements
% y is the matrix of responses
% columns of y are responses y1, y2(e.g. mol fraction of component 1 and 2)
% rows of y are y values at the values of the indep variable (time) in x
% first row of y is initial value of response
% the program uses the Levenbreg-Marquart method to estimate parameters
% and calculate -done in leasqr and dfdp
% the L-M requires the model to be calculated- this is done in modelmulti.m
% and assumes the model is a series of ODEs, with the number of ODEs is
% equal to the number of responses. The ODEs are calculated in ODEfunm.
% Note that this function must use the correct model for each y
% time data (min)
T=[0 60 180 300]

nt=length (T)
x(1:nt-1)=T(2:nt)
x
nx=length(x)

% 4-methylphenol concentration data (mol/L)
CAX=[0.226123
0.185071
0.143882
0.114825];

% DDO concentration data (mol/L)
CBX=[0.024646849

```

```
0.057222816
0.087081926
0.109486825];
```

```
% HYD concentration data (mol/L)
```

```
CCX=[0.006378
0.01528
0.02612
0.033382];
```

```
for j=1:nt-1
    y1(j)=CAX(j+1);
    y2(j)=CBX(j+1);
    y3(j)=CCX(j+1);
```

```
end
```

```
nvar=3;
x0=0;
```

```
oldx=x;
nx= length(x);
y=[y1';y2';y3'];
% y=[y1';y2'];
newy=y(:);
oldy=reshape(newy,nx,nvar);
x=x';
newx=[x;x;x];
%newx=[x;x;]
y01(1:nx)=CAX(1);
```

```

y02(1:nx)=CBX(1);
y03(1:nx)=CCX(1);

newy0=[y01';y02';y03'];
%newy0=[y01';y02'];
%INPUT DATA NOW IN CORRECT COLUMN FORMAT
y0=newy0
x=newx
y=newy

%provide initial parameter guesses
theta=[0.001 0.009];
np=length(theta)
pin=theta
nxcheck=size(x)
nycheck=size(y)

%Begin calculation by calling L-M least squares routine

[f,p,kvg,iter,corp,covp,covr,stdresid,Z,r2]=leasqr(x,y,pin,'modelmulti',0.00001,100000);
disp('RESPONSE:')
if kvg==1
    disp('PROBLEM CONVERGED')
elseif kvg==0
    disp('PROBLEM DID NOT CONVERGE')
end
format shortEng
oldf=reshape(f,nx,nvar);
oldr=reshape(y-f,nx,nvar);
disp('X-values:')

```

```

disp(oldx')
disp('Y-values')
disp(oldy)
disp('f-values - i.e. model calculated responses')
disp(oldf)
disp('Residuals:')
disp(olldr)
% disp('Standardized residuals:')
% disp(stdresid)
disp ('Estimated parameter values are;')
disp (p)
disp ('Covariance of estimated parameters - sqrt of diagonal gives CL')
disp (covp)
disp ('R2 values is;')
disp (r2)
plot (oldx,oldy,'d'), hold, plot (oldx,oldf)
figure
subplot(3,3,1)
plot(oldx(:),oldy(:,1),'o',oldx(:),oldf(:,1),'--')
title('4MP')
xlabel('Time (min)')
ylabel('Concentration (mol/L)')
subplot(3,3,2)
plot(oldx(:),oldy(:,2),'o',oldx(:),oldf(:,2),'--')
title('DDO')
xlabel('Time (min)')
ylabel('Concentration (mol/L)')
subplot(3,3,3)
plot(oldx(:),oldy(:,3),'o',oldx(:),oldf(:,3),'--')
title('HYD')

```

```
xlabel('Time (min)')
```

```
ylabel('Concentration (mol/L)')
```

(2) ODE code

```
function yprime=ODEfunm(xatx,yatx,pin)
```

```
global nvar nx x0 y0 xstep
```

```
% disp('*****YPRIME')
```

```
% disp(knt)
```

```
% nx
```

```
k1=pin(1);
```

```
k2=pin(2);
```

```
%ntest=(knt/nx);
```

```
yp(1)=-k1*yatx(1)-k2*yatx(1);
```

```
yp(2)=k1*yatx(1);
```

```
yp(3)=k2*yatx(1);
```

```
yprime=[yp(1)';yp(2)';yp(3)'];
```

An example of rate constant calculation results by matlab code in Appendix D.1:

Table D.2: Calculated rated constants of APC supported Mo₂C catalysts prepared at 600 and 650 °C.

Catalyst	k'_{DDO}	$\Delta k'_{\text{DDO}}$	$k^{\text{T}}_{\text{DDO}}$	$\Delta k^{\text{T}}_{\text{DDO}}$	k_{DDO}	Δk_{DDO}	k'_{HYD}	$\Delta k'_{\text{HYD}}$	$k^{\text{T}}_{\text{HYD}}$	$\Delta k^{\text{T}}_{\text{HYD}}$	k_{HYD}	Δk_{HYD}	K'	$\Delta K'$
Mo600_APC-90	0.003	3E-04	5E-04	1.0095E-05	0.0028	0.0003	7E-04	2E-04	0.0002	1.047E-05	0.0006	0.0002	0.003	6E-04
Mo650_APC-90	0.004	2E-04	5E-04	1.0095E-05	0.0031	0.0002	6E-04	2E-04	0.0002	1.047E-05	0.0005	0.0002	0.004	4E-04

Where k'_{DDO} - rate constant for DDO route; $\Delta k'_{\text{DDO}}$ - standard deviation of rate constant for DDO route; k'_{HYD} - rate constant for HYD route; $\Delta k'_{\text{HYD}}$ - standard deviation of rate constant for HYD route; $k^{\text{T}}_{\text{DDO}}$ - rate constant for DDO route from thermal reaction; $\Delta k^{\text{T}}_{\text{DDO}}$ - standard deviation of rate constant for DDO route from thermal reaction; $k^{\text{T}}_{\text{HYD}}$ - rate constant for HYD route from thermal reaction; $\Delta k^{\text{T}}_{\text{HYD}}$ - standard deviation of rate constant for HYD route from thermal reaction; k_{DDO} - rate constant for DDO route excluding thermal reaction; Δk_{DDO} - standard deviation of rate constant for DDO route excluding thermal reaction; k_{HYD} - rate constant for HYD route excluding thermal reaction; Δk_{HYD} - standard deviation of rate constant for HYD route excluding thermal reaction.

Note: The unit of all the rate constants reported here is [1/min].

After unit conversion:

Catalyst	k_{DDO}	Δk_{DDO}	k_{HYD}	Δk_{HYD}	K	ΔK
Mo600_APC-90	4.665	0.534	0.954	0.422	5.618	0.956
Mo650_APC-90	5.404	0.376	0.786	0.286	6.189	0.662

Note: The unit of all rate constants reported here is [mL/g_{Mo}.min]

D.2 Matlab Code for HDS of Dibenzothiophene in Batch Reactor

The following codes were used to model the HDS of DBT in batch reactor. The activity data of Ni_{0.19}Mo₂C/AC-550 catalyst were used as an example to show the process of this calculation.

Since the catalyst could go through a sulfidation in the 1st hour of the HDS reaction, the experimental data obtained after 1 h were used for kinetic analysis. The ODE code was written based on reaction pathways.

(1) Main Body

```
>> clear all
global nvar nx x0 y0
global verbose
global n1 n2 n3 n4 H2
verbose(1:2)=1;

% x is the indep variable vector e.r. time measurements
% y is the matrix of responses
% columns of y are responses y1, y2 (e.g. mol fraction of component 1 and 2)
% rows of y are y values at the values of the indep variable (time) in x
% first row of y is initial value of response
% the program uses the Levenberg-Marquart method to estimate parameters
% and calculate done in m-files of leasqr and dfdp
% these two m-files are designed for single response
% the L-M requires the model to be calculated- this is done in modelmulti.m
% and assumes the model is a series of ODEs, with the number of ODEs is
% equal to the number of responses.
% The ODEs are calculated in ODEfunm.
% Note that this function must use the correct model for each y
% the calculated rate constants are in the unit of [1/min]

% Time data (min)
T=[60 180 300]

nt=length(T)
```

```
x(1:nt-1)=T(2:nt)
```

```
nx=length(x)
```

```
% DBT concentration data (mol/L)
```

```
CAX=[8.1175E-02
```

```
6.3547E-02
```

```
5.6010E-02];
```

```
% THDBT concentration data (mol/L)
```

```
CBX=[1.0873E-03
```

```
2.0758E-03
```

```
2.6117E-03];
```

```
% BPh concentration data (mol/L)
```

```
CCX=[1.3937E-02
```

```
2.6506E-02
```

```
3.3690E-02];
```

```
% CHB concentration data (mol/L)
```

```
CDX=[7.5116E-04
```

```
3.1119E-03
```

```
4.2710E-03];
```

```
for j=1:nt-1
```

```
    y1(j)=CAX(j+1);
```

```
    y2(j)=CBX(j+1);
```

```
    y3(j)=CCX(j+1);
```

```
    y4(j)=CDX(j+1);
```

```
end
```

```
nvar=4;
```

```
x0=0;
```

```
oldx=x;
```

```
nx=length(x);
```

```
y=[y1';y2';y3';y4'];
```

```
%y=[y1';y2';y3'];
```

```
newy=y(:);
```

```

oldy=reshape(newy,nx,nvar);
x=x';
newx=[x;x;x;x];
%newx=[x;x;x]
y01(1:nx)=CAX(1);
y02(1:nx)=CBX(1);
y03(1:nx)=CCX(1);
y04(1:nx)=CDX(1);

newy0=[y01';y02';y03';y04'];
%newy0=[y01';y02';y03'];
%INPUT DATA NOW IN CORRECT COLUMN FORMAT
y0=newy0
x=newx
y=newy

%provide initial parameter guesses
theta=[0.001 0.001 0.00001];
np=length(theta)
pin=theta
nxcheck=size(x)
nycheck=size(y)

%Begin calculation by calling L-M least squares routine

[f,p,kvg,iter,corp,covp,covr,stdresid,Z,r2]=leasqr(x,y,pin,'modelmulti',0.00001,10000);
disp('RESPONSE:')
if kvg==1
    disp('PROBLEM CONVERGED')
elseif kvg==0
    disp('PROBLEM DID NOT CONVERGE')
end
format shortEng
oldf=reshape(f,nx,nvar);
oldr=reshape(y-f,nx,nvar);
disp('X-values:')
disp(oldx)
disp('Y-values')
disp(oldy)

```

```

disp('f-values - i.e. model calculated responses')
disp(oldf)
disp('Residuals:')
disp(olldr)
% disp('Standardized residuals:')
% disp(stdresid)
disp ('Estimated parameter values are;')
disp (p)
disp ('Covariance of estimated parameters - sqrt of diagonal gives CL')
disp (covp)
disp ('R2 values is;')
disp (r2)
plot (oldx,oldy,'d'), hold, plot (oldx,oldf)
figure
subplot(3,3,1)
plot(oldx(:),oldy(:,1),'o',oldx(:),oldf(:,1),'--')
title('DBT')
xlabel('Time (min)')
ylabel('Concentration (mol/L)')
subplot(3,3,2)
plot(oldx(:),oldy(:,2),'o',oldx(:),oldf(:,2),'--')
title('THDBT')
xlabel('Time (min)')
ylabel('Concentration (mol/L)')
subplot(3,3,3)
plot(oldx(:),oldy(:,3),'o',oldx(:),oldf(:,3),'--')
title('BPh')
xlabel('Time (min)')
ylabel('Concentration (mol/L)')
subplot(3,3,4)
plot(oldx(:),oldy(:,4),'o',oldx(:),oldf(:,4),'--')
title('CHB')
xlabel('Time (min)')
ylabel('Concentration (mol/L)')

```

(2) Modelmulti code

```

function f= modelmulti (x,pin)
% Solve a simple system of ODE's - response variables
% find the solution at sepcified x values - corresponding to measured data

```

```

% first data point in x corresponds to initial condition
global nvar nx x0 y0
global verbose

nxx=length(x);
yzero=reshape(y0,nx,nvar);

for i= 1:nx
    xf=x(i);
    xoo=x0;
    yzed=yzero(i,:);
    [xmodel,ymodel]=ode45 (@ODEfunm,[xoo,xf],yzed,[],pin);
    yfinal(i,:)=ymodel(end,:);
end
f=yfinal(:);

```

(3) ODE code

```

function yprime=ODEfunm(xatx,yatx,pin)
global nvar nx x0 y0 xstep

% disp('*****YPRIME')
% disp(knt)
% nx
k1=pin(1);
k2=pin(2);
k3=pin(3);

%ntest=(knt/nx);

yp(1)=-k1*yatx(1)-k2*yatx(1);
yp(2)=k1*yatx(1)-k3*yatx(2);
yp(3)=k2*yatx(1);
yp(4)=k3*yatx(2);

yprime=[yp(1)';yp(2)';yp(3)';yp(4)'];

```

(4) Calculation of Jacobian matrix

```

function prt=dfdp(x,f,p,dp,func)
% numerical partial derivatives (Jacobian) df/dp for use with leasqr

m=length(x); n=length(p); % dimensions
ps=p;prt=zeros(m,n);del=zeros(n,1); % initialize Jacobian to Zero
for j=1:n
    del(j)=dp(j).*p(j); % cal delx=fract(dp)*param value(p)
    if p(j)==0
        del(j)=dp(j); % if param=0 delx=fraction
    end
    p(j)=ps(j)+del(j);
    if del(j)~=0, fl=feval(func,x,p);
        if dp(j)<0, prt(:,j)=(fl-f)./del(j);
            else
                p(j)=ps(j)-del(j);
                prt(:,j)=(fl-feval(func,x,p))./(2.*del(j));
            end
        end
    end
    p(j)=ps(j); %restore p(j)
end
return

```

(5) Least square code

```

function [f,p,kvg,iter,corp,covp,covr,stdresid,Z,r2]= ...
    leasqr(x,y,pin,F,stol,niter,wt,dp,dFdp,options)
%function [f,p,kvg,iter,corp,covp,covr,stdresid,Z,r2]=
%    leasqr(x,y,pin,F,{ stol,niter,wt,dp,dFdp,options })
%
% Levenberg-Marquardt nonlinear regression of f(x,p) to y(x).
%
% Version 3.beta
% Optional parameters are in braces {}.
% x = column vector or matrix of independent variables, 1 row per
% observation: x = [x0 x1...xm].
% y = column vector of observed values, same number of rows as x.
% wt = column vector (dim=length(x)) of statistical weights. These
% should be set to be proportional to (sqrt of var(y))^-1; (That is,
% the covariance matrix of the data is assumed to be proportional to

```

```

% diagonal with diagonal equal to (wt.^2)^-1. The constant of
% proportionality will be estimated.); default = ones(length(y),1).
% pin = column vec of initial parameters to be adjusted by leasqr.
% dp = fractional increment of p for numerical partial derivatives;
% default = .001*ones(size(pin))
% dp(j) > 0 means central differences on j-th parameter p(j).
% dp(j) < 0 means one-sided differences on j-th parameter p(j).
% dp(j) = 0 holds p(j) fixed i.e. leasqr wont change initial guess: pin(j)
% F = name of function in quotes; the function shall be of the form y=f(x,p),
% with y, x, p of the form y, x, pin as described above.
% dFdp = name of partial derivative function in quotes; default is "dfdp", a
% slow but general partial derivatives function; the function shall be
% of the form prt=dfdp(x,f,p,dp,F) (see dfdp.m).
% stol = scalar tolerance on fractional improvement in scalar sum of
% squares = sum((wt.*(y-f))^2); default stol = .0001;
% niter = scalar maximum number of iterations; default = 20;
% options = matrix of n rows (same number of rows as pin) containing
% column 1: desired fractional precision in parameter estimates.
% Iterations are terminated if change in parameter vector (chg) on two
% consecutive iterations is less than their corresponding elements
% in options(:,1). [ie. all(abs(chg*current parm est) < options(:,1))
% on two consecutive iterations.], default = zeros().
% column 2: maximum fractional step change in parameter vector.
% Fractional change in elements of parameter vector is constrained to be
% at most options(:,2) between sucessive iterations.
% [ie. abs(chg(i))=abs(min([chg(i) options(i,2)*current param estimate]))].],
% default = Inf*ones().
%
% OUTPUT VARIABLES
% f = column vector of values computed: f = F(x,p).
% p = column vector trial or final parameters. i.e, the solution.
% kvg = scalar: = 1 if convergence, = 0 otherwise.
% iter = scalar number of iterations used.
% corp = correlation matrix for parameters.
% covp = covariance matrix of the parameters.
% covr = diag(covariance matrix of the residuals).
% stdresid = standardized residuals.
% Z = matrix that defines confidence region (see comments in the source).
% r2 = coefficient of multiple determination.

```

```

%
% All Zero guesses not acceptable

% A modified version of Levenberg-Marquardt
% Non-Linear Regression program previously submitted by R.Schrager.
% This version corrects an error in that version and also provides
% an easier to use version with automatic numerical calculation of
% the Jacobian Matrix. In addition, this version calculates statistics
% such as correlation, etc....
%
% Version 3 Notes
% Errors in the original version submitted by Shrager (now called version 1)
% and the improved version of Jutan (now called version 2) have been corrected.
% Additional features, statistical tests, and documentation have also been
% included along with an example of usage. BEWARE: Some the the input and
% output arguments were changed from the previous version.
%
% Ray Muzic <rfm2@ds2.uh.cwru.edu>
% Arthur Jutan <jutan@charon.engga.uwo.ca>

% Richard I. Shrager (301)-496-1122
% Modified by A.Jutan (519)-679-2111
% Modified by Ray Muzic 14-Jul-1992
% 1) add maxstep feature for limiting changes in parameter estimates
% at each step.
% 2) remove forced columnization of x (x=x(:)) at beginning. x could be
% a matrix with the ith row of containing values of the
% independent variables at the ith observation.
% 3) add verbose option
% 4) add optional return arguments covp, stdresid, chi2
% 5) revise estimates of corp, stdev
% Modified by Ray Muzic 11-Oct-1992
% 1) revise estimate of Vy. remove chi2, add Z as return values
% Modified by Ray Muzic 7-Jan-1994
% 1) Replace ones(x) with a construct that is compatible with versions
% newer and older than v 4.1.
% 2) Added global declaration of verbose (needed for newer than v4.x)
% 3) Replace return value var, the variance of the residuals with covr,
% the covariance matrix of the residuals.

```

```

% 4) Introduce options as 10th input argument. Include
% convergence criteria and maxstep in it.
% 5) Correct calculation of xtx which affects coveraince estimate.
% 6) Eliminate stdev (estimate of standard deviation of parameter
% estimates) from the return values. The covp is a much more
% meaningful expression of precision because it specifies a confidence
% region in contrast to a confidence interval.. If needed, however,
% stdev may be calculated as stdev=sqrt(diag(covp)).
% 7) Change the order of the return values to a more logical order.
% 8) Change to more effcient algorithm of Bard for selecting epsL.
% 9) Tighten up memory usage by making use of sparse matrices (if
% MATLAB version >= 4.0) in computation of covp, corp, stdresid.
% Modified by Francesco Potort?
% for use in Octave
%
% References:
% Bard, Nonlinear Parameter Estimation, Academic Press, 1974.
% Draper and Smith, Applied Regression Analysis, John Wiley and Sons, 1981.
%
%set default args

% argument processing
%

%if (sscanf(version,'%f') >= 4),
vernum= sscanf(version,'%f');
if vernum(1) >= 4,
    global verbose
    plotcmd='plot(x(:,1),y,"+",x(:,1),f); figure(gcf)';
else
    plotcmd='plot(x(:,1),y,"+",x(:,1),f); shg';
end;
if (exist('OCTAVE_VERSION'))
    global verbose
    plotcmd='plot(x(:,1),y,"+;data;" ,x(:,1),f,";fit;");';
end;

if(exist('verbose')~=1), %If verbose undefined, print nothing
    verbose=0; %This will not tell them the results

```

```

end;

if (nargin <= 8), dFdp='dfdp'; end;
if (nargin <= 7), dp=.001*(pin*0+1); end; %DT
if (nargin <= 6), wt=ones(length(y),1); end; % SMB modification
if (nargin <= 5), niter=20; end;
if (nargin == 4), stol=.00001; end;
%

y=y(:); wt=wt(:); pin=pin(:); dp=dp(:); %change all vectors to columns
% check data vectors- same length?
m=length(y); n=length(pin); p=pin;[m1,m2]=size(x);
if m1~=m ,error('input(x)/output(y) data must have same number of rows ') ,end;

if (nargin <= 9),
    options=[zeros(n,1), Inf*ones(n,1)];
    nor = n; noc = 2;
else
    [nor, noc]=size(options);
    if (nor ~= n),
        error('options and parameter matrices must have same number of rows'),
    end;
    if (noc ~= 2),
        options=[options(:,1), Inf*ones(nor,1)];
    end;
end;
pprec=options(:,1);
maxstep=options(:,2);
%

% set up for iterations
%
f=feval(F,x,p); fbest=f; pbest=p;
r=wt.*(y-f);
ss=r'*r;
sbest=ss;
nrm=zeros(n,1);
chgprev=Inf*ones(n,1);
kvg=0;

```

```

epsLlast=1;
epstab=[.1, 1, 1e2, 1e4, 1e6];

% do iterations
%
for iter=1:niter,
    pprev=pbest;
    prt=feval(dFdp,x,fbest,pprev,dp,F);
    r=wt.*(y-fbest);
    spre=sbest;
    sgoal=(1-stol)*spre;
    for j=1:n,
        if dp(j)==0,
            nrm(j)=0;
        else
            prt(:,j)=wt.*prt(:,j);
            nrm(j)=prt(:,j)'*prt(:,j);
            if nrm(j)>0,
                nrm(j)=1/sqrt(nrm(j));
            end;
        end
        prt(:,j)=nrm(j)*prt(:,j);
    end;
% above loop could ? be replaced by:
% prt=prt.*wt(:,ones(1,n));
% nrm=dp./sqrt(diag(prt'*prt));
% prt=prt.*nrm(:,ones(1,m))';
[prt,s,v]=svd(prt,0);
s=diag(s);
g=prt'*r;
for jjj=1:length(epstab),
    epsL = max(epsLlast*epstab(jjj),1e-7);
    se=sqrt((s.*s)+epsL);
    gse=g./se;
    chg=((v*gse).*nrm);
% check the change constraints and apply as necessary
ochg=chg;
idx = ~isinf(maxstep);
limit = abs(maxstep(idx).*pprev(idx));

```

```

chg(idx) = min(max(chg(idx),-limit),limit);
if (verbose & any(ochg ~= chg)),
    disp(['Change in parameter(s): ', ...
        sprintf('%d ',find(ochg ~= chg)), 'were constrained']);
end;
aprec=abs(pprec.*pbest);    %---
% ss=scalar sum of squares=sum((wt.*(y-f))^2).
if (any(abs(chg) > 0.1*aprec)),%--- % only worth evaluating function if
    p=chg+pprev;           % there is some non-miniscule change
    f=feval(F,x,p);
    r=wt.*(y-f);
    ss=r'*r;
    if ss<sbest,
        pbest=p;
        fbest=f;
        sbest=ss;
    end;
    if ss<=sgoal,
        break;
    end;
end;           %---
end;
epsLlast = epsL;
if (verbose),
    eval(plotcmd);
end;
if ss<eps,
    break;
end
aprec=abs(pprec.*pbest);
% [aprec, chg, chgprev]
if (all(abs(chg) < aprec) & all(abs(chgprev) < aprec)),
    kvg=1;
    if (verbose),
        fprintf('Parameter changes converged to specified precision\n');
    end;
    break;
else
    chgprev=chg;

```

```

end;
if ss>sgoal,
    break;
end;
end;

% set return values
%
p=pbest;
f=fbest;
ss=sbest;
kvg=((sbest>sgoal)|(sbest<=eps)|kvg);
if kvg ~= 1 , disp(' CONVERGENCE NOT ACHIEVED! '), end;

% CALC VARIANCE COV MATRIX AND CORRELATION MATRIX OF PARAMETERS
% re-evaluate the Jacobian at optimal values
jac=feval(dFdp,x,f,p,dp,F);
msk = dp ~= 0;
n = sum(msk);      % reduce n to equal number of estimated parameters
jac = jac(:, msk); % use only fitted parameters

%% following section is Ray Muzic's estimate for covariance and correlation
%% assuming covariance of data is a diagonal matrix proportional to
%% diag(1/wt.^2).
%% cov matrix of data est. from Bard Eq. 7-5-13, and Row 1 Table 5.1

if exist('sparse') % save memory
    Q=sparse(1:m,1:m,1./wt.^2);
    Qinv=sparse(1:m,1:m,wt.^2);
else
    Q=diag((0*wt+1)./(wt.^2));
    Qinv=diag(wt.*wt);
end
resid=y-f;          % un-weighted residuals
covr=resid'*Qinv*resid*Q/(m-n); % covariance of residuals
Vy=1/(1-n/m)*covr; % Eq. 7-13-22, Bard % covariance of the data

jtgjinv=inv(jac'*Qinv*jac); % argument of inv may be singular
covp=jtgjinv*jac'*Qinv*Vy*Qinv*jac*jtgjinv; % Eq. 7-5-13, Bard % cov of parm est

```

```

d=sqrt(abs(diag(covp)));
corp=covp./(d*d');

if exist('sparse')
    covr=spdiags(covr,0);
    stdresid=resid./sqrt(spdiags(Vy,0));
else
    covr=diag(covr);          % convert returned values to compact storage
    stdresid=resid./sqrt(diag(Vy)); % compute then convert for compact storage
end
Z=((m-n)*jac*Qinv*jac)/(n*resid'*Qinv*resid);

%%% alt. est. of cov. mat. of parm.:(Delforge, Circulation, 82:1494-1504, 1990
%%disp('Alternate estimate of cov. of param. est.')
%%acovp=resid'*Qinv*resid/(m-n)*jtgjinv

%Calculate R^2 (Ref Draper & Smith p.46)
%
r=corrcoef([y(:),f(:)]);
r2=r(1,2).^2;

% if someone has asked for it, let them have it
%
if (verbose),
    eval(plotcmd);
    disp(' Least Squares Estimates of Parameters')
    disp(p')
    disp(' Correlation matrix of parameters estimated')
    disp(corp)
    disp(' Covariance matrix of Residuals' )
    disp(covr)
    disp(' Correlation Coefficient R^2')
    disp(r2)
    sprintf(' 95%% conf region: F(0.05)(%.0f,%.0f)>= delta_pvec"*Z*delta_pvec',n,m-n)
    Z
% runs test according to Bard. p 201.
n1 = sum((f-y) < 0);
n2 = sum((f-y) > 0);
nrun=sum(abs(diff((f-y)<0)))+1;

```

```

if ((n1>10)&(n2>10)), % sufficient data for test?
zed=(nrun-(2*n1*n2/(n1+n2)+1)+0.5)/(2*n1*n2*(2*n1*n2-n1-n2)...
/((n1+n2)^2*(n1+n2-1)));
if (zed < 0),
prob = erfc(-zed/sqrt(2))/2*100;
disp([num2str(prob),'% chance of fewer than ',num2str(nrun),' runs.']);
else,
prob = erfc(zed/sqrt(2))/2*100;
disp([num2str(prob),'% chance of greater than ',num2str(nrun),' runs.']);
end;
end;
end;
end;

```

D.3 Matlab Code for Deactivation Constant Calculation

The exponential decay rate law ($a=e^{-k_d t}$) was used to study the deactivation of Mo₂C/APC catalysts in the presence of S and N. The calculated decay constant (k_d) can be used to describe how fast the deactivation could be. Take 10% Mo₂C/APC catalyst in HDS of DBT as an example. The transition period data is reported in Table D.3.

Table D.3: DBT conversion and initial rate of reaction in HDS of DBT for 10% Mo₂C/APC catalyst as a function of time on stream.

TOS (sec)	χ_{DBT} (%)	$-\ln(1 - \chi_{DBT})$	k' [mol _{DBT} /g _{cata} .s]	Initial-r _{DBT} (g _{DBT} /g _{cata} .s)	Initial-r _{DBT} (mol _{DBT} /g _{cata} .s)
3600	98.02	3.9222	1.0586E-06	1.9539E-04	1.0604E-06
5400	83.76	1.8180	3.5049E-07	6.4689E-05	3.5108E-07
7500	69.06	1.1730	2.2614E-07	4.1738E-05	2.2652E-07
9120	65.45	1.0628	2.0490E-07	3.7818E-05	2.0524E-07
10980	64.73	1.0420	2.0089E-07	3.7078E-05	2.0123E-07

(1) Main body

```

clear all
clc
global x0 y0 a
global verbose
verbose(1:2) = 1;
% Activity term parameter estimation
% input number of responses
%
format shortEng
nvar=1;
x0=0.;
y0=0.;

%-----
% t,sec

x_s=[3600
5400
7500
9120
10980];

oldx=x_s;
[nx,mx] = size(x_s)

%-----
%DBT consumption rate

yT2=[1.0604E-06
3.51076E-07

```

```

2.26517E-07
2.05244E-07
2.01226E-07];

%-----
y = yT2;
oldy=y;

%kd A0
% 1st order
theta=[.0001];
% 2nd order
%theta=[1e-1];
%reciprocal power/Modified 1st order with H2S/NH3 conc
%theta=[0.0001 0.00001];
%coke
%theta=[5];

np=length(theta);
pin=theta;

% Begin calculation by calling L-M least squares routine
[a_s,p,kvg,iter,corp,covp,covr,stdresid,Z,r2]=leasqr(x_s,y,pin,'KS_modelmulti_HW',0.00001,10
000);

disp('RESPONSE:')
if kvg ==1
    disp ('PROBELM CONVERGED')
elseif kvg == 0
    disp('PROBLEM DID NOT CONVERGE')

```

end

```
r=y-a_s;
disp ('X-values:')
disp (oldx)
disp ('Y-values:')
disp (oldy)
disp ('activity values for all of run')
disp (a)
disp ('a-values - i.e. model calculated responses')
disp (a_s)
disp ('Residuals:')
disp (r)
disp ('Standardized residuals')
disp (stdresid)
disp ('Estimated parameter values are:')
disp (p)
disp ('Covariance of estimated parameters:')
disp (covp)
disp ('R2 values is:')
disp (r2)
disp ('No. of iterations:')
disp (iter)

subplot(2,1,1);
plot (oldx,a_s,'-R','linewidth',2)
hold on
plot(oldx,oldy,'ok','MarkerSize',10) %plot the data using open black circles
xlabel('time (sec)')
ylabel('DBT consumption rate, mol/(sec.gcat)')
```

```

subplot(2,1,2);
plot (oldy,a_s,'o'), hold, plot(oldy,oldy,'black')
xlabel('Experimental, mol/(sec.gcat)')
ylabel('Calculated, mol/(sec.gcat)')

```

(2) Modelmulti code

```

% Effect of S/N activity model.
% Modified by Haiyan Wang-20170416.
function a_s = KS_modelmulti_HW (x_s,pin)
global x0 y0 a
%n=3;
%T,K t,h
x=x_s;

%-----
% H2S or NH3 concentration, mmol

s=[0.01071639
0.008991737
0.007185979
0.00674708
0.006654635];

%-----
a(1)=1.0;
ro=1.0604E-06; % Initial experimental rate data

[nxx,mxx]=size(x);

```

```

for i = 2:nxx;
    z(1,1)=0;
    z(i,1)=(x(i,1)-x(1,1));% Divide 0.8 before

    kd=pin(1);

% 1st order
a(i)=a(i-1)*exp(-kd*(z(i,1)-z(i-1,1)));

%H2S modified 1st order
%a(i)=a(i-1)*exp(-kd*(s(i)^n*z(i,1)-s(i-1)^n*z(i-1,1)))
end

[nxs,mxs]=size(x_s);
for j=1:nxs
    a_s(j)=ro*a(j);
end

a_s = a_s';

```

Then calculated results are presented as below:

Table D.4: Calculated decay constant (k_d) from exponential decay rate law for 10Mo₂C/APC in HDS of DBT at 350 °C and 4.1 MPa.

kd	4.2211E-04	s ⁻¹	2.5327E-02	h ⁻¹
Covp	9.2679E-09			
SD	9.6270E-05	s ⁻¹	5.7762E-03	h ⁻¹
R²	9.3116E-01			

Appendix E Supplementary Figures and Tables

E.1 Supplementary Information for Chapter 2

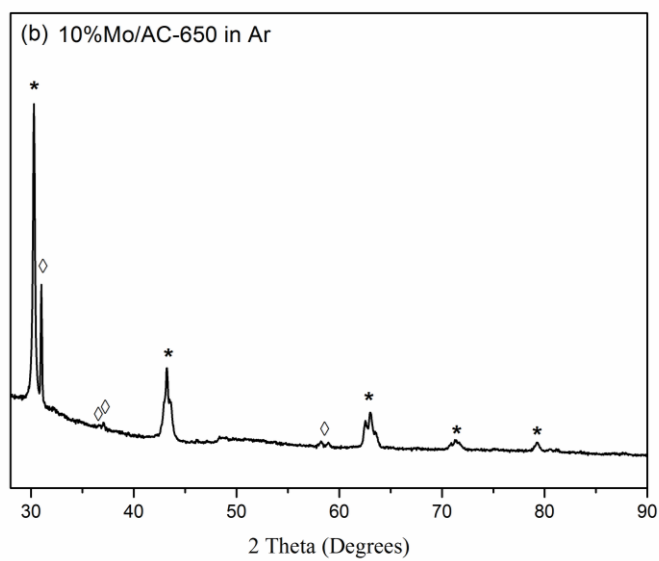


Figure E.1: XRD pattern of 10% Mo/AC-650 prepared in Ar atmosphere. (\diamond) - SiO_2 ; (*) - MoO_2 .

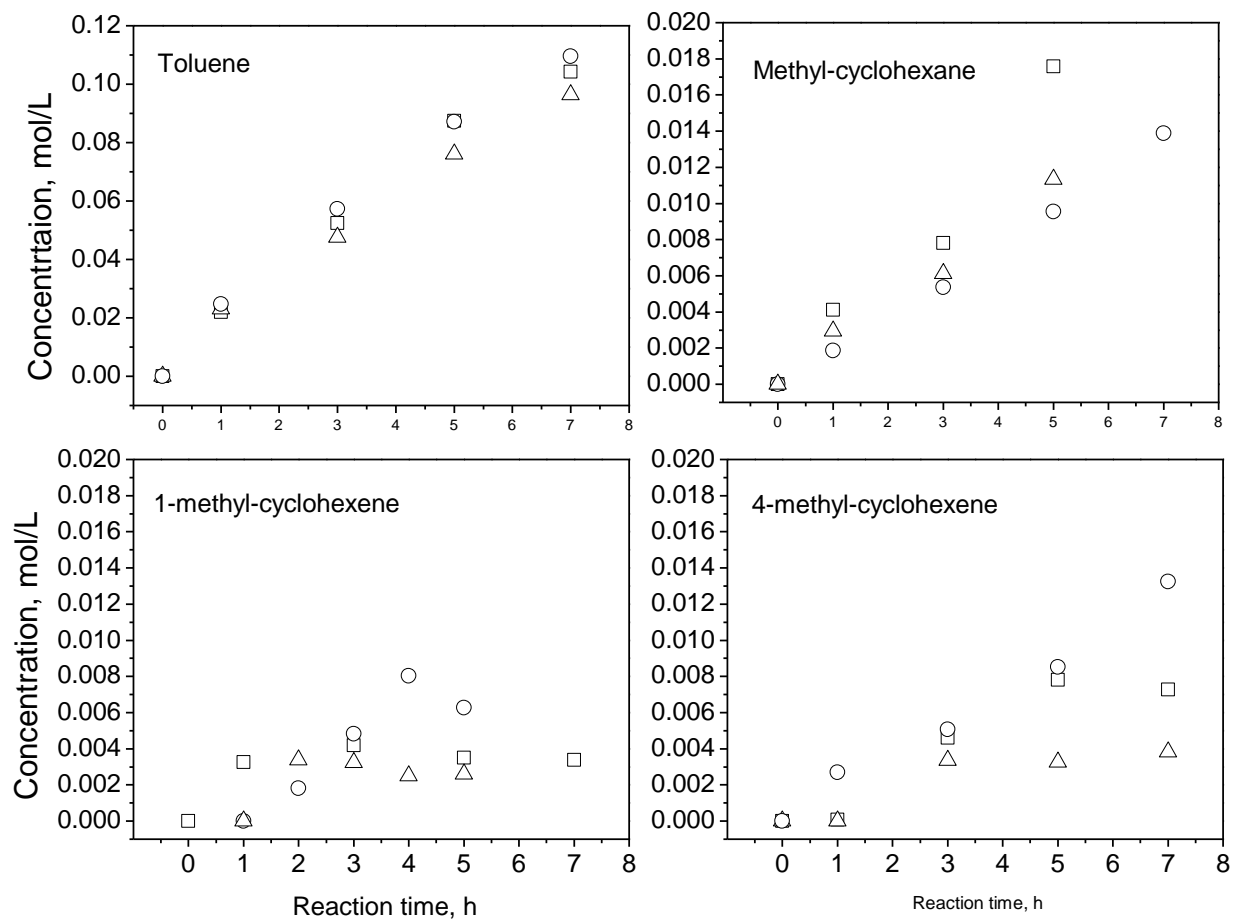


Figure E.2: Product concentrations as a function of reaction time during 4-methylphenol hydrodeoxygenation at 350°C and 4.3 MPa H₂. (□) 10%Mo-AC600, (o) 10%Mo-AC-650 and (Δ) 10%Mo-AC-700.

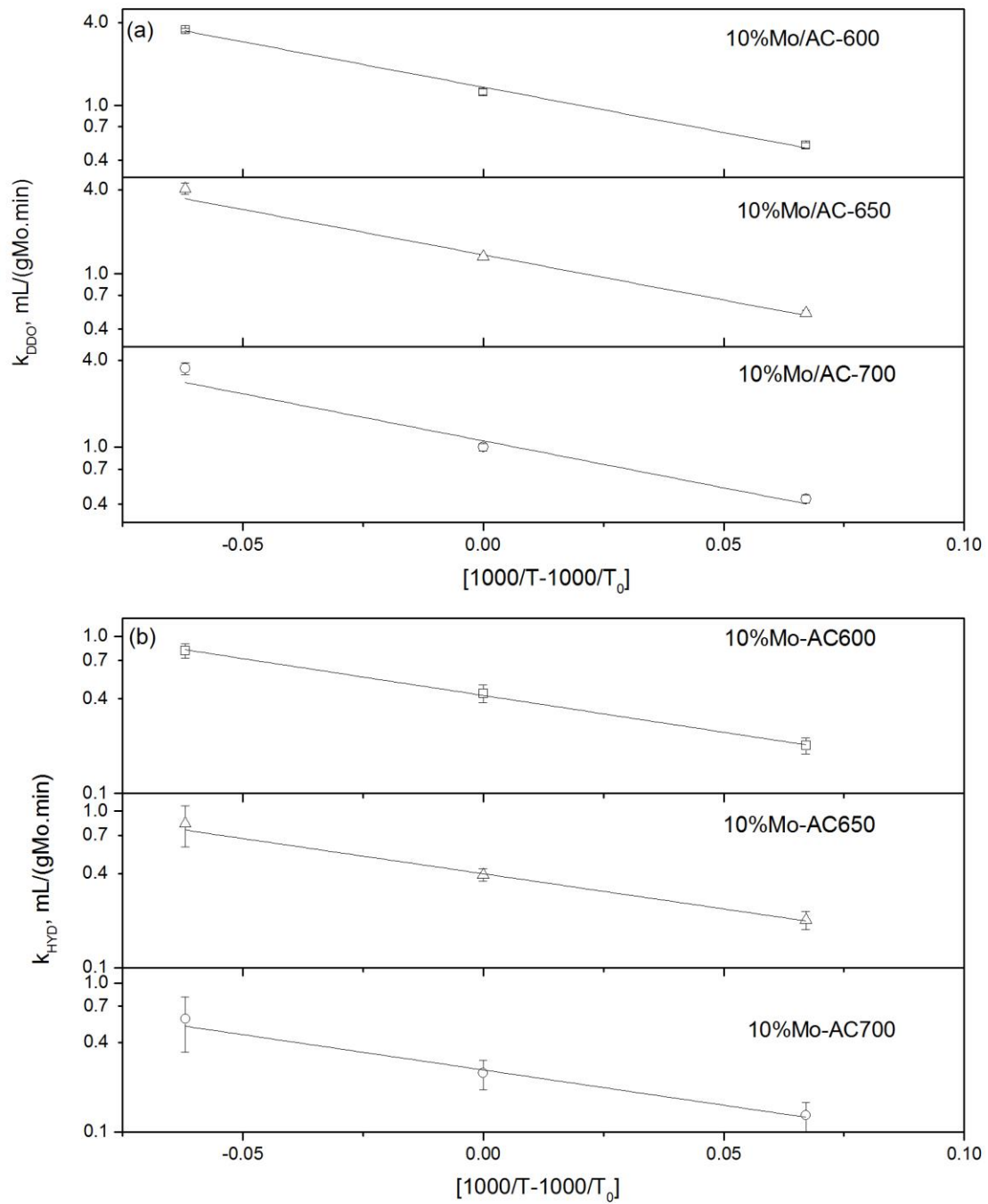


Figure E.3: Arrhenius plots for 1st-order rate constants of (a) DDO and (b) HYD reactions. Data centered at $T_0 = 350^\circ\text{C}$.

Table E.1: Kinetic parameters measured for thermal reaction of 4-methylphenol.

	k_{DDO}^T	k_{HYD}^T
Temperature, °C	$\times 10^4 \text{ min}^{-1}$	
325	1.505±0.140 ^a	0.751±0.014
350	5.175±0.200	1.551±0.200
375	13.94±0.700	4.050±0.788

E.2 Supplementary Information for Chapter 3

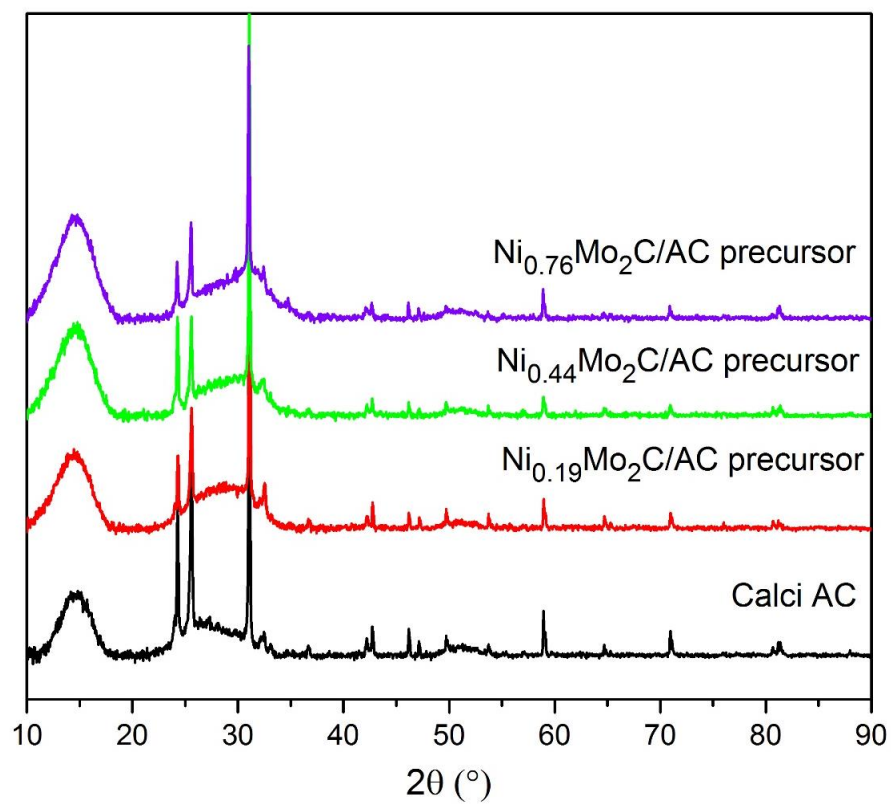


Figure E.4: XRD patterns of calcined Ni-Mo₂C/AC catalyst precursors.

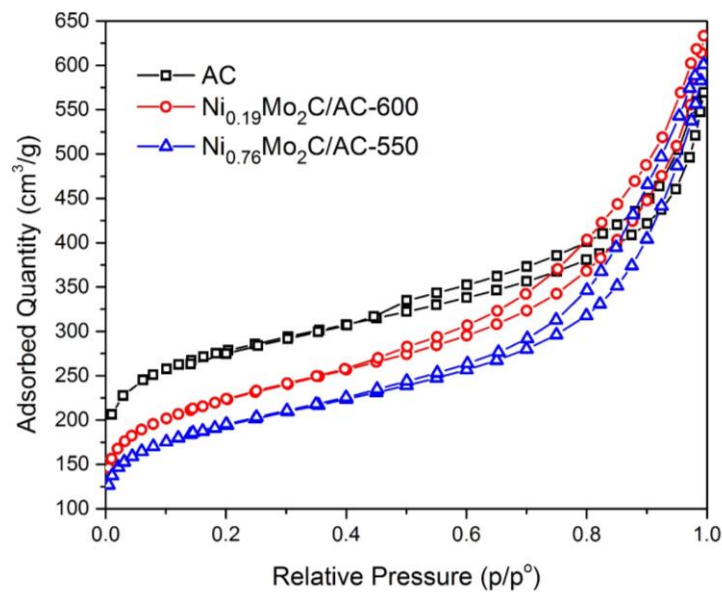


Figure E.5: N₂ adsorption-desorption isotherms of nitrogen at -193 °C for the AC support and Ni-Mo₂C/AC catalysts.

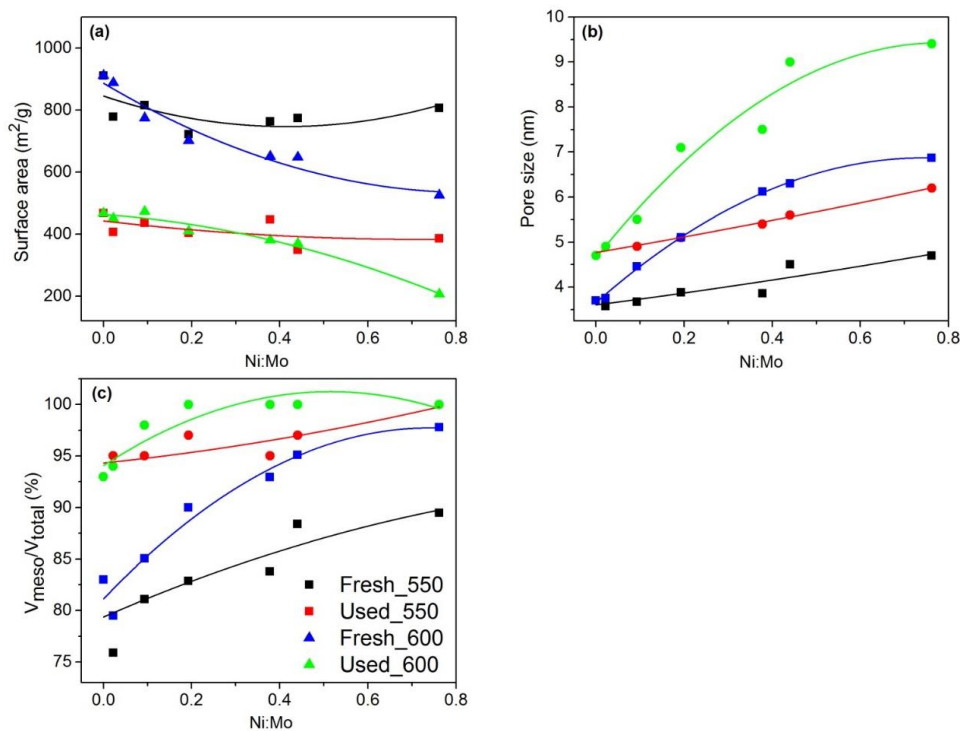


Figure E.6: The effect of Ni:Mo on (a) surface area, (b) pore size, (c) $V_{\text{meso}}/V_{\text{total}}$, for fresh and used Ni-Mo₂C/AC catalysts at reduction temperatures of 550 °C and 600 °C. — Trend line.

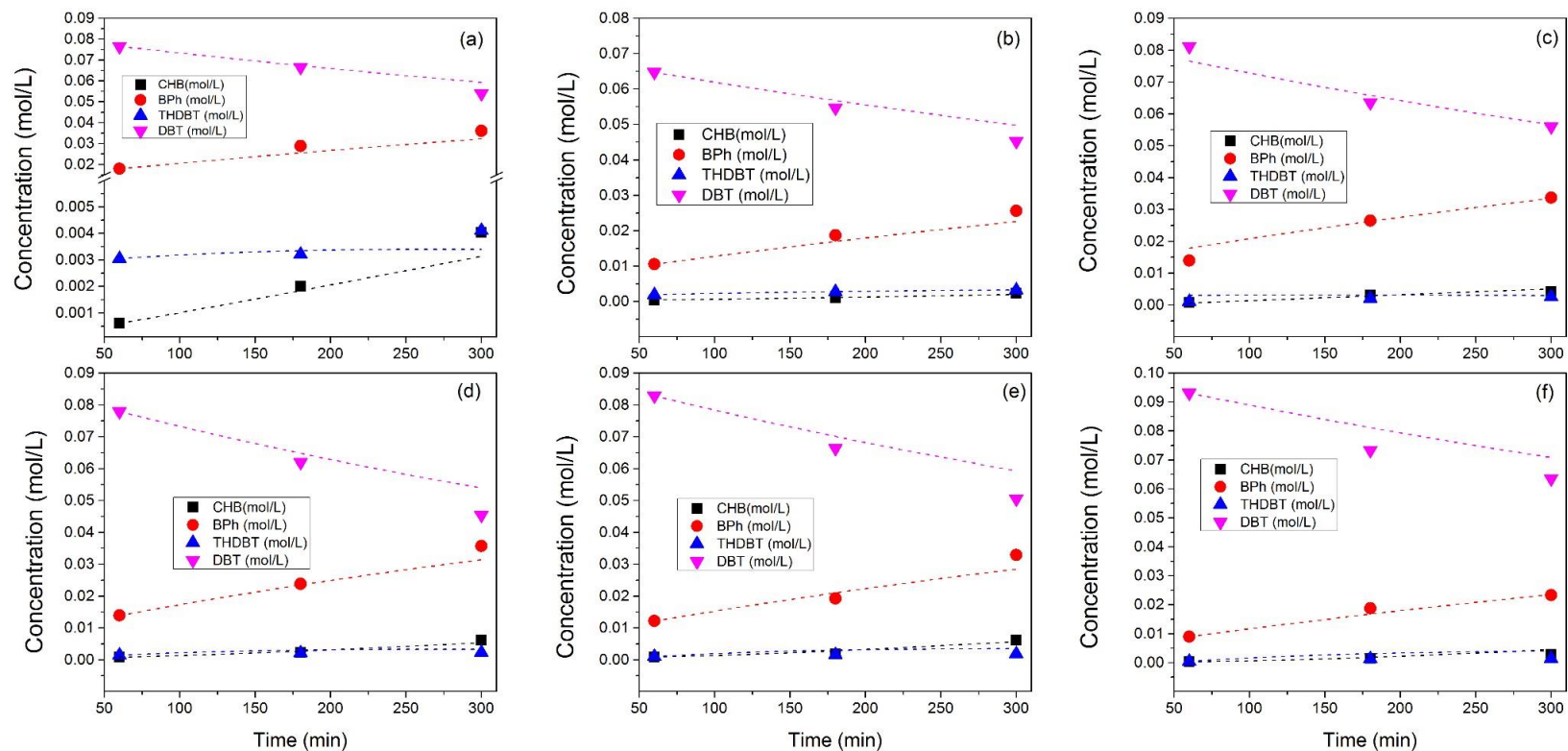


Figure E.7: Experimental and model concentration data versus reaction time of different Ni-Mo₂C catalysts prepared at 550 °C: Dibenzothiophene (DBT, ▼); Biphenyl (BPh, ●); tetrahydro-dibenzothiophene (THDBT, ▲); cyclohexylbenzene (CHB, ■). (a) Ni_{0.02}Mo₂C/AC-550; (b) Ni_{0.09}Mo₂C/AC-550; (c) Ni_{0.19}Mo₂C/AC-550; (d) Ni_{0.38}Mo₂C/AC-550; (e) Ni_{0.44}Mo₂C/AC-550; (f) Ni_{0.76}Mo₂C/AC-550.

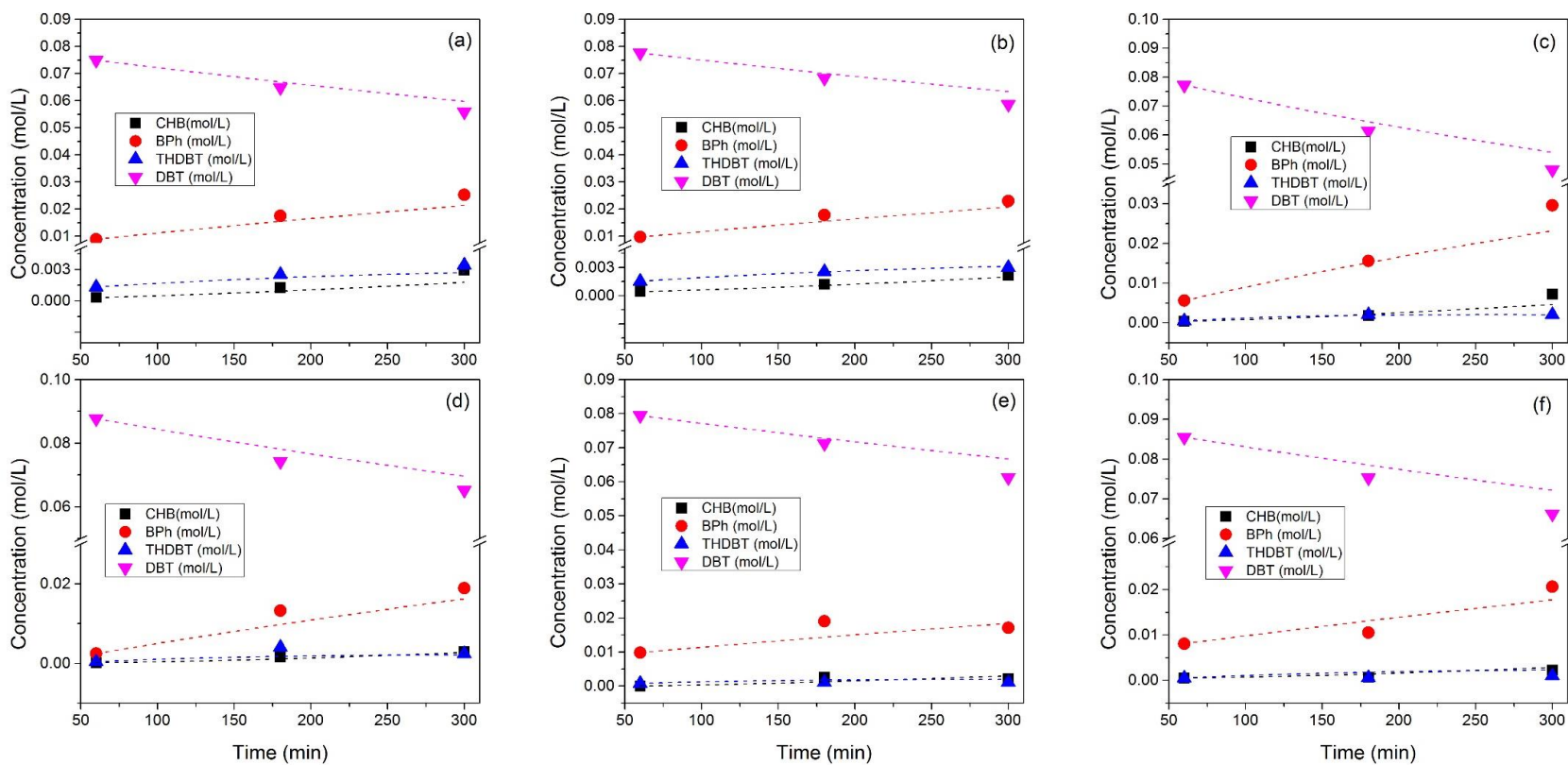


Figure E.8: Experimental and model concentration data versus reaction time of different Ni-Mo₂C catalysts prepared at 600 °C: Dibenzothiophene (DBT, ▼); Biphenyl (BPh, ●); tetrahydro-dibenzothiophene (THDBT, ▲); cyclohexylbenzene (CHB, ■). (a) Ni_{0.02}Mo₂C/AC-600; (b) Ni_{0.09}Mo₂C/AC-600; (c) Ni_{0.19}Mo₂C/AC-600; (d) Ni_{0.38}Mo₂C/AC-600; (e) Ni_{0.44}Mo₂C/AC-600; (f) Ni_{0.76}Mo₂C/AC-600.

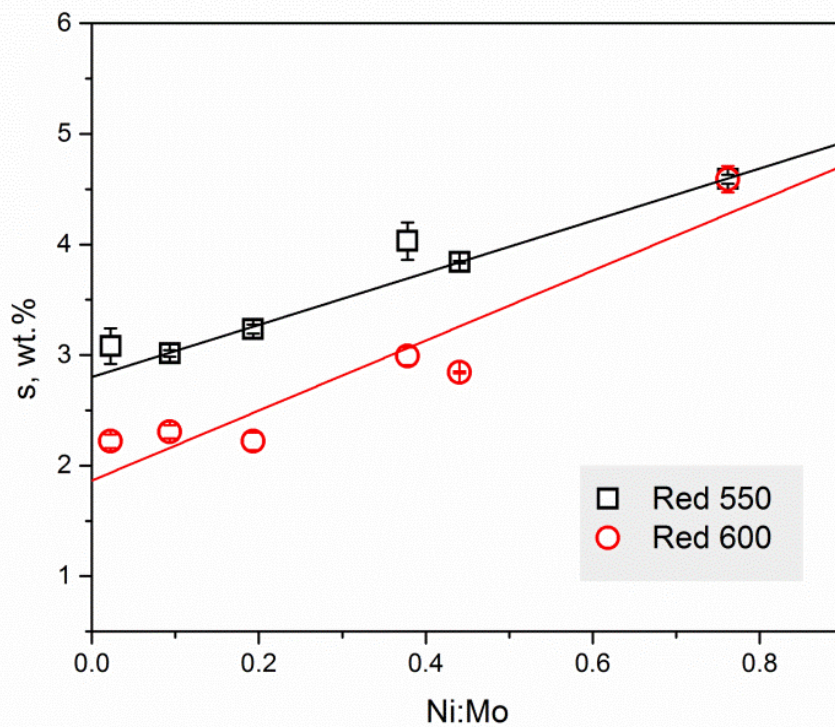


Figure E.9: Correlation of Ni/Mo ratio determined by ICP and adsorbed S wt% determined by CHNS analyzer for Ni-Mo₂C/AC reduced at different temperatures (□: reduced at 550 °C; ○: reduced at 600 °C).

The solid lines represent the correlation equation:

for (□), $S \text{ (wt\%)} = (2.357 \pm 0.082^a) \times \text{Ni:Mo ratio} + (2.801 \pm 0.036)$;

for (○), $S \text{ (wt\%)} = (3.164 \pm 0.548) \times \text{Ni:Mo ratio} + (1.865 \pm 0.219)$.

^a represents standard deviation.

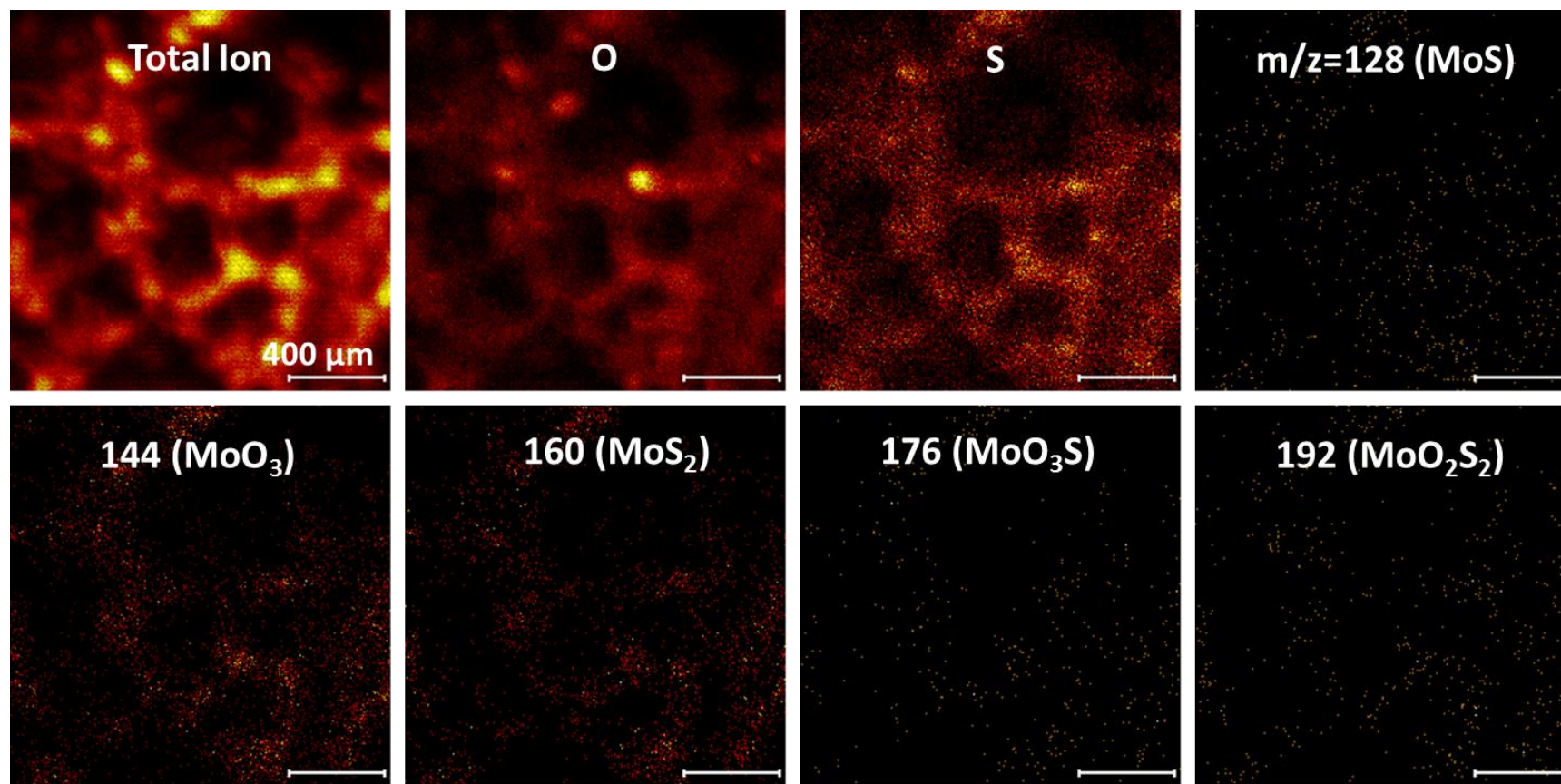


Figure E.10: TOF-SIMS spectrum of used Ni_{0.19}Mo₂C/AC-550 catalyst based on spot of scan area.

E.3 Supplementary Information for Chapter 4

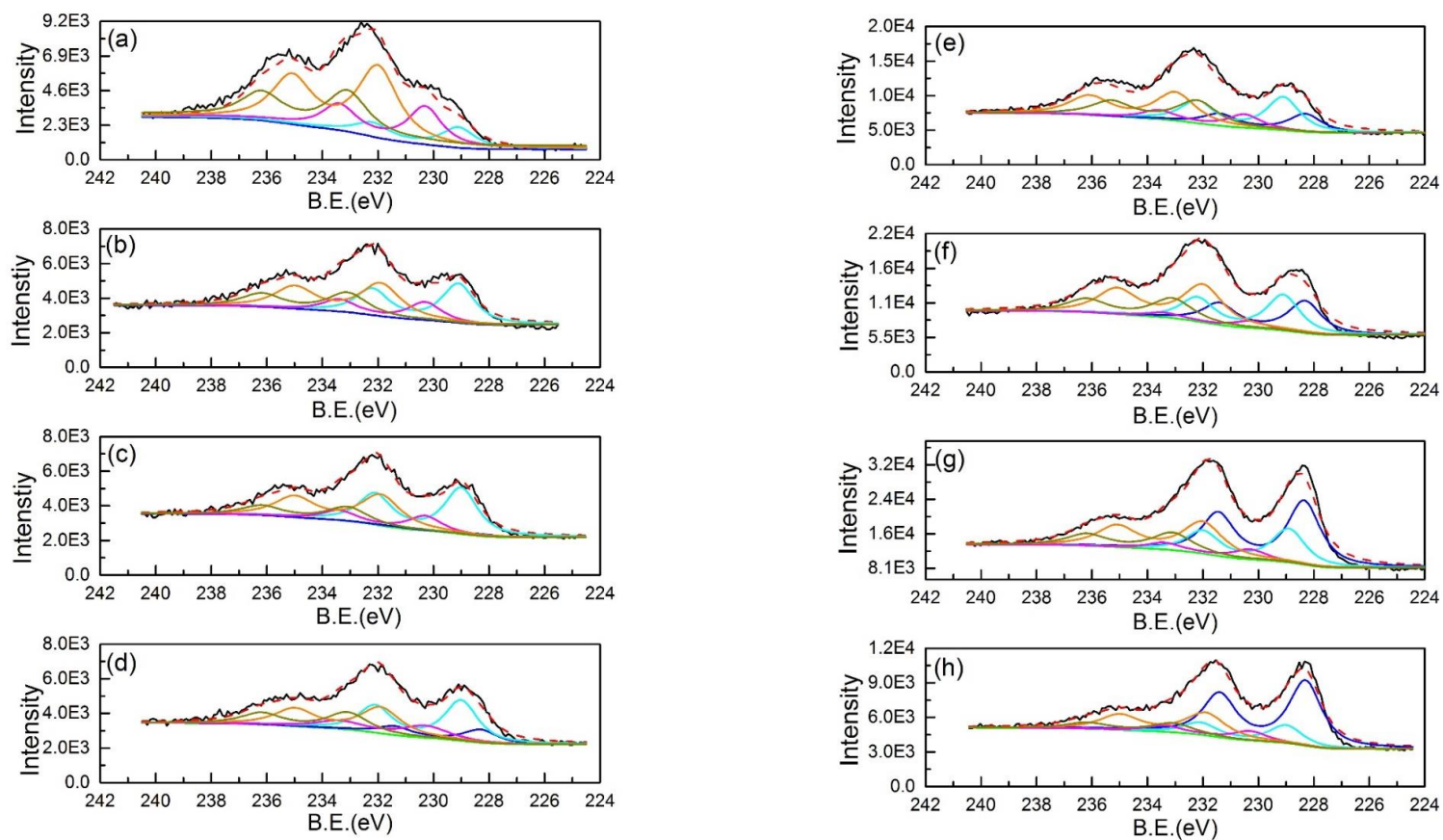


Figure E.11: Mo (3d) XPS narrow scan spectra deconvolution of APC supported Mo₂C catalysts at different CHR temperatures: (a) Mo400_APC; (b) Mo500_APC; (c) Mo550_APC; (d) Mo600_APC; (e) Mo650_APC; (f) Mo700_APC; (g) Mo750_APC; (h) Mo800_APC.

A XPS analysis of Mo 3d peak deconvolution of fresh Mo/APC samples prepared at different CHR temperatures with and without holding for 90 min are presented in Figure E.11 and E.12. Also, an atomic percentage of Mo 3d, O 1s and C 1s as obtained from XPS survey scans are reported in Table E.2.

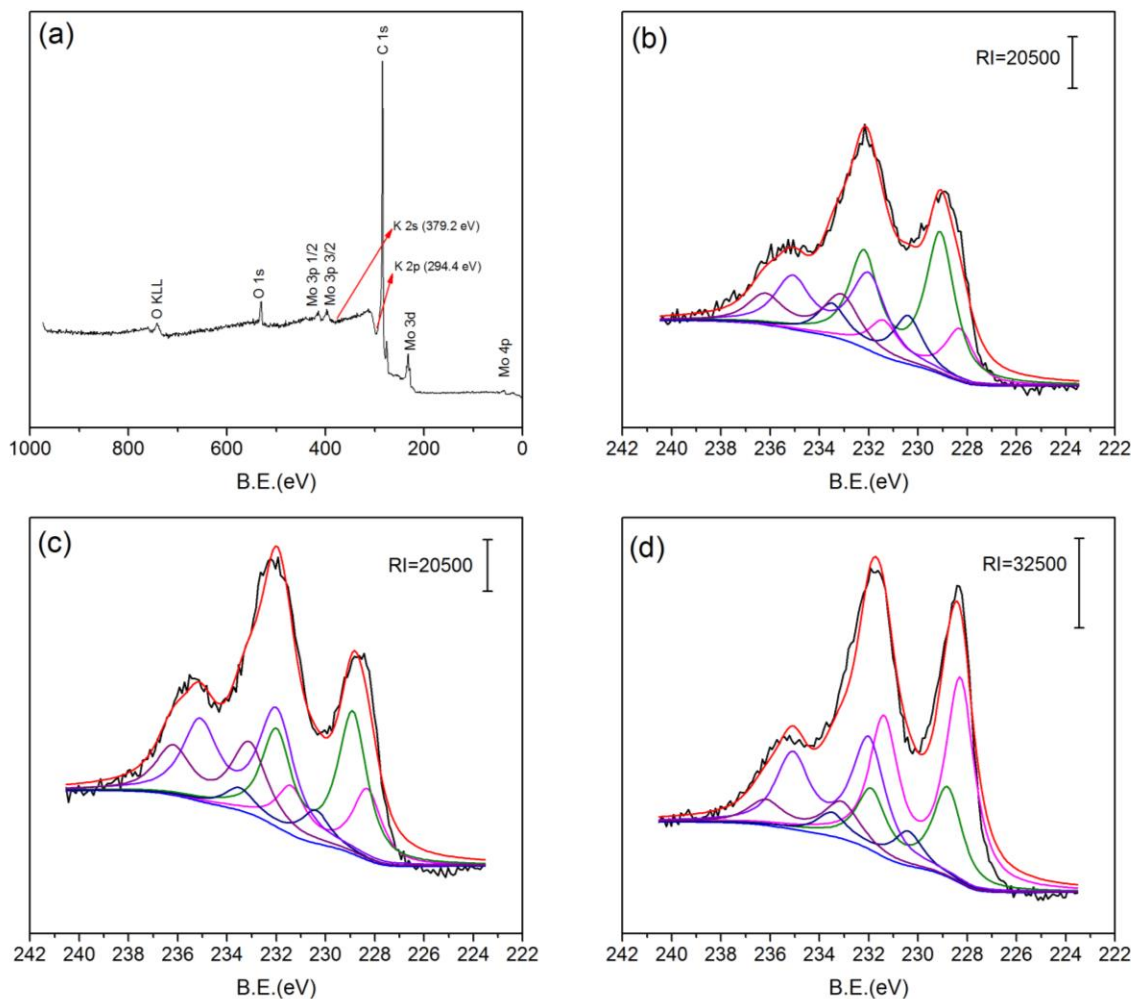


Figure E.12: The deconvolution of Mo 3d narrow scan spectra of fresh Mo/APC samples with different CHR temperatures holding for 90 min: (a) survey scan of Mo600_APC; (b) Mo600_APC; (c) Mo650_APC; (d) Mo700_APC. (“—” Mo²⁺; “—” Mo³⁺; “—” Mo⁴⁺; “—” Mo⁵⁺; “—” Mo⁶⁺)

Table E.2: Elemental compositions of fresh and used Mo/APC (after HDO of 4-MP) samples with different CHR temperatures holding for 90 min.

At%	Mo600_APC-90		Mo650_APC-90		Mo700_APC-90	
	Fresh	Used	Fresh	Used	Fresh	Used
Mo3d	1.41	1.30	1.84	1.80	2.90	2.99
C1s	94.18	94.06	92.54	92.73	91.14	90.99
O1s	4.40	4.64	5.62	5.47	5.96	6.01
Sum	99.99	100.00	100.00	100.00	100.00	99.99

The isothermal curves of APC supported Mo samples are presented as below:

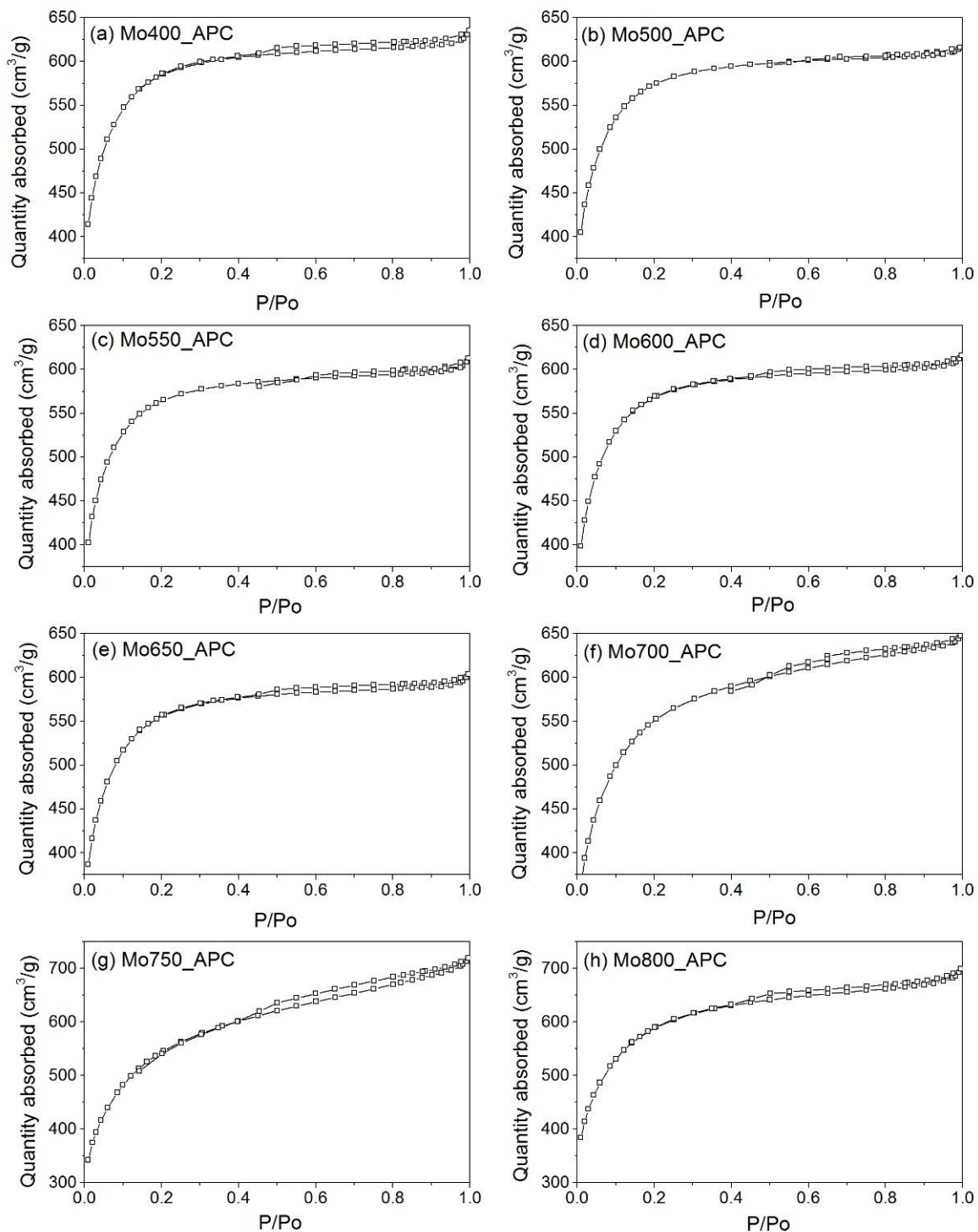


Figure E.13: Isotherms of APC supported Mo₂C catalysts with different CHR temperatures.

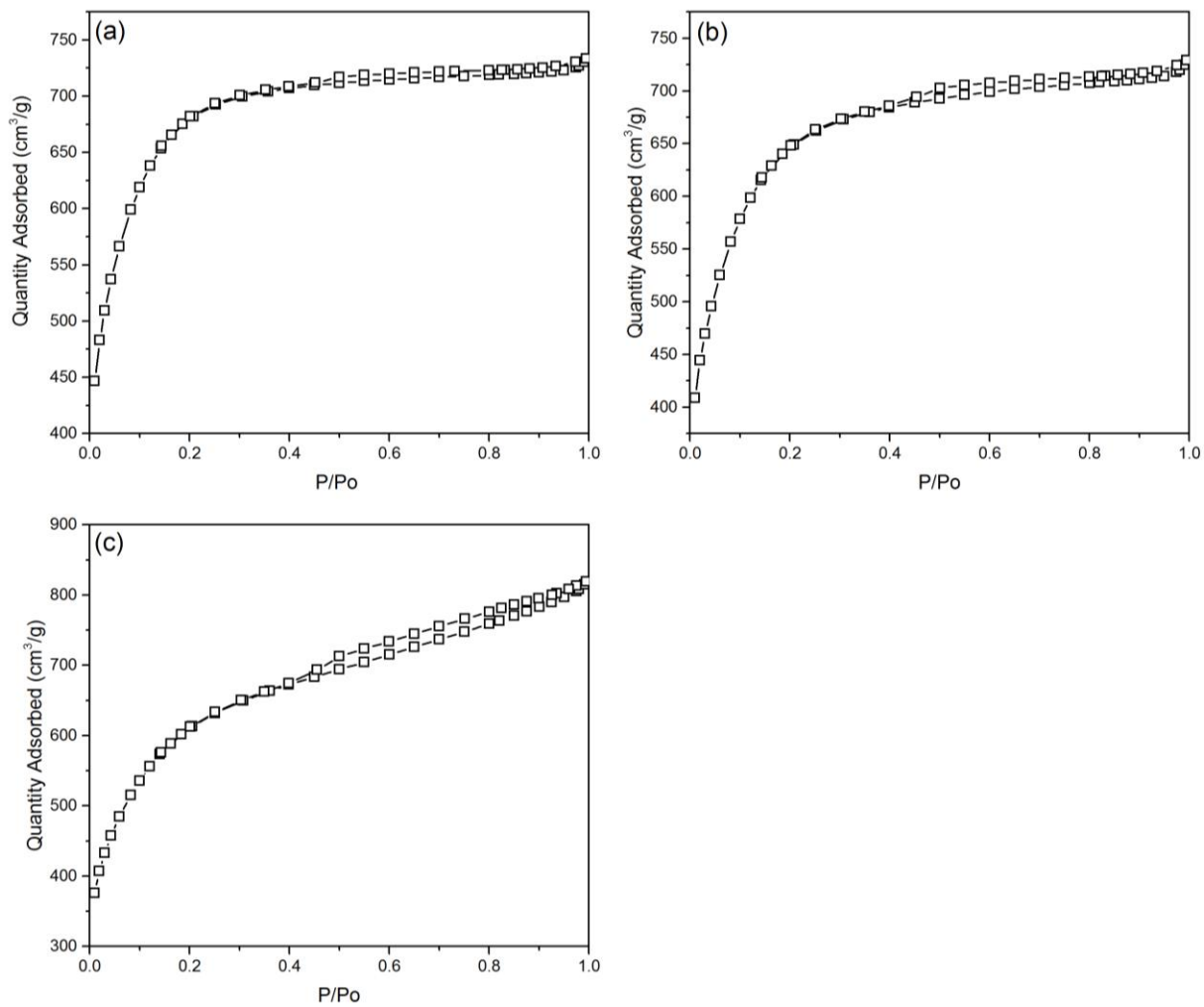
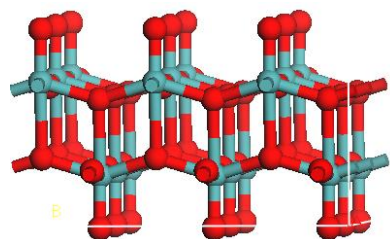
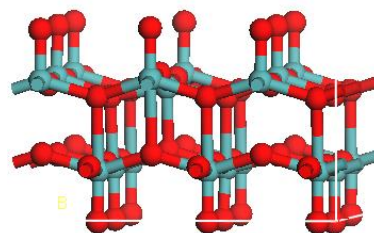


Figure E.14: Isotherms of APC supported Mo₂C catalysts with different CHR temperatures holding for 90 min: (a) Mo600_APC-90; (B) Mo650_APC-90; (c) Mo700_APC-90.

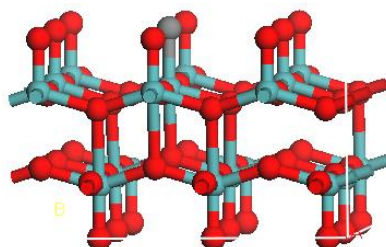
Molecular models for DFT calculation:



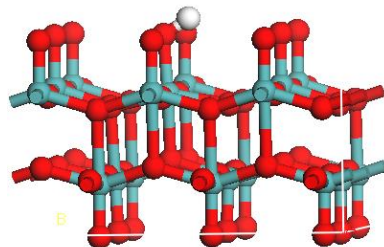
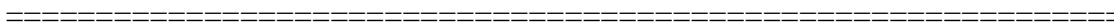
MoO₃ (010)



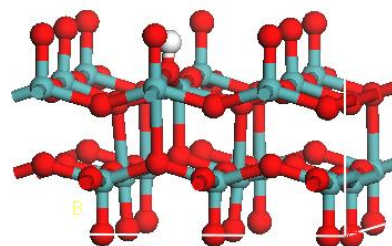
MoO₃ (010) with one oxygen vacancy



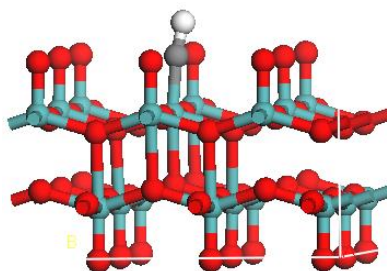
MoO₃C (010)



H-MoO₃



H-Ov-MoO₃



H-MoO₃C

Figure E.15: H adsorption energy on MoO₃ (010), MoO₃ (010) with one oxygen vacancy and MoO₃C(010).

Table E.3: H adsorption energy on MoO₃ (010), MoO₃ (010) with one oxygen vacancy and MoO₃C (010).

Status	MoO ₃ (010)		
	MoO ₃ (010)	with O vacancy	MoO ₃ C
H adsorption energy (eV)	-1.10	-1.21	-2.46

The results of activity tests are shown in Figure E.16.

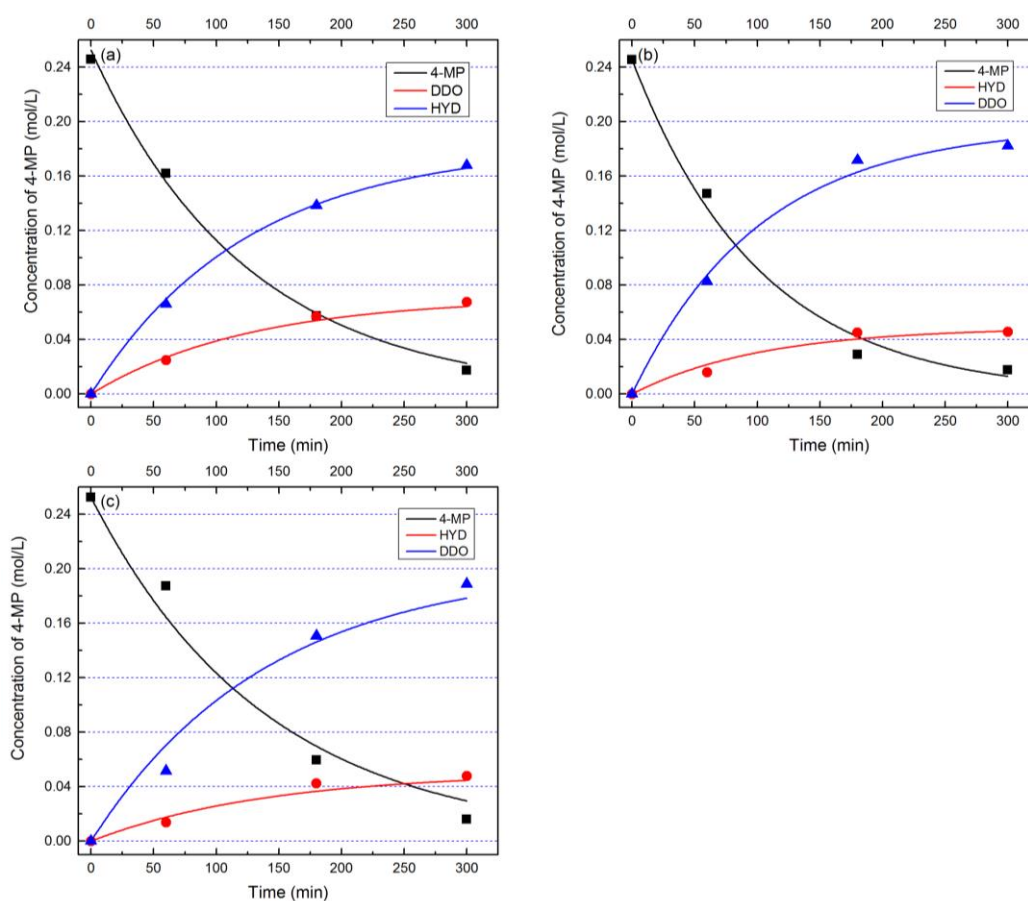


Figure E.16: Experimental and model concentration data versus reaction time of different catalysts with different CHR temperatures. (a) Mo600_APC-90; (b) Mo650_APC-90; (c) Mo700_APC-90. (■) Reactant: 4-MP; (●) HYD products; (▲) DDO products.

E.4 Supplementary Information for Chapter 5

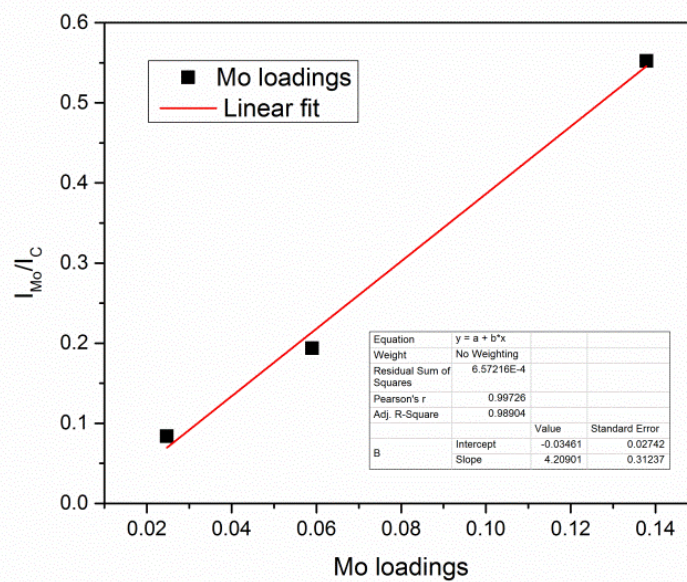


Figure E.17: A correlation of Mo loadings for the fresh Mo₂C/APC catalysts with various Mo loadings and I_{Mo}/I_C .

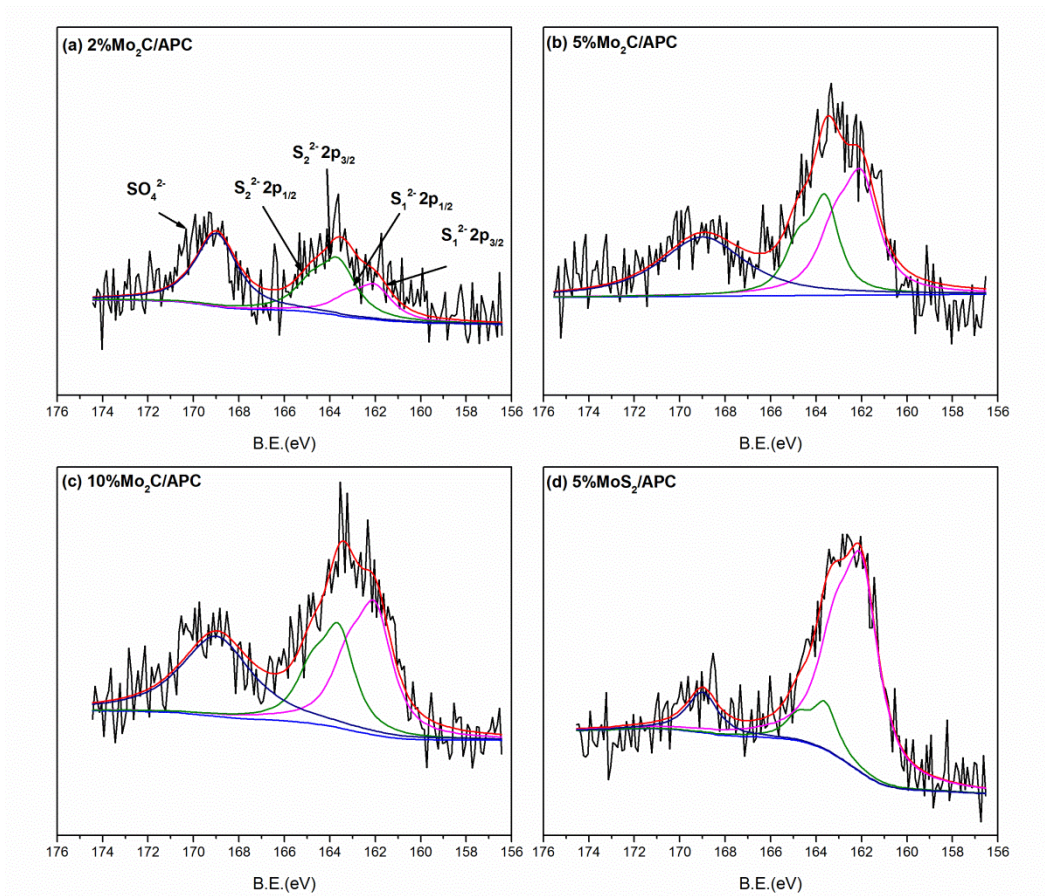


Figure E.18: The deconvolution of S 2p of used Mo₂C/APC catalysts: (a) 2Mo₂C/APC; (b) 5Mo₂C/APC; (c) 10Mo₂C/APC; (d) 5MoS₂/APC.

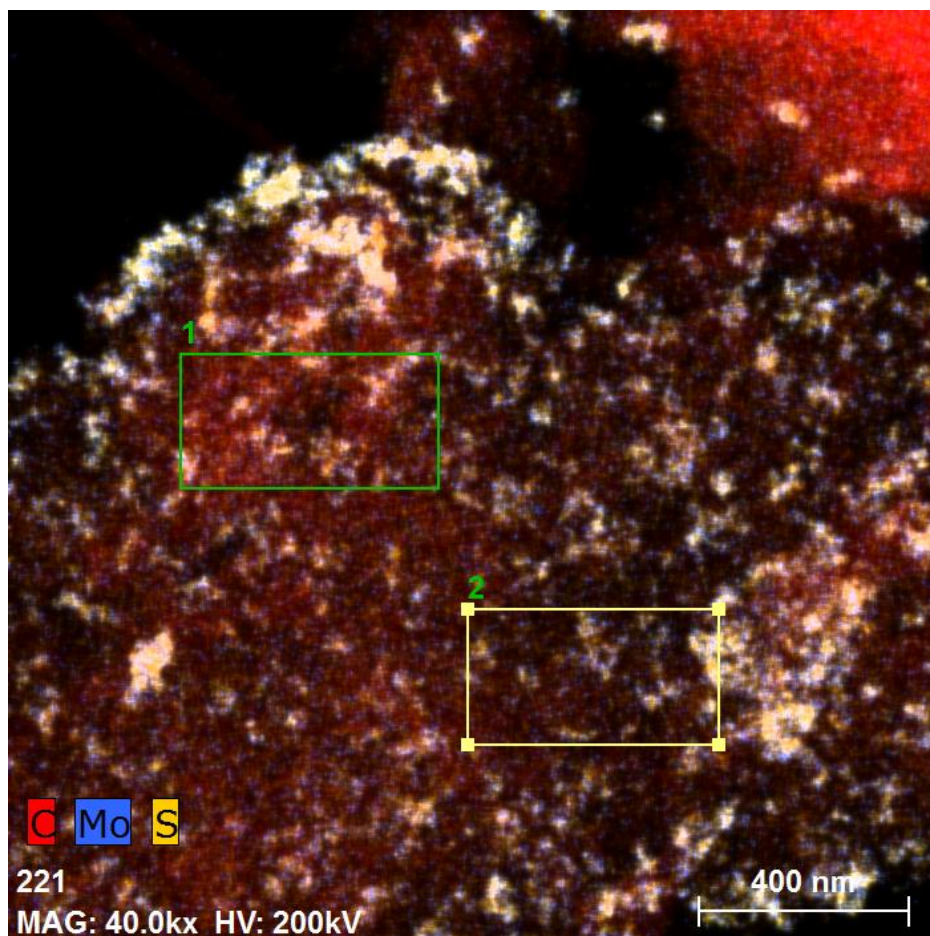


Figure E.19: A correlation of Mo, C, and S from HADDF-STEM-EDX mapping with two selected areas.

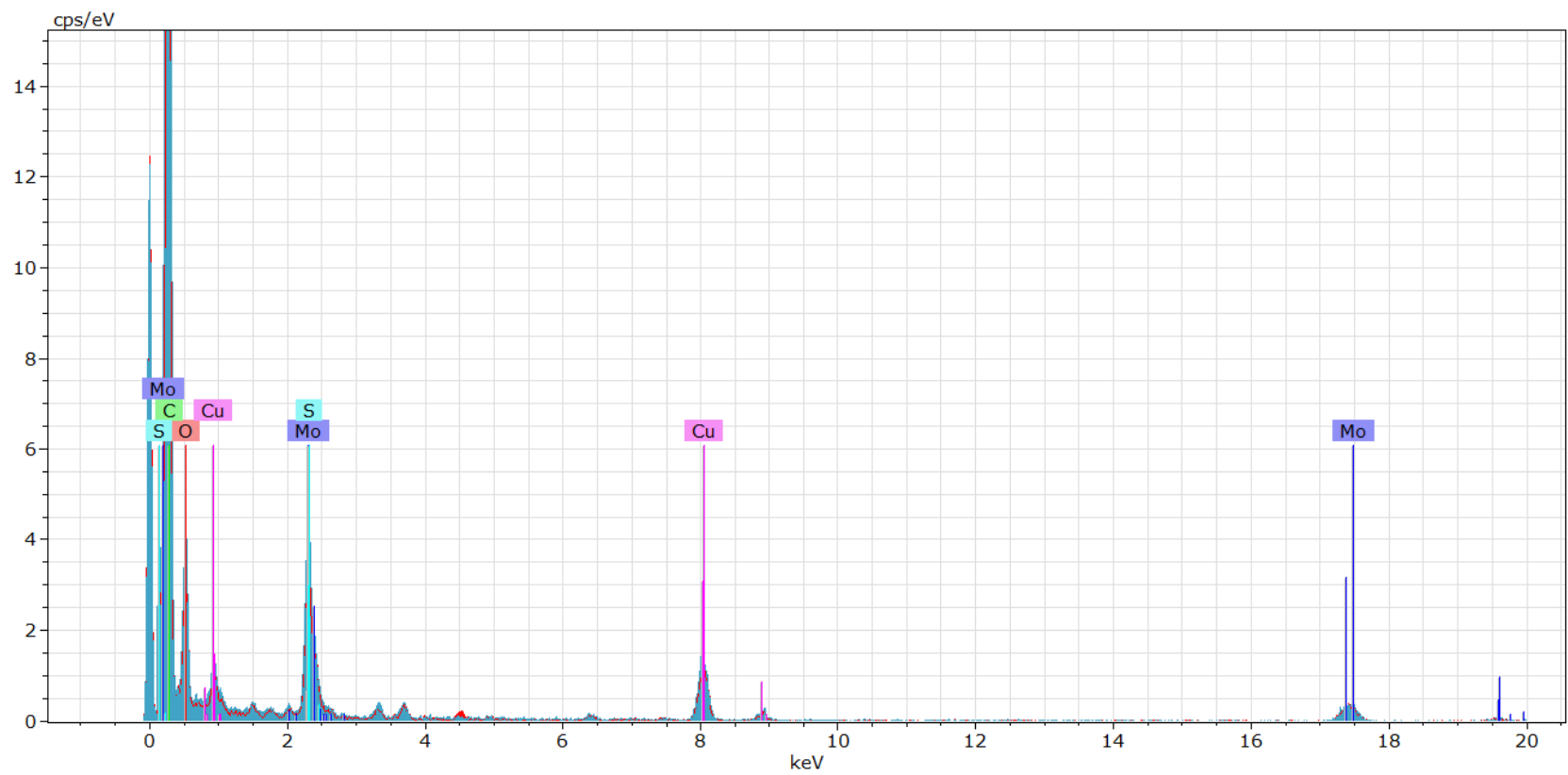


Figure E.20: EDX mapping for two selected areas of used $2\text{Mo}_2\text{C}/\text{APC}$ catalyst.

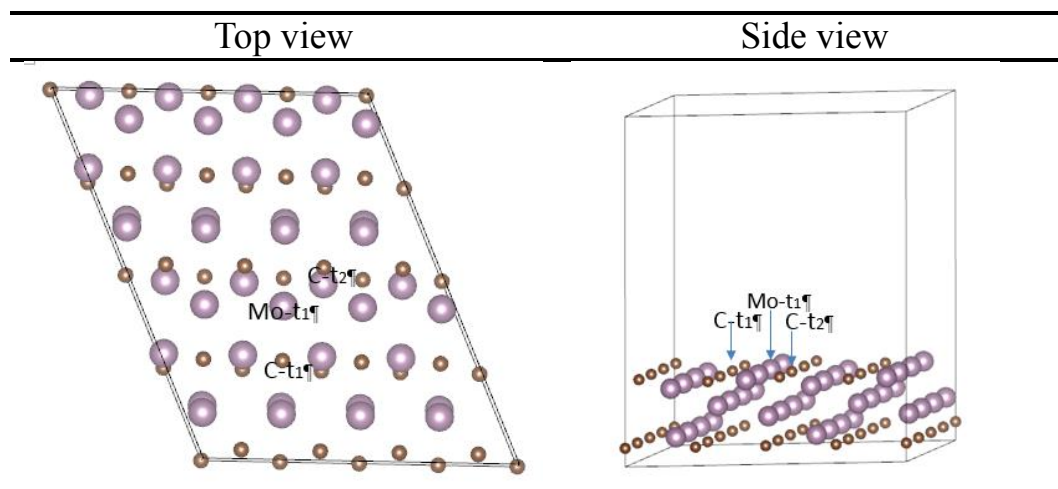


Figure E.21: Terminal positions of Mo_2C (101) surface used in DFT calculation. (Terminal Mo site: Mo-t1; terminal C sites: C-t1 and C-t2, respectively)

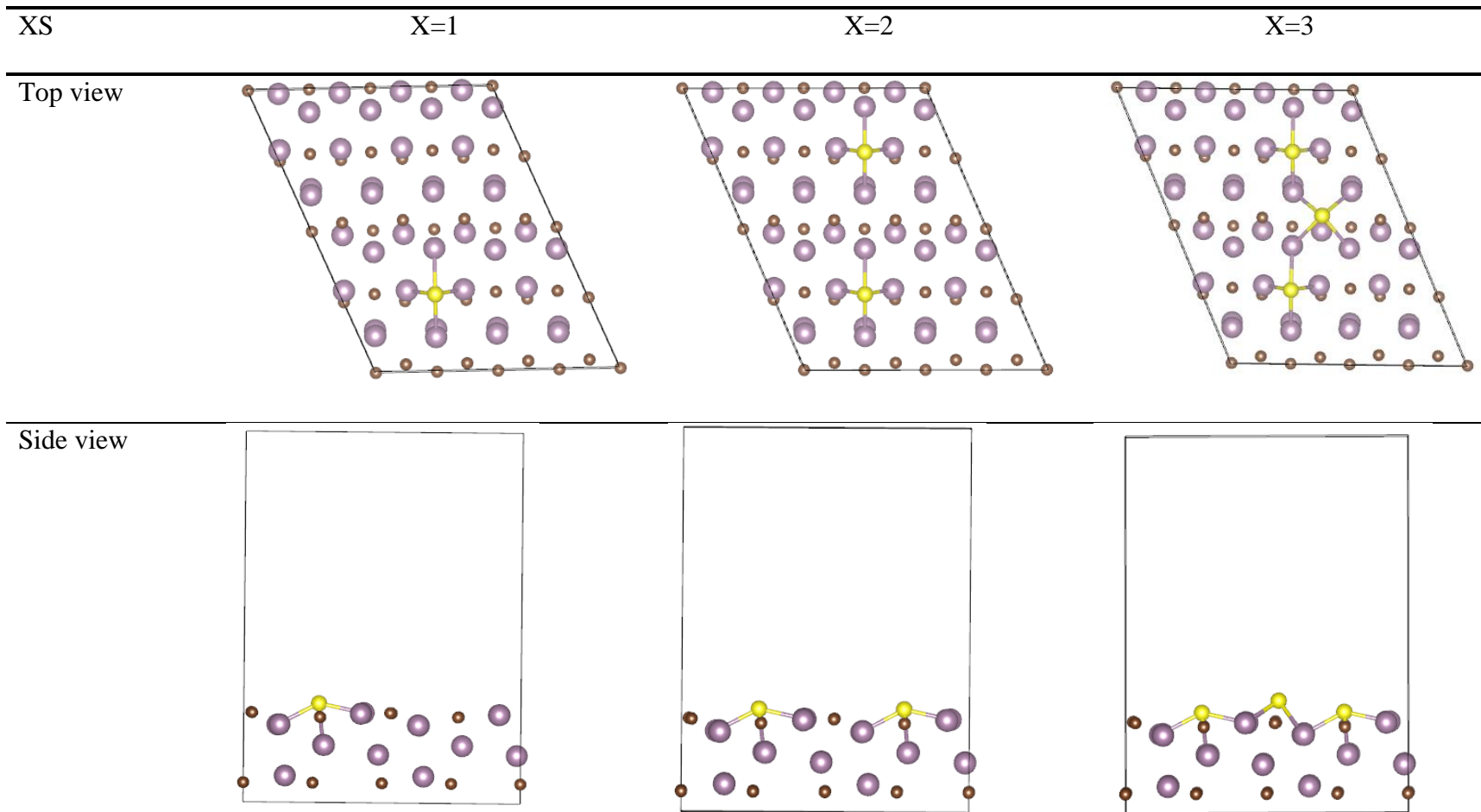


Figure E.22: Diagram of different S atoms replaced Mo₂C (101) surface for DBT adsorption energy calculation (Top and side views).

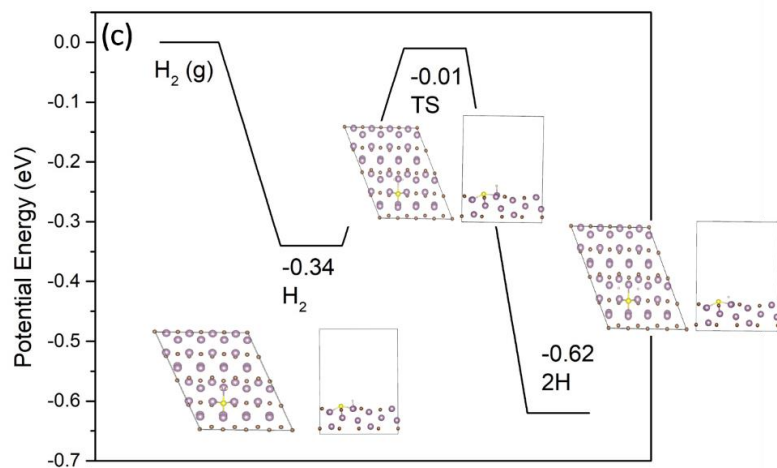
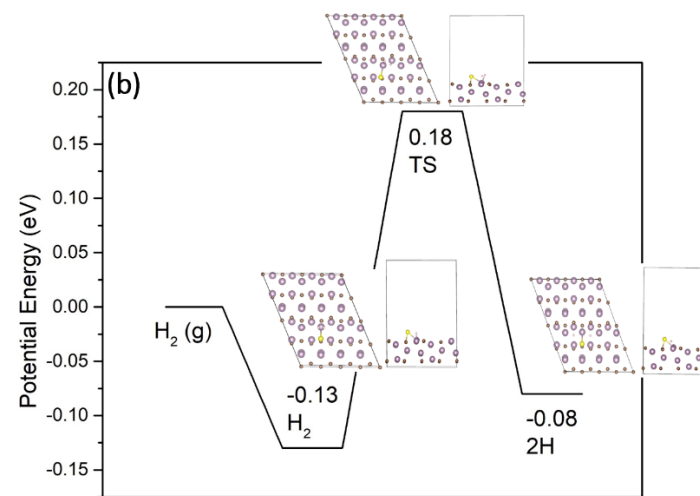
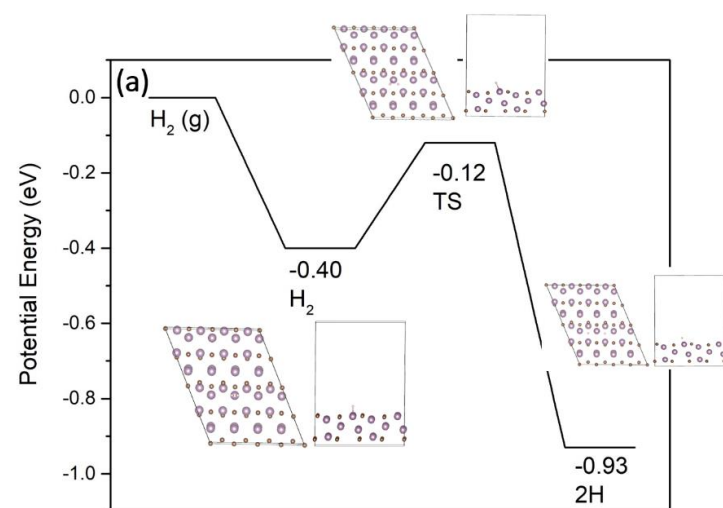


Figure E.23: Potential energy during dissociative adsorption of H₂ on three surfaces: (a) clean Mo₂C (101) surface; (b) S adsorbed Mo₂C (101) surface; (c) S replaced Mo₂C (101) surface.

Orientation name	DBT-V1		DBT-V2	
Top view & Side view				
Gibbs Free Adsorption Energy (eV)	-0.94		-1.01	
Orientation name	DBT-H1		DBT-H2	
Top view & Side view				
Gibbs Free Adsorption Energy (eV)	-1.53		-1.58	

Table E.4: Gibbs free adsorption energy of DBT on Mo-t1 site of Mo₂C (101) clean surface with different orientations.

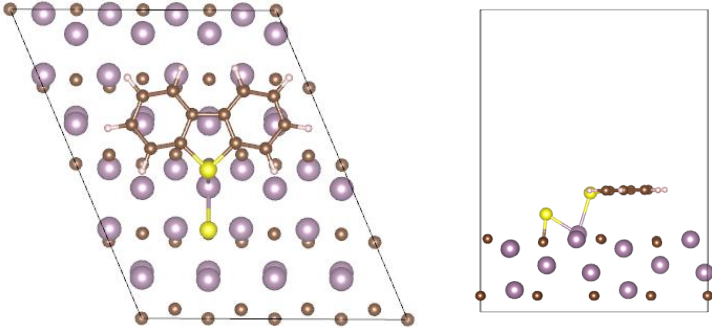
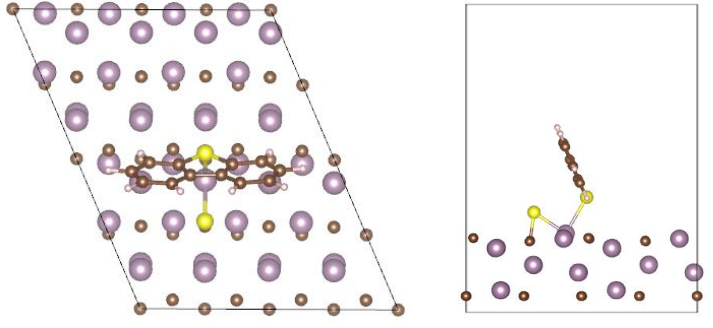
Orientation name	DBT-H1	DBT-V1
Top view & Side view		
Gibbs Free Adsorption Energy (eV)	-1.21	-0.99

Table E.5: Gibbs free adsorption energy of DBT on Mo-t1 site of S adsorbed Mo₂C (101) surface with different orientations.

E.5 Supplementary Information for Chapter 6

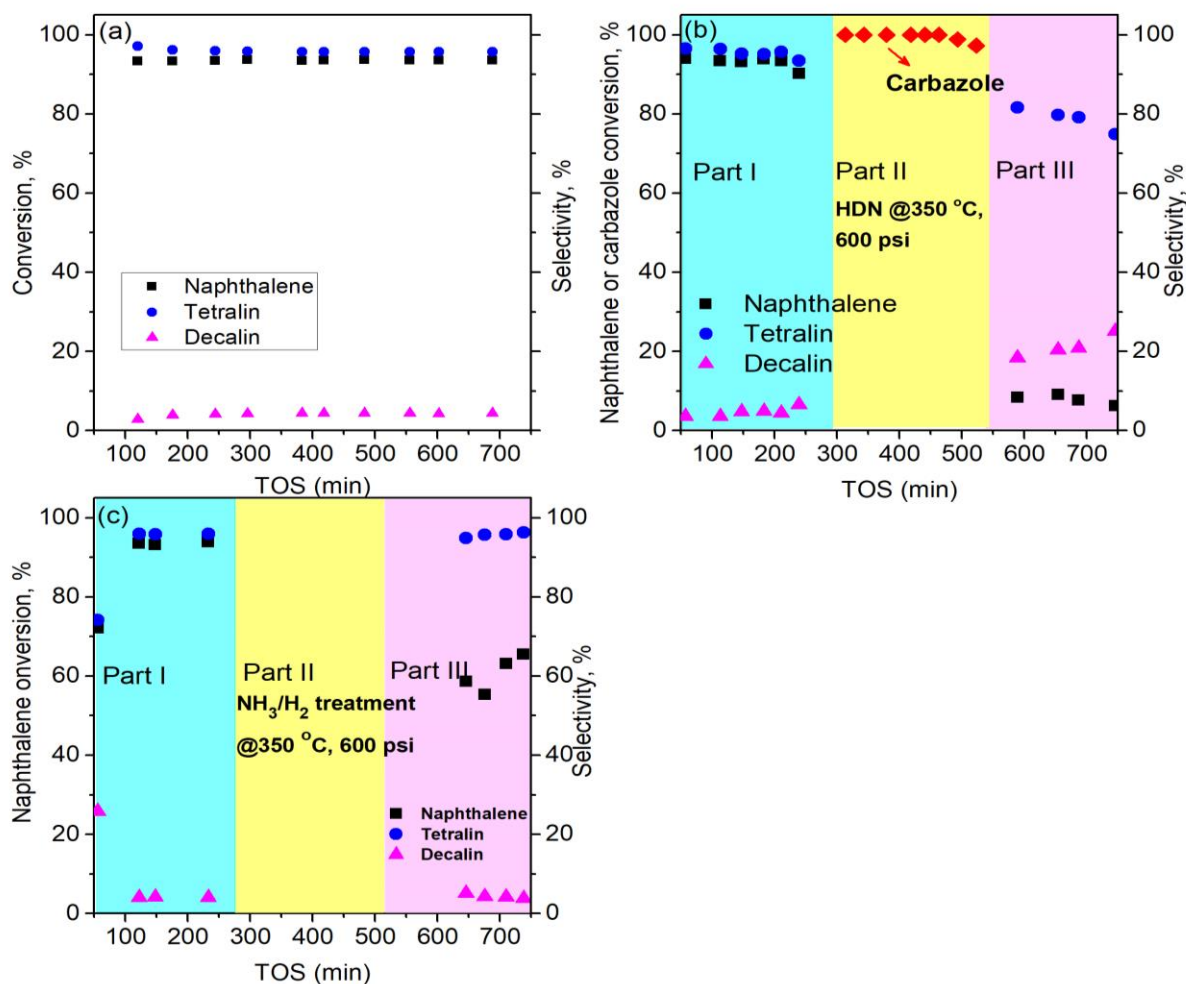


Figure E.24: Designed experiments for N effect study of 10Mo₂C/APC catalyst at 350 °C and 4.1 MPa: (a) naphthalene hydrogenation reaction at 250 °C and LHSV = 4 h⁻¹; (b) Part I-naphthalene hydrogenation, Part II-HDN of carbazole at 350 °C and 4.1 MPa, Part III-naphthalene hydrogenation; (c) Part I-naphthalene hydrogenation; Part II-NH₃/H₂ treatment at 350 °C and 4.1 MPa; Part III-Naphthalene hydrogenation.

The N could seriously affect the Mo₂C/APC catalyst as reported in Chapter 6. Several experiments were designed to see how does the catalyst has been modified in the presence of N. Figure E.24 (a) has clearly shown the strong hydrogenation ability of naphthalene on

10Mo₂C/APC catalyst with 93% conversion at 250 °C and 4.0 MPa. In Figure E.24 (b), the experiment has been designed into three phases, first with a hydrogenation of naphthalene, then HDN of carbazole and finally a hydrogenation of naphthalene again. After the 1st phase of hydrogenation reaction, it found that the catalyst is still active for HDN reaction (almost 100% conversion), indicative of the unchanged catalyst surface. Followed by HDN, another hydrogenation of naphthalene was conducted, where a huge drop on naphthalene conversion was observed in phase III. It suggests that most of the hydrogenation ability is lost after HDN reaction. In order to see if this change is caused by the released product-NH₃, NH₃/H₂ has been introduced in the 2nd phase of the experiment as shown in Figure E.24 (c). An equivalent amount of NH₃ (150 ppm) was used here with similar treatment time. It is interested to see that the conversion of naphthalene could fall to 65%, which is not severe than HDN of carbazole reaction. This phenomenon indicates the effect of N as NH₃, but it is not all the sources for this deactivation.

Appendix F Error Analysis and Repeatability

F.1 Carbon Balance

The carbon balance should be 100% for each experiment. However, due to sampling and experimental errors (GC-MS, operation etc.), it is hard to get a 100% carbon balance. It needs to be monitored during the data processing to see the accuracy of the experiment.

Table F.1 presents the reactant and products concentration of Ni_{0.19}Mo₂C/AC-550 and Ni_{0.38}Mo₂C/AC-550 catalysts over time for the reaction of HDS of DBT in batch reactor as reported in Chapter 3.

Table F.1: Reactant (DBT) and products concentration for HDS of dibenzothiophene over Ni_{0.19}Mo₂C/AC-550 and Ni_{0.38}Mo₂C/AC-550 catalysts.

Ni_{0.19}Mo₂C/AC-550 catalyst							
Time (h)	CHB(mol/L)	BPh (mol/L)	THDBT (mol/L)	DBT (mol/L)	Total mole of C (mol)	Total mole of C in Feed (mol)	Carbon balance error
1	7.5116E-04	1.3937E-02	1.0873E-03	8.1175E-02	1.1634E-01	1.1657E-01	0.20%
3	3.1119E-03	2.6506E-02	2.0758E-03	6.3547E-02	1.1429E-01	1.1657E-01	1.96%
5	4.2710E-03	3.3690E-02	2.6117E-03	5.6010E-02	1.1590E-01	1.1657E-01	0.58%

Ni_{0.38}Mo₂C/AC-550 catalyst							
Time (h)	CHB(mol/L)	BPh (mol/L)	THDBT (mol/L)	DBT (mol/L)	Total mole of C (mol)	Total mole of C in Feed (mol)	Carbon balance error
1	8.0949E-04	1.3931E-02	1.4353E-03	7.7898E-02	1.1289E-01	1.1657E-01	3.16%
3	2.2574E-03	2.3836E-02	2.2044E-03	6.1945E-02	1.0829E-01	1.1657E-01	7.11%
5	6.1666E-03	3.5773E-02	2.3100E-03	4.5395E-02	1.0757E-01	1.1657E-01	7.72%

F.2 Petcoke Activation Repeatability

Table F.2: Petroleum coke activation results from different batches.

Batch No.	Ratio of KOH to Petcoke	Mixture (KOH + Petcoke) Weight in boat (g)	Petcoke in ceramic boat (g)	Recoverd Petcoke (g)	Burn-off %
Batch1	2.96	13.51	3.41	2.25	34.06
Batch2	2.96	14.30	3.61	2.36	34.58
Batch3	3.00	13.18	3.29	2.08	36.87
Batch4	3.00	14.62	3.65	2.45	32.97
Batch5	2.97	13.97	3.52	2.21	37.28
Batch6	2.97	14.47	3.65	2.38	34.61
Batch7	2.97	13.70	3.45	2.20	36.22
Batch8	2.97	13.78	3.47	2.17	37.38
Batch9	3.00	13.39	3.35	2.13	36.34
Batch10	3.00	14.06	3.52	2.39	32.17
Batch11	3.00	14.38	3.60	2.19	39.06
Batch12	3.00	13.72	3.43	2.60	24.12
Batch13	3.00	14.36	3.59	2.53	29.51
Batch14	3.00	13.20	3.30	2.53	23.29
Batch15	3.00	13.54	3.39	2.15	36.42
Batch16	3.00	14.26	3.57	2.25	36.85
<i>Average</i>				2.31	33.86
<i>Std. dev. (SD)</i>				0.16	4.46

F.3 Reaction Repeatability

To observe the repeatability of the experiments, several experiments were repeated to quantify the error associated with the experiments.

(1) Batch reactor

Here, Ni_{0.19}Mo₂C/AC-550 and Ni_{0.38}Mo₂C/AC-550 catalysts tested in HDS of DBT were put here as an example. The obtained rate constants were reported in Table F.2.

Table F.3: Kinetic parameters for HDS of dibenzothiophene in batch reactor.

Catalysts	Run No.	k ₁ (mL/min.gmetal)	k ₂ (mL/min.gmetal)	k ₃ (mL/min.gmetal)
Ni _{0.19} Mo ₂ C/AC-550	1	2.1956E-01	7.8671E-01	4.7529E+00
	2	2.7313E-01	7.8574E-01	3.6545E+00
	Average	2.4635E-01	7.8622E-01	4.2037E+00
	Std.dev. (SD)	2.6787E-02	4.8463E-04	5.4921E-01
Ni _{0.38} Mo ₂ C/AC-550	1	2.9860E-01	8.1009E-01	4.8360E+00
	2	2.4624E-01	7.1025E-01	3.4768E+00
	Average	2.7242E-01	7.6017E-01	4.1564E+00
	Std.dev. (SD)	2.6179E-02	4.9917E-02	6.7962E-01

(2) Fixed bed reactor

2% Mo₂C/APC catalyst was used in the HDS reaction of DBT (0.2 wt%, eqv. 340 ppm S) in fixed bed reactor. The reaction was conducted at 350 °C, 600 psi, LHSV = 4 h⁻¹ with 0.77 g catalyst loading.

Table F.4: Catalyst properties of 2%Mo₂C/APC catalyst.

Catalyst	Exp. No.	Burn-off rate of the catalyst, %
2%Mo ₂ C/APC	T8	29.66
2%Mo ₂ C/APC	T13	28.43

The experimental data of T8 is reported as follows:

Table F.5: Experimental data of 2%Mo₂C/APC in HDS of DBT at 350 °C and 4.1 MPa from experiment T8.

TOS (min)	Conversion of DBT (%)	Selectivity (%)			
		THDBT	BPh	CHB	BCH
30	99.56	0.00	31.25	53.05	15.70
63	99.65	0.00	41.03	51.68	7.29
90	99.63	0.00	61.34	33.47	5.19
120	99.40	0.00	74.44	21.37	4.19
152	99.27	0.17	77.34	18.45	4.04
177	98.97	0.48	77.18	18.69	3.66
213	98.40	1.02	76.50	18.18	4.30
244	97.77	1.44	76.36	18.20	3.99
268	96.24	1.60	76.65	17.85	3.89
306	95.42	1.71	76.35	17.90	4.03
332	95.22	1.73	76.24	18.35	3.68
362	95.18	1.72	76.27	17.92	4.09
389	94.93	1.79	76.45	17.89	3.87
418	95.01	1.79	76.07	18.39	3.76
444	94.68	1.81	75.83	18.04	4.32
476	94.92	1.79	75.96	18.12	4.14
<i>Ave. value after 300 min</i>					
	97.00	1.02	73.62	20.43	4.93

The experimental data of T13 is reported in Table F.6:

Table F.6: Experimental data of 2%Mo₂C/APC in HDS of DBT at 350 °C and 4.1 MPa from experiment

T13.

TOS (min)	Conversion of DBT (%)	Selectivity (%)			
		THDBT	BPh	CHB	BCH
30	98.79	1.83	34.31	48.61	15.25
58	98.95	0.20	31.13	57.95	10.71
92	99.76	0.08	41.01	51.13	7.78
123	99.89	0.00	54.54	38.92	6.54
154	99.91	0.04	69.91	24.40	5.64
193	99.93	0.06	73.40	21.22	5.32
227	99.80	0.40	73.60	20.72	5.29
255	98.31	0.79	74.02	20.69	4.50
288	97.54	0.94	73.31	20.53	5.22
312	97.16	1.01	73.44	20.17	5.39
346	97.18	1.00	73.46	20.51	5.03
376	97.11	1.01	73.60	20.38	5.00
404	96.84	1.05	73.96	20.32	4.68
434	97.02	1.04	73.37	20.54	5.05
467	96.98	1.02	73.64	20.61	4.73
496	96.71	1.05	73.84	20.46	4.65
<i>Ave. value after 300 min</i>					
	95.05	1.76	76.17	18.09	3.98
	97.00 ^a	1.02 ^a	73.62 ^a	20.43 ^a	4.93 ^a
Ave. ^b	96.03	1.39	74.89	19.26	4.46
Std. dev. (SD) ^b	0.98	0.37	1.27	1.17	0.47

a. These data were adopted from Table F.4.

b. These values were calculated by comparing T8 and T13.

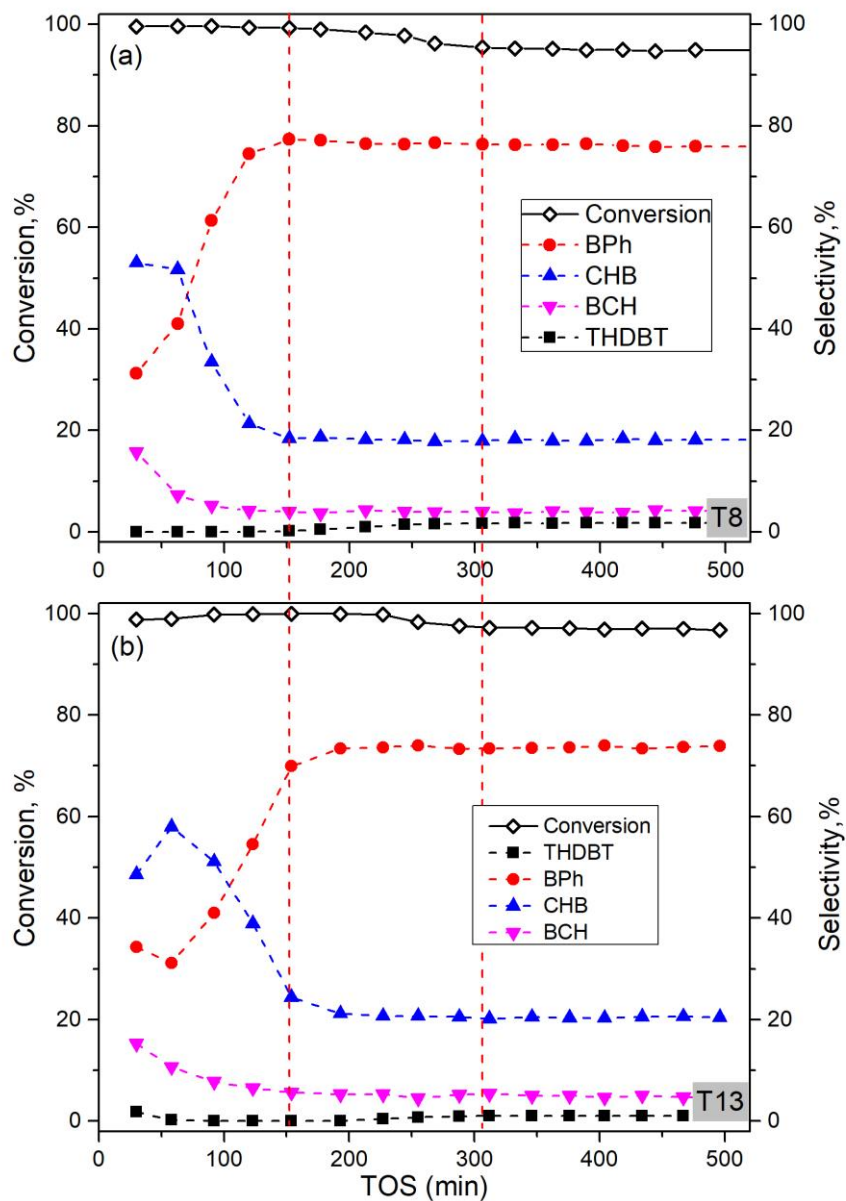


Figure F.1: DBT conversion and products selectivity for 2%Mo₂C/APC catalyst as a function of time on stream in two trails (T8 and T13).

From Table F.5, Table F.6 and Figure F.1, it can be observed that the experiment is repeatable.

F.4 Statistical Analysis of Kinetic Model

One way ANOVA analysis and F statistic test were conducted to see if the kinetic model fitted well with the experimental data. The probability (P) was set at 0.05. Both the experimental and kinetic model fitted data of Ni_{0.19}Mo₂C/AC-550 catalyst in HDS of DBT at 350 °C and initial pressure of 2.1 MPa were reported in Table F.7.

Table F.7: Comparison between experimental and kinetic model fitted data of different products and reactant in HDS of DBT by Ni_{0.19}Mo₂C/AC-550 catalyst.

Time (h)	CHB (mol/L)		BPh (mol/L)		THDBT (mol/L)		DBT (mol/L)	
	Experimental	Model	Exp.	Model	Exp.	Model	Exp.	Model
1	7.51E-04	4.00E-04	1.39E-02	1.00E-02	1.09E-03	2.30E-03	8.12E-02	9.10E-02
3	3.11E-03	2.73E-03	2.65E-02	2.65E-02	2.08E-03	4.43E-03	6.35E-02	7.00E-02
5	4.27E-03	5.80E-03	3.37E-02	3.92E-02	2.61E-03	4.79E-03	5.60E-02	5.39E-02
Ave.	2.71E-03	2.98E-03	2.47E-02	2.52E-03	1.92E-03	3.84E-03	6.69E-02	7.16E-02

The used formulas are summarized in Table F.8.

Table F.8: Summary of ANOVA used calculation formula.

Symbol	Definition	Formula
SS _{WG}	Sum of squares within groups	$SS_{WG} = \sum_{i=1}^m (X_i^2 + x_i^2) - \frac{(\sum_{i=1}^m X_i)^2 + (\sum_{i=1}^m x_i)^2}{m}$
SS _T	Total sum of squares	$SS_T = \sum_{i=1}^m (X_i^2 + x_i^2) - \frac{(\sum_{i=1}^m X_i + x_i)^2}{m}$, m is the number of data
SS _{BG}	Sum of squares between groups	$SS_{BG} = SS_T - SS_{WG}$
df _{WG}	Degrees of freedom within groups	$df_{WG} = \sum_{i=1}^z (m - 1)_i$, z means the set of data
df _{BG}	Degrees of freedom between groups	$df_{BG} = z - 1$
MS _{WG}	Mean square within groups	$MS_{WG} = \frac{SS_{WG}}{df_{WG}}$
MS _{BG}	Mean square between groups	$MS_{BG} = \frac{SS_{BG}}{df_{BG}}$
F _{ANOVA}	F value by ANOVA	$F_{ANOVA} = \frac{MS_{BG}}{MS_{WG}}$

The ANOVA analysis of the experimental and model data of different chemicals (DBT, CHB, BPh and THDBT) are reported in the Table F.9, Table F.10, Table F.11 and Table F.12.

Table F.9: ANOVA analysis of DBT concentration data in HDS of DBT by Ni_{0.19}Mo₂C/AC-550 catalyst.

DBT	SS	df	MS	F _{ANOVA}	F(1,4)
Between groups	3.35E-05	1	3.35E-05	1.31E-01	7.709
Within groups	1.02E-03	4	2.56E-04		
Sum	1.06E-03	5			

Note: F(1,4), P=0.05 was obtained from reference [192].

Table F.10: ANOVA analysis of CHB concentration data in HDS of DBT by Ni_{0.19}Mo₂C/AC-550 catalyst.

CHB	SS	df	MS	F _{ANOVA}	F(1,4)
Between groups	1.06E-07	1	1.06E-07	2.01E-02	7.709
Within groups	2.11E-05	4	5.28E-06		
Sum	2.12E-05	5			

Table F.11: ANOVA analysis of BPh concentration data in HDS of DBT by Ni_{0.19}Mo₂C/AC-550 catalyst.

BPh	SS	df	MS	F _{ANOVA}	F(1,4)
Between groups	4.14E-07	1	4.14E-07	2.64E-03	7.709
Within groups	6.28E-04	4	1.57E-04		
Sum	6.29E-04	5			

Table F.12: ANOVA analysis of THDBT concentration data in HDS of DBT by Ni_{0.19}Mo₂C/AC-550 catalyst.

THDBT	SS	df	MS	F _{ANOVA}	F(1,4)
Between groups	5.49E-06	1	5.49E-06	4.58E+00	7.709
Within groups	4.79E-06	4	1.20E-06		
Sum	1.03E-05	5			

From all these calculation, it found that all the $F_{ANOVA} < F(1,4, P=0.05)$, which means there is no significant difference between these two set of data, the model fitted data is fitted well with experimental data.

F.5 Characterization Repeatability

The sample standard deviation (SD) is used to describe the scatter of the obtained data. It can be calculated by Eq. F-1. Also, the mean value (μ) of the replicate measurements can be calculated as given in Eq. F-2. In the present study, both of them have been applied in various characterization data of BET, CO uptake, CHNS, EDX mapping, TOF-SIMS and GC/FID for in-situ CHR process as shown in the following tables.

$$SD = \sqrt{\frac{\sum_{i=1}^n (x_i - \mu)^2}{n-1}} \quad (\text{Eq. F-1})$$

$$\mu = \frac{\sum_{i=1}^n x_i}{n} \quad (\text{Eq. F-2})$$

$$\% \text{Error} = \frac{SD}{\mu} \quad (\text{Eq. F-3})$$

where x_i is the sample variable, μ is the average number of the samples' value, and n is the number of the samples.

Table F.13: Calculated error associated with the physical properties test of activated petroleum coke (APC).

Sample	Repeat No.	Surface area based on BET model (m ² /g)	Total pore volume (cm ³ /g)	Ave. pore size (nm)
Activated petcoke	1	2240	0.99	1.8
	2	2385	1.14	1.9
	3	2343	1.12	1.9
Mean value (μ)		2322	1.08	1.9
Std. dev. (SD)		61	0.07	0.1
% Error		2.6	6.5	5.3

Table F.14: Calculated error associated with the CO uptake.

Sample	Repeat No.	CO uptake ($\mu\text{mol/g}_{\text{cata.}}$)
10%Mo ₂ C/AC-600 fresh catalyst synthesized	1	16.7
	2	20.7
Mean value (μ)		18.7
Std. dev. (SD)		2.0
% Error		10.7
10%Mo ₂ C/APC-650 passivated catalyst	1	27.6
	2	22.4
Mean value (μ)		25.0
Std. dev. (SD)		2.6
% Error		10.4

Table F.15: Calculated error associated with CHNS analysis for raw petroleum coke.

Element	Repeated No.	Carbon	Hydrogen	Nitrogen	Sulfur	Oxygen
Raw petcoke	1	83.26	3.59	1.97	6.59	4.59
	2	83.28	3.61	2.07	6.57	4.47
Mean value (μ)		83.27	3.60	2.02	6.58	4.53
Std. dev. (SD)		0.01	0.01	0.05	0.01	0.06
% Error		0.012	0.28	2.48	0.15	1.32

Table F.16: Calculated error associated with EDX-mappings for raw petroleum coke and APC_800.

	Elements				
Sample	C	O	S	Al	Si
<i>PC-Raw Petroleum Coke</i>					
PC1	90.06	6.48	3.03	0.18	0.24
PC2	89.21	5.44	4.51	0.24	0.38
PC3	90.60	5.82	3.19	0.18	0.21
Ave.	89.96	5.91	3.58	0.20	0.28
Std. Dev.	0.57	0.43	0.66	0.03	0.07
% Error	0.63	7.28	18.44	15.00	25.00
<i>APC-Activated Petroleum Coke at 800 °C (APC_800)</i>					
APC1	92.87	6.92	0.00	0.22	0.00
APC2	93.86	6.14	0.00	0.00	0.00
APC3	92.40	7.27	0.00	0.33	0.00
Ave.	93.04	6.78	0.00	0.18	0.00
Std. Dev.	0.61	0.47	0.00	0.05	0.00
% Error	0.66	6.93	0.00	27.78	0.00

Table F.17: Calculated error associated with TOF-SIMS analysis for used 10%Mo₂C/AC-650 and Ni_{0.19}Mo₂C/AC-600 catalysts after HDS of DBT in batch reactor (Chapter 3).

Sample	130	146	162	178	194	Total ion (ΣI^+)	Total Identified MoS species ($\Sigma MoOxSy^-$)	S (ΣS^-)	Normalized S ($\Sigma S^-/\Sigma I^+$)	Normalized Identified total MoS species($Ri=\Sigma MoOxS^-$ $y^-/\Sigma I^+$)	Normalized MoS ($m/z=130$) ($Ri'=100MoS^-$ $\Sigma MoOxSy^-$)	Normalized MoOS ($m/z=146$) ($Ri'=100MoO$ $S/\Sigma MoOxSy^-$)	Normalized MoO2S or MoS2 ($m/z=162$) ($Ri'=100MoO2$ $S/\Sigma MoOxSy^-$)	Normalized MoO3S or MoOS2 ($m/z=178$) ($Ri'=100MoO3$ $S/\Sigma MoOxSy^-$)	Normalized MoO2S2 or MoS3 ($m/z=194$) ($Ri'=100MoO2$ $S2/\Sigma MoOxSy^-$)
	MoS	MoOS	MoO ₂ S	MoO ₃ S	MoO ₂ S ₂										
	MoO ₂	MoO ₃	MoS ₂	MoOS ₂	MoS ₃										
Ni:Mo=0.19	651	5242	2547	416	585	3541990	9441	76159	2.15E-02	2.67E-03	6.90	55.52	26.98	4.41	6.20
Ni:Mo=0.19	617	5099	2376	398	523	3509877	9013	79214	2.26E-02	2.57E-03	6.85	56.57	26.36	4.42	5.80
Ni:Mo=0.19	598	4663	2163	375	510	3506899	8309	84121	2.40E-02	2.37E-03	7.20	56.12	26.03	4.51	6.14
AVE	622	5001	2362	396	539	3519589	8921	79831	2.27E-02	2.53E-03	6.98	56.07	26.46	4.45	6.05
Std. Dev.	22	246	157	17	33	15887	467	3280	1.02E-03	1.23E-04	0.16	0.43	0.39	0.05	0.17
Ni:Mo=0.00	594	2356	1092	326	183	3840918	4551	76854	2.00E-02	1.18E-03	13.05	51.77	23.99	7.16	4.02
Ni:Mo=0.00	767	2825	1294	340	181	4219830	5407	73420	1.74E-02	1.28E-03	14.19	52.25	23.93	6.29	3.35
Ni:Mo=0.00	602	2643	1245	318	190	3536102	4998	70630	2.00E-02	1.41E-03	12.04	52.88	24.91	6.36	3.80
AVE	654	2608	1210	328	185	3865617	4985	73635	1.91E-02	1.29E-03	13.09	52.30	24.28	6.60	3.72
Std. Dev.	80	193	86	9	4	279677	350	2545	1.22E-03	9.37E-05	0.87	0.46	0.45	0.40	0.28

Note: Ni: Mo=0.19 stands for Ni_{0.19}Mo₂C/AC-600 catalyst; Ni: Mo=0.00 stands for 10%Mo₂C/AC-650 catalyst.

Table F.18: Calculated error associated with in-situ exit gas analysis of 2%Mo₂C/APC-700 by carbothermal hydrogen reduction.

Temperature (°C)	Exp1		Exp2		Mean value (μ)	Std.dev. (SD)	%Error
	Time interval (min)	CH ₄ mol%	Time interval (min)	CH ₄ mol%			
91	66	0	66	0	0	0	—
265	240	0	240	0	0	0	—
340	315	0	315	0	0	0	—
421	396	0.105056	396	0.104056	0.104556	0.0005	0.478213
464	439	0.164288	439	0.165288	0.164788	0.0005	0.30342
487	462	0.224928	462	0.223928	0.224428	0.0005	0.222789
558	533	0.502131	535	0.502238	0.502185	5.37E-05	0.010699
588	563	0.62465	566	0.653348	0.638999	0.014349	2.245537
626	601	1.04215	605	1.104975	1.073563	0.031413	2.926027
652	627	1.615816	631	1.579067	1.597441	0.018374	1.150245
678	653	2.463443	655	2.479983	2.471713	0.00827	0.334587
700	675	3.080209	670	2.9567	3.018454	0.061754	2.045897
700	700	3.017785	699	3.0249	3.021343	0.003557	0.117739
700	720	2.921921	726	2.943344	2.932633	0.010712	0.36526
700	736	2.864935	740	2.8954	2.880167	0.015233	0.528876
700	750	2.834814	755	2.8644	2.849607	0.014793	0.519122
700	765	2.802529	770	2.7095	2.756014	0.046514	1.687738

Appendix G Mass Transfers and Heat Transfer Effects

In order to show if the experiments obtained in fixed-bed reactor have been controlled by mass transfer, several calculations have been applied to illustrate the external and internal mass diffusion phenomenon. Also, a heat transfer calculation was conducted by Mears' Criterion. As an example, 10%Mo₂C/APC catalyst in HDS of DBT (0.2 wt%) at 350 °C and P=600 psi has been put here. The details of the catalyst bed, reaction condition, and catalyst properties are shown in Table G.1.

Table G.1: The details of catalyst bed, catalyst physical properties and related kinetic parameters.

Symbol	Definition	Calculation formula/Source	Value	Unit
$-r_{\text{DBT(obs)}}$	Observed reaction rate	Calculated from experimental data	1.81E-10	[kmol/gcat·s]
k_1	Stabilized kinetic parameter	Calculated from experimental data	1.67E-02	[s ⁻¹]
V_c	Loaded catalyst volume	Measured	0.50	[mL]
V_{sic}	Loaded inert volume	Measured	2.00	[mL]
V_{bed}	Total volume of catalyst bed	$V_{\text{bed}}=V_c+V_{\text{sic}}$	2.50	[mL]
L_{bed}	Length of the catalyst bed	Measured	4.20	[cm]
ρ_{bsic}	Catalyst bed density with SiC and catalyst	$\rho_{\text{bsic}}=m_{\text{total}}/V_{\text{bed}}$	1.4680	[g/cm ³]
ρ_c	Catalyst density	Calculated by 1.48 [g/cm ³] x 80% + 8.90 [g/cm ³] x 20%, where $\rho_{\text{AC}}=1.48$ [g/cm ³]; $\rho_{\text{Mo}_2\text{C}}=8.90$ [g/cm ³]	2.9640	[g/cm ³]
ρ_{sic}	SiC density	—	3.2100	[g/cm ³]
ρ_{solid}	Solid catalyst density	$\rho_{\text{solid}}=(\rho_c V_c+\rho_{\text{sic}} V_{\text{sic}})/(V_c+V_{\text{sic}})$	3.1608	[g/cm ³]
m_{cat}	Mass of loaded catalyst	Measured	0.16	[g]
m_{sic}	Mass of SiC	Measured	3.51	[g]
m_{total}	Mass of loaded catalyst bed	$m_{\text{total}}=m_{\text{cat}}+m_{\text{sic}}$	3.67	[g]
\emptyset	Porosity or void fraction of packed bed	$\emptyset=1-\rho_{\text{bsic}}/\rho_{\text{solid}}$	0.5356	—
ρ_b	Bulk density of catalyst bed	$\rho_b=\rho_c*(1-\emptyset)$	1.3766	[g/cm ³]
d_p	Catalyst particle diameter	Measured	1.35E-04	[m]
R	Catalyst particle radius	$R=d_p/2$	6.75E-05	[m]
n	reaction order	—	1	—
V_o	Total pore volume of the catalyst	Measured	1.16	[cm ³ /g]
$S_{\text{cat.}}$	Surface area of the catalyst	Measured	1651	[m ² /g]
r_{pore}	Pore radii of the catalyst	Measured	1.40521E-07	[cm]
\emptyset_p	Catalyst particle porosity	$\emptyset_p=V_o/(V_o+1/\rho_c)$	0.7747	—
τ	Tortuosity factor	—	3	—
σ_c	Constriction factor	—	0.8	—
γ	Shape factor	$\gamma = \frac{\text{External surface area}}{\pi d_p^2}$	1.00E+00	—

G.1 External Mass Transfer Effect

The details of feed properties were calculated by ASPEN Plus with Wilson method as reported in Table G.2.

Table G.2: The details of reaction conditions and feed properties as calculated from Aspen Plus.

Symbol	Definition	Calculation formula/Source	Value	Unit
T_{rxn}	Reaction temperature	—	623.15	[k]
P_{rxn}	Reaction pressure	—	40.83	[atm]
M_{DBT}	Mole weight of DBT	—	184.256	[g/mol]
M_{H_2}	Mole weight of H_2	—	2.016	[g/mol]
$M_{Decalin}$	Mole weight of Decalin	—	138.25	[g/mol]
$T_{DBT,c}$	Critical point temperature of DBT	—	897	[k]
$\tilde{V}_{DBT,c}$	Critical volume of DBT	—	525	[mL/g-mol]
ρ_{mix}	Density of feed mixture density at 350 °C and 600 psi	0.1667 cc/min 0.2 wt% DBT in decalin, 100 cc/min H_2	2.07	[kg/m ³]
μ_{mix}	Dynamic viscosity of the mixture	—	1.51E-05	[kg/m.s]
ν_{mix}	kinetic viscosity of mixture	—	7.32E-06	[m ² /s]
M_{mix}	Feed molecular weight	—	2.24E+00	[g/mol]
P_{H_2}	Partial pressure of H_2	—	41.93	[atm]
P_{DBT}	Partial pressure of DBT	—	1.08E-04	[atm]
$P_{Decalin}$	Partial pressure of Decalin	—	6.98E-02	[atm]
P_{total}	Total pressure in the system at 350 oC and 600 psi	—	41.9999	[atm]
C_{H_2}	Bulk gas concentration of H_2 at 350 °C and 600 psi	—	1.0333	[kmol/m ³]
C_{DBT}	Bulk gas concentration of DBT at 350 °C and 600 psi	—	2.89E-08	[kmol/m ³]

Table G.3: The details of external mass transfer calculation by Mears criterion.

Symbol	Definition	Calculation formula/Source	Value	Unit
U	Superficial gas velocity	$U = \gamma_{mix} / A$	2.85E-02	[m/s]
γ_{mix}	Volumatic flow rate	100 [cc/min H ₂] + 0.1667 [cc/min] Feed	1.67E-06	[cm ³ /s]
A	Cross section area of the reactor	$A = \pi r_{bed}^2$ ($\gamma_{bed} = 0.432$ cm)	5.86E05	[m ²]
σ_{DBT}	Lennard-Jones parameters for DBT/characteristic length	$\sigma_{DBT} = 0.841 * \tilde{V}_{DBT,c}^{1/3}$	6.7845	[Å]
σ_{H2}	Lennard-Jones parameters for H ₂ /characteristic length	—	2.915	[Å]
σ_{DBT-H2}	Lennard-Jones parameters for DBT-H ₂ /characteristic length	$\sigma_{DBT-H2} = \frac{1}{2} (\sigma_{DBT} + \sigma_{H2})$	4.8497	[Å]
$\epsilon_{DBT/K}$	Lennard-Jones parameters for DBT/Boltzmann's constant	$\epsilon_{DBT/K} = 0.77 T_{DBT,C}$	690.69	[k]
$\epsilon_{H2/K}$	Lennard-Jones parameters for H ₂ /Boltzmann's constant	—	38	[k]
$\epsilon_{DBT-H2/K}$	Lennard-Jones parameters for DBT-H ₂ /Boltzmann's constant	$\frac{\epsilon_{DBT-H2}}{K} = \sqrt{\frac{\epsilon_{DBT-H2}}{K} \times \frac{\epsilon_{H2}}{K}}$	162.00	[k]
T*	Dimensionless temperature	$T^* = K T_{rxn} / \epsilon_{DBT-H2}$	3.8464	[k]
$\Omega_{D, DBT-H2}$	Collision integral, calculated by ignore the last two terms	$\Omega_{D, DBT-H2} = \frac{1.06036}{T^{*0.15610}} + \frac{0.19300}{\exp(0.47635T^*)}$	0.8902	—
D_{DBT-H2}	Binary bulk phase diffusivity	$D_{CH4-He} = \frac{0.0018583}{P_{rxn} \sigma_{DBT-H2}^2 \Omega_{D, DBT-H2}} \sqrt{T^3 \left(\frac{1}{M_{DBT}} + \frac{1}{M_{H2}} \right)}$	2.39E-06	[m ² /s]
Sc	Schmidt number	$Sc = v_{mix} / D_{DBT-H2}$	3.06E+00	—
Sh	Sherwood number	$Sh = 2 + 0.6 Re^{1/2} Sc^{1/3}$	2.93E+00	—
Re	Reynolds number	$Re = \frac{U \rho d_p}{\mu}$	5.26E-01	—
Re'	Reynolds number considering void fraction	$Re' = \frac{Re}{(1-\phi)\gamma}$	1.13E+00	—
kc	Mass transfer coefficient	$kc = \frac{Sh \times D_{DBT-H2}}{d_p}$	5.19E-02	[m/s]
MC	Mears' criterion for external difussion	—	1.12E-11	—

Based on Mears' criterion [193], the calculated value is accorded with $\frac{-r_{DBT(Obs)}\rho_b Rn}{k_c C_{DBT}} \ll 0.15$,

thus the external mass transfer effects can be neglected.

G.2 Internal Mass Transfer Effect

Table G.4: The details of internal mass transfer by Weisz-Prater criterion.

Symbol	Definition	Calculation formula/Source	Value	Unit
D_{DBT-H2}	Binary bulk phase diffusivity	D_{CH4-He} $= \frac{0.0018583}{P_{rxn} \sigma_{DBT-H2}^2 \Omega_{D,DBT-H2}} \sqrt{T^3 \left(\frac{1}{M_{DBT}} + \frac{1}{M_{H2}} \right)}$	2.39E-06	[m ² /s]
$D_{eff, DBT-H2}$	Effective diffusivity	$D_{eff, DBT-H2} = \frac{D_{DBT-H2} \phi_P \sigma_C}{\tau}$	4.95E-07	[m ² /s]
$D_{knudsen}$	Knudsen diffusivity	$D_{knudsen} = \frac{2r_{pore}}{3} \sqrt{\frac{(8 \cdot R_g) \cdot T}{\pi \cdot M_{mix}}}$	2.27E-06	[m ² /s]
$D_{eff, knudsen}$	Effective knudsen diffusivity	$D_{eff, knudsen} = \frac{D_{knudsen} \phi_P \sigma_C}{\tau}$	4.69E-07	[m ² /s]
$D_{eff, rxn}$	Effective diffusivity in this reaction	$\frac{1}{D_{eff, rxn}} = \frac{1}{D_{eff, DBT-H2}} + \frac{1}{D_{eff, knudsen}}$	2.41E-07	[m ² /s]
ϕ_1	Thiele modulus for 1st order reaction	$\phi_1 = R \sqrt{\frac{k_1}{D_{eff, rxn}}}$	1.78E-02	—
η	Internal effectiveness factor	$\eta = \frac{3}{\phi_1^2} (\phi_1 \coth \phi_1 - 1)$	1.00E+00	—
C_{wp}	Weisz-Prater criterion	—	3.17E-04	—

Based on Weisz-Prater criterion [193], the calculated value of $C_{WP} = \eta \phi_1^2 = \frac{-r_{DBT(obs)} \rho_c R^2}{D_{eff, rxn} C_{AS}} \ll 1$,

thus there are no internal diffusion limitations.

G.3 Heat Transfer Effect

Table G.5: The details of heat transfer calculation by Mears Criterion.

Symbol	Definition	Calculation formula/Source	Value	Unit
	Thermal conductivity			
kt	calculated by semiempirical method for polyatomic gases	$kt = \left(\frac{\hat{C}_{p,(H_2)} + 5R}{4M_{H_2}} \right) \mu_{mix}$	2.98E-01	[W/(m.K)]
$\hat{C}_{p(H_2)}$	Heat capacity of H ₂ at Trxn	—	14500	[J/Kg·K]
ΔH_{rxn}	Heat of reaction	Primary reaction: $C_{12}H_8S + 2H_2 \rightarrow C_{12}H_{10} + H_2S$	-45.5	KJ/mol
Ea	Activation energy	Estimated based on literature	150000	[J/mol]
Pt	Prandtl number	$Pr = \mu_{mix} \cdot \hat{C}_p / kt$	7.38E-01	—
Nu	Nusselt number	$Nu = 2 + 0.6Re^{1/2} Pr^{1/3}$	2.58E+00	—
h	Heat transfer coefficient	$h = \frac{Nu \cdot kt}{d_p}$	5.68E+03	[W/(m ² ·K)]
Rg	Gas constant	—	8.314	[J/(mol·k)]
MC'	Mears' criterion for isothermal operation	—	6.25E-18	—

Based on Mears' criterion [193, 194], the calculated value of $\left| \frac{-\Delta H_{rxn}(-r_{DBT,obs})\rho_b R E}{hT^2 R_g} \right| \ll 0.15$,

thus there is no temperature gradient during reaction.

G.4 Precheck of Fixed-bed Reactor Operating Condition

In order to ensure the kinetic data are free from the influence of unwanted transport effects, including wall effect and axial dispersion, some criteria have been applied to evaluate the designed reactor bed [195].

Table G.6: The geometry parameters for prechecking of fixed-bed reactor operating condition.

Symbol	Definition	Value	Unit
d_p	Catalyst particle diameter	1.35E-04	m
L_{bed}	Length of catalyst bed	4.20E-02	m
D_{bed}	Fixed-bed tube diameter	8.64E-01	m
$\frac{D_{bed}}{d_p}$	—	6.40E+03 > 10	—
$\frac{L_{bed}}{d_p}$	—	3.11E+02 > 50	—

From Table G.6, it find that the value of $\frac{D_{bed}}{d_p} > 10$, suggesting that the reactor wall effect can be eliminated. The value of $\frac{L_{bed}}{d_p} > 50$ indicates that the axial effect can be ignored as well.

G.5 External and Internal Mass Transfers in Batch Reactor

All the kinetic data reported in Chapter 2 and 3 were obtained from a batch reactor operation after excluding external and internal mass transfer's effects. Ni_{0.09}Mo₂C/AC-550 catalyst was put here as an example.

Table G.7: A detailed list of external and internal mass transfer coefficient calculation for Ni_{0.09}Mo₂C/AC-550 in HDS of DBT in batch reactor.

Symbol	Definition	Value	Unit
k_{La}	Liquid-side mass transfer coefficient ^a	4.37E-02	s ⁻¹
k_{DBT}	Kinetic parameter	1.77E-05	s ⁻¹
R	Catalyst particle radius	6.75E-05	m
ϕ_1	Thiele modulus for 1 st order reaction	4.04E-04	—
$D_{\text{eff, DBT-H}_2}$	Effective diffusivity	4.95E-07	m ² /s
η	Internal effectiveness factor	1.00E+00	—
Ω	Overall effectiveness factor ^b	1.00E+00	—

a. This number was adopted from [196] since the operating system was the same as the previous group member's.

b.
$$\Omega = \frac{\eta}{(1 + \frac{\eta k_{DBT}}{k_{La}})}$$

As shown in Table G.7, $k_{La} \gg k_{DBT}$ and $\eta = \Omega = 1$, thus the external and internal mass transfer can be neglected under present conditions.

Appendix H Additional Calculation and Experimental Data

H.1 Carbon Efficiency Calculation for Mo₂C Formation

Take 10%Mo₂C/APC-700 as an example (The carbon burn-off% is 30.35%):

For 1 g of 10%AHM/APC precursor,

The mole of Mo is $\frac{0.1 \text{ gMo}}{95.94 \text{ g/mol}} = 1.04 \times 10^{-3} \text{ mol}$

The required amount of C for Mo₂C formation = $\frac{1.04 \times 10^{-3} \text{ mol}}{2} \times 12 \frac{\text{g}}{\text{mol}} = 6.25 \times 10^{-3} \text{ g}$

The lost C calculated from burn-off% = $0.9 \text{ g} \times 30.35\% = 0.27 \text{ g}$

The carbon efficiency is $\frac{6.25 \times 10^{-3}}{0.27} = 2.32\%$

H.2 Comparison between 10%MoS₂/Al₂O₃, 10%MoS₂/AC, and 10%Mo₂C/AC

Catalysts

The performance of 10%MoS₂/Al₂O₃, 10%MoS₂/AC, and 10%Mo₂C/AC catalysts were tested in HDS of DBT at 350 °C with an initial pressure of 2.1 MPa in a batch reactor. The DBT conversion and products selectivity were reported in Table H.1.

Table H.1: DBT conversion and products selectivity of 10%MoS₂/Al₂O₃, 10%MoS₂/AC, and 10%Mo₂C/AC catalysts in HDS of DBT at 350 °C and initial pressure of 2.1 MPa.

Catalysts	DBT Conv. (%)	Time (h)	Product selectivity (%)		
			BPh	THDBT	CHB
10%MoS ₂ /Al ₂ O ₃	8.87	1	34.92	54.28	10.80
	25.38	3	34.80	49.84	15.36
	34.68	5	34.19	47.05	18.76
10%MoS ₂ /AC	10.68	1	76.28	21.21	2.51
	33.03	3	70.15	14.34	15.51
	44.04	5	69.87	15.41	14.72
10%Mo ₂ C/AC	14.87	1	83.69	11.55	4.76
	27.68	3	82.67	13.15	4.18
	40.31	5	78.91	14.25	6.71

H.3 Mesoporous Carbon Development by Ni-Mo₂C on APC

Table H.2: Physical properties of APC supported Ni-Mo₂C catalysts.

Sample	BET Surface area (m ² /g)	BJH surface area (m ² /g)	Total Pore volume (cm ³ /g)	t-plot micro pore volume (cm ³ /g)	BJH pore volume (cm ³ /g)	V _{BJH} /V _{total} ratio	Ave Pore size (nm)	BJH pore size (nm)	Yield (%)
APC_800	2413	447	1.17	0.78	0.30	25.99	1.9	2.7	66.14
APC_800-redH ₂ 500-600C	2420	512	1.17	0.78	0.33	28.23	1.9	2.7	86.95
1%Ni/APC precursor	2180	402	1.05	0.71	0.27	25.98	1.9	2.7	N/A
1%Ni/APC-redH ₂ 500-600	2394	434	1.15	0.76	0.29	25.33	1.9	2.7	90.16
1%Ni-10%Mo ₂ C/APC	2014	911	1.52	0.41	1.07	70.54	3.0	4.7	64.47
2%Ni_10%Mo ₂ C/APC	1690	995	1.89	0.23	1.68	88.62	4.5	6.7	38.04

In order to study the effect of Ni on pore development, APC_800 support with 1 wt% of Ni was prepared (recorded as 1%Ni/APC precursor). From Table H.2, it found that the CHR could bring a similar pore development effect with or without Ni at 600 °C (Compare sample APC_800-redH₂ 500-600C and 1%Ni/APC-redH₂ 500-600C). Ni alone couldn't bring a big influence on pore development. However, the BJH pore volume was significant increased for 1%Ni-Mo₂C/APC sample with account of 70% BJH porosity by 1 wt.% of Ni. It indicates that Ni may immerse into the structure of Mo₂C, accelerating the C burn-off rate by generating more mesopores.